Upgrading of Oleic Acid, Olive Oil, and Used Cooking Oil via Bubbling Ozonolysis

Rungrote Kokoo

A thesis submitted in partial fulfilment of the requirements for the degree of
Doctor of Philosophy

The University of Sheffield

Faculty of Engineering

Department of Chemical and Biological Engineering

June 2015

Preface

This thesis is submitted for the degree of Doctor of Philosophy at the University of Sheffield, and is available for library use as a learning material. The purpose of this thesis is to introduce ozonolysis via a bubbling technique for upgrading bio-chemicals i.e., oleic acid and olive oil and to reduce the free fatty acid content in used cooking oil under supervision of Professor William B. J. Zimmerman in the Department of Chemical and Biological Engineering.

I certify that all the results and works described in this dissertation are original and have not been submitted in whole or any part for other degrees at this or any other universities.

Rungrote Kokoo
University of Sheffield
June 2015

Abstract

In this study, ozonolysis applied via a bubbling technique at different temperatures was used to upgrade bio-chemicals, i.e., oleic acid and olive oil, to form valuable products, especially 1-nonanal. Short-chain alcohols (C1-C4) were added to these chemicals to increase productivity. Used cooking oil mixed with methanol was also ozonised to reduce the free fatty acid content for biodiesel production. The by-product from olive oil ozonolysis was subsequently used as a reactant for bio-kerosene production via conventional transesterification. Two techniques were used to generate bubbles, namely, with and without the use of a fluidic oscillator. The bubble column reactor used in this study was designed using Aspen Plus and COMSOL Multiphysics. The Henry's Law constant and the diffusion coefficient were determined using Aspen Plus. The inlet ozone concentration and specific interfacial area were evaluated using the KI method and an optical technique, respectively. All samples from bio-chemical ozonolysis were analysed by GC-MS, and samples from used cooking oil ozonolysis were analysed using both GC-MS and ASTM D974.

In the case of ozonolysis of pure oleic acid, the results show that 1-nonanal is the major product with a 93.5±3.4% yield at 20^{o}C, whereas 9-oxononanoic acid is the minor product; the yields increase with increasing temperature. Additional products from the decomposition of higher molecular weight species (secondary reactions) were observed at higher temperatures. The reaction rate constant is 9.19×10^{5} $M^{-1}s^{-1}$ at 20^{o}C, which represent a fast pseudo first-order reaction. In addition, the yield of 1-nonanal increases in the case of mixed with alcohols, whereas the Criegee intermediates and carboxylic acids are converted to alkyl esters depending on the molecular structure of the alcohols. Methanol is found to be a suitable solvent for increasing productivity, and the optimum molar ratio is 1:1.

In the case of ozonolysis of pure olive oil, the results show that only 1-nonanal is observed, and its yield increases with increasing temperature. The reaction rate constant of olive oil ozonolysis at 20^{o}C is estimated as 4.88×10^{8} $M^{-1}s^{-1}$. For ozonolysis of olive oil mixed with methanol, 1-nonanal is the major short-chain product with 88.0±2.6% yield, whereas nonanoic acid methyl ester is observed as the minor short-chain product. In addition, in the case of transesterification, the by-product from olive oil mixed with methanol ozonolysis is a suitable reactant for use in bio-kerosene production. The products found after transesterification are nonanoic acid methyl ester, 9-oxononanoic methyl ester, azelaic acid dimethyl ester, and octanoic acid methyl ester, and their compositions are 0.093, 0.08, 0.776, and 0.052, respectively.

In the case of ozonolysis of used cooking oil mixed with methanol, the results from the GC-MS show that all saturated free fatty acids (including palmitic acid, stearic acid, and myristic acid) are converted to methyl esters within 20 hours of 60^{o}C ozonolysis, whereas trace amounts of these chemicals remain at lower temperatures. The results also show that the conversion of oleic acid to form oleic acid methyl ester is 91.16% after 32 hours of ozonolysis at 60^{o}C. Therefore, the free fatty acid content in used cooking oil is less than 1.33%, which makes it suitable as a reactant for biodiesel production. However, this result is different from the result provided by ASTM D974 in that the acid numbers decrease dramatically by 25% at the beginning of ozonolysis followed by a plateau.

Moreover, if the fluidic oscillator is used to generate bubbles in ozonolysis of oleic acid mixed with methanol and olive oil mixed with methanol, the results show that the yields of 1-nonanal increase by 30% and 44%, respectively. This observation means that ozonolysis of oleic acid and olive oil is relative to the specific interfacial area.

Keywords: *Ozonolysis, bubbles, oleic acid, olive oil, used cooking oil*

Acknowledgements

Above all, I would like to express appreciation to Ministry of Science and Technology, Thailand and the Thai people for financial support.

I would like to express my sincere gratitude to my research supervisor, Professor William B. J. Zimmerman for his guidance, patience, and encouragement throughout research work.

I would also like to thankful all technical staff of the Department of Chemical and Biological Engineering and the Department of Chemistry for the technical support in fabricating the research equipment especially, Mr. Andy Patrick, Mr. Mark Jones, Mr, Keith Penny, Mr. Daniel Jackson, and Mr. Simon Thorpe. Without their support, it would have been more difficult to set up the experiment.

I would like to thank the people in my research group especially, Dr. Dmitriy Kuvshvinov, Dr. James Hanotu, Dr. Stuart Brittle, Dr. Thomas David Holmes, and Dr. Adam Samuel who order chemicals and research equipment and all my friends for their support and collaborative work. Additionally, I sincerely appreciate Dr. Matthana Khangkhamano for English correction.

Finally, I would like to thank my family for their infinite love, support and encouragements.

List of contents

List of figures

List of tables

List of abbreviations

10-OxA	10-oxo-octadecanoic acid
9-OxA	9-oxo-octadecanoic acid
AA	azelaic acid
AAHP	α-acyloxyalkyl hydroperoxide
CAHP	cyclic acyloxy hydroperoxide
CBD	coplanar discharge
CI	Criegee intermediate
DBD	dielectric barrier discharge
DE-AA	azelaic acid, diethyl ester
DE-NA	2-octanol, nonane, 1, 1-diethoxy
DE-NN	nonanal diethyl acetal
DM-2OcA	2-octanol, 8, 8-dimethoxy
DM-AA	azelaic acid, dimethyl ester
DM-NN	nonanal dimethyl acetal
DP	diperoxide
E-HA	heptadecanoic acid, ethyl ester
E-NA	nonanoic acid, ethyl ester
E-OA	9-oxonananoic acid, ethyl ester
E-OcA	octanoic acid, ethyl ester
E-PA	palmitic acid, ethyl ester
FFAs	free fatty acids
FFMA	free fatty acid methyl ester
FO	fluidic oscillator
HA	heptadecanoic acid
HeA	hexanoic acid

HMWP	higher molecular weight product
HN	hexanol
HP	hydroperoxide
KI	iodometric method
LA	lauric acid
MA	myristic acid
M-AA	azelaic acid, methyl ester
MaA	malonic acid
M-CI	Criegee intermediate ending with methyl group
MDA	malondialdehyde
M-HA	heptadecanoic acid, methyl ester
MHP	methoxyhydroperoxide
M-MA	myristic acid, methyl ester
M-NA	nonanoic acid, methyl ester
M-OA	9-oxonananoic acid, methyl ester
M-OcA	octanoic acid, methyl ester
M-OL	oleic acid methyl ester
M-PA	palmitic acid, methyl ester
M-SA	stearic acid, methyl ester
NA	nonanoic acid
NA1	e-non-2-enoic acid
NN	1-nonanal
NN1	2-nonenal
OA	9-oxonananoic acid
OAA	ozonised oil ending with azelaic acid
OAAHP	ozonised oil ending with AAHP
OcA	octanoic acid

OCI	ozonised oil ending with CI
ODP	ozonised oil ending with DP
OL	oleic acid
OMAA	ozonised oil ending with azelaic acid, methyl ester
OOA	ozonised oil ending with aldehyde
OOcA	ozonised oil ending with OcA
OOM	ozonised oil with methanol
OOP	ozonised oil
OpA	3-oxopropanoic acid
PA	palmitic acid
PFA	perfluoroalkoxy
PHA	peroxyhemiacetal
PO	primary ozonide
PTFE	polytetrafluoroethylene
PVA	polyvinylalkoxy
PVC	polyvinylchloride
SA	stearic acid
SD	surface discharge
SOZ	secondary ozonide
UCO	used cooking oil
UP	unidentified product
VD	volume discharge

List of symbols

A	KOH volume required for titration of sample
a	specific interfacial area
B	KOH volume required for titration of blank
Bo	Bond number
C	concentration
C_d	drag coefficient
C_{pl}	heat capacity of liquid
D	diffusion coefficient
d_{32}	sauter mean bubble diameter
d_b	diameter of the bubble
D_C	bubble column diameter
d_{vs}	volume surface mean diameter
Ei	instantaneous reaction factor
g	gravity vector
H	Henry’s Law constant
Ha	Hatta number
J	mass flux
k	reaction rate constant
k_B	Boltzmann’s constant (1.381×10^{-23} J/K)
k_G	mass transfer coefficients for the gas phase
k_L	mass transfer coefficients for the liquid phase
k_l	thermal conductivity of liquid
k^{surf}	reaction rate constant on the surface
l	diffuso-reactive length
M	molarity of the KOH
m	national logarithm of the geometric mean bubble size
m_{gl}	mass transfer rate from gas to liquid
Mo	Morton number
MW	molecular weight
N	number of bubbles per unit aerated liquid volume
N_A	rate of mass transfer of A
N_t	normality

P	partial pressure
Q	heat source
R	gas constant (0.082 atm K^{-1} M^{-1})
r_A	reaction rate
r_b	radius of the bubble
Re	Reynolds number
r_p	radius of the particle
S	adsorption coefficient or interfacial area
S_b/V_b	surface area to volume ratio of bubble
S_p/V_p	surface area to volume ratio of particle
T	temperature
t	time
u_g	gas velocity
u_l	liquid velocity
u_{slip}	relative velocity between gas and liquid
U_t	rise velocity
V	volume of bubble
V_A	molar volume of ozone at its boiling temperature
V_t	volume of sodium triosulfate used
W	sample used for titration
x_i	mole fraction of species i in liquid phase
y_i	mole fraction of species i in vapour phase
z	ratio between the coefficients

Greek Letters

ϕ_s	association factor
ε	characteristic Lennard-Jones energy
δ	depth of the surface layer
λ	diameter ratio
δ_L	film thickness parameter for the film theory
ρ	fluid density
f	fugacity

ϕ	fugacity coefficient
ε_G	gas holdup
β	liquid holdup
$\bar{c}$	mean kinetic speed of an O_3 molecule in the gas phase (3.6×10^4 cm s^{-1})
γ_{means}	measured uptake coefficient
$\mu_n^{'}$	moment of distribution
γ	reactive uptake coefficient
δ_r	reacto-diffusive length of ozone in oleic acid
Γ_{diff}	uptake caused by the diffusion of gas species
Γ_{diff}^{p}	uptake caused by the particle phase reactant diffusion
Γ_{rxn}	uptake caused by the reaction in the bulk
Γ_{surf}	uptake caused by the reaction on the surface
ϕ_g	volume fraction of gas phase
ϕ_l	volume fraction of liquid phase
μ	dynamic viscosity
α	mass accommodation coefficient
σ	standard deviation or characteristic length

CHAPTER 1

INTRODUCTION

In this chapter, the background and general statement of the study are described in Section 1.1. The objectives, scope, and aims of the study are presented in Section 1.2, Section 1.3, and Section 1.4, respectively. Section 1.5 summarises the utilisation of the study, and Section 1.6 represents the thesis outline.

1.1 Background and general statement of the study

Oleic acid (OL) is a monounsaturated fatty acid that can react with ozone to form a number of valuable products, including 1-nonanal (NN), 9-oxononanoic acid (OA), nonanoic acid (NA), and azelaic acid (AA), as shown in Figure 1.1 (Hung et al. 2005). These products are used in a wide range of such applications as flavours, perfumes, and plasticiser and lacquer preparation. It is interesting that two major products (NN and OA) are highly expensive compared with the reactant as shown in Table 1.1.

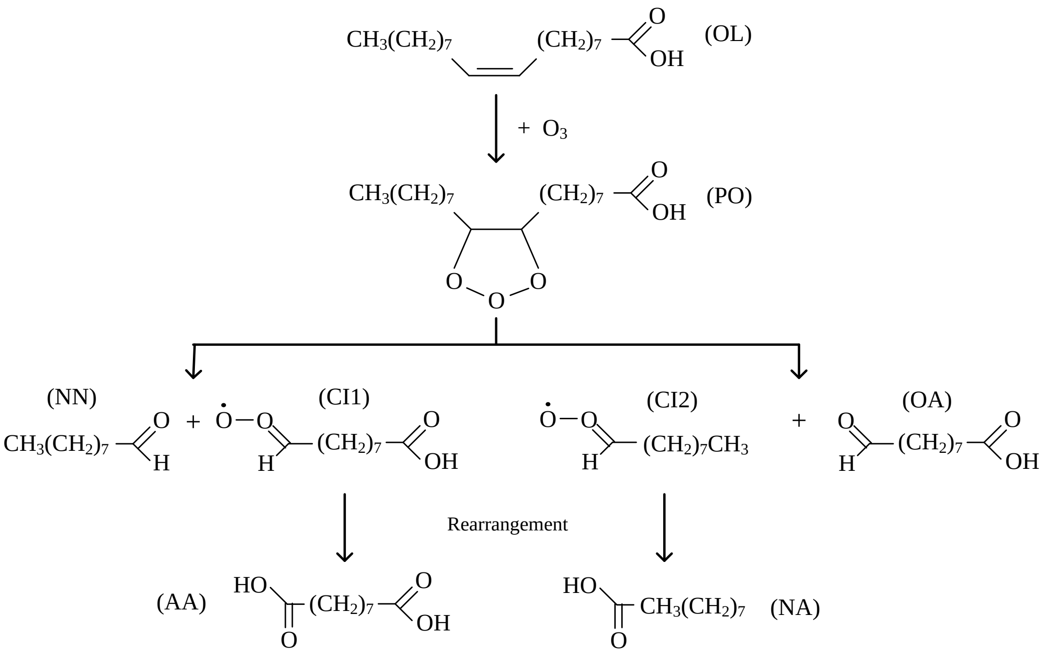

Figure 1.1 Possible products from ozonolysis of OL

Table 1.1 Physical properties and prices of products and reactants

Reactants & products	**Molecular formula**	**MW.**	**BP(ºC)**	**Cost £/kg**
Oleic acid (OL)	$C_{18}H_{34}O_2$	282.46	360	~0.84
1-nonanal (NN)	$C_9H_{18}O$	142.24	195	~20.72
9-oxononanoic acid (OA)	$C_9H_{16}O_3$	172.22	304.78	-
Nonanoic acid (NA)	$C_9H_{18}O_2$	158.23	254	~2.52
Octanoic acid (OcA)	$C_8H_{16}O_2$	144.21	239.7	~2.24
Azelaic acid (AA)	$C_9H_{16}O_4$	188.22	286 At 100 mmHg	~5.60
Olive oil	-	-	300	~0.50
Used cooking oil	-	-	-	~0.10

As reviewed in Chapter 2, conventional contact methods such as atomised droplets in sprays or thin films in trickle reactors or along tubular walls are unlikely to achieve high yield production of these valuable products from ozonolysis of OL. In addition, the commercial production of NN by hydroformylation of 1-octene over a rubidium or cobalt catalyst is fairly expensive because of high pressure operation and the difficulty of recycling the homogeneous catalyst (Janssen *et al.* 2010, Koeken *et al.* 2011). Therefore, the hypothesis of this research is that these expensive products (NN, OA, NA, and AA) can be produced using an inexpensive OL as the reactant and a simple and low cost technique to generate ozone bubbles. To test this hypothesis, the experiments must be redesigned based on the application of bubbling ozone bubbles to react with the liquid phase of OL in the bubble column reactor to form such products. This approach is necessary because earlier experiments, based on the literature, were conducted using ozonolysis of either droplets or coated-wall flow tube of OL to observe the effects of the reaction in the atmosphere. These results provided insufficient information (e.g., kinetic data) for reactor and process system design.

Several benefits can be gained from this idea, e.g., the production cost of ozone using a plasma reactor and microbubbles generated by a fluidic oscillator is low compared with other conventional techniques. Ozonolysis of OL studied in previous research takes place at the fluid interface, and thus microbubbles, which have higher surface area to volume ratio than fine bubbles, are a better option. Ozonolysis is a clean technology that uses oxygen as the feed chemical, produces no pollutant product molecules, and can be conducted at atmospheric pressure without the use of a catalyst, which results in reduced operating costs. Moreover, it is interesting to note that olive oil (triglyceride) can be used as an alternative reactant due to the many oleic acid structures contained in its molecular structures (approximately 85%); additionally, the cost of olive oil is also less than OL (Galtier *et al.* 2007).

1.2 Objective of the study

The main objective of this research is to upgrade low price bio-fuels, i.e., OL and olive oil to form a number of high value products, i.e., NN, OA, NA, and AA, using an ozonolysis technique. Therefore, the reaction between liquid reactants and ozone bubbles is studied at various operating temperatures, reaction times, and with different ozone concentrations. Optimum conditions are identified because these parameters are useful for commercial production. Product selectivity, conversion of OL and olive oil, and kinetic parameters (reaction rate constant) are also determined. Various protic solvents that dissolve in OL and olive oil are also added to OL and olive oil to increase product selectivity. The optimum percentages of the protic solvents are determined and all previously described parameters are considered. The ozonised oil, which is the by-product from ozonolysis of olive oil and contains substantial amounts of the short-chain triglyceride, is used as a reactant for transesterification in a feasibility study for bio-kerosene production. Moreover, used cooking oil, which has high free fatty acid content, is ozonised to reduce the percentage of free fatty acid content for standard biodiesel production.

1.3 Scope of the study

This research consists of two main components, namely, simulations and experiments. Aspen Plus, COMSOL Multiphysics, and COMSOL Reaction Engineering Lab software are used in the first component. The reactor and cooling system employed in this experiment are designed using this software. Aspen Plus is used to estimate all required parameters, which are not found in the literature, including the Henry’s Law constant, diffusion coefficient, and thermodynamic properties. Thermal ozone decomposition is also studied using COMSOL Reaction Engineering Lab.

The second component consists of experiments with several sub-sections. The first section measures the inlet ozone concentrations and the specific interfacial area of the bubbles at different fluid temperatures. The second section focuses on the study of ozonolysis of OL at different reaction times and temperatures. The third section consists of the study of ozonolysis of OL in mixtures (protic solvents) to increase the product selectivity. The best protic solvent is selected to investigate the effect of its composition on product selectivity. The fourth section covers the study of ozonolysis of olive oil. All parameters described in the previous sections are also determined. The fifth section presents ozonolysis of olive oil mixed with the best protic solvent. The sixth section describes transesterification of ozonised oil from pure olive oil ozonolysis and mixed olive oil ozonolysis. The last section deals with ozonolysis of used cooking oil in the best protic solvent.

1.4 Aims of the study

The principal aims of this research are:

1. To design the bubble column reactor and the cooling system, and to find the appropriate location for installation of a sampling tube and a thermometer using both Aspen Plus and COMSOL Multiphysics software.

2. To determine the Henry's Law constant and the diffusion coefficient using Aspen Plus and Polymath V5.1.

3. To observe the thermal decomposition of ozone via COMSOL Reaction Engineering Lab.

4. To estimate the production rates of both OL and olive oil ozonolysis via Aspen Plus.

5. To find the appropriate protic solvents for both OL and olive oil via Aspen Plus.

6. To determine the inlet ozone concentration using the KI method.

7. To estimate the specific interfacial area in the reactor using a high speed camera and ImageJ software.

8. To determine the kinetic parameters, conversion of OL, and product selectivity of the ozonolysis of OL and to find the optimum operating temperature, reaction time, and ozone concentration.

9. To increase the product selectivity by adding selected protic solvents into OL and to find the optimum percentage of these solvents.

10. To find the kinetic parameters, conversion rate of olive oil, and product selectivity of the ozonolysis of olive oil; to find the optimum operating temperature, reaction time, and ozone concentration; to study the product composition after transesterification of ozonised oil.

11. To increase the product selectivity by adding a selected protic solvent from the previous section into olive oil, to find the optimum percentage of these solvents, and to investigate the feasibility of using ozonised oil for bio-kerosene production via transesterification reaction.

12. To reduce the percentage of free fatty acid content in used cooking oil for conventional biodiesel production.

1.5 Utilisation of the study

The research results include operating conditions, kinetic parameters, and an appropriate protic solvent that might be useful for commercial production. The by-product from ozonolysis of olive oil might also be used as the reactant for bio-kerosene production. Moreover, ozonolysis of used cooking oil offers a possible alternative technique to reduce the free fatty acid content for biodiesel production.

1.6 Thesis outline

This thesis contains eight chapters. Chapter 1 gives an introduction to the thesis, i.e., background and general statement of the study, objectives, scope, aims of the study, and utilisation of the study. Chapter 2 presents a comprehensive literature review of ozonolysis of oleic acid, ozone production, and bubble formation. Chapter 3 describes the simulation techniques, simulation methods, and simulation results obtained from Aspen Plus, COMSOL Multiphysics, and COMSOL Reaction Engineering Lab that are applied to achieve aims 1 to 5. Chapter 4 presents the experimental methods and results for estimation of the inlet ozone concentration and bubble characterisation necessary to achieve aims 6 and 7. Chapter 5 describes the experimental methods and results of ozonolysis of oleic acid and mixtures to complete aims 8 and 9. Chapter 6 illustrates the experimental methods and results from ozonolysis of olive oil, its mixtures and transesterification of ozonised oil to achieve aims 10 and 11. Chapter 7 provides the experimental methods and results of ozonolysis of used cooking oil in a suitable protic solvent to achieve aim 12. Chapter 8 summarises conclusions and suggestions for the future work.

CHAPTER 2

A COMPREHENSIVE LITERATURE REVIEW

This chapter focuses on a comprehensive literature review that consists of three main sections. Section 2.1 presents a literature review of the recent research on ozonolysis which focuses primarily on oleic acid, oleic acid methyl ester, and vegetable oils. The background of free fatty acids and olive oil describing how to produce free fatty acid and olive oil is provided in Section 2.1.1. Ozonolysis of oleic acid, which explains the characteristics of ozonolysis as well as the kinetics of the reactions, is covered in Section 2.1.2. The effect of operating conditions on the product formation of ozonolysis of oleic acid is described in Section 2.1.3. Ozonolysis of oleic acid methyl ester is discussed in Section 2.1.4 and focuses on the differences between oleic acid and oleic acid methyl ester in terms of the reaction mechanism and products. Ozonolysis of vegetable oils is discussed in Section 2.1.5. Section 2.1.6 addresses discussion of the issues raised by an analysis of the literature. The summarised data from previous research is also listed in Section 2.1.7.

Section 2.2 concentrates primarily on ozone production. The histories of ozone, physical properties, and applications are summarised in Section 2.2.1, 2.2.2, and 2.2.3, respectively. Suitable ozone production techniques used in these experiments are discussed in Section 2.2.4. The proper reactant feed for ozone production is reviewed in Section 2.2.5. Ozone decomposition due to various aspects (i.e., pH and temperature) is discussed in Section 2.2.6. The design features of the ozone generator are also discussed in Section 2.2.7. A suitable measurement technique for ozone concentration in the gas phase is reviewed in Section 2.2.8. The safety aspects and material requirements for contact with ozone in laboratory use are discussed in Section 2.2.9 and 2.2.10, respectively. Section 2.2.11 concerns the kinetics of the direct ozone reactions and contains several equations used to clarify the characteristics of the gas phase reaction between ozone and the reactants.

Section 2.3 focuses on bubble formation. The effects of bubble formation, primarily fluid properties and operating conditions are described in Section 2.3.1. The rise velocity of the bubbles due to various aspects, including the size and shape of bubbles, purity, viscosity, and temperature of the liquid is described in Section 2.3.2. Design and scale-up of the bubble column and microbubble generation are also described in Section 2.3.3 and Section

2.3.4, respectively. The bubble characterisation is discussed in Section 2.3.5. Section 2.4 presents a summary.

2.1 Ozonolysis of unsaturated fatty acid

This section provides useful information on experimental designs and experimental techniques from previous research results, including reaction time, reaction temperature, and suitable protic solvents. The details are described in the following sub-sections.

2.1.1 Background of free fatty acid and olive oil

Fatty acids, methyl esters, and alcohols produced from both plant oils and animal fats are crucial reactants that can be used as starting materials for the production of surfactants and lubricants. The production of these bio-chemicals, which are known as oleochemicals, has dramatically increased over the last decade due to high demands for biodiesel and ethanol in transportation. Moreover, these renewable reactants are quite inexpensive and are available around the world (Metzger 2009, Biermann *et al.* 2011).

$$\begin{array}{l}
Triglycerides + Water \leftrightarrow Diglycerides + Fatty\ acid \\
Diglycerides + Water \leftrightarrow Monoglyceride + Fatty\ acid \\
Monoglyceride + Water \leftrightarrow Glycerol + Fatty\ acid \\
\hline
Triglycerides + 3\,Water \leftrightarrow Glycerol + 3\,Fatty\ acid
\end{array}$$

Figure 2.1 Hydrolysis of oils and fats

Currently, hydrolysis of plant oils and animal fats is the conventional technique used to produce fatty acids. Either oils or fats react with water to form fatty acids and glycerol, as shown in Figure 2.1. The operating temperature and pressure are 250°C and 50 bar, respectively. The reaction time required to achieve 96-99% conversion without use of a catalyst is approximately two hours. Solid catalysts are also used in the hydrolysis process so that the process can be operated at moderate temperature and pressure to obtain higher conversion. In addition, enzyme hydrolysis is an alternative method used to produce fatty acid, but this approach requires a longer reaction time (Noor *et al.* 2003, Satyarthi *et al.* 2011).

In nature, most plant oils and fats are primarily composed of triglycerides with a glycerine backbone attached to fatty acid radicals (Canakci and Van Gerpen 2001). There are two types of fatty acids: unsaturated fatty acids and saturated fatty acids. The first category contains at least one double bond in their molecules, e.g., oleic acid, linoleic acid, erucic acid, and petroselinic acid, whereas those molecules in the second category do not contain a double bond, e.g., palmitic acid and stearic acid. The compositions of fatty acids in oils and fats are listed in Table 2.1.

Table 2.1 Percentages of fatty acids in oils and fats

Oils and Fats	14:0	16:0	18:0	18:1	18:2	18:3
Soybean[1]	-	6-10	2-5	20-30	50-60	5-11
Corn[1]	1-2	8-12	2-5	19-49	34-62	Trace
Peanut[1]	-	8-9	2-3	50-65	20-30	-
Olive[1]	-	9-10	2-3	73-84	10-12	Trace
Cottenseed[1]	0-2	20-25	1-2	23-25	40-50	Trace
Hi linoleic safflower[1]	-	5.9	1.5	8.8	83.8	-
Hi oleic safflower[1]	-	4.8	1.4	74.1	19.7	-
Hi oleic rapeseed[1]	-	4.3	1.3	59.9	21.1	32.2
Hi erucic rapeseed[1]	-	3.0	0.8	13.1	14.1	9.7
Butter[1]	7-10	24-26	10-13	28-31	1-2.5	0.2-0.5
Lard[1]	1-2	28-30	12-18	40-50	7-13	0-1
Tallow[1]	3-6	24-32	24-32	37-43	2-3	-
Linseed oil[1]	-	4-7	4-7	25-40	35-40	25-60
Yellow grease[1]	2.43	23.24	23.24	44.32	6.97	0.67
Brow grease[2]	1.66	22.83	12.54	42.36	12.09	0.82

Myristic acid (14:0), Palmitic acid (16:1), Stearic acid (18:0), Oleic acid (18:1), Linoleic acid (18:2), Gamma/alpha linoleic acid (18:3). 1= (Linstromberg 1970), 2 = (Canakci and Van Gerpen 2001)

In addition to triglycerides, free fatty acids (FFAs) are found in plant oils and fats. The amount of FFAs in oils and fats depends on their chemical nature. Most of the edible oils contain a small amount of FFAs, whereas non-edible oil or used cooking oils (UCO) contain large amounts of FFAs, up to 5-25% by weight (Russbueldt and Hoelderich 2009).

Table 2.2 Triglyceride contents in olive oil

Triglycerides	MW (g/mol)	Triglyceride range %	
		(Galtier *et al.* 2007)	(Dimitrios 2006)
LLL	879.38	0.03-0.35	trace
OLnL	879.40	0.17-0.51	trace
PLnL	853.36	0.01-0.14	trace
LOL	881.41	1.02-4.61	trace
OLnO	881.41	0.97-2.26	trace
PLL	855.37	0.12-1.89	trace
PLnO	855.37	0.26-1.03	trace
LOO	883.43	10.2-18.0	12.5-20.0
PoOO	819.35	0.90-3.31	trace
PLO	857.39	3.04-11.29	5.5-7.0
PoOP	793.31	0.23-1.71	trace
PLP	831.35	0.15-1.62	trace
OOO	885.44	26.47-61.78	40.0-59.0
SLO	847.40	0.49-1.31	trace
POO	821.37	16.01-23.54	12.0-20.0
POP	833.37	1.77-4.24	trace
SOO	887.46	2.09-4.89	3.0-7.0
SOP	823.38	0.34-1.35	trace
POA	860.44	0.29-0.68	trace
P = palmitic (C16:0), Po = palmitoleic (C16:1), S = stearic (C18:0), O = oleic (C18:1), L = linoleic (C18:2), Ln = linolenic (C18:3), A = arachidic (C20:0)			

As listed in Table 2.1, olive oil is an alternative reactant used to produce valuable short-chain products. Olive oil consists primarily of two groups of chemical compounds. Triglycerides are the major compound in olive oil at 97-99%, and the 1-3% of minor compounds includes monoglycerides, diglycerides, FFAs, hydrocarbons, and esters. Triglycerides primarily include OL, a moderate amount of linoleic and linolenic acid, and trace amounts of palmitic acid and stearic acid. The composition of fatty acids in olive oil might differ depending on several factors, such as production zone, latitude, and climate

(Dimitrios 2006, Peri 2014). The major hydrocarbon content in olive oil is squalene, which is an antioxidant that acts as a biological filter. Extra-virgin olive oil contains 200 – 700 mg of squalene per 100 g of oil (Peri 2014).

The composition of olive oil is listed in Table 2.2. Because of the abundance of OL content in olive oil, aldehyde products (especially NN) and carboxylic acids (especially NA) might be formed after ozonolysis of olive oil. It should be noted that vegetable oils suitable for ozonolysis should contain a substantial amount of unsaturated fatty acids (especially monounsaturated) because both NN and NA can be produced by ozonolysis of monounsaturated fatty acids.

2.1.2 Reaction of OL and ozone

Oleic acid is a monounsaturated fatty acid with 18 carbon atoms that have a double bond at the C9 position. This compound normally reacts with common gas phase oxidants such as O_3, NO_3, and OH. In our environment, particles of OL are emitted from various sources, including marine aerosols (Fang *et al.* 2002, Mochida *et al.* 2002) and cooking, which is the main source in urban environments (Schauer *et al.* 1999, Robinson *et al.* 2006). Reactions among these materials have been studied by a number of researchers to observe the effect of these reactions on the global climate (Zahardis and Petrucci 2007). Although the reactions of OL with many gas-phase oxidants have been studied, certain researchers have focused on the reaction between OL and ozone known as ozonolysis using two techniques (i.e., droplets and a coated-wall flow tube) because the ozone concentration in the troposphere is much higher than that of other gas-phase oxidants (Finlayson-Pitts and Pitts 2000). These previous studies have investigated reaction kinetics (Hearn and Smith 2004, Thornberry and Abbatt 2004, Knopf *et al.* 2005, Ziemann 2005), studied reaction mechanisms (Thornberry and Abbatt 2004, Hung *et al.* 2005, Ziemann 2005), measured the reactive coefficient (Moise and Rudich 2002, Smith *et al.* 2002), monitored product yields (Moise and Rudich 2002, Katrib *et al.* 2004, Hung *et al.* 2005, Ziemann 2005), investigated secondary reactions (Hearn *et al.* 2005), determined the chemical compositions of the particles (Katrib *et al.* 2004), examined product yields at different ambient conditions and humidity values (Vesna *et al.* 2009), calculated the OL-O_3 reaction stoichiometry (Sage *et al.* 2009), investigated the oxidation rate at different physical states and temperatures (Hung and Tang 2010), studied the reaction in multi-components (Katrib *et al.* 2005, Knopf *et al.* 2005), and observed the OL lifetime (Knopf *et al.* 2005).

2.1.2.1 Pathways and products in ozonolysis of OL

The existence of three-step mechanism has been proven for ozonolysis of OL at room temperature, as shown in Figure 2.2A. The first step of this reaction mechanism is the formation of an unstable species known as primary ozonide (PO), which is stable at notably low temperatures (Criegee 1975). The second step of the mechanism is decomposition of the PO, which leads to two separate routes. The first route is the formation of aldehydes, i.e., NN, and carbonyl oxides known as the Criegee intermediate (CI1), which was named by the German chemist who proposed the ozonolysis mechanism (Criegee 1975). The second route is the formation of OA and the Criegee intermediate (CI2) (Hearn and Smith 2004, Katrib *et al.* 2004, Thornberry and Abbatt 2004, Ziemann 2005, Hung and Ariya 2007, Vesna *et al.* 2009, Lee *et al.* 2012). The last step of the mechanism is the reaction of either CI1 or CI2 (which are energy-rich species) with other substances in the system via many reaction pathways, including isomerisation, OL attack on the double bond, and stabilisation, among others. For the isomerisation/rearrangement pathway, CI1 can isomerise to form AA (Hearn and Smith 2004, Katrib *et al.* 2004, Thornberry and Abbatt 2004, Ziemann 2005, Hung and Ariya 2007, Last *et al.* 2009, Vesna *et al.* 2009, Lee *et al.* 2012), octanoic acid (OcA), and carbon dioxide (Hung *et al.* 2005) or cyclic acyloxy hydroperoxide (CAHP1) (Ziemann 2005), whereas CI2 can isomerise to form NA (Hearn and Smith 2004, Katrib *et al.* 2004, Thornberry and Abbatt 2004, Ziemann 2005, Hung and Ariya 2007, Last *et al.* 2009, Vesna *et al.* 2009). In the case of OL attack on the double bond, CI1 can react with OL at the double bond to form OA and 10-oxo-octadecanoic acid (10-OxA) via pathway 1 (Hung and Ariya 2007) and to form OA and 9-oxo-octadecanoic acid (9-OxA) via pathway 2 (Katrib *et al.* 2004, Hung and Ariya 2007), whereas the products of CI2 after attack at the double bond of OL are AA and 10-OxA via pathway 1 and NN and 9-OxA via pathway 2, as shown in Figure 2.2A (Katrib *et al.* 2004, Hung and Ariya 2007). For stabilisation, both CI1 and CI2 can react with OL or primary products to form α-acyloxyalkyl hydroperoxide (AAHPs) and secondary ozonides (SOZs) (Ziemann 2005, Hung and Ariya 2007, Vesna *et al.* 2009). As a result of both OL attacks on the double bond and stabilisation reactions, the stoichiometry of the reaction between OL and O_3 is greater than 2:1 (Sage *et al.* 2009). The CI1s can react with each other to form diperoxide (DP1) (Ziemann 2005, Hung and Ariya 2007, Vesna *et al.* 2009), which subsequently decomposes to produce two molecules of OA and O_2 (Hearn and Smith 2004, Hung *et al.* 2005). The CI2s can also react with each other to form DP2 (Ziemann 2005, Hung and Ariya 2007, Vesna *et al.* 2009), which subsequently decomposes to produce two molecules of NN and O_2 (Hearn and Smith 2004, Hung *et al.* 2005). The CI1 can react with CI2 to form DP3 (Hearn and Smith 2004, Vesna *et al.* 2009), which decomposes to OA, NN, and O_2 (Hearn and Smith 2004, Hung *et al.* 2005). Moreover, in the presence water in the system, CI1 can react with water to form hydroperoxide (HP1), and CI2 can react with water to form HP2. The HP1 decomposes to form OA and H_2O_2/AA and water, and HP2 decomposes to form NN and H_2O_2/NA and water, as shown in Figure 2.2B (Pryor *et al.* 1995, Finlayson-Pitts and Pitts 2000, Vesna *et al.* 2009).

Moreover, the products of combination among three to five species of the primary products have been observed by Hung and Ariya (2007) and Last and co-workers (2009). These researchers proposed that peroxyhemiacetal (PHA) with a peak at 501 m/z can be formed by the reaction between OA and CI1/CI2 followed by addition of OA/NN. The peak at 519 m/z might represent the product of either reactions among OA, CI1, and CI2 or those between NN and 2CI1. The peak at 535 m/z might indicate the product of reactions between 2CI1 and CI2. The peak at 565 m/z could be the product of reactions of 3CI1. For the peak at 611 m/z or 642 m/z, the products are either the reaction between AAHP (CI1/CI2 + OL) and NN/OA or the reaction between OA and 2CI2 for the peak at 611 m/z or the reactions among OA, CI1, and CI2 for the peak at 642 m/z. The peak at 693 m/z might indicate the product of reactions between 2CI1 and 2CI2. The peak at 706 m/z predicts that it is either the reaction between NN and 3CI1 or the reaction among OA, CI2, and 2CI1. The peak at 721 m/z might represent the products from the reaction between 3CI1 and CI2. The peak at 753 m/z might be the products from the reaction of 4CI1. The peak at 881 m/z might represent the products from the reaction between 3CI1 and 2CI2, and the peak at 911 m/z might indicate the products from the reaction between 4CI1 and 1CI2 (Hung and Ariya 2007, Last *et al.* 2009).

2.1.2.2 Valuable products from ozonolysis of OL

The commonly observed products from ozonolysis with molecular weights less than that of OL are NN, AA, OA, and NA, as reviewed by Zahardis and Petrucci (2007). The NN was found as the major product from the second step of ozonolysis of OL via pathway 1, as illustrated in Figure 2.2A (Moise and Rudich 2002, Hearn and Smith 2004, Thornberry and Abbatt 2004, Hung *et al.* 2005, Last *et al.* 2009, Sage *et al.* 2009, Vesna *et al.* 2009). The NN is difficult to measure because it is considered to be the most volatile of the observed products (Last *et al.* 2009, Lee *et al.* 2012). By observing ozonolysis of droplets of OL, an NN yield of 84% in both phases was measured by Hearn and Smith (2004). This amount is greater than the AA yield by a factor of seven. Similar results were observed by Vesna and co-workers (2008), who found that the NN yield is greater than the AA yield by a factor of 8.8, which is approximately 60% of the NN detected in both phases. The NN yields also have been measured solely in the condensed phase by Hung and co-workers (2005). A yield of 30% of NN was detected in this phase, whereas 48% of carbon could not be detected. If undetected carbon is assumed to be NN, the total yield of NN might reach 78%. Unquantified NN was observed by Last and co-workers (2009) and Sage and co-workers (2009). Using the coated-wall flow tube technique, Moise and Rudich (2002) measured an NN yield of 28% in the gas phase alone, and Thornberry and Abbatt (2004) detected an NN yield of 50% in the same phase. Moreover, this yield increases with increasing operating temperature (Moise and Rudich 2002), reaction time (Sage *et al.* 2009), and size of the OL particles (Hung and Ariya 2007). In contrast, Sage and co-workers (2009) found that the amount of NN accumulated in the system during ozonolysis deceases sharply in the presence of a substantial amount of ozone after all of the OL was ozonised.

The 9-oxononanoic acid was reported as the second major product from ozonolysis of OL via pathway 2, as illustrated in Table 2.3 (Hearn and Smith 2004, Katrib *et al.* 2004, Hung *et al.* 2005, Ziemann 2005). By observing the ozonolysis of droplets of OL, Ziemann (2005) reported that a OA yield of 28% was detected, whereas only 14% was found by Hung and co-workers (2005). Hearn and Smith (2002) suggested that the OA yield is five times higher than the NA yield. Unquantified OA was identified by a number of researchers (Smith *et al.* 2002, Last *et al.* 2009, Vesna *et al.* 2009, Lee *et al.* 2012). In a coated-wall flow tube study, Katrip and co-workers (2004) found that an OA yield of 20-35% is formed in the liquid phase and also concluded that the OA yield increases with increasing layer thickness. This observation means that the decomposition of PO to OA and CI2 might take place in the liquid bulk, and it was evident that OA yield also increases with ozone exposure (Hung *et al.* 2005). In contrast, Last and co-workers (2009) found that OA decreases sharply with increasing time.

Azelaic acid was observed as the minor product in heterogeneous ozonolysis via the rearrangement of the CI1, as summarised in Table 2.3 (Moise and Rudich 2002, Hearn and Smith 2004, Katrib *et al.* 2004, Hung *et al.* 2005, Ziemann 2005, Hung and Ariya 2007, Vesna *et al.* 2009, Lee *et al.* 2012). In aerosol experiments, AA yield was detected at 12%, 6%, and 4% by Hearn and Smith (2004), Hung and co-workers (2005), and Ziemann (2005), respectively. An unquantified AA yield also has been observed by a number of researchers (Hung and Ariya 2007, Last *et al.* 2009, Vesna *et al.* 2009, Lee *et al.* 2012). Using a coated-wall experiment, an unquantified AA yield was been detected by Moise and Rudich (2002) and King and co-workers (2009). An AA yield of 1-3% was found by Katrib and co-workers (2004), who also found that the AA yield increased slightly with increasing OL thickness because the rearrangement reaction of CI1 to form AA might occur in the liquid bulk instead of at the fluid interface. Last and co-workers (2009) also found that the AA yield is quite low and remains constant throughout the reaction times because CI1 prefers to react with OL, CIs, and primary products instead of rearrangement to form AA.

Nonanoic acid also has been observed as the minor product in heterogeneous ozonolysis via rearrangement of the CI2, as summarised in Table 2.3 (Hearn and Smith 2004, Katrib *et al.* 2004, Hung *et al.* 2005, Ziemann 2005). The reasons for these observations might be the same as those for the formation of AA in that CI2 prefers to react with OL, CIs, and primary products instead of rearrangement to form NA. For the aerosol experiments, an NA yield of 7% was detected by Hung and his team (2005), whereas unquantified NA has been observed by many researchers (Hearn and Smith 2004, Hung and Ariya 2007, Last *et al.* 2009, Vesna *et al.* 2009, Lee *et al.* 2012). An NA yield of 1-3% was also measured by Katrib and his team (2004) in coated-wall experiments, and unquantified NA was observed by Moise and Rudich (2002). Surprisingly, King and his team (2009) proposed that NA is the major product, with approximately 87% formed during the reaction by coating droplets of water. Moreover, Last and co-workers (2009) found that NA yield increases with increasing reaction time.

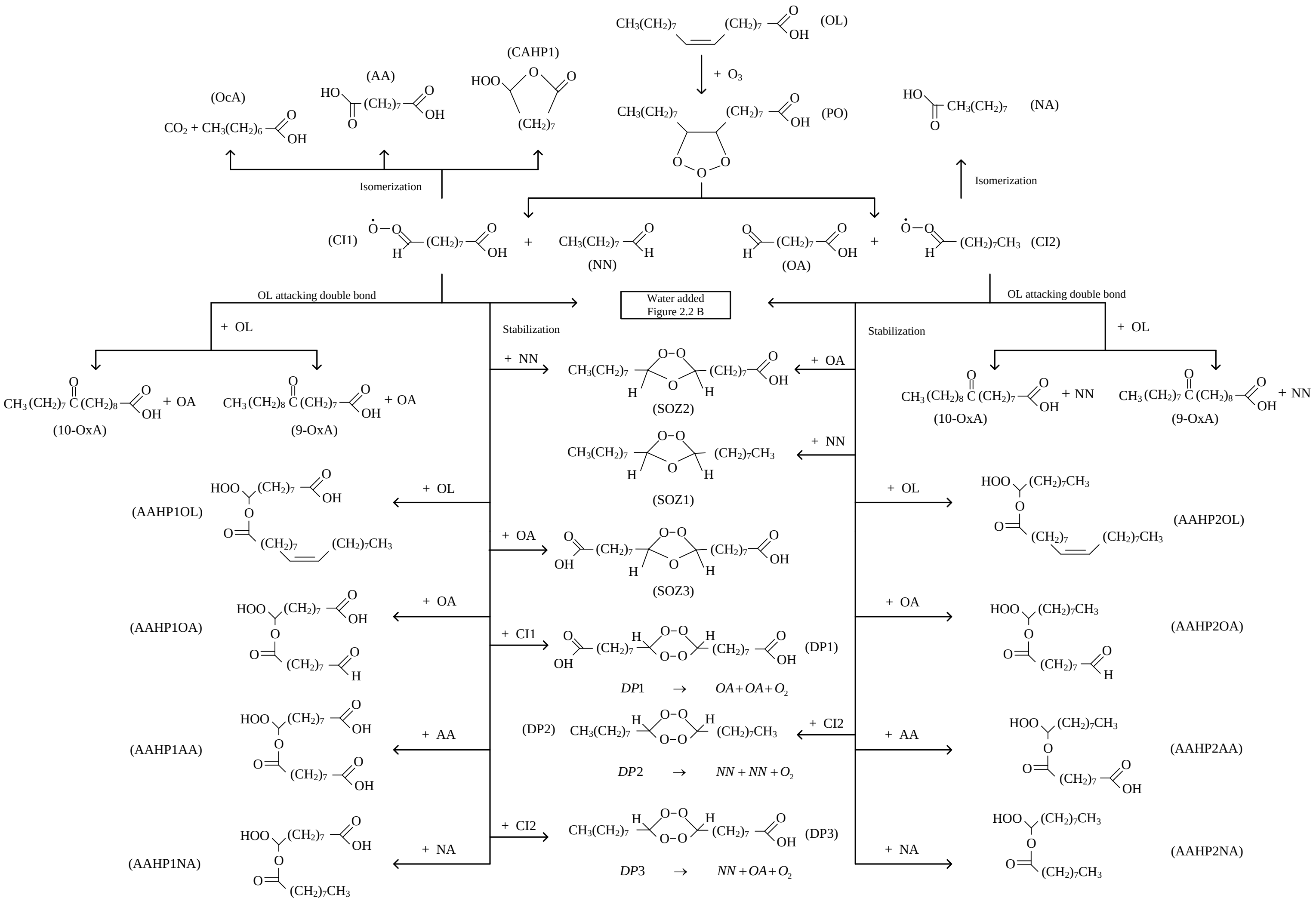

Figure 2.2A Reaction pathways of ozonolysis

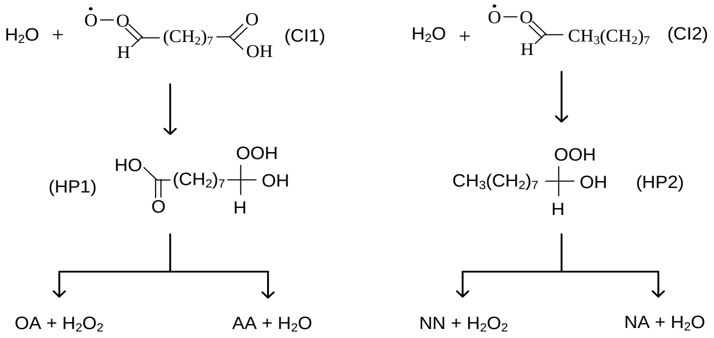

Figure 2.2B Reaction pathways of ozonolysis: water added

2.1.2.3 Secondary products of ozonolysis of OL

In addition to the low molecular weight products, peroxides and hydroperoxides (which are higher molecular weight species from the reaction between CIs and other species) have been observed as secondary products (Katrib *et al.* 2004, Ziemann 2005, Vesna *et al.* 2009). Ziemann and co-workers (2005) found that organic peroxides are observed at 68% in the aerosol particles. Vesna and co-workers (2009) also found that peroxides represent the largest fraction of products with approximately 50% found in the particles. Katrib and co-workers (2004) reported that peroxide products of 35-50% are observed, and the percentage yields of these peroxides decrease with increasing layer thickness. This observation means that the reaction of organic peroxides occurs at the gas-liquid interface or because an abundance of the CIs accumulated at the surface results in the high reaction rate between OL and CIs. It should be noted that the efficiency of the reaction between CI and protic species that forms hydroperoxide products is higher than that of the reaction between CI and aldehyde (Vesna *et al.* 2009). Moreover, lower molecular weight products might be formed from decomposition of peroxide products (Zahardis and Petrucci 2007).

However, Thornberry and Abbatt (2004) found that the amount of secondary products is quite small because the aldehyde product rapidly desorbs from the film, resulting in a reduction of the secondary ozonide formation.

2.1.2.4 Reactive uptake of ozone

The loss of gas phase species to the particle phase is always described as gas-phase uptake. Several processes exist for gas-phase uptake by a particle, including diffusion of gas species through the gas phase to the surface, adsorption or desorption at the surface, mass accommodation, reaction at the surface/in the bulk, and particle phase reactant diffusion. All of these processes can be described using an electric circuit resistance model, as illustrated in Figure 2.3 (Worsnop *et al.* 2002).

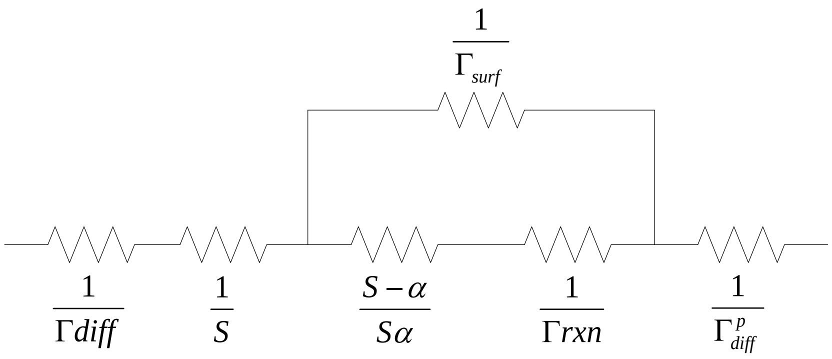

Figure 2.3 Electric circuit resistant model (Worsnop *et al.* 2002)

If this model is combined, a new parameter referred to as the measured uptake coefficient (γ_{meas}) is drawn, as shown in Eq. 2-1 (Smith *et al.* 2002, Worsnop *et al.* 2002).

$$\frac{1}{\gamma_{meas}} = \frac{1}{\Gamma_{diff}} + \frac{1}{S} + \frac{1}{\Gamma_{surf} + \frac{1}{\frac{S-\alpha}{S\alpha} + \frac{1}{\Gamma_{rxn}}}} + \frac{1}{\Gamma^{p}_{diff}} \qquad (2\text{-}1)$$

Worsnop and co-workers (2002) reported that the loss of species in the particle phase, i.e., OL, can be described in terms of the reactive uptake coefficient (γ). The change in OL concentration therefore can be expressed using this parameter with the assumptions that all of the reactive gas molecules react with the particle phase species and that the reaction is irreversible (Smith *et al.* 2002, Worsnop *et al.* 2002).

$$\frac{d[OL]}{dt} = -\gamma\left(\frac{P_{O_3}\bar{c}}{4RT}\right)\frac{S_p}{V_p} \qquad (2\text{-}2)$$

In this expression, γ is the reactive uptake coefficient, which is the probability of collision of ozone with a liquid particle on the surface and in the bulk that results in the reaction, P_{O_3} is the partial pressure of O_3 (atm), $\bar{c}$ is the mean kinetic speed of an O_3 molecule in the gas phase (3.6×10^{4} cm s^{-1}), R is the gas constant (0.082 atm K^{-1} M^{-1}), T is the gas temperature (K), and S_p/V_p is the surface area to volume ($3/r_p$, where r_p is the particle radius).

Before solving Eq. 2-2, γ must be known because it is a function of OL concentration. Smith and co-workers (2002) also reported that loss of O_3 in the reaction with OL is due to both reaction in the bulk and reaction on the surface. Thus, the net reactive uptake of O_3 is the sum of the uptake caused by both reaction on the surface (Γ_{surf}) and reaction in the bulk (Γ_{rxn}), as shown in Eq. 2-3. It should be noted that the non-reactive uptake terms, including the diffusion of gas species through the gas phase to the surface, the adsorption or desorption at the surface, mass accommodation, and the particle phase reactant diffusion, are sufficiently fast. The measured uptake coefficient is therefore equal to the reactive uptake coefficient (Hearn *et al.* 2005).

$$\gamma = \Gamma_{surf} + \Gamma_{rxn} \tag{2-3}$$

For ease of calculation, two major cases must be assumed to determine the reactive coefficient by fitting to the measured concentration of OL (Smith *et al.* 2002, Worsnop *et al.* 2002, Hearn *et al.* 2005).

Case 1: Γ_{surf} is negligible in comparison with Γ_{rxn} such that γ equals Γ_{rxn}. The equation for Γ_{rxn} is shown in Eq. 2-4.

$$\Gamma_{rxn} = \frac{4H^{cp}RT}{\bar{c}} \frac{D_{O_3}}{l} \left[\coth\left(r_p / l\right) - \left(l / r_p\right)\right] \tag{2-4}$$

In these expressions, k_2 is the reaction rate constant for the reaction of O_3 with OL in the bulk ($M^{-1} \cdot s^{-1}$), D_{O_3} is the diffusion coefficient of O_3 in OL ($cm^2 \cdot s^{-1}$), H^{cp} is the Henry's Law constant (M/atm), l is the diffuso-reactive length $l = \left[D_{O_3} / \left(k_2 \left[C_{OLb}\right]\right)\right]^{1/2}$, and C_{OLb} is the OL concentration in the bulk. Moreover, case 1 can be subdivided into two cases described as follows:

Case 1a: Rapid diffusion of O_3 within the particle or slow reaction, which means that the rate of reaction will not be limited by O_3 diffusion. In other words, O_3 is constant throughout the particle (Smith *et al.* 2002, Worsnop *et al.* 2002, Hearn *et al.* 2005). With this assumption, the $[\coth(r_p/l)-(l/r_p)]$ term in Eq. 2-4 is approximately $\frac{r_p}{3l}$, and this equation reduces to:

$$\Gamma_{rxn} = \gamma = \frac{4H^{cp}RT}{\bar{c}}\frac{r_p}{3}k_2[C_{OLb}] \tag{2-5}$$

The reduction of OL as a function of time can be written by substituting Eq. 2-5 into Eq. 2-2 and solving the differential equation as shown in Eq. 2-6.

$$[C_{OLb}] = [C_{OLb}]_0 \exp(-P_{O_3}H^{cp}k_2t) \tag{2-6}$$

Case 1b: The reaction of O3 near the surface of the particle or rapid reaction, which means that the rate of reaction will be limited by O3 diffusion (diffuso-reactive length <5% of particle radius) (Smith *et al.* 2002, Worsnop *et al.* 2002, Hearn *et al.* 2005). With this assumption, the $[\coth(r_p/l)-(l/r_p)]$ term in Eq. 2-4 is approximately equal to 1, and this equation reduces to

$$\gamma = \frac{4H^{cp}RT}{\bar{c}}\sqrt{D_{O_3}k_2}\sqrt{[C_{OLb}]} \tag{2-7}$$

The reduction of OL concentration as a function of time can be described by substituting Eq. 2-7 into Eq. 2-2 and solving the differential equation as shown in Eq. 2-8.

$$\sqrt{[C_{OLb}]} = \sqrt{[C_{OLb}]_0} - \frac{3P_{O_3}H^{cp}\sqrt{D_{O_3}k_2}}{2r}t \tag{2-8}$$

Case 2: A reaction occurs on the surface, which means that Γ_{rxn} is negligible compared with Γ_{surf}, and thus γ equals Γ_{surf}. With this assumption, the equation of Γ_{surf} can be written as shown in Eq. 2-9 (Smith *et al.* 2002, Worsnop *et al.* 2002, Hearn *et al.* 2005).

$$\Gamma_{surf} = \gamma = \frac{4H^{cp}RT}{\bar{c}}\delta^2 k_2^{surf}[C_{OLb}] \tag{2-9}$$

The expression of OL as a function of time can be described by substituting Eq. 2-9 into Eq. 2-2 and solving the differential equation, as shown in Eq. 2-10.

$$\left[C_{OLb}\right] = \left[C_{OLb}\right]_0 \exp\left(-\frac{3\delta^2}{r_p} P_{O_3} H^{cp} k_2^{surf} t\right) \tag{2-10}$$

In this expression, k_2^{surf} is the reaction rate constant for the reaction of O_3 with OL on the surface (cm^2/molecule · s), and δ is depth of the surface layer (cm).

By fitting all of the equations listed above, Hearn and co-workers (2005) concluded that the reaction between OL and O_3 occurs on the surface (case 2). In contrast, the previous results, which were examined by Smith and his team (2002), showed that the reaction occurs in both case 1b and case 2, but case 1b shows a better fit than case 2. Moise and Rudich (2002) also concluded that the reaction occurs quite close to the surface (case 1b) because the reactive uptake coefficient of liquid phase is higher than that of the solid phase by at least an order of magnitude. Moreover, the experimental results reported by Morris and co-workers (2002) show that the reduction of OL concentration increases with decreasing particle diameter. This observation confirms that the reaction not only takes place at the surface but also in the liquid bulk.

Smith and co-workers (2002) found that the reactive uptake coefficient decreases with increasing particle diameter due to the limitation of self-diffusion of OL in the particles. Although the self-diffusion of OL measured by Iwahashi and co-workers (2000) is quite high, it can be assumed that the rate of reaction is not limited by OL diffusion. During the reaction, the formation of higher molecular weight products might inhibit the diffusion of OL in the particles. Therefore, the self-diffusion of OL at the fluid interface (reaction zone) is not sufficiently rapid to maintain the uniform concentration profile of OL that accounts for the decrease in reactive uptake of larger particles if OL must diffuse through a longer distance. These groups also found that the particle diameters increase with increasing ozone exposure because of the formation of ozonolysis products. Moreover, the formation of ozonolysis products might affect the diffusion of ozone, thus resulting in a change in the rate of uptake, but it would not lead to an observed size dependence in the reactive uptake coefficient (Smith *et al.* 2002).

2.1.2.5 Reaction rate constant on the surface

Previous experiments show that ozonolysis of OL takes place near the gas-liquid (OL) surface (10 – 20 nm) and does not depend on O_3 diffusion (Moise and Rudich 2002, Hearn *et al.* 2005). Therefore, the reaction between OL and O_3 can be considered to be "on surface", and consequently, the rate loss of OL can be displayed as shown in Eq. 2-11 (Rosen *et al.* 2008).

$$\frac{d[C_{OLs}]}{dt} = -k_2^{surf}\left[C_{O_3s} \cdot C_{OLs}\right] \tag{2-11}$$

In this expression, C_{OLs} is the surface concentration of OL (molecules/cm^2), and C_{O_3s} is the surface concentration of O_3 (molecules/cm^2).

If the flow rate of ozone is steady, the ozone concentration is assumed to be constant. Therefore, the reaction between OL and ozone is likely a pseudo-first-order reaction. If $k^{'} = k_2^{surf}[C_{O_3s}]$, Eq. 2-12 can be rewritten as:

$$\frac{d[C_{OLs}]}{dt} = -k^{'}[C_{OLs}] \tag{2-12}$$

After solving Eq. 2-12, the linear equation can be written as shown in Eq. 2-13.

$$\ln[C_{OLs}] = k^{'}t + \ln[C_{OLs}]_0 \tag{2-13}$$

Therefore, $k^{'}$ (s^{-1}), which is the slope of the linear equation, can be calculated if $\ln[C_{OLs}]$ is plotted against the reaction times (Gonzalez-Labrada *et al.* 2007).

2.1.3 Effect of operating conditions on the formation of ozonolysis products

It is evident from the previous experiments that many factors (temperature, time, humidity, and ozone concentration) affect the yield of products during ozonolysis. These factors are described below.

The effect of temperature: Moise and Rudich (2002) found that NN yield increases with increasing operating temperature in both the solid and liquid phases of OL, whereas the reactive uptake coefficient shows no significant differences with temperatures in both phases. Thornberry and Abbatt (2004) concluded that the reactive uptake coefficient increases with increasing operating temperature, which means that the reaction between OL and ozone appears to behave in an Arrhenius manner. However, Hung and Tang (2010) have concluded that reaction temperature has a small effect on the oxidation rate of liquid phase and also suggested that the α-acyloxyalkyl hydroperoxide yield increases with increasing reaction temperature.

The effect of reaction time: Smith and co-workers (2002) and Vesna and co-workers (2009) found that the concentration of OL decreases with increasing reaction time, whereas the primary product concentration increases. Last and co-workers (2009) concluded that the OA yield decreases dramatically with increasing reaction time, and the NA yield increases. The increase of NN yield during ozonolysis was also observed by Sage and co-workers (2009).

The effect of humidity: It is evident that increasing the humidity during ozonolysis of the condensed phase of OL results in an increase of primary product yields, except for NN. The formation of peroxide products also decreases because CIs react with water before they react with primary products (Vesna *et al.* 2009). In contrast, Lee and co-workers (2012) concluded that in the presence/absence of water, the reaction showed the same results for oxidation of OL because only small amount of water can dissolve in OL.

The effect of ozone concentration: Gonzalez and co-workers (2007) claim that the concentration of OL decreases with increasing ozone concentration. Hung and co-workers (2005) report that that the mole ratio of OL to ozone affects the product yields. If the ratio is much less than unity, the expected products are NN, OA, or CIs. However, if the ratio is much greater than unity (in the coated wall experiments and in an organic chemist's beaker), the expected products are higher molecular weight species from the additional reactions between CIs and primary products. Moreover, these groups suggest that the OL loss and the product formation are expected to be linear for the ordinate of ozone exposure "atm·s" if the molar ratio of ozone to OL is much less than unity and also concluded that if ozone concentrations are sufficiently low, the reaction rates are first order in ozone concentration**.** Moreover, Hearn and Smith (2004) reported that additional NN and OA yields might be formed for a system in the presence of high ozone concentration because the concentration of CIs might be much higher than that at low ozone concentration, resulting in an increase in the self-reaction rate and an increase of NN and OA yields.

2.1.4 Ozonolysis of methyl oleate

Ozonolysis of aerosol particles of methyl oleate (M-OL) was studied to observe the formation of higher molecular weight products (Mochida *et al.* 2006). Although the reaction pathways of ozonolysis of M-OL are quite similar to ozonolysis of OL, as shown in Figure 2.2A, several pathways for polymerisation are absent, and the formation of certain species are different. For example, NN and M-CI1, which is the Criegee intermediate ending with a methyl ester group, are formed when the reaction follows pathway 1, whereas 9-oxononanoic acid, methyl ester (M-OA) and CI2 are formed when the reaction follows pathway 2. For ozonolysis of pure M-OL, Mochida and co-workers (2006) found that the secondary ozonide products formed from the reactions among NN, M-CI1, M-OA, and CI2 are the major compounds found in the higher molecular weight products. However, compared with mixed particles of myristic acid and M-OL, AAHP compounds were observed in high yields for M-OL mole fractions of 0.5 or less. This result means that the reaction rate of the CIs with carboxylic acid groups that form AAHP compounds is higher than the reaction rate of the CIs with aldehyde groups from the secondary ozonide products. It is surprising that M-CI1 or CI2 do not react with M-OL efficiently because of the methyl group (Hearn *et al.* 2005).

Moreover, ozonolysis of the M-OL monolayer at the air-water interface has been studied by Pfrang and co-workers (2014), who observed the oxidation kinetics and the reaction products. These researchers found that the kinetic reaction is a pseudo-first-order reaction, the reaction rate constant is approximately nine times larger than that of ozonolysis of OL, and the observed products are the same as those proposed by Mochida and co-workers (2006), except for octanoic acid methyl ester.

2.1.5 Ozonolysis of vegetable oils

The reactions between olive oil and ozone occur almost exclusively at the carbon-carbon double bonds (Bailey 1978). Many products are observed from this reaction, such as aldehydes and peroxides produced via the Criegee mechanisms (Brackbill *et al.* 1992, Rebrovic 1992, Pryor *et al.* 1995). Diaz and co-workers (2006) found that both the viscosity and acidity values of ozonised oil (olive oil and sunflower oil) increase due to the formation of peroxidic substances and carboxylic acids. The peroxide values of ozonised sunflower oil are higher than those of ozonised olive oil because more numerous double bonds are observed in sunflower oil. These researchers also found that the iodine value decreases as result of the reduction of double bonds. These results are similar to those reported by Sodowska and co-workers (2008).

Ozonolysis of sunflower oil also has been studied by Soriano and co-workers (2003). The degradation of linoleate was observed to be 1.5 and 1.8 times higher than that of the oleate in the absence and presence of water, respectively, because a larger number of double bonds are found in the linoleate molecule. These researchers also found that the ratio between aldehyde and ozonised products is 10.5:89.5 and 46.6:53.4 in the absence and presence of water, respectively. This observation could be due to the formation of hydroxyalkyl hydroperoxide in the presence of water, which decomposes to form hydrogen peroxide and aldehyde, as discussed in the previous section. Moreover, ozonised vegetable oils, i.e., soybean oil, rapeseed oil, and palm oil (1.0-1.5% by weight), were mixed with neat biodiesel produced from these materials to observe their physical properties. The density, flash point, and viscosity of mixed biodiesel all increase with the increasing percentage of ozonised oils, whereas the pour point decreases (Soriano *et al.* 2006). The increase of both density and viscosity might be due to the triglyceride backbone content of ozonised oil. The increase in the flash point is possibly a result of the formation of aldehyde, i.e., NN (flash point, 71°C), or nonanoic acid (flash point, 114°C).

Ozonolysis of canola oil with different solvents, i.e., ethyl acetate, methanol, and ethanol, has been described in the work performed by Omonov and co-workers (2011). The major products observed using ethyl acetate as the solvent are NN and NA, whereas 1-hexanal and hexanoic acid are the minor products. If alcohols are used as the solvents, NN and 1-hexanal are still the major product and minor product, respectively, whereas nonanoic alkyl ester was observed, but the reaction mechanism is unclear. Moreover, these researchers found that if ozonolysis of canola oil is continued after all double bonds are cleaved, the aldehyde products decrease, whereas the carboxylic acids and esters increase because aldehyde products are oxidised by ozone to form carboxylic acids, and the carboxylic acids might react with methanol to form methyl esters (Omonov *et al.* 2011).

2.1.6 Discussion of the literature review

Several necessary parameters for the bubble column reactor design and process design (i.e., the kinetic parameters and the product selectivity) are investigated in this research for the purpose of scale-up for commercial production. Therefore, ozonolysis of OL must be revisited for many reasons. First, previous studies were performed using the small droplets or coated-wall flow tube methods of oleic acid reaction with ozone, which is quite different from the methods intended for this research. Second, the previous results provided inefficient information for both reactor and process system design. However, certain clues from previous research might be used to design experiments to test our hypotheses. For example, the reduction of oleic acid concentration is a function of surface area, as shown in Eq. 2.2, and the reaction between OL and ozone takes place at the fluid interface such that ozone micro-bubbles are the correct option for this research because they have a higher surface-area-to-volume ratio than fine bubbles. The reduction of OL concentration is a function of reaction time, and product yields are a function of operating temperature; consequently, this research studies various reaction times and operating temperatures to find the kinetic parameters. The reduction of OL concentration is also a function of ozone concentration, and therefore, various ozone concentrations must be studied in this research to find the optimum ozone concentration and to confirm the assumption of the kinetic regime. Because NN is a volatile product, it might be evaporated during the reaction, and thus, a condenser must be installed to condense all vapour-phase products. In addition, the NN yield increases with the presence of protic solvent in the system (humidity), and therefore, various protic solvents are added in mixtures with oleic acid at different percentages to increase productivity, and the optimum percentage of the protic solvents is determined.

In addition to OL, vegetable oils or used cooking oil, which contain a substantial amount of unsaturated fatty acid and are much lower cost than OL, can be used as a reactant for highly valuable chemicals. The by-product, which is a short-chain triglyceride, also might be used as a reactant for bio-kerosene/bio-gasoline production via the conventional transesterification reaction.

In this research program, the kinetic parameters (i.e., the reaction rate constant and the product selectivity) are investigated for the purpose of reactor and process system design intended for commercial production. A suitable protic solvent and the relevant percentages are studied to increase productivity.

2.1.7 Summary of previous research

The summaries of previous research are listed in Table 2.3.

Table 2.3 Summaries of previous research

Researchers	Techniques for Generating Ozone	Techniques for Analysing products	Ozone concentration	Conditions			Products (%)					Aims/Techniques/Others
				Time	Temp.	Press.	NN	OA	NA	AA	CHO_T	
(Moise and Rudich 2002)	-	EIMS for gas phases and HPLC	4 ppm	0.1 s	267-291 K	3-9 Torr	28_g	n/a	p	p	n/a	To measure the reactive uptake coefficient and to monitor volatile and some of liquid-phase products 1. Coated-wall flow tube 2. Liquid phase and solid phase 3. $\gamma = 8.3 \pm 0.2 \times 10^{-4}$ for liquid phase 4. $\gamma = 5.2 \pm 0.1 \times 10^{-5}$ for solid phase
(Morris *et al.* 2002)	-	AMS	10^{-5} atm	7 s	-	1 atm	-	-	-	-	-	To study the kinetics of OL, to determine the size change due to the uptake of ozone, and to assess the reaction stoichiometry 1. Droplet particles, between 200 nm and 600 nm 2. Liquid phase 3. The stoichiometry is 1:1 4. The reduction in concentration of OL is a function of particle diameter. 5. $\gamma = 1.6 \pm 0.2 \times 10^{-3}$
(Smith *et al.* 2002)	(Pacific Ozone Technology, model L11)	single-particle mass spectrometer	138 ppm	8 s	-	-	-	p	-	-	-	To measure the reactive uptake coefficient as a function of particle size 1. Droplet particles, between 200 nm and 600 nm 2. Liquid phase 3. The γ of ozone is the summation of the surface uptake and bulk uptake. 4. $\gamma = 7.3 \pm 1.5 \times 10^{-3}$ for small particles 5. $\gamma = 0.99 \pm 0.09 \times 10^{-3}$ for large particles
(Thornberry and Abbatt 2004)	UV source	A chemical ionization mass spectrometer (CIMS)	10% of O_3 in O_2 and He	vary	vary	1.3 Torr	50	-	-	-	-	To investigate the kinetics and mechanisms of loss of gas-phase ozone 1. Coated-wall flow tube 2. Liquid phase 3. Reaction take place very close to the surface.

												4. The independence of reaction rate constant on the ozone concentration 5. The temperature dependence of the reactive uptake coefficient 6. $\gamma = 8.0 \pm 1.0 \times 10^{-4}$
(Katrib *et al.* 2004)	UV source	AMS	1-30 ppm	3 s	298	1/ N_2 bar	n/a	20-35	1-3	1-3	35-50	To determine the chemical composition of particles and product yields 1. Coating on particles 2. Condensed phase 3. Varying thickness of OL between 2 to 30 mm 4. 30% of the particle is evaporated. 5. Reaction take place at the surface and in the bulk.
(Hearn and Smith 2004)	model L11, Pacific Ozone Technology	Aerosol CIMS	80-120 ppm	4 s	-	-	84	p	p	12	-	To investigate ozonolysis of OL particles 1. Droplet particles with diameter of ~800 nm 2. Condensed phase 3. The number of double bonds affect the rate of reaction. 4. The reactive uptake coefficient is independent of particle sizes. 5. $\gamma = 7.5 \pm 1.2 \times 10^{-4}$
(Hearn *et al.* 2005)	model L11, Pacific Ozone Technology	Aerosol CIMS	10-100 ppm	4.5 s	-	-	-	-	-	-	-	To investigate the secondary reactions and surface reaction 1. Droplet particles with diameter of ~800 nm 2. Condensed phase 3. Reaction take place at the surface 4. 36% loss of OL is due to secondary reaction 5. $\gamma = 8.8 \pm 0.5 \times 10^{-4}$
(Hung *et al.* 2005)	UV source	ATR-IR, GC-MS, and LC-MS	30-300 ppm	2000 s	298	1/air bar	30	14	7	6	n/a	To investigate the mechanisms of reactions, and characterization of products 1. Droplet particles, ~2.7 mm 2. Condensed Phase

												3. Viscosity of droplets increases after the reaction. 4. If ozone concentrations are low enough, all significant rates are the first order in ozone concentration.
(Knopf *et al.* 2005)	UV source	CIMS	0.08-1.6 ppm	-	298	2-3 Torr	-	-	-	-	-	To study the reaction of ozone with OL/alkanoic acid mixtures. To gain a better understanding of the reactions on multi-components, reactivity and OL life time 1. Coated-wall flow tube 2. Liquid phase and solid phase 3. γ decrease with increasing the ratio of LA and MA 4. Reaction might occur in the bulk and on the surface 5. $\gamma = 7.9 \pm 0.3 \times 10^{-4}$ for liquid 6. $\gamma = 0.64 \pm 0.05 \times 10^{-4}$ for solid
(Ziemann 2005)	A Welsbach T-408	A Dasibi 1003-AH (for ozone) HPLC with TDPBMS	2.8 ppm	-	296	97 kPa	-	28	-	4	68	To investigate the products, mechanisms, and kinetics 1. Droplet particles with diameter of ~0.02-0.5 µm 2. Condensed phase 3. NN is assumed to evaporate before reacting with the CIs. 4. $\gamma = 6.1 \pm 5 \times 10^{-4}$ 5. $k = 0.015 \pm 0.01\ s^{-1}$ for 2.8 ppmv of ozone
(Katrib *et al.* 2005)	-	AMS	1-50 ppm	7 s	298	1/ N_2 bar	-	-	-	-	-	To investigate ozonolysis of OL mixed with stearic acid 1. Droplet particles 2. Condensed Phase 3. $\gamma = 1.25 \pm 0.2 \times 10^{-3}$
(Hung and Ariya 2007)	UV source	UV-vis spectrometer (for ozone con.) FT-ICR-MS	20 ppm and 500 ppm	6000 s	298	1 atm	-	-	p	p	-	To investigate heterogeneous ozonolysis of OL 1. Droplet particles 2. Condensed Phase 3. OL of 70% is consumed by secondary reactions. 4. The physical properties of droplets/particles are changed after reacting with ozone. 5. $\gamma = 3.2 \pm 0.5 \times 10^{-4}$

(Gonzalez-Labrada *et al*. 2007)	UV source: Pen-Ray lamp	PAT-1 surface tensionmeter for analysing surface	Vary	-	296	-	-	-	-	-	-	To observe a change in surface activity of OL 1. Coated over surface of an aqueous pendant drop 2. Liquid phase 3. $\gamma = 2.6\pm0.1\times10^{-6}$ 4. $k^{`} = 9.4\pm0.5\times10^{-18}$ $cm^3 molecule^{-1} s^{-1}$
(Rosen *et al*. 2008)	model L11, Pacific Ozone Technology	ATOFMS, SEM, and AFM	4-25 ppm	Vary	298	1 atm	-	-	-	-	-	To investigate the reaction on two different inorganic core particles 1. Coating on particles 2. Condensed phase 3. The kinetic rate of PSL is higher than silica particle. 4. The reaction of large and small size are identical. 5. The kinetic rate does not have a statistically significant association with OL vapor pressure. 6. $\gamma_{oleic} = 2.5\times10^{-5}$ on PSL at ozone 4 ppm 7. $\gamma_{oleic} = 1.6\times10^{-5}$ on silica at ozone 4 ppm
(King *et al*. 2009)	UV source: Pen-Ray lamp	Neutron reflection	0.16 – 4.78 ppm	10000 – 30000 s	-	-	-	-	87±14	p	-	To investigate the oxidation of a monolayer of OL over air-water interface 1. coated over aqueous solution 2. Condensed phase 3. OL is removed from the interface by oxidation reaction and replaced by NA. 4. $\gamma = 4.0\times10^{-6}$
(Vesna *et al*. 2009)	UV source	GC-MS and UV-spectrometry	200 -1800 ppb	60-360 s	298	1	56	p	p	p	~50	To investigate product yields at different ambient condition and humidity 1. Droplet particles 2. Condensed phase 3. All products yields increase with increasing RH except NN. 4. Peroxides are the largest product.
(Sage *et al*. 2009)	-	A quadrupole aerosol mass spectrometer (Q-AMS)	12 ppb	Vary	-	-	p	-	-	-	-	To measure a change in the reactivity of initial OL and to calculate the OL-O_3 reaction stoichiometry 1. Droplet particles

												2. Condensed phase 3. The ratio between OL and O_3 is excess 2:1. 4. A yield of NN increases during the period between 0 - 4 hrs. 5. $\gamma = 8.0\times10^{-4}$
(Last *et al.* 2009)	Plasma discharge	FT-IR, Electrospray mass spectrometry (ES)	1.6%	8 min	-	-	p	p	p	p	p	To establish a laboratory method for ozonolysis reactions 1. Bubbling a fine stream of bubbles by using a needle 2. A yield of OA decreases with increasing the reaction time, while NA increases. 3. A yield of AA remains small throughout the reaction time.
(Hung and Tang 2010)	UV source	UV-vis spectrometer (for ozone con.) ATR-FTIR	~5 ppm	>6000 s	273-298		-	-	-	-	-	To investigate the oxidation rate at different physical states and temperatures 1. Droplet particles (3mm and 10μm) 2. Condensed phase and solid phase 3. Rate constant of small particles is higher than large particle. 4. $\gamma = 3.2\pm1.1\times10^{-3}$
(Lee *et al.* 2012)	UV source (Appleton Woods)	Thermo Scientific, 49i (for ozone concentration), An ultra-high resolution mass spectrometer	2 ppm	>100 hours	298	1 atm	-	p	p	p	-	To investigate the effect of humidity on ozonolysis 1. Aerosol particles 2. Condensed phase 3. No effect of humidity on the product distribution

n/a represents that analysis method was not used for these chemical species. P represents that the chemical species was found but their yields were not quantified. OL is oleic acid. LA is lauric acid. MA is myristic acid. NN is 1-nonanal. OA is 9-oxononanoic acid. NA is nonanoic acid. AA is azelaic acid. CHO_T is other organic molecules.

2.2 Ozone

Similar to Section 2.1, this section provides useful information for the experimental set-up i.e., the technique for generating ozone, the technique for inlet ozone measurement, and suitable materials for contact with ozone. This section also provides the kinetic equation used to estimate the reaction rate constant. The details are described in the following sub-sections.

2.2.1 History of ozone

Ozone was named in 1839 by Professor Schonbein, who worked on electrolysis at the University of Basel, after he noticed the odour of ozone. Before ozone was named, the same odour was also noticed near an electrostatic machine in 1785 by natural scientist Martinus van Marum, and near an anode in 1801 by Cruikshank, who worked on water electrolysis. In 1865, J L Soret found that ozone consisted of three atoms (Becker 2005). Non-equilibrium air plasma at atmospheric pressure is a technique used for industrial ozone generation because ozone molecules decay quite rapidly at high temperature. Simultaneously, a high operating pressure is preferred as a result of the three-body reaction of an oxygen atom and oxygen molecule. In 1857, Siemens invented the dielectric barrier discharge (silent discharge) method for ozone generation and also worked with Professor Ohlmuller at the Imperial Prussian Department of Health to investigate the effect of ozone on cholera, typhus and E. coli bacteria, and their results showed that ozone could completely kill all of these bacteria. After successful laboratory experiments, industrial ozone production began at a small water treatment plant in Holland (1893), followed by Germany (1901), Russia (1905), France (1907), in Spain (1910). Currently, several European countries, Canada, the USA, and Japan prefer ozone technology for disinfection of water because certain by-products from the chlorination technique can cause cancer (Becker 2005).

2.2.2 Physical properties

Ozone is a triangle shaped molecule (MW: 47.9982) that exists as a colourless gas at room temperature; its bond angle and bond length are 117^o and 0.128 nm, respectively. Ozone forms an indigo blue liquid (which is highly explosive) at temperature below -112°C and a deep blue-violet solid at temperatures below -193°C. As a result of the explosion hazard, ozone must be diluted before use in either a gas or water stream, and its solubility is approximately 1 kg/m^3 in water. Ozone is always produced on site and is neither stored nor shipped because of difficulties in storage, handling and transportation (Becker 2005). The conversion of gas phase concentrations is also illustrated in Table 2.4 (Gottschalk *et al.* 2009).

Table 2.4 Conversion of ozone gas phase concentration (Gottschalk *et al.* 2009)

C_g (Weight %)	C_g (volume %)	C_g (g/m^3)
1	0.7	14.1
5	3.4	71.7
10	6.9	145.8
15	10.5	222.6
20	14.3	302.1
At STP: T = 0 °C, P = 1.013×10^5 Pa (1 ppm = 2 mg/m^3, 20 °C, 101.3 kPa ; 1ppm = 1cm^3/m^3		

2.2.3 Applications

Ozone is a powerful oxidant that is used in many industries. For example, ozone is used in the chemical, food, and water treatment industries (Khadre *et al.* 2001, Plaue and Czerwinski 2003, Akbas and Ozdemir 2008, Azarpazhooh and Limeback 2008, Tiwari *et al.* 2010). Moreover, Ozone is used to replace such hazardous oxidants as chlorine for reduction of environmental and hazardous issues in wastewater treatment (Becker 2005).

2.2.4 Production techniques

Several techniques are used to generate ozone, including ultraviolet light and electrolytic and non-equilibrium plasmas. However, the first two techniques are not suitable for commercial production because the ultraviolet light technique generates only small yields of ozone and requires a large amount of energy, whereas the electrolytic technique is more expensive due to the high current and high potential needed to electrolyse water. Therefore, non-equilibrium plasmas are the most suitable technique for ozone production and are used in this study.

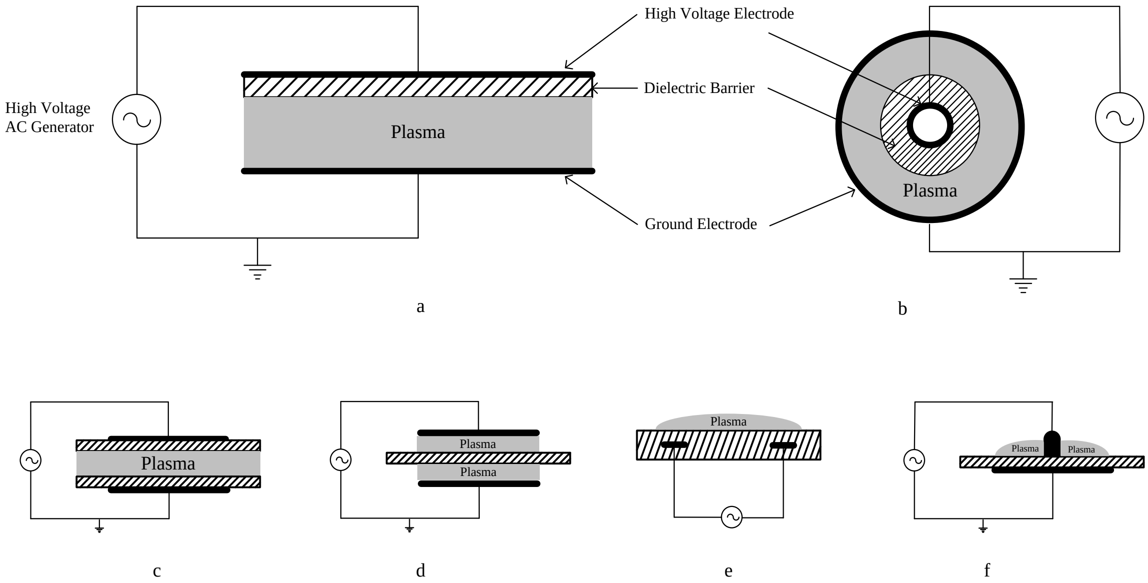

Figure 2.4 Dielectric barrier discharges at different configurations

Although several techniques exist for generating non-equilibrium plasmas, i.e., glow discharge, corona discharge, and dielectric barrier discharge (DBD), DBD is the technique commonly adopted for worldwide ozone production. A defining feature of dielectric barrier discharge is that at least one electrode must be covered by a dielectric layer, i.e., glass, quartz, ceramic or polymers. Three basic types of silent discharge are available, including volume discharge (VD) shown in Figure 2.4(a, b, c, and d), coplanar discharge (CBD) shown in Figure 2.4e, and surface discharge (SD) shown in Figure 2.4f. Because of a combination between glow and corona discharge, dielectric barrier discharges can be operated at high pressure and can also run using an AC power supply with a voltage of 1–10 kV and frequencies of 50 - 1 MHz. Therefore, dielectric barrier discharge methods are suitable for large-scale production and are in use for ozone production in water treatment processes around the world (Eliasson and Kogelschatz 1991, Conrads and Schmidt 2000). Moreover, DBD reactors can be operated using either air or pure O_2 as the reactant, but use of pure O_2 produces a higher ozone concentration than air (Pietsch and Gibalov 1998). The DBD reactors can also be operated at high pressure between 1 bar and 3 bar, frequencies from a few Hz to MHz, and a gap that is in the mm range (Pietsch and Gibalov 1998, Becker 2005). The DBD technique is used for generation of ozone in this study for many reasons. For example, DBD can be operated at atmospheric pressure, and consequently, neither an air compressor nor vacuum pump is necessary in the system. This method has a higher active volume; thus, large ozone yields can be generated. The DBD method can also be operated using AC current as a power supply, which is the lowest cost option for running the plasma reactor (Becker 2005).

2.2.5 Reactant feed

As mentioned previously, both pure oxygen and air can be used as a feed gas for ozone production, and the details are described below.

Pure oxygen feed: Several large ozone generators use pure oxygen as a reactant because use of air is more complicated. Ozone is always formed in a three-body reaction among oxygen atoms and two molecules of oxygen. A total of 131 reactions can form ozone using pure oxygen, including electron impact excitation, electron impact ionisation, electron impact dissociation, two-body reactions, three-body reactions, and two-body reactions of excited species. The reaction time required to reach 99% of equilibrium yield for ozone formation at atmospheric pressure is 0.01 seconds (Lozano-Parada and Zimmerman 2010).

The initial reaction is the dissociation of O_2 (dissociation energy: 5.16 eV), and many side reactions occur that can also destroy O_3 molecules at high temperatures, which means that ozone generators operated at high temperature should be avoided because their reaction rates increase with increasing operating temperature. At 100% efficiency for ozone formation (which is related to the enthalpy of formation), the energy efficiency is 1.22 kg/kWh. However, the best experimental values obtained from laboratory are in the range of 0.25-0.3 kg/kWh (Becker 2005).

Dry air feed: The presence of N_2 in the feed gas complicates the process, which means that the reaction time is longer compared with that of pure air feed, nearly 100 µs. Certain nitrogen oxide species are also generated that can prevent ozone formation, as represented in Eq. 2-14 to Eq. 2-16. The maximum energy efficiency is decreased to 0.2 kg/kWh because higher electron energy is needed to dissociate N_2 (Becker 2005).

$$O + NO + M \rightarrow NO_2 + M \tag{2-14}$$

$$O + NO_2 \rightarrow NO + O_2 \tag{2-15}$$

$$O + NO_3 \rightarrow NO_2 + O_2 \tag{2-16}$$

Moreover, if the feed gas contains water vapour, the reaction system will be further complicated for several reasons. For instance, the surface conductivity and micro-discharge properties are altered by only traces of humidity, and the presence of OH and HO_2 from electron impact dissociation of H_2O can limit the production of ozone following Eq. 2-17 through Eq. 2-19 (Becker 2005).

$$e + H_2O \rightarrow e + OH + H \tag{2-17}$$

$$OH + O_3 \rightarrow HO_2 + O_2 \tag{2-18}$$

$$HO_2 + O_3 \rightarrow OH + 2O_2 \tag{2-19}$$

As mentioned previously, the feed gas preparation process is an important step for ozone production. Therefore, many large ozone production systems prefer oxygen prepared by pressure swing or swing adsorption-desorption techniques as a feed gas (Becker 2005). However, dry air is used as a reactant for ozone production in this research because maximum efficiency of ozone production is not necessary, and safety is a significant concern.

2.2.6 Ozone decomposition from various aspects

The decomposition of ozone has been studied for nearly a century (Sehested *et al.* 1991). Many effects result from the disappearance of ozone, including pH, composition of gases, and temperature. The effect of pH on the ozone decomposition occurring at the fluid interface is shown in Figure 2.5, as plotted by Beltran (2004). Beltran (2004) deduced that the ozone decomposition reaction at pH values lower than 12 will not interfere with the direct ozone reactions of the fast or instantaneous kinetic regime, whereas at pH values higher than 12, the ozone decomposition reaction is the only method of ozone loss.

For the effect of temperature, Sehested and co-workers (1991) concluded that the decomposition of ozone increases dramatically with increasing temperature. The effects of thermal decomposition of ozone with various gases, including O_2, O_3, CO_2, N_2, and He, were also studied by Sidney and Axworthy (1957). The simple mechanisms of the decomposition reactions are shown in Eq. 2-20 through Eq. 2-22.

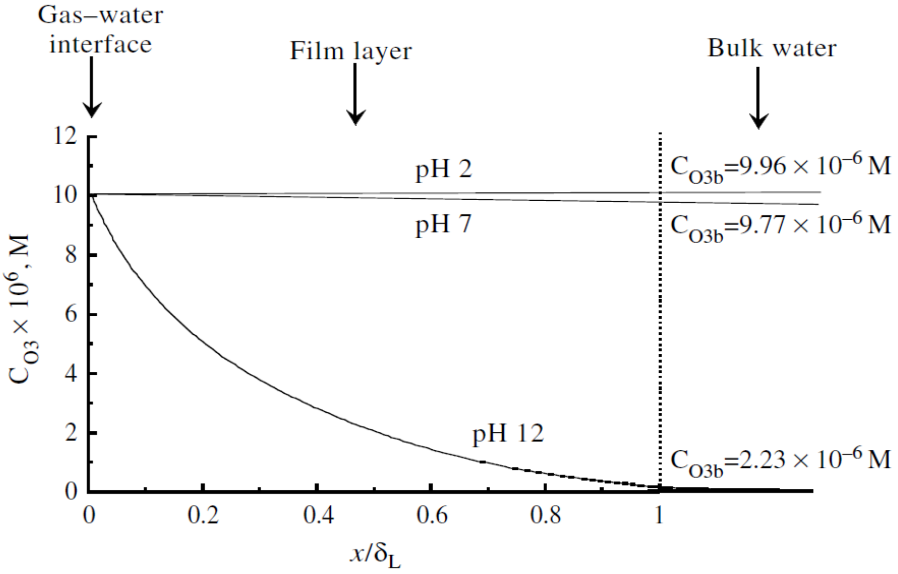

Figure 2.5 Variation of the concentration of ozone with the depth of liquid water and organic free at steady state of 20°C (Beltrán 2004)

$$M + O_3 \underset{k_2}{\overset{k_1}{\leftrightarrow}} M + O_2 + O \tag{2-20}$$

$$O + O_3 \underset{k_4}{\overset{k_3}{\leftrightarrow}} 2O_2 \tag{2-21}$$

$$O + O + M \underset{k_6}{\overset{k_5}{\leftrightarrow}} O_2 + M \tag{2-22}$$

In this expression, M in Eq. 2-20 indicates O, O_2, O_3, CO_2, N_2 or He. The relative efficiencies of O, O_2, N_2 CO_2, and He compared with O_3 are 0.44, 0.44, 0.41, 1.06, and 0.34, respectively (Benson and Axworthy 1957, Heimerl and Coffee 1980). For Eq. 2-22, M might be O, O_2, or O_3. The relative efficiencies of O and O_3 compared with O_2 are 3.6 and 1.0, respectively (Heimerl and Coffee 1980).

For further understanding based on this information, the COMSOL Reaction Engineering Lab is used to model the effect of temperature on the decomposition of ozone with various gases in the bubble. The details and results are described in Chapter 4.

2.2.7 Design features

It is evident that ozone decomposition increases with increasing temperature of the system. Therefore, to obtain a high ozone yield, the dielectric materials should have low dielectric constant and thermal conductivity because they can contribute to restriction of the gas temperature rise. The optimum gap is in the range of 0.6-0.8 mm (Sung and Sakoda 2005). Moreover, the cooling system and the power density are important design features because O_3 molecules deteriorate at high temperature. Therefore, the features of ozone generators are fabricated in a manner similar to those of heat exchangers. It is essential that the operating temperature should be maintained as low as possible, usually less than 100°C (Becker 2005).

2.2.8 Ozone measurement

Several techniques are available for measuring ozone concentration in the gas and liquid phase. The indigo method is appropriate for the liquid phase, and the iodometric and UV absorption methods are suitable for both phases. All details are summarised in Table 2.5 (Gottschalk *et al.* 2009).

Table 2.5 Analytical methods of ozone

Method	Gas	Liquid	Detection limit	Advantages	Disadvantages
Iodometric	+	+	100 µg/L	- No expensive	- No selectivity - Time consuming
UV-Absorption	+	+	depending on the system	- Easy & simple	- Aromatic components can disturb - Expensive
Indigo trisulfate		+	5 µg/L	- No expensive - Fast reaction - Secondary products do not interfere	- Need calibration - Natural colour of water does not disturb

As summarised in Table 2.5, if the gas phase of ozone must be measured, either the iodometric method (KI) or UV-absorption method should be selected. Although the UV-absorption method is the easiest technique for analysis of ozone concentration, this technique is quite expensive, and the detection limit depends on the system. Therefore, KI is used to analyse the ozone concentration in this research. The analysis steps are described as follows: The dissolved ozone gas from the bubbles reacts first with KI, and the products of this reaction react with $Na_2S_2O_3$ to form a pale yellow colour, as shown in Eq. 2-23 and Eq. 2-24. The ozone concentration is calculated if the consumption of $Na_2S_2O_3$ is measured. It should be noted that the KI method is directly applicable in the range of 1-200 g/m^3 and is used as the calibration method for the UV-absorption method (Masschelein 1998).

$$2KI + O_3 + H_2O \rightarrow I_2 + O_2 + 2KOH \tag{2-23}$$

$$I_2 + 2S_2O_3^{2-} \rightarrow 2I^- + S_4O_6^{2-} \tag{2-24}$$

2.2.9 Safety aspects

As a safety precaution, it is highly important to destroy excess ozone in the vent gas via installation of destruction units. Many techniques are used for this purpose and depend on the scale of ozone production. Either thermal destruction ($T \geq 300°C$) or catalytic destruction (manganese or palladium: T = 40°C to 80°C) is normally applied. Recycling of oxygen is a common technique used for large-scale systems in which ozone is generated by electrical discharges. In small-scale systems, a packed column filled with granulated activated carbon (d_P = 1-2 mm) is also employed (Gottschalk *et al.* 2009). Furthermore, ozone detectors must be installed in lab-scale applications to ensure that personnel in the workplace will not be harmed in the case of leaks.

2.2.10 Materials in contact with ozone for laboratory

Many pieces of equipment are used in the experiments, i.e., ozone generators, tubes, valves, flow metres, diffusers and reactors. To obtain the best results, all materials that contact ozone must be highly corrosion resistant because ozone is a notably strong oxidiser. The effect of ozone decay on materials should also be considered. Therefore, appropriate materials for the experimental setup are glass, stainless steel, ceramics, polyvinylchloride (PVC), polytetrafluoroethylene (PTFE), perfluoroalkoxy (PFA), and polyvinylalkoxy (PVA) (Gottschalk *et al.* 2009).

2.2.11 Kinetics of the direct ozone reactions

The kinetics of the direct ozone reactions can be observed from experiments by following two different approaches to find the rate constant of the reactions. The first approach is a homogeneous ozonisation reaction in which ozone and other compounds react with each other in the same phases, and their concentrations are monitored throughout the reaction time. The reaction rate is a function of the concentration of the reactants for irreversible reactions, and it is a function of the concentration of both reactants and products for reversible reactions. The second approach, which is used in this thesis, involves heterogeneous gas-liquid ozonisation reactions in which ozone must transfer from the gas phase (which might contain oxygen or air) to the liquid phase simultaneously with reactions to other chemicals in the liquid phase.

2.2.11.1 Physical absorption

Because the kinetics of heterogeneous reactions are controlled by both gas absorption and chemical reactions, a fundamental understanding of these two theories is important to describe the phenomena that occur during the reaction. For the gas physical absorption phenomenon, when both gas and liquid phases are in contact, the gas phase (assumed as component A) is transferred to the liquid phase to reach equilibrium. The rate of mass transfer or absorption rate can be written as shown in Eq. 2-25, and the concentration profile of the gas component A is shown in Figure 2.6.

$$N_A = k_G(P_{Ab} - P_i) = k_L(C_A^* - C_{Ab}) \qquad (2\text{-}25)$$

In this expression, N_A is the rate of mass transfer of A (mol/m^2 s); k_G and k_L are the mass transfer coefficients for the gas and liquid phase (m/s), respectively; P_{Ab} and P_i are the partial pressures of A at the gas interface, respectively; and C_A^* and C_{Ab} are the molar concentrations of A at the liquid interface and in the bulk (mol/m^3), respectively

Because it is difficult to find the mass transfer coefficients and the interfacial concentrations, the theoretical expressions for mass transfer coefficients can be written in terms of the microscopic mass balance equation of the transferred component A, as shown in Eq. 2-26, where the left-hand side term is the molecular and turbulent transport rate of

A, and the convection and accumulation rates are represented in the right-hand side terms, respectively.

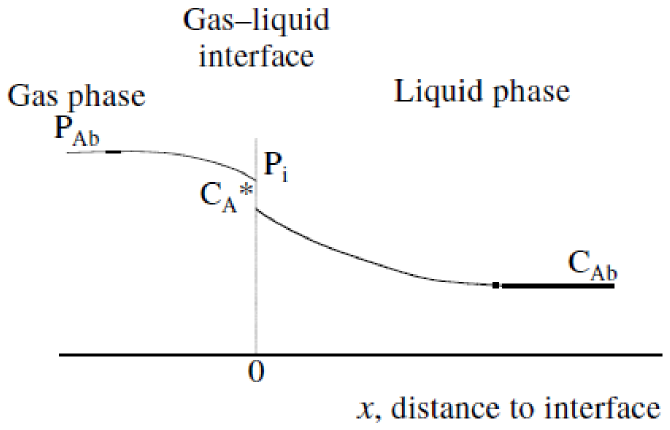

Figure 2.6 Concentration profile of a gas component A with the distance to the interface during its absorption in a liquid (Beltrán 2004)

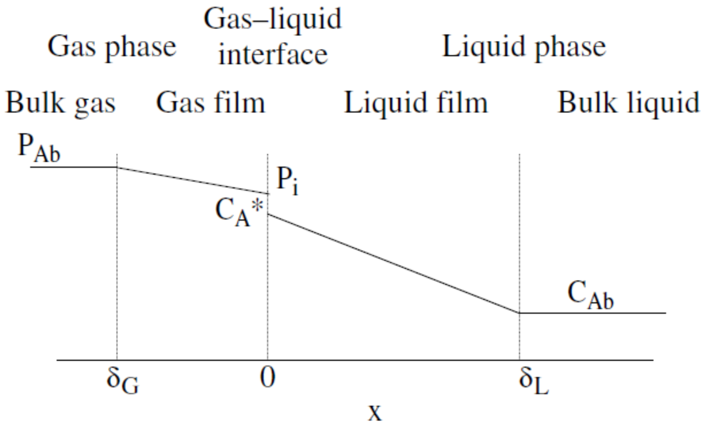

Figure 2.7 Concentration profile of gas A based on the film theory (Beltrán 2004)

$$D_T \nabla^2 C_A = U \nabla C_A + \frac{\partial C_A}{\partial t} \tag{2-26}$$

Two theories are used to simplify the previous equation, including the film theory and the surface renewal theory. The film theory is the simplest approach and was proposed by Lewis and Whitman; mass transfer though the film is only caused by diffusion, and the concentration profiles are reached immediately with distance to the interface. Two films, i.e., the gas film and liquid film, are bubbled into the liquid phase, as shown in Figure 2.7.

After solving Eq. 2-27 based on the conditions of Figure 2.7, the rate of mass transfer is:

$$N_{Ao} = -D_A \frac{dC_A}{dx_{x=0}} = \frac{D_A}{\delta_L}\left(C_A^* - C_{Ao}\right) \tag{2-28}$$

By comparing Eq. 2-28 with Eq. 2-25, the mass transfer coefficient for liquid is:

$$k_L = \frac{D_A}{\delta_L} \tag{2-29}$$

In this expression, D_A is the diffusion coefficient, and δ_L is the film thickness parameter for the film theory.

2.2.11.2 Chemical absorption

When chemical reactions take place at the fluid interface during diffusion, the reaction rate (r_A) will be added to the microscopic mass balance of Eq. 2-26, which becomes:

$$D_T \nabla^2 C_A + r_A = U \nabla C_A + \frac{\partial C_A}{\partial t} \tag{2-30}$$

The reactions might be first-order, pseudo-first-order, or second-order reactions, as shown below:

For a first-order reaction

$$A \quad \xrightarrow{k_1} \quad P; \qquad r_A = -k_1 C_A \tag{2-31}$$

For a pseudo-first-order reaction

$$A + zB \quad \xrightarrow{k_1^{'}} \quad P; \qquad r_A = -k_1^{'} C_A C_B = k_1 C_A \tag{2-32}$$

For a second-order reaction

$$A + zB \quad \xrightarrow{k_2} \quad P; \qquad r_A = -k_2 C_A C_B; \quad r_B = -z k_2 C_A C_B \tag{2-33}$$

where z is the ratio between the coefficients of B and A, and k is the reaction rate constant (s^{-1} for first-order, L/mol·s for second-order) (Fogler 2006). To solve Eq. 2-25, the film theory must be applied. The reaction order is also assumed. For an irreversible first-order or pseudo-first-order reaction with application of the film theory, Eq. 2-30 becomes:

$$D_A \frac{\partial^2 C_A}{\partial x^2} = -r_A = k_1 C_A \tag{2-34}$$

For an irreversible second-order reaction with application of the film theory, Eq. 2-34 becomes:

$$D_A \frac{\partial^2 C_A}{\partial x^2} = -r_A = k_2 C_A C_B \tag{2-35}$$

$$D_B \frac{\partial^2 C_B}{\partial x^2} = -r_B = z k_2 C_A C_B \tag{2-36}$$

2.2.11.3 Kinetic regimes

Many kinetic regimes exist and must be assumed to determine the reaction rate constant or the mass transfer coefficient based on the film theory describes the concentration profiles of A and B through the liquid, including very slow, diffusional, fast, fast pseudo-first-order, and instantaneous kinetic regimes, as show in Figure 2.8A through 2.8E. Each regime has its own kinetic equation used to determine the rate of mass transfer (N_{AO}), as shown in Table 2.6. The rate of mass transfer is also used to determine the reaction rate constant, mass transfer coefficient, or specific interfacial area, depending on the kinetic regime.

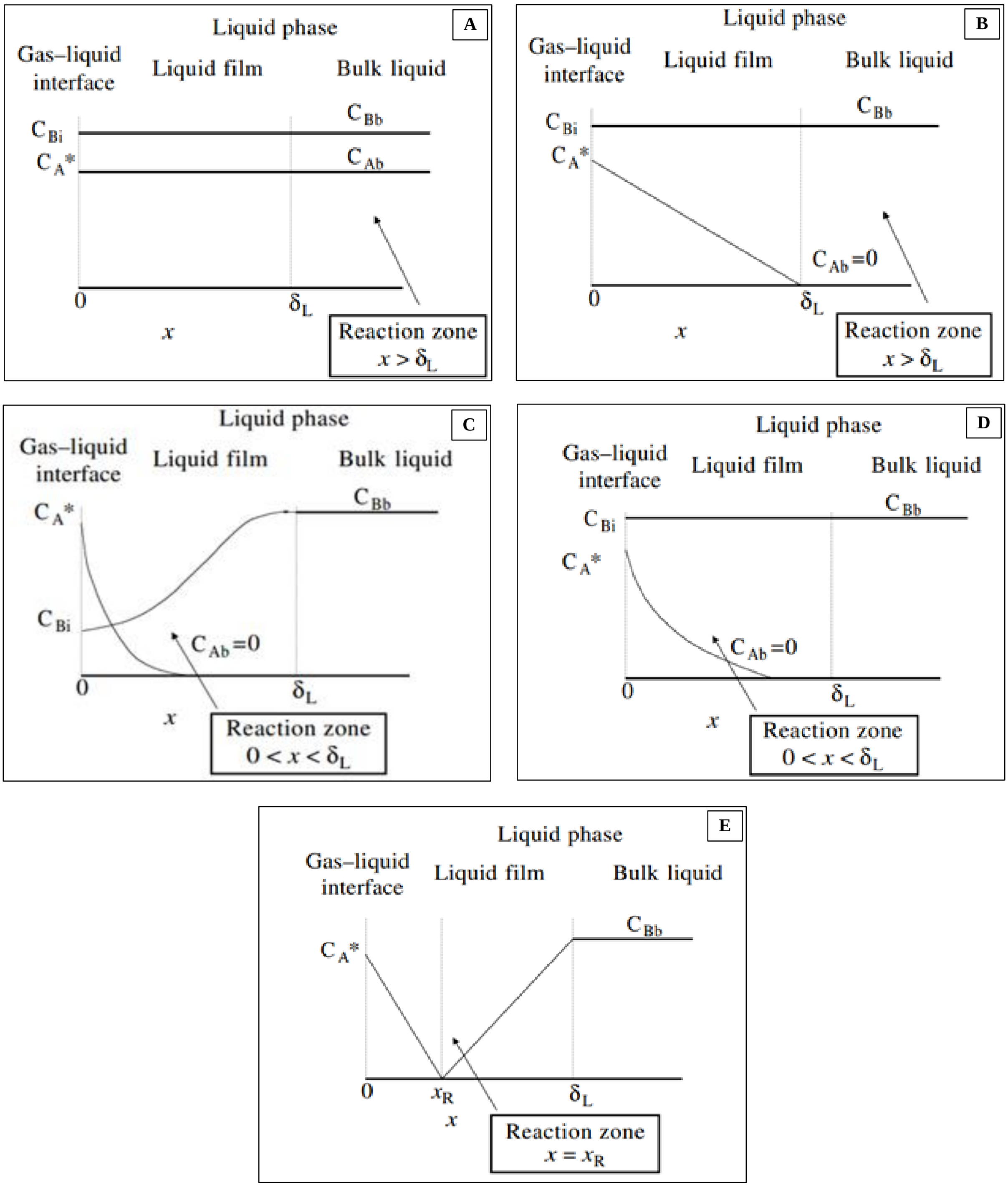

Figure 2.8 Film theory; A = very slow kinetic regime, B = diffusional kinetic regime, C = fast kinetic regime, D = fast pseudo first order kinetic regime, and E = instantaneous kinetic regime (Beltrán 2004)

Table 2.6 Absorption rate law equation for different kinetic regimes (Beltrán 2004)

Kinetic regime	**Kinetic equation**	**Condition and parameter to determine**
Very slow	$N_{Ao} = \frac{k_2 \beta C^*_{Ao} C_{Bb}}{a}; \qquad C^*_{Ao} = C_{Ab}$	$Ha_2 < 0.02, \quad C_{Ab} \neq 0$ Rate constant
Diffusional	$N_{Ao} = k_L C^*_A$	$0.02 < Ha_2 < 0.3, \quad C_{Ab} = 0$ Mass transfer coefficient
Fast	$N_{Ao} = k_L C^*_A \frac{Ha_2}{\tanh Ha_2}$	$Ha_2 > 3, \quad C_{Ab} = 0$ Rate constant or Mass transfer coefficient
Fast pseudo first-order	$N_{Ao} = C^*_A \sqrt{k_2 D_A C_{Bb}}$	$3 < Ha_2 < E_i / 2, \quad C_{Ab} = 0$ Rate constant or specific interfacial area
Instantaneous	$N_{Ao} = k_L C^*_A E_i$	$Ha_2 > nE_i, \quad C_{Ab} = 0$ Mass transfer coefficient
β is the liquid holdup which is the ratio of liquid to total volume, Ha is the dimensionless Hatta number, $Ha_2 = \frac{\sqrt{k_2 D_A C_{Bb}}}{k_L}$. $E_i = 1 + \frac{D_B C_{Bb}}{z D_A C^*_A}$		

2.2.11.4 Reaction rate constant calculation

As summarised in Table 2.6, three regimes can be used to determine the reaction rate constant, i.e., very slow kinetic, fast, and fast pseudo-first-order kinetic regimes. In this research, all of these regimes are studied to investigate the reaction rate constant via expression of the chemical disappearance rate of OL because the concentration of ozone during the reaction time is difficult to measure. Therefore, the mass balance of OL in a bubble column reactor becomes:

$$-\frac{dC_{OLb}}{dt} = zN_{O_3}a \tag{2-37}$$

A. Fast kinetic regime

Because of difficulty in using the equation for a fast regime, the equation for a fast pseudo-first-order kinetic regime is used by assuming that the concentration of OL is constant through the film layer and the same as the bulk concentration, as shown in Figure 2.8D. Therefore, Eq. 2-37 becomes:

$$-\frac{dC_{OLb}}{dt} = zaC^*_{O_3}\sqrt{k_2 C_{OLb} D_{O_3}} = \frac{C_{O_{3i}}RT}{H} za\sqrt{k_2 C_{OLb} D_{O_3}} \tag{2-38}$$

The limits of the equation above are:

$$t = 0 \qquad C_{OLb} = C_{OLb0}$$
$$t = t \qquad C_{OLb} = C_{OLb}$$

Eq. 2-38 can be integrated to become:

$$\sqrt{C_{OLb}} = \sqrt{C_{OLb0}} - \frac{zaC_{O_3 i}RT}{H^{pc}}\sqrt{k_2 D_{O_3}}\,t = \sqrt{C_{OLb0}} - At \tag{2-39}$$

In these expressions, C_{OL} is the concentration of OL (M), $H^{pc}$is the Henry's Law constant (atm/M), a is the specific interfacial area (cm^{-1}), $C_{O_3 i}$ and $C^*_{O_3}$ are the concentration of ozone at the inlet and interface, respectively (M), and D_{O_3} is the diffusion coefficient of ozone in oleic acid (cm^2/s). By plotting the square root of the concentration of OL against the reaction time, the reaction rate constant (which is a function of the slope) can be calculated. The experiments must be performed at different ozone concentrations to obtain the different slopes. In addition, by plotting the slopes against the ozone concentrations, linearity should be observed to confirm the value of the reaction rate constant. It should be noted that if the assumption of a fast reaction regime is correct, the condition must be fulfilled by equation in Table 2.6.

In the case of secondary reactions, the initial rate method shown in Eq. 2-40 can be used to determine the reaction rate constant by plotting $(1/z)(-dC_{OLb}/dt)_{t=0}$ against $C^*_{O_3}C^{0.5}_{OLb}$. The plotting result should appear as linear line such that the reaction rate can be calculated from the slope. The result should also be confirmed using the equation in Table 2.6.

$$-\frac{dC_{OLb}}{dt_{t=0}} = zaC^*_{O_3}\sqrt{k_2 C_{OLb0} D_{O_3}} = \frac{C_{O_3 i}RT}{H^{pc}} za\sqrt{k_2 C_{OL0} D_{O_3}} \tag{2-40}$$

Moreover, another possible method can be applied to avoid the effect of secondary reactions because the ozone concentration is removed from the equation. This method involves mixing between compound B and reference compound R with a known rate constant and stoichiometry ratio. The equation is shown below:

$$\ln\frac{C_{OLb}}{C_{OLb0}}=\frac{zk_2}{z_Rk_{2R}}\ln\frac{C_{Rb}}{C_{Rb0}} \tag{2-41}$$

By plotting $\ln\left(C_{OLb}/C_{OLb0}\right)$ against $\ln\left(C_{Rb}/C_{Rb0}\right)$, the plot leads to a straight line, and the reaction rate can be calculated from the slope of this line.

B. Very slow kinetic regime

The very slow kinetic regime can also be used to determine the reaction rate constant in a bubble column reactor by expression of the chemical disappearance rate of compound OL. Thus, the equation for this regime becomes:

$$-\frac{dC_{OLb}}{dt}=z\beta k_2C_{O_3}^{*}C_{OLb}=\frac{C_{O_3i}RT}{H^{pc}}z\beta k_2C_{OLb} \tag{2-42}$$

Integration of Equation 2-42 leads to

$$\ln\frac{C_{OLb}}{C_{OLb0}}=-z\beta k_2C_{O_3}^{*}t=\frac{C_{O_3i}RT}{H^{pc}}z\beta k_2t \tag{2-43}$$

A plot of $\ln\left(C_{OLb}/C_{OLb0}\right)$ against the reaction time becomes a straight line such that the slope is the product of the reaction rate constant, the stoichiometry ratio, liquid holdup, and ozone concentration. If the assumption of very slow kinetic regime is correct, the condition must be fulfilled by the equation in Table 2.6.

2.3 Bubble generation

Similar to both Section 2.1 and Section 2.2, this section provides useful information for bubble reactor design, i.e., the materials used for diffusers, effect for bubble formation, and the microbubble generation using a fluidic oscillator. Bubble characterisation is also provided to estimate the specific interfacial area. The details are described in the following sub-sections.

2.3.1 Factors that affect the bubble formation

Many parameters affect the bubble formation and bubble size, including fluid properties (liquid viscosity, surface tension, liquid density, and gas density), operating parameters (gas flow rate and flow/static condition of the liquid, temperature, and pressure), and orifice configurations (orifice submergence and orifice materials). All details are described in the following sub-sections

2.3.1.1 Effect of liquid properties

Viscosity of the liquid: Although the effect of liquid viscosity on bubble formation is not obvious, three contradictions can be given: 1) Bubble size increases with increasing liquid viscosity, 2) liquid viscosity has a slight effect on bubble size, and 3) no relationship exists between the two parameters (Gerlach *et al.* 2007, Ma *et al.* 2012).

Surface tension of the liquid: The surface tension force varies significantly with the gas flow rate through the nozzle, although it is small. Both the bubble size and the detachment time increase with increasing surface tension. However, for a small diameter nozzle, the effect of surface tension is negligible at high gas flow rates (Kulkarni and Joshi 2005, Gerlach *et al.* 2007, Ma *et al.* 2012).

Density of the liquid: High liquid density causes an increase in the buoyancy force. As a result of high buoyancy force, the bubble detaches earlier with small amount of gas in the bubble. The bubble size therefore decreases with increasing liquid density (Gerlach *et al.* 2007, Ma *et al.* 2012).

Density of the gas: High gas density via use of a higher molecular weight gas or operation at higher pressure results in a reduction of the buoyancy force. At low buoyancy force, the bubble requires a larger amount of gas before detachment. Thus, the bubble size increases with increasing gas density (Kulkarni and Joshi 2005).

2.3.1.2 Effect of operating conditions

Gas flow rate and liquid condition: Ma and co-workers (2012) reported that the average bubble size obviously increases with increasing orifice gas velocity. In contrast, the average bubble size gradually decreases with increasing liquid velocity under co-current conditions because the bubble detaches from the orifice more easily and rapidly, accounting for the reduction in both bubble size and bubble detachment time.

Pressure: The experimental result reported by Luo and co-workers (1998) shows that the increase of pressure does insignificantly change the bubble size although the gas momentum force increases dramatically. The reason for this observation is that the increase in the gas momentum force can be counterbalanced by the decrease in the buoyancy force and the increase of the Basset and liquid drag forces.

2.3.1.3 Effect of orifice configuration

Orifice submergence: There are three methods used to submerge an orifice, namely, top submergence, bottom submergence, and side submergence. The last two techniques are normally found in the chemical process industry. Kulkarni and Joshi stated in their review (2005) that the bubble size decreases exponentially with the increasing orifice submergence, but under a constant gas flow rate and constant pressure conditions, orifice submergence has an insignificant effect on the bubble size.

Orifice material: As discussed previously, the surface force acting on the bubble depends on the contact angle between the gas and liquid, which primarily depends on the wetting properties of the material of construction. Suitable materials based on the hydrophilic or hydrophobic nature of the liquid (wettability) and the polarity have been reviewed by Ponter and Surati (1997). The effect of wetting conditions on bubble formation was also studied under low gas flow rates by Gnyloskurenko and co-workers (2003), who found that the final bubble size that detached from the orifice increased dramatically as the wetting conditions worsened. Therefore, the orifice materials should be sufficiently wettable to obtain smaller bubbles.

Multi-orifice: The bubbles generated by multi-orifice systems are much more complex than those produced by a single submerged orifice. Therefore, instead of the bubble size, the bubble size distribution is used in the system design. However, the bubbles generated by a porous plate with notably fine holes ($20\ \mu m < d_h < 200\ \mu m$), for which the pressure drop across the plate is notably high, show the equality of bubble formation from all orifices that results in a highly narrow bubble size distribution over the porous plate region (Kulkarni and Joshi 2005). Moreover, the smallest bubbles can be formed using sieve plates with the largest spacing and a high viscosity liquid. Therefore, a large pitch space is required to suppress the coalescence effect in the sparger region. However, the arrangement of bubbles in the dispersion zone is not affected by pitch space.

2.3.2 Bubble rise velocity

In addition to bubble size, the rise velocity is an important control parameter that determines the gas-phase residence time. The rise velocity can generally be referred to as the terminal rise velocity in stagnant liquid and as the slip velocity in moving liquid. Several parameters can affect the rise of the bubbles in Newtonian liquids, including bubble characteristics (size and shape), properties of gas-liquid systems (density, viscosity, surface tension, and concentration of solute), liquid motion (direction), and operating conditions (temperature, pressure, and gravity) (Kulkarni and Joshi 2005).

2.3.2.1 Effect of size and shape

The shape of bubbles moving in Newtonian liquids can be identified generally as spherical, ellipsoidal, spherical/ellipsoidal cap, etc., as shown in Figure 2.9. The shape of bubbles primarily depends on the forces acting on the bubble, including surface tension force, viscous force, and buoyancy force. If the dominant forces change with the increase in bubble size, the bubble shape will transform from a spherical to ellipsoidal to spherical cap shape (Yang *et al.* 2007).

Three crucial dimensionless groups, i.e., the Reynolds number (Re), Bond number (Bo), and Morton number (Mo), are normally employed to characterise the bubble shapes and the rise behaviours, as defined in Eq. 2-44 through Eq. 2-46:

$$\mathrm{Re} = \frac{\rho_l u_b d_b}{\mu_l} \tag{2-44}$$

$$Bo = \frac{g \Delta\rho d_b^2}{\sigma} \tag{2-45}$$

$$Mo = \frac{g \Delta\rho \mu_l^4}{\sigma^3 \rho_l^2} \tag{2-46}$$

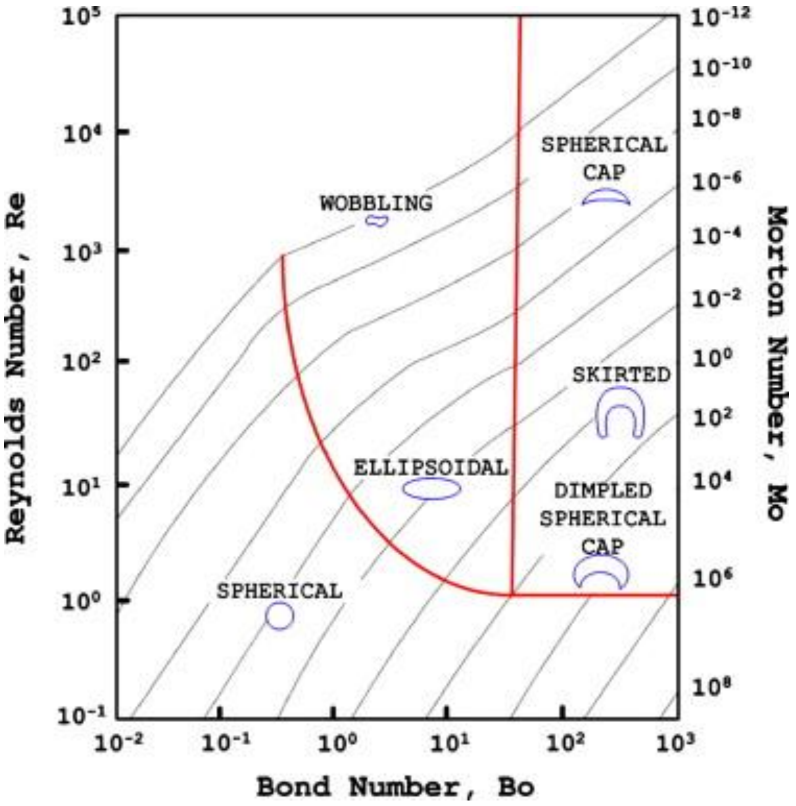

Figure 2.9 Shape regimes for bubbles and drops in unhindered gravitational motion through liquid (Clift *et al.* 1978)

In these expressions, μ_l is the fluid viscosity, and $\Delta\rho$ is the density difference between the liquid and gas phases. Viscous force and surface tension force are two dominating forces acting on the bubble, and its shape is in the spherical/nearly spherical regime. The bubble size in this regime is usually less than 1.3 mm in diameter, and the ratio of minor to major axis is less than 10% (Amaya-Bower and Lee 2011). Stoke's theory and Hadamard-Rybczynski theory were applied to describe the spherical bubble rise velocity at low Reynolds numbers (R_e <1), as described in Eq. 2-47 and Eq. 2-48, respectively (Parkinson *et al.* 2008). Although Stoke's theory presents the simplest equation, the correlation is indeed limited for a solid particle or a notably small-sized bubble in a contaminated liquid (immobile surfaces) for which the internal circulation is quite small. However, Clift (1978) and Sam and co-workers (1996) suggested that the surface of a bubble with a size below 300-400 μm is rigid even though it is formed in a clean liquid. Therefore, both theories can be used to describe the rise velocity of the microbubbles in this research, according to the experiment performed by Parkinson and his team. These researchers concluded that excellent agreement is observed with use of the H-R equation if air, nitrogen, and helium are applied in ultra-clean water. In contrast, the values calculated from Stoke's equation are slightly lower than those obtained from the experiments (Parkinson *et al.* 2008). The equation for the bubble rise velocity based on boundary layer theory was also obtained by Levich at higher Reynolds numbers (Levich 1962). The rise velocity of the bubble in this regime is proportional to the size of the bubble, as shown in Figure 2.10.

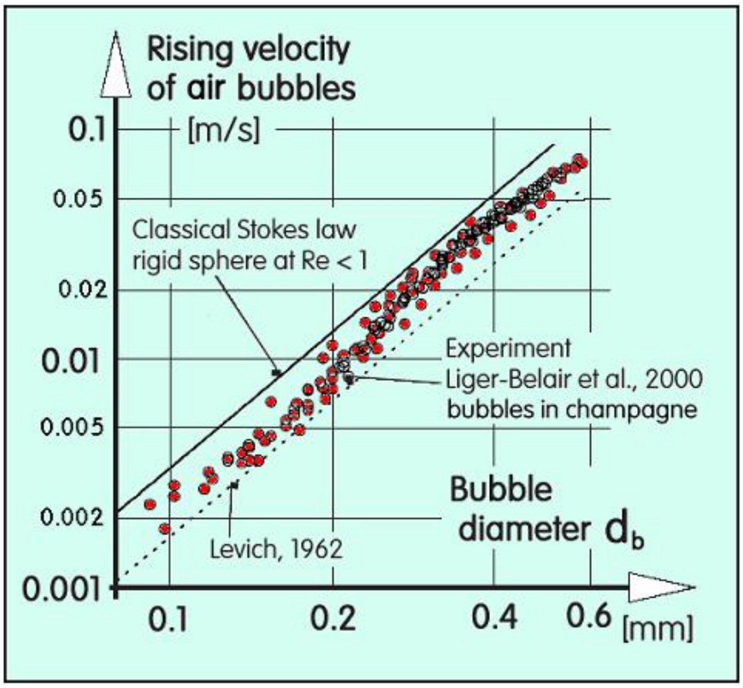

Figure 2.10 Rise velocity of bubbles as displayed theoretically (Levich) and experimentally (Zimmerman and Rees 2009)

$$U_{t(ST)} = \frac{2r_b^2 \Delta\rho g}{9\mu_l} \tag{2-47}$$

$$U_{t(H-R)} = \frac{2\Delta\rho g r_b^2}{3\mu_l} \frac{\mu_l + \mu_g}{2\mu_l + 3\mu_g} \tag{2-48}$$

where r_b is the radius of the bubble, and μ_g is the gas viscosity. If the internal viscosity of the fluid drop is low compared with the fluid viscosity ($\mu_g \langle\langle \mu_l$), Eq. 2-48 can be rearranged as shown in Eq. 2-49.

$$U_{t(H-R)} = \frac{\Delta\rho g r_b^2}{3\mu_l} = \frac{3}{2} U_{t(ST)} \tag{2-49}$$

The shape and the dynamics of motion of the bubbles in the ellipsoidal regime with a bubble size between 1.3 mm to 6.0 mm are primarily controlled by the surface tension force and buoyancy force. Their motion begins to oscillate when the bubbles lose their spherical shape. The range for the Bond number is from 0.25 to 40. Because of the slight effect on viscous resistance to internal circulation, the drag and bubble rise velocity are highly sensitive to contamination (Amaya-Bower and Lee 2011).

For large bubbles or in the spherical cap regime for which the bubble size is normally larger than 6.0 mm, the buoyancy force dominates, whereas the effects of surface tension, viscosity, and purity of the liquid on the bubbles are negligible. The Reynolds numbers and Bond numbers of this regime are greater than 1.2 and 40, respectively (Yang *et al.* 2007, Haapala *et al.* 2010, Amaya-Bower and Lee 2011).

2.3.2.2 Effect of purity of liquid

The rise velocity characteristics of a bubble are altered significantly depending on contamination, i.e., surfactants, electrolytes, and concentration of liquid used. The effect of surfactants on the rise velocity is similar to that of an electrolyte solution. In the case of Newtonian liquids, the bubble surface is dragged backward together with the liquid if the solution contains a surfactant, resulting in an increase in drag and a decrease in the mobility of the gas-liquid interface. The rise velocity of the bubble in a contaminated liquid is therefore less than that of the bubble in a clean liquid at the same bubble size (Kulkarni and Joshi 2005).

2.3.2.3 Effect of liquid viscosity

Kulkarni and Joshi (2005) stated that the viscosity of the liquid influences both the rise velocity and the bubble size and also reported that the rise velocity decreases with increasing liquid viscosity.

2.3.2.4 Effect of liquid temperature

In an ideal gas at constant pressure, the volume of gas increases with increasing temperature. The size of the bubble is therefore increased after heat transfer across the interface from the heated liquid. The density difference between the bubble and liquid phase also decreases, resulting in a reduction of the rise velocity of the bubble. Leifer and co-worker (2000) investigated the effect of the rise velocity of the bubble (0.1 mm to 3.5 mm in size) at various temperatures (0°C to 40°C) and found that for bubble sizes less than 0.3 mm, the rise velocity increases with increased temperature. In the case of the bubble sizes between 0.3 mm to 0.67 mm, the rise velocity also increases with the temperature. Nevertheless, at temperatures above 25°C, the rise velocity decreases with increased temperature. For larger bubbles, the rise velocity is inversely proportional to the processing temperature, as shown in Figure 2.11.

2.3.2.5 Effect of external pressure

The reactors used in industry are normally operated at high pressure, unlike those used at an ambient pressure in a laboratory. Luo and co-workers (1997) performed experiments at high pressures and concluded that the rise velocity of the bubble decreases with increasing external pressure because the bubble size at high pressure is smaller than that at low pressure.

2.3.2.6 Effect of the wall

According to Krishna and co-workers (1999), the wall has slight effect on the bubble motion. This observation is in good agreement with the work published by Clift and co-workers (1978), which stated that the wall has minor effect on the deformation of the bubbles at the diameter ratio (λ) less than 0.6; $\lambda = d_b / D_C$.

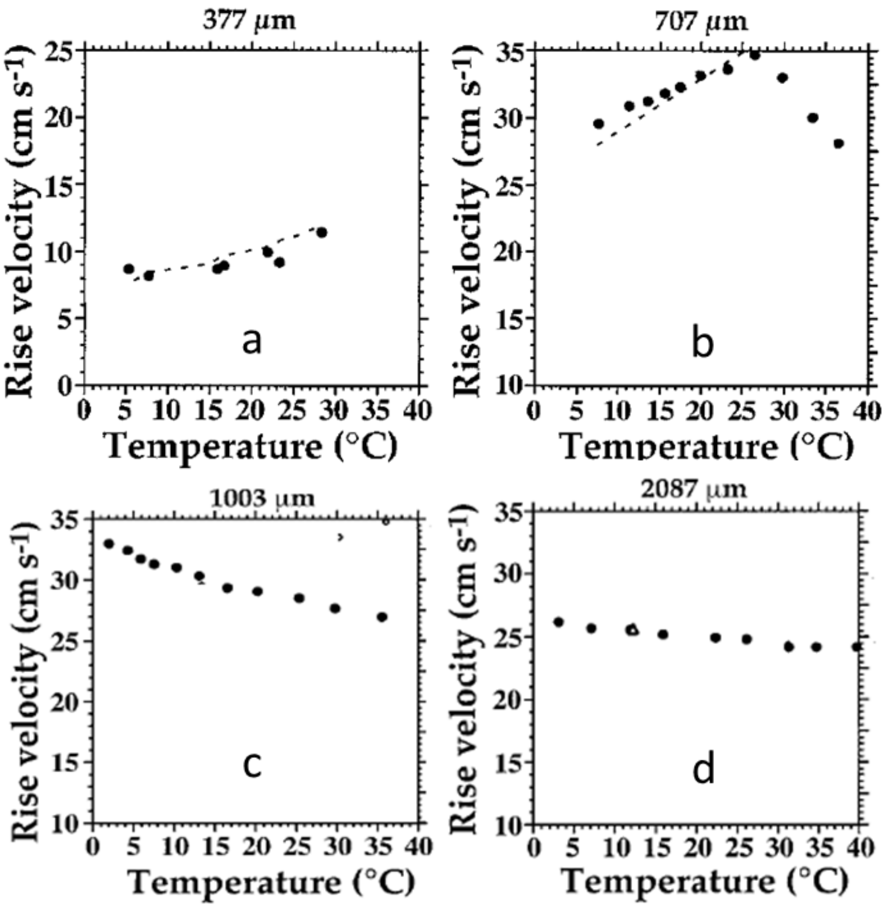

Figure 2.11 Observed velocity as a function of temperature; (a) 377 μm, (b) 707 μm, (c) 1003 μm, and (d) 2087 μm (Leifer *et al.* 2000).

2.3.3 Bubble column reactors

Bubble columns are widely used as multiphase reactors in a wide range of chemical, petrochemical, pharmaceutical, and environmental applications due to their various advantages. For example, their heat and mass transfers are excellent, and their maintenance and operating costs are low because of the simple structure of the reactors (Kantarci *et al.* 2005). This section presents the design and scale-up, fluid dynamics and regime, gas holdup, mass transfer coefficient, and heat transfer coefficient of the bubble reactors.

2.3.3.1 Design and scale-up

The assembly of bubble columns is quite simple, but an understanding of multiphase fluid dynamics and their influence on successful design and scale-up are required. Normally, the ratio of length to diameter of a bubble column operated in an industrial sector is at least 5, but this value varies between 2 and 5 for biochemical applications (Degaleesan *et al.*

2001, Kantarci *et al.* 2005). However, three main phenomena that engineers should understand before design and scale-up of bubble column reactors are the heat and mass transfer characteristics, mixing characteristics, and chemical kinetics of the reacting system. To understand these phenomena, the specific interfacial area, Sauter mean bubble diameter, overall heat transfer coefficient, mass transfer coefficient for all species, gas holdup, and physicochemical properties of the liquid medium must be measured before design and scale-up of bubble column reactors. Therefore, specialised measuring devices are necessary in experimental studies.

2.3.3.2 Fluid dynamics and regime analysis

The three flow regimes observed in the bubble columns, i.e., the homogenous regime (bubbly flow), heterogeneous regime (churn-turbulent), and slug flow regime, are found to be dependent on the superficial gas velocity, as shown in Figure 2.12 (Hyndman *et al.* 1997). Kantarci and co-workers (2005) reported that the slug flow regime can be observed only in a small-diameter (up to 15 cm at a high gas flow rate) laboratory column and also reported that the churn-turbulent regime consists of a mixture of small bubbles and larger bubbles with ranges from a few millimetres to a few centimetres. The superficial gas velocity of this regime is greater than 5 cm/s and is usually observed in industries that use large-diameter columns. It should be noted that the gas-liquid mass transfer coefficient of the churn-turbulent regime is lower than that of the bubbly flow regime. For the bubbly flow regime, the superficial gas velocity is less than 5 cm/s, resulting in the formation of small bubble size and rise velocity. A uniform bubble distribution is observed in this regime over the entire cross-sectional area of the column. Moreover, the gas holdup of the bubbly flow regime proportionally increases with the superficial gas velocity.

2.3.3.3 Gas holdup

The transport phenomena in the bubble column can be characterised by the gas holdup, which is a dimensionless parameter used for bubble column design and is defined as the volume fraction of the gas phase occupied by the gas bubbles. Kantarci and co-workers (2005) stated that the gas holdup decreases with increased liquid viscosity but increases with the superficial gas velocity and the operating pressure. Gas holdup also increases with addition of a surface-active reagent to the liquid phase. However, the column size has no effect on the gas holdup if the column diameter is larger than 10-15 cm and the height is over 1-3 m.

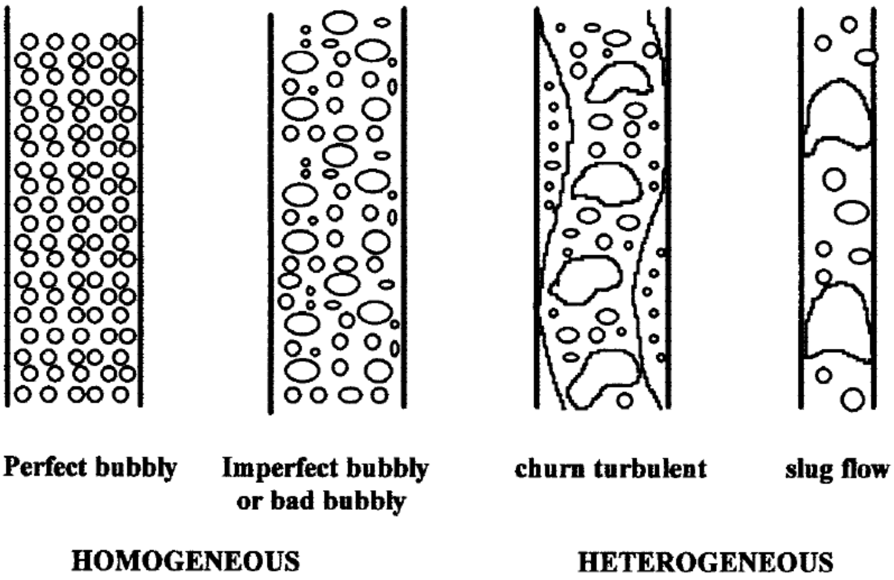

Figure 2.12 Flow regimes in the bubble columns (Bouaifi *et al.* 2001)

2.3.3.4 Mass transfer coefficient

Mass transfer in a bubble column is the crucial phenomenon for chemical reactions, and thus, prior to design and scale-up of bubble columns, it is necessary to estimate the mass transfer coefficient. If it is assumed that the mass transfer coefficient of the gas-side is negligible, the overall mass transfer coefficient in the bubble column is only governed by the liquid-side. The specific interfacial area is also the key parameter used to determine the overall mass transfer rate. Because the shapes of the microbubbles are spherical, the specific interfacial area (a) can be written as a function of the gas holdup (ε_G) and the sauter mean bubble diameter (d_{32}), as shown in Eq. 2-50.

$$a = \frac{6\varepsilon_G}{d_{32}} \tag{2-50}$$

Kantarci and co-workers (2005) reported that the volumetric mass transfer $k_l a$ increases with increasing gas velocity, gas density, and pressure and decreases with increasing liquid viscosity as a result of larger bubble formation. These researchers also reported that the $k_l a$ value increases if a surfactant is present because of small bubble formation. It should be noted that for effective mass transfer in the bubble column, the formation of large bubbles should be avoided.

2.3.3.5 Heat transfer

In addition to mass transfer, heat transfer is a crucial parameter in many industrial productions because chemical reactions usually take place via heat supply or heat removal operations. The bubble column has a heat transfer rate that is higher than that of a single phase reactor by a factor of approximately 100, as reviewed by Kantarci and co-workers (2005), who also reported that the heat transfer coefficient increases with increasing superficial gas velocity and temperature as a result of reduction in liquid viscosity and decreases with increasing liquid viscosity. In addition, the heat transfer coefficient in the distributor region is less than that in the bulk region. The heat transfer coefficient in the centre of the column is higher than that at the wall region because of large bubbles formed at the centre.

2.3.4 Microbubbles generated by fluidic oscillation

Microbubbles (diameter of 1-999 µm) are used for several industrial applications because their surface to volume ratios are higher than that of fine bubbles (diameter of 1-2 mm), and thus, microbubbles can increase the mass transfer rate and mixing efficiencies. Generally, microbubbles can be produced using three techniques. The first technique uses compression to dissolve air into the liquid phase. The second technique uses power ultrasound to induce cavitation. The third technique is referred to low-power microbubble generation by using the fluidic oscillator (Zimmerman *et al.* 2008). The first two methods of microbubble generation are usually associated with high power densities and power consumption by either the compression or ultrasonic treatment. Therefore, the fluidic oscillation technique is the suitable technique for use in generation of microbubbles because of low power consumption. In addition, the fluidic oscillator structure is simple resulting in lower maintenance costs (Zimmerman *et al.* 2008, Zimmerman *et al.* 2009, Zimmerman and Rees 2009, Zimmerman *et al.* 2011a, Zimmerman *et al.* 2011b).

2.3.4.1 Fluidic oscillation

A fluidic oscillator is an important device in the airlift loop bioreactor pioneered by Zimmerman and co-workers (2009). When the fluidic oscillator is connected with a steady air supply at sufficient frequency, it can generate uniform microbubbles that have the same size as the pore. The fluidic oscillator offers many advantages, such as no moving parts, no need for electricity, good reliability and robustness, and low cost (Zimmerman *et al.* 2011b). The ability of the fluidic oscillator to divert the jet passing through the supply nozzle is controlled by terminals X_1 and X_2, as displayed in Figure 2.13. It is interesting to note that the frequency of the oscillation can be changed by adjusting the length of the feedback loop and the supply flow rate. The geometry and photographs of this device are illustrated in Figure 2.14 (Tesar *et al.* 2006, Zimmerman *et al.* 2009).

In addition to the length of the feedback loop and the supply flow rate that controls the size of the bubbles, the surface wetting properties of the diffuser have an effect on the size of the bubbles, as discussed earlier. If the pore’s surface is hydrophilic, it will develop a thin water film between the bubble and the pore material. The bullet shape of the bubbles is observed at the pores because the hydrophobic gas cannot stick on the pore’s surface as a result of the water film. Moreover, nanobubbles will be formed if the flow rate of air is as small as possible and the frequency is as large as possible (Zimmerman *et al.*, 2008).

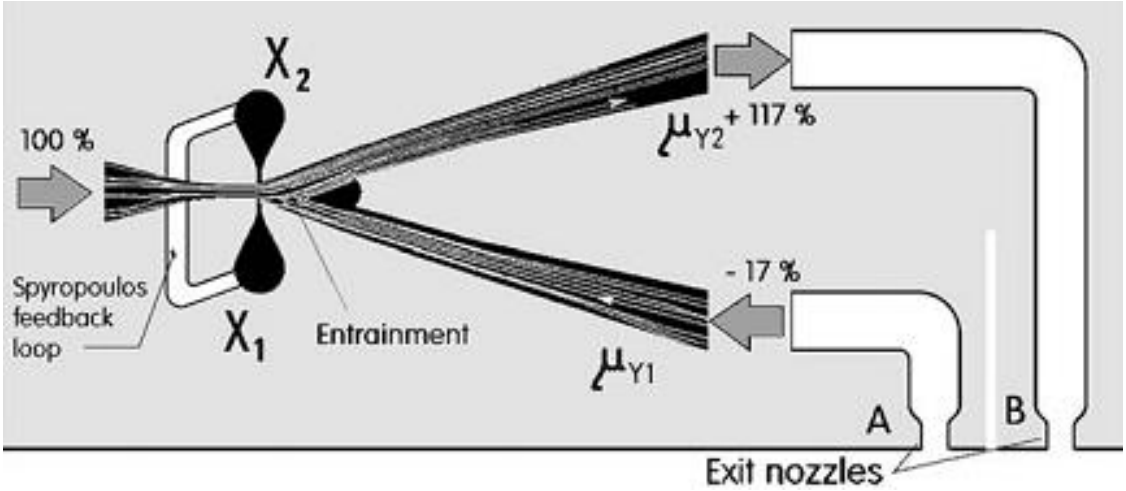

Figure 2.13 Jet of fluidic amplifier (Zimmerman *et al.*, 2008)

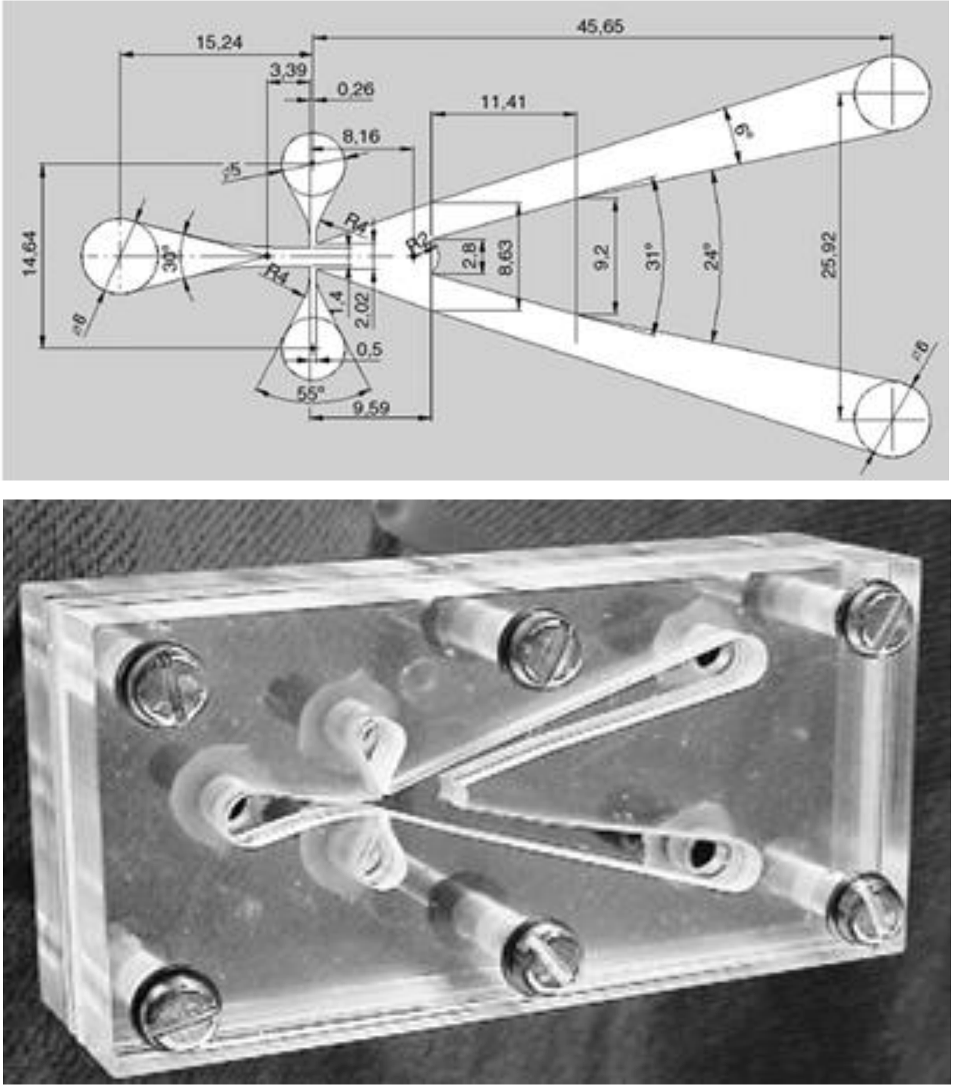

Figure 2.14 Geometry of the fluidic amplifier (Top) and the assembled fluidic amplifier (Bottom) (Zimmerman *et al*., 2008)

2.3.4.2 Benefits of microbubbles

The use of microbubbles in gas-liquid phase applications offers many advantages. The major benefit is a surface area to volume ratio (S_b/V) that is larger than that of large bubbles. The surface-area-to-volume ratio also increases with decreasing bubble radius, as shown in Eq. 2-51.

$$\frac{S_b}{V} = \frac{4\pi r_b^2}{(4/3)\pi r_b^3} = \frac{3}{r_b} \tag{2-51}$$

For example, if one litre of air is generated to form 100 μm microbubbles, this system will have 10 m^2 of interfacial area. Therefore, mass flux can increase with increasing interfacial area (reducing bubble size), as described in Eq. 2-52, and the transfer benefit of microbubbles is shown in Figure 2.15 (Zimmerman *et al.* 2009).

$$J = k_L S(c_g - c_l) \qquad (2\text{-}52)$$

In this expression, J is mass flux (mol/s), k_L is the mass transfer coefficient (m/s), c_g and c_l are the molar concentrations of the gas and liquid phases, respectively, and S is the interfacial area (m^2).

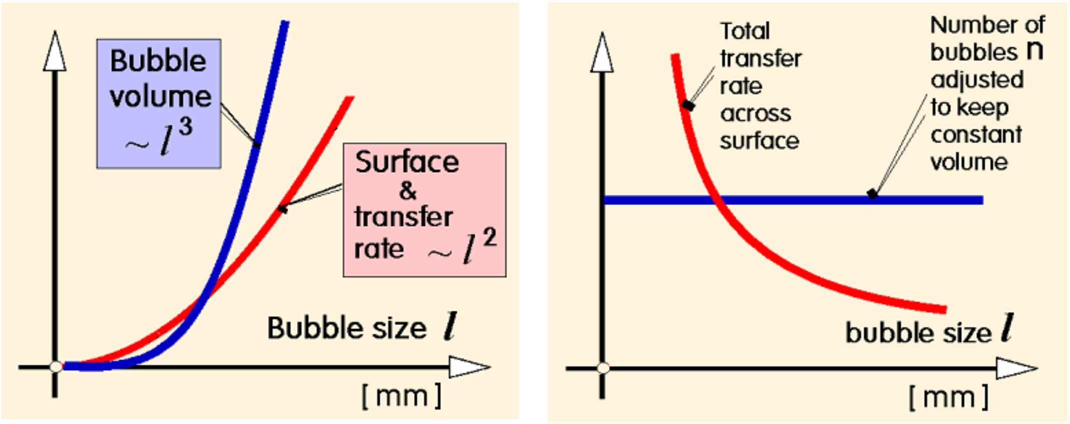

a

b

Figure 2.15 Transfer benefit of microbubbles; (a) The surface area & transfer rate scale (b) Total transfer rate across surface

In addition to a higher surface-area-to-volume ratio, the residence time of microbubbles is longer than that of large bubbles, which means that microbubbles have sufficient time to react with the liquid surrounding them, although their transfer momentum is lower. The residence time of microbubbles in a viscous liquid can be described by Eq. 2-48 (classical Stokes law), and the rise velocity of bubbles is illustrated in Figure 2.10.

2.3.5 Bubble characterisation

In addition to the bubble rise velocity, other crucial parameters that must be measured in the bubble column are the bubble size and void fraction. These parameters are subsequently used to determine the bubble size distribution and the specific interfacial area. To date, two main techniques have been used to obtain these parameters, namely, optical and acoustical techniques. The accuracy of bubble size characterisation using an optical technique depends on the quality of the optical device, e.g., light medium clarity, transparent walls, and software used for bubble analysis, which might affect the accuracy of prediction of bubble diameters. This technique is also time consuming (Hanotu *et al.* 2012). Thus, the techniques used for setting up the camera and the light source are highly important to obtaining the best clear figure.

Bubble size distribution is one of the most basic characteristics of bubble column reactors because the bubbles generated from a diffuser have a variety of sizes in reality. It is therefore important to understand the entire range of bubble sizes in bubble columns, which is often described statistically as the bubble size distribution. The number of measured bubbles from the figure should be greater than 500 for reliable results (Garcia-Salas *et al.* 2008). To describe the variable distribution, two models are normally employed, i.e., the Gaussian or normal distribution and the log-normal distribution. The normal distribution, which is a bell-shaped and symmetrical curve, is often assumed to describe random variation using the two values of arithmetic mean $\bar{x}$ and standard deviation *s*. The log-normal distribution is usually characterised in terms of log-transformed variables that are symmetrical against the log scale. This distribution is particularly useful if the mean values are low, the variances are large, and the values are positive. In other words, the log-normal distribution corresponds to a left-skewed distribution. Therefore, for bubble size distributions in bubble columns connected with a fluidic oscillator, which are normally believed to be skewed (Hanotu *et al.* 2012), the log-normal distribution is the appropriate model used to describe this characteristic. The probability density function can be expressed using Eq. 2-53 (Akita and Yoshida 1974, Limpert *et al.* 2001).

$$f(x) = \frac{1}{\sigma \cdot x\sqrt{2\pi}} \exp\left(\frac{-(\ln x - m)^2}{2\sigma^2} \right), \qquad x > 0 \tag{2-53}$$

In this expression, $f(x)$ is the probability density function, x is the geometric mean of the each size range ($\sqrt{upper \times lower}$), m is the natural logarithm of the geometric mean bubble size, and σ is the standard deviation. Both m and σ, which are functions of the

nth moment of distribution (μ_n'), are defined by Eq. 2-54 and Eq. 2-55, respectively. The value of μ_n' is also defined by Eq. 2-56.

$$\sigma = \sqrt{\frac{2}{3}\ln \mu_3' - \ln \mu_2'} \tag{2-54}$$

$$m = \frac{3}{2}\ln \mu_2' - \frac{2}{3}\ln \mu_3' \tag{2-55}$$

$$\mu_n' = \int_0^\infty x^n f(x)\,dx = \int_0^1 x^n \, dF \tag{2-56}$$

In addition, F is the distribution function defined by Eq.2-57.

$$F(x) = \int_0^x f(x)\,dx \tag{2-57}$$

As discussed, the specific interfacial area is a highly important parameter in this thesis and is one of several parameters used for estimation of reaction rate constants in the bubble column. The specific interfacial area (a) related to the gas holdup (ε_G) and the volume-surface mean bubble diameter (d_{vs}) is defined by Eq. 2-58.

$$a = \frac{6\varepsilon_G}{d_{vs}} \tag{2-58}$$

The gas holdup and the volume-surface mean bubble diameter are determined by Eq. 2-59 and Eq. 2-60, respectively.

$$d_{vs} = \frac{\mu_3'}{\mu_2'} \tag{2-59}$$

$$\varepsilon_G = \frac{\pi}{6} N \int_0^\infty x^3 f(x)\,dx \tag{2-60}$$

In this expression, N is the number of bubbles per unit aerated liquid volume. From Eq. 2-56 through Eq. 2-60, we obtain:

$$a = \pi \cdot N\int_{0}^{\infty} x^2 f(x)\,dx = \pi \cdot N\int_{0}^{1} x^2 dF \tag{2-61}$$

It is interesting that the volume-surface mean bubble diameter is equal to the Sauter mean diameter (d_{32}), which widely considered as the mean bubble size as represented in Eq. 2-62. The specific interfacial area is possibly calculated by Eq. 2-63.

$$d_{32}(i) = \frac{\sum_{j=1}^{N} n(d_j)d_j^3}{\sum_{j=1}^{N} n(d_j)d_j^2} \tag{2-62}$$

$$a = \sum_{i=1}^{N} a(i) = \sum_{i=1}^{N} \frac{6\varepsilon_G}{d_{32}} \tag{2-63}$$

2.4 Summary

In Section 2.1, a wide range of useful information gained from the previous studies is presented and applied in this work for experimental design. For example, ozonolysis of OL under higher surface area conditions results in a higher production rate, and thus ozone microbubbles are the correct option for this research. The reduction of OL and the product formation during ozonolysis are functions of both reaction time and temperature, and consequently, these experiments must be studied at various reaction times and temperatures to find the kinetic parameters. The decrease of OL concentration is also a function of ozone concentration, and therefore, various ozone concentrations must be studied to find an optimum ozone concentration and to confirm the assumption of the kinetic regime. Protic solvents are added into the reaction system to increase the productivity, and the optimum percentage of the best protic solvent is determined. Moreover, a condenser is installed to condense all volatile products and reactants.

In Section 2.2, dry air is used as a reactant for ozone production and is generated via non-equilibrium plasma. All equipment in contact with ozone is constructed from corrosion-resistant materials. For example, the reactor is made of glass and stainless steel, and PTFE is used for all tubing and valves. The inlet ozone concentration is measured using the KI method. Ozone decomposition due the effect of pH is negligible due to the low pH of OL, and the thermal decomposition of ozone is discussed in Chapter 4. Based on previous studies, the fast pseudo-first-order kinetic regime is selected to estimate the reaction rate constant. The experiments are performed at different temperatures to determine the pre-exponential factor and the activation energy. The experiments are also conducted at different inlet ozone concentrations to confirm the kinetic regime. Moreover, the Henry's Law constant and the diffusion coefficient must be estimated before determining the reaction rate constant. These details are discussed in Chapter 4.

Section 2.3 describes the parameters that influence the formation and the rise velocity of the bubbles, i.e., the gas and liquid properties, the operating conditions, and the characteristics of the diffuser. Smaller bubbles are formed under lower fluid viscosity, and their rise velocity is lower than that of the larger bubbles. The diffuser should display wettability to achieve formation of smaller bubbles. A fluidic oscillator is used for microbubble generation. An optical technique and Image J software are used for bubble characterisation to determine the bubble size distribution and the specific interfacial area.

CHAPTER 3

EXPERIMENTAL DESIGN

This chapter primarily focuses on the experimental designs produced using Aspen Plus, COMSOL Multiphysics, and COMSOL Reaction Engineering Lab. Section 3.1 describes the process simulation with Aspen Plus used to model all possible reactions summarised from previous research to determine the possible products and to observe the effect of heat of reaction for the purpose of designing a cooling/heating system. Section 3.2 discusses the condenser design via Aspen Plus intended to condense all volatile products and reactants. In Section 3.3, Aspen Plus is also used to find suitable protic solvents in terms of mixing characteristics for increased productivity. Section 3.4 covers determination of the minimum fluid level in the bubble column reactor using both Aspen Plus and COMSOL Multiphysics. Section 3.5 details the reactor design in COMSOL Multiphysics used to observe the transport phenomena and to find the appropriate location of the thermometer and sampling tube. Section 3.6 provides a summary.

3.1 Process simulation using Aspen Plus

In the experimental design, all possible reaction mechanisms summarised in Figure 2.2A and Figure 2.2B must be investigated because these reaction mechanisms were only predicted by previous researchers without a complete understanding of the reaction mechanisms and the thermodynamic properties. This necessary information is further used to design the reactor, separation system, and piping system. In this section, Aspen Plus is used to estimate the standard free energy of formation of all possible products and reactants to identify which reactions are spontaneous based on the standard free energy theory. Aspen Plus is also used to estimate the enthalpy of formation of all substances, and these parameters are used to determine the enthalpy of reactions. This information is further used to classify types of chemical reactions as endothermic or exothermic reactions. The estimated values of enthalpy of reaction are used to design the heating system in the case of an endothermic reaction or the cooling system in the case of an exothermic reaction. The temperature at equilibrium is also evaluated for the purpose of finding an appropriate range for the reaction temperatures. Moreover, Aspen Plus is used to model the process of OL ozonolysis to determine the production rate of all products at different reaction temperatures and to estimate the amount of heat generated/consumed during the reaction.

In the first section, Aspen Plus was applied to determine the enthalpy of formation (ΔH_f^o) and the standard free energy of formation (ΔG_f^o) of both the vapour and liquid phases of all possible products, as shown in Figure 2.2A and Figure 2.2A. The molecular structures and the chemical formulas of the substances, which are not found in the simulation database, must be drawn and input to the User Defined Component mode prior to estimation. After estimating ΔH_f^o and ΔG_f^o, the enthalpy of reaction (ΔH_{rxn}^o) and the standard free energy (ΔG_{rxn}^o) of all reactions were calculated using Eq. 3-1 and Eq. 3-2, respectively. The entropy change (ΔS^o) was also calculated using Eq. 3-3.

$$\Delta H_{rxn}^o = \sum n\Delta H_f^o(\text{products}) - \sum m\Delta H_f^o(\text{reactants}) \tag{3-1}$$

$$\Delta G_{rxn}^o = \sum n\Delta G_f^o(\text{products}) - \sum m\Delta G_f^o(\text{reactants}) \tag{3-2}$$

$$\Delta G = \Delta H - T\Delta S \tag{3-3}$$

For ΔH_{rxn}^o, the reaction is endothermic when its value is positive; in contrast, the reaction is exothermic if its value is negative. The value of ΔG_{rxn}^o can be used to conclude whether a reaction is spontaneous or non-spontaneous under standard conditions: The reaction is spontaneous in the forward direction if its value is negative, the reaction is nonspontaneous in the forward direction if its value is positive, and the reaction is at equilibrium if ΔG_{rxn}^o is zero. Moreover, ΔH and ΔS can be used to predict whether a given reaction will spontaneously occur at constant temperature and pressure. If both ΔH and -TΔS are negative, ΔG will always be negative, and the process will be spontaneous at all temperatures. Similarly, if both ΔH and -TΔS are positive, ΔG will always be positive and the process will be nonspontaneous at all temperatures, but the reverse reaction will be spontaneous at all temperatures. When both ΔH and ΔS are negative, resulting in a positive sign for -TΔS, ΔG will be negative at low temperatures, whereas ΔG will be positive at high temperatures. Similarly, if both ΔH and ΔS are positive, resulting in a negative sign of -TΔS, ΔG will be negative at high temperature, whereas ΔG will be positive at low temperature (Smith *et al.* 2005, Brown 2006).

Normally, ΔH and ΔS vary slightly with temperature and thus can be assumed as constants for determination of the temperature at equilibrium (ΔG=0) using Eq. 3-3. Note that the sign of ΔG can be used to indicate which reactions are spontaneous, nonspontaneous or at equilibrium, but it cannot be used to predict the reaction rate (Brown 2006).

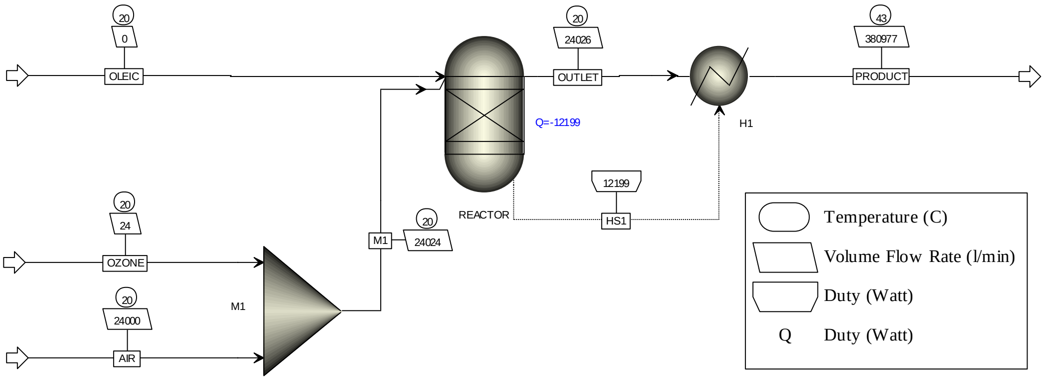

Figure 3.1 Process simulation of ozonolysis of OL

In addition to ΔH_f^o and ΔG_f^o, Aspen Plus was employed in the second section to model the process of OL ozonolysis and find the percentage of the products and the outlet temperature of the PRODUCT stream. The property method employed in this simulation is WILSON. As displayed in Figure 3.1, the OLEIC stream (which is pure OL at a molar flow rate of 1 mol/min, 20°C, and atmospheric pressure) was fed to the reactor (R1) to react with ozone in an M1 stream. The M1 stream is the combination of an OZONE stream with a molar flow rate of 1 mol/min with an AIR stream at 20°C and atmospheric pressure. The composition of ozone in the M1 stream after mixing with air was set to 1500 ppm according to the maximum rate of ozone generation used in the laboratory. All reactions summarised in Figure 2.2A and Figure 2.2B were also added into R1. The temperatures of the reactor were set at 20°C, 40°C, and 60°C and atmospheric pressure. The HS1 stream, which is the heat stream, and form R1 were connected to a heater (H1) to determine the outlet temperature of the PRODUCT stream.

Results and discussions of the process simulation

The estimated values of ΔH_f^o and ΔG_f^o of both the gas phase and liquid phase at standard conditions of all products and reactants are illustrated in Table 3.1. The enthalpy of reaction, standard free energy, entropy, and equilibrium temperature (ΔG=0) of all reactions calculated using Eq. 3-1, Eq. 3-2, and Eq. 3-3 are also displayed in Table 3.2. The results show that the spontaneous reactions at standard conditions are reactions No. 1, 2, 3, 4, 5, 6, 10, 11, 33 and 35 because the standard free energies of these reactions are negative. The enthalpy of reaction is also negative. In addition, the reactions are nonspontaneous in the forward direction. Therefore, the possible reactions of ozonolysis of OL are exothermic. The possible products formed after the ozonolysis based on free energy theory are PO, NN, CI1, OA, CI2, AA, OcA, CO_2, NA, 10-OxA, and 9-OxA.

Moreover, by considering the enthalpy of reaction and the entropy in Table 3.3, the results show that the ΔH and -TΔS of reactions No. 1, 2, and 3 are negative, and therefore, these reactions will be spontaneous at all temperatures. This observation means that PO, NN, CI1, OA and CI2 can be formed at all temperatures, whereas the ΔH and -TΔS of reactions No. 7, 20, 21, 22, 23, 24, 25, 26 and 34 are positive, and thus, these reactions will be nonspontaneous at all temperatures. The ΔH and ΔS of reactions No. 4, 5, 6, 8, 9, 10, 11 27, 28 29, 32, 33, and 35 are negative, resulting in the forward direction at low temperatures, whereas the ΔH and ΔS of reactions No. 12, 13, 14, 15, 16, 17, 18, 19, 30, and 31 are positive, resulting in the forward direction at high temperatures.

The equilibrium temperatures of reactions No. 4, 5, 6, 10, and 11, with ΔG values that are negative at the standard conditions, are 434.5 K, 462.0 K, 504.0 K, 306.3 K, and 306.3 K, respectively, which means that all products from these reactions, including AA, NA, OcA, CO_2, NN, 9-OxA, and 10-OxA, will be formed at temperatures less than 504.0 K. Moreover, the equilibrium temperatures of both reactions No. 8 and 9 (positive sign of ΔG at 298.15 K) are 284.7 K, which means that the products of these reactions, i.e., OA, 9-OxA, and 10-OxA, will be formed at temperatures less than 284.7 K. However, the undesired products (AAHPs) gained from reactions No. 12 to No. 19 might be formed at high temperatures. Therefore, ozonolysis of OL should be run at low temperatures to avoid the formation of undesired products and to increase the formation of valuable products.

Table 3.1 Heat of formation and standard free energy of formation at 25°C, 1 atm

No.	**Name**	**Formula**	**MW**	ΔH_f^o (kJ/mol)×10^2 (gas)	ΔH_f^o (kJ/mol)×10^2 (liquid)	ΔG_f^o (kJ/mol)×10^2 (gas)	ΔG_f^o (kJ/mol)×10^2 (liquid)
1	Oleic acid	$C_{18}H_{34}O_2$	282.47	-7.10	-8.21	-2.28	-2.79
2	Primary ozonide	$C_{18}H_{34}O_5$	330.46	-8.91	-9.57	-4.73	-5.37
3	9-Oxononanoic acid	$C_9H_{16}O_3$	172.22	-6.56	-7.23	-4.19	-4.55
4	Azelaic acid	$C_9H_{16}O_4$	188.22	-9.27	-10.41	-6.57	-7.12
5	Octanoic acid	$C_8H_{16}O_2$	144.21	-5.56	-6.35	-3.25	-3.54
6	1-nonanal	$C_9H_{18}O$	142.24	-3.11	-3.68	-0.76	-0.95
7	Nonanoic acid	$C_9H_{18}O_2$	158.24	-5.77	-6.62	-3.17	-3.50
8	Cyclic acyloxy hydroperoxide	$C_9H_{16}O_4$	188.22	-6.24	-6.96	-5.27	-5.64
9	Stabilized Criegee intermediate1	$C_9H_{16}O_4$	188.22	-9.17	-9.80	-5.95	-6.61
10	Stabilized Criegee intermediate2	$C_9H_{18}O_2$	158.24	-5.67	-6.31	-2.51	-2.91
11	10-Oxooctodecanoic acid	$C_{18}H_{34}O_3$	298.47	-8.68	-9.32	-3.72	-4.31
12	9-Oxooctodecanoic acid	$C_{18}H_{34}O_3$	298.47	-8.68	-9.32	-3.72	-4.31
13	α-acyloxyalkyl hydroperoxide1OL	$C_{27}H_{50}O_6$	470.69	-12.67	-13.56	-6.42	-7.07
14	α-acyloxyalkyl hydroperoxide2OL	$C_{27}H_{52}O_4$	440.71	-9.17	-9.92	-2.98	-3.56
15	α-acyloxyalkyl hydroperoxide1OA	$C_{18}H_{32}O_7$	360.45	-12.80	-13.49	-8.97	-9.78
16	α-acyloxyalkyl hydroperoxide2OA	$C_{18}H_{34}O_5$	330.46	-9.29	-9.92	-5.53	-6.17
17	α-acyloxyalkyl hydroperoxide1NA	$C_{18}H_{34}O_6$	346.46	-11.98	-12.65	-7.98	-8.72
18	α-acyloxyalkyl hydroperoxide2NA	$C_{18}H_{36}O_4$	316.48	-8.48	-9.10	-4.54	-5.08
19	α-acyloxyalkyl hydroperoxide1AA	$C_{18}H_{32}O_8$	376.45	-15.48	-16.26	-11.42	-12.32
20	α-acyloxyalkyl hydroperoxide2AA	$C_{18}H_{34}O_6$	346.46	-11.98	-12.65	-7.98	-8.72

No.	**Name**	**Formula**	**MW**	ΔH_f^o (kJ/mol)×10^2 (gas)	ΔH_f^o (kJ/mol)×10^2 (liquid)	ΔG_f^o (kJ/mol)×10^2 (gas)	ΔG_f^o (kJ/mol)×10^2 (liquid)
21	Secondary ozonides1	$C_{18}H_{36}O_3$	300.48	-6.35	-6.98	-1.29	-1.72
22	Secondary ozonides2	$C_{18}H_{34}O_5$	330.46	-9.85	-10.50	-4.73	-5.37
23	Secondary ozonides3	$C_{18}H_{32}O_7$	360.45	-13.34	-14.02	-8.17	-9.02
24	Diperoxide1	$C_{18}H_{32}O_8$	376.45	-12.75	-13.44	-9.15	-10.05
25	Diperoxide2	$C_{18}H_{36}O_4$	316.48	-5.75	-6.40	-2.27	-2.74
26	Diperoxide3	$C_{18}H_{34}O_6$	346.46	-9.25	-9.91	-5.71	-6.40
27	Hydroperoxide1	$C_9H_{18}O_5$	206.24	-8.45	-9.07	-7.00	-7.71
28	Hydroperoxide2	$C_9H_{20}O_3$	176.26	-4.96	-5.59	-3.56	-3.99
29	Oxygen	O_2	31.9	0	-0.76	0	0.13
30	Ozone	O_3	47.99	1.43	1.36	1.63	1.73
31	Water	H_2O	18.02	-2.42	-2.87	-2.29	-2.37
32	Hydrogen peroxide	H_2O_2	34.01	-1.36	-1.88	-1.05	-1.20
33	Carbon dioxide	CO_2	44.01	-3.94	-4.01	-3.94	-3.85
* All parameters are estimated using Aspen Plus.							

Table 3.2 Enthalpy of reaction and standard free energy of OL ozonolysis at 25^{o}C and 1 atm.

No.	Reactions	ΔH_{rxn}^{o} (kJ/mol) $\times 10^2$	ΔS^{o} (J/mol·K) $\times 10^2$	ΔG_{rxn}^{o} (kJ/mol) $\times 10^2$	**Temp. (K) at which** $\Delta G = 0$	References
	Primary ozonolysis					
1	$OL + O_3 \rightarrow PO$	-2.79	4.78	-4.21	-	[1, 2, 3, 5, 6, 7, 9]
2	$PO \rightarrow NN + CI1$	-1.30	1.30	-1.69	-	[1, 2, 3, 5, 6, 7, 9]
3	$PO \rightarrow OA + CI2$	-1.27	1.06	-1.61	-	[1, 2, 3, 5, 6, 7, 9]
	Isomerization					
4	$CI1 \rightarrow AA$	-3.22	-7.41	-1.01	434.5	[1, 3, 5, 6, 7, 8]
5	$CI2 \rightarrow NA$	-2.99	-6.48	-1.07	462.0	[1, 3, 5, 6, 7, 8]
6	$CI1 \rightarrow OcA + CO_2$	-3.17	-6.29	-1.28	504.0	[4]
7	$CI1 \rightarrow CAHP1$	0.23	-0.79	0.45	-	[5]
	OL attacking double bond					
8	$CI1 + OL \rightarrow OA + 10{,}OxA$	-1.15	-4.04	0.039	284.7	[6]
9	$CI1 + OL \rightarrow OA + 9{,}OxA$	-1.15	-4.04	0.039	284.7	[2, 6]
10	$CI2 + OL \rightarrow NN + 10{,}OxA$	-1.16	-3.80	-0.038	306.3	[6]
11	$CI2 + OL \rightarrow NN + 9{,}OxA$	-1.16	-3.80	-0.038	306.3	[6]
	Stabilization					
12	$CI1 + OL \rightarrow AAHP1OL$	1.84	0.04	1.83	-	[6]
13	$CI2 + OL \rightarrow AAHP2OL$	1.92	0.84	1.67	-	[6]
14	$CI1 + OA \rightarrow AAHP1OA$	0.93	0.21	0.879	-	[5, 7, 8]
15	$CI2 + OA \rightarrow AAHP2OA$	0.94	0.42	0.81	-	[5, 7]
16	$CI1 + NA \rightarrow AAHP1NA$	1.16	0.95	0.89	-	[7]
17	$CI2 + NA \rightarrow AAHP2NA$	1.15	1.08	0.85	-	[7]
18	$CI1 + AA \rightarrow AAHP1AA$	1.34	1.44	0.91	-	[7]

No.	**Reactions**	ΔH^o_{rxn} (kJ/mol) $\times 10^2$	ΔS^o (J/mol·K) $\times 10^2$	ΔG^o (kJ/mol) $\times 10^2$	**Temp. (K) at which** $\Delta G = 0$	**References**
19	$CI2 + AA \rightarrow AAHP2AA$	1.39	1.88	0.83	-	[7]
20	$CI1 + OA \rightarrow SOZ3$	0.40	-4.14	1.64	-	[5, 7]
21	$CI2 + OA \rightarrow SOZ2$	0.37	-4.21	1.61	-	[5, 7]
22	$CI1 + NN \rightarrow SOZ2$	0.37	-4.45	1.69	-	[5, 6, 7]
23	$CI2 + NN \rightarrow SOZ1$	0.33	-4.49	1.66	-	[5, 6, 7]
24	$CI1 + CI1 \rightarrow DP1$	0.94	-4.13	2.17	-	[5, 7, 8]
25	$CI2 + CI2 \rightarrow DP2$	0.85	-4.26	2.12	-	[5, 7]
26	$CI1 + CI2 \rightarrow DP3$	0.91	-4.18	2.14	-	[1, 7]
	Decomposition					
27	$DP1 \rightarrow OA + OA + O_2$	-1.78	-7.33	1.08	-	[1,4]
28	$DP2 \rightarrow NN + NN + O_2$	-1.72	-6.72	0.97	-	[1,4]
29	$DP3 \rightarrow NN + OA + O_2$	-1.76	-7.04	1.03	-	[1]
	Water added					
30	$CI1 + H_2O \rightarrow HP1$	0.99	0.68	0.769	-	[7]
31	$CI2 + H_2O \rightarrow HP2$	0.906	0.28	0.812	-	[7]
32	$HP1 \rightarrow OA + H_2O_2$	-0.04	-6.72	1.96	-	[7]
33	$HP1 \rightarrow AA + H_2O$	-4.21	-8.09	-1.78	520.4	[7]
34	$HP2 \rightarrow NN + H_2O_2$	0.03	-6.08	1.84	-	[7]
35	$HP2 \rightarrow NA + H_2O$	-3.9	-6.76	-1.88	576.9	[7]

[1] = (Hearn and Smith 2004), [2] = (Katrib *et al.* 2004), [3] = (Thornberry and Abbatt 2004), [4] = (Hung *et al.* 2005), [5] = (Ziemann 2005), [6] = (Hung and Ariya 2007), [7] = (Vesna *et al.* 2009), [8] = (Last *et al.* 2009), [9] = (Lee *et al.* 2012)

The process simulation results show that all molecules of ozone react with OL to form a number of products, as discussed previously. The NN, OcA, and carbon dioxide are the major products found in the PRODUCT stream, whereas NA, OA, and trace amounts of AA are considered the minor products. The volume fractions of NN, OcA, NA, and OA in the liquid phase at 20°C are 0.48 PPB, 0.52 PPB, 584 PPB, and 29 PPM, respectively. These results also show that formation of these products is temperature independent, as illustrated in Table 3.3.

It is clear that the major products estimated by Aspen Plus are NN and OcA. By considering the liquid fraction from the simulation results, the decomposition of PO that follows reaction pathway 1 to form NN and CI1 is approximately 100%, whereas the remaining PO follows the reaction pathway 2 to form OA and CI2. This situation occurs because an O-O bond, (which closes the alkyl group and might be the weaker bond) and a C-C bond are cleaved to form a large amount of NN and CI1 and also shows that most of the CI1 transforms to OcA and CO_2, and a small amount of CI1 isomerises to generate AA. In pathway 2, all CI2 isomerises to form NA. Although the ΔG of reactions No. 10 and No. 11 are negative, no signs of 10-OxA and 9-OxA are observed because a small amount of CI2 is formed and is completely converted to NA.

The amount of NN from the simulation result is similar to that of the experimental results reported by many researchers in which 50-84% of NN was observed (Hearn and Smith 2004, Thornberry and Abbatt 2004, Hung *et al.* 2005, Vesna *et al.* 2009). The amount of AA is also similar to the observation of King and co-workers (2009) that a trace amount of AA is found during ozonolysis of OL. Moreover, the volume percentage of NA is quite similar to the experimental observation from Hung and co-workers (2005) in which NN of 7% was detected.

Table 3.3 Liquid product yields at different reaction temperatures using the REqui.

Volume fraction	**Temperature (°C)**		
	20	**40**	**60**
AA	Trace	Trace	Trace
OcA	0.480	0.480	0.480
NN	0.520	0.520	0.520
NA	584 PPB	6 PPM	19 PPM
OA	29 PPM	3 PPM	286 PPB

However, the simulation results are different from the experimental observation reported by Katrib and co-workers (2004) and Ziemann (2005), who found that OA was one of the major products with 14-35% observed. These researchers also found that the composition of Criegee intermediates and their related products is 35-68%, which is not shown in these simulation results.

In addition, during the reaction, the effect of the exothermic reaction increases the outlet temperature by 21°C. However, the concentration of ozone used in this experiment is notably low, and a large amount of inert air is fed to the reactor. This effect can be minimised by removing the insulation materials from the reactor so that heat generated from the exothermic reactions can be transferred from the reactor to the surroundings. Therefore, a cooling system is unnecessary for the bubble column reactor used in this study.

In the case of water addition to increase productivity, Vesna and co-workers (2009) concluded that increasing the humidity during ozonolysis of OL results in an increase of primary product yields because CI will react with water before it reacts with the primary products. Nevertheless, the simulation results displayed in Table 3.2 show that the standard free energies of reactions No. 30 and No. 31 are positive. Therefore, both HP1 and HP2 cannot be formed during ozonolysis, accounting for unobserved products from reactions No. 32, 33, 34, and 35. In contrast, if CI1 reacts with water to form AA and water or if CI2 reacts with water to form NA and water, the standard free energies of these reactions are negative. Therefore, the primary product yields might be increased by following these reaction paths, according to the research performed by Vesna and co-workers (2009).

Temperature effects on product formation were modelled over the studied temperatures of 20°C, 40°C, and 60°C, as summarised in Table 3.3. The results show that the product formation is temperature independent. Furthermore, AAHPs will be formed at higher operating temperatures, which is in good agreement with the experimental results published by Hung and Tang (2010).

3.2 Condenser design using Aspen Plus

As discussed in Chapter 2, NN (which is the product with the lowest volatility) might be evaporated if experiments are performed at high temperatures. Therefore, in this section, Aspen Plus was used to determine the heat exchanger area of the condenser needed to condense all volatile products. As displayed in Figure 3.2, the gas phase from the reactor (which is assumed to be pure air) is fed to the condenser at a volumetric flowrate of 0.2

L/min at 60°C and atmospheric pressure. The outlet temperature of the gas stream and the inlet temperature of the water stream at a volumetric flowrate of 0.1 L/min are set at 20°C and 18°C, respectively. The physical properties used in this simulation for the gas phase and water are IDEAL and STEAM-TA, respectively. The overall heat transfer coefficient of the condenser with air and water as the fluids was also set at 10 W/m^2·K (Incropera 2011).

Results and discussions of the condenser design

The results show that 0.14 Watts of heat must be removed from the gas stream to reduce the gas temperature from 60°C to 20°C, and the required heat exchanger area is 10.78 cm^2. Therefore, the conventional coil glass condenser used in all laboratories can be employed in this experiment because its exchanger area is approximately 200 cm^2.

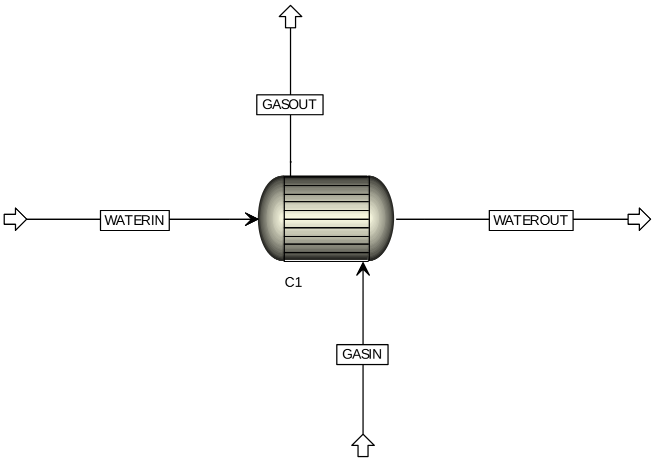

Figure 3.2 Condenser design

However, during ozonolysis with protic solvents, the substance used in this study with the lowest boiling is methanol. The boiling point of methanol is much lower than that of NN; thus, the designed condenser is tested by bubbling dry air at a volumetric flowrate of 0.1 L/min at 20°C into methanol at temperatures of 20°C, 40°C, and 60°C for 36 hr to determine the loss rate of methanol. The loss rate was subsequently recorded such that extra methanol could be added during the reaction according to this loss rate.

3.3 Suitable protic solvents predicted using Aspen Plus

As discussed previously, CIs are considered undesirable species because they react with valuable products as well as with OL, thus accounting for the decrease in productivity of valuable products. However, Vesna and co-workers (2009) proposed that the presence of water, which is a protic solvent, results in an increase of productivity of NN. Finlayson-Pitts and Pitts (2000) also proposed that the presence of hydrogen peroxide, methanol, ethanol, and formic acid, which are all protic solvents, can trap the reactions between CIs and primary products. Therefore, the protic solvents, which can dissolve in OL to form a homogeneous phase, are selected to increase the productivity instead of water because OL is insoluble in water.

To find the appropriate solvents, Aspen Plus was used to plot the ternary map of OL, water and protic solvents, i.e., methanol, ethanol, n-propanol, iso-propanol, n-butanol, formic acid, and acetic acid. The physical property method used in this simulation is UNIFAC-LL, which is described in the thermodynamics book (Smith *et al.* 2005).

Results and discussions of Suitable protic solvents

The results displayed in Figure 3.3 show that a small amount of OL dissolves in water (less than 2%), whereas OL cannot dissolve in formic acid at all compositions. In contrast, Batista and co-workers (1999) reported that OL dissolves in acetic acid as well as in short-chain alcohols at all compositions. Therefore, the short-chain alcohols, including methanol, ethanol, n-propanol, iso-propanol, n-butanol, and acetic acid, are used in this work to dissolve OL to increase the productivity.

It is well known that the ozonolysis of alcohols results in formation of aldehydes and ketones at 53-83% yields under mild conditions. The reaction rate constant of ozonolysis of alcohols is strongly dependent on the alcohol structure, as shown in Table 3.4. First-order kinetics are also observed for ozonolysis of alcohols (Rakovsky 2009).

The data listed in Table 3.4 show that the reaction rate constant for ozonolysis of methanol is the lowest compared with ethanol, n-propanol, iso-propanol, and n-butanol by an order of magnitude. Therefore, due to its lesser reactivity with ozone, methanol might be a suitable solvent for enhancing productivity. In addition, it could be assumed that the reactivities of methanol and ozone are negligible when they are mixed with unsaturated compounds because the reaction rate constant of ozonolysis of unsaturated compounds is several times higher than those found in methanol, especially in the liquid phase.

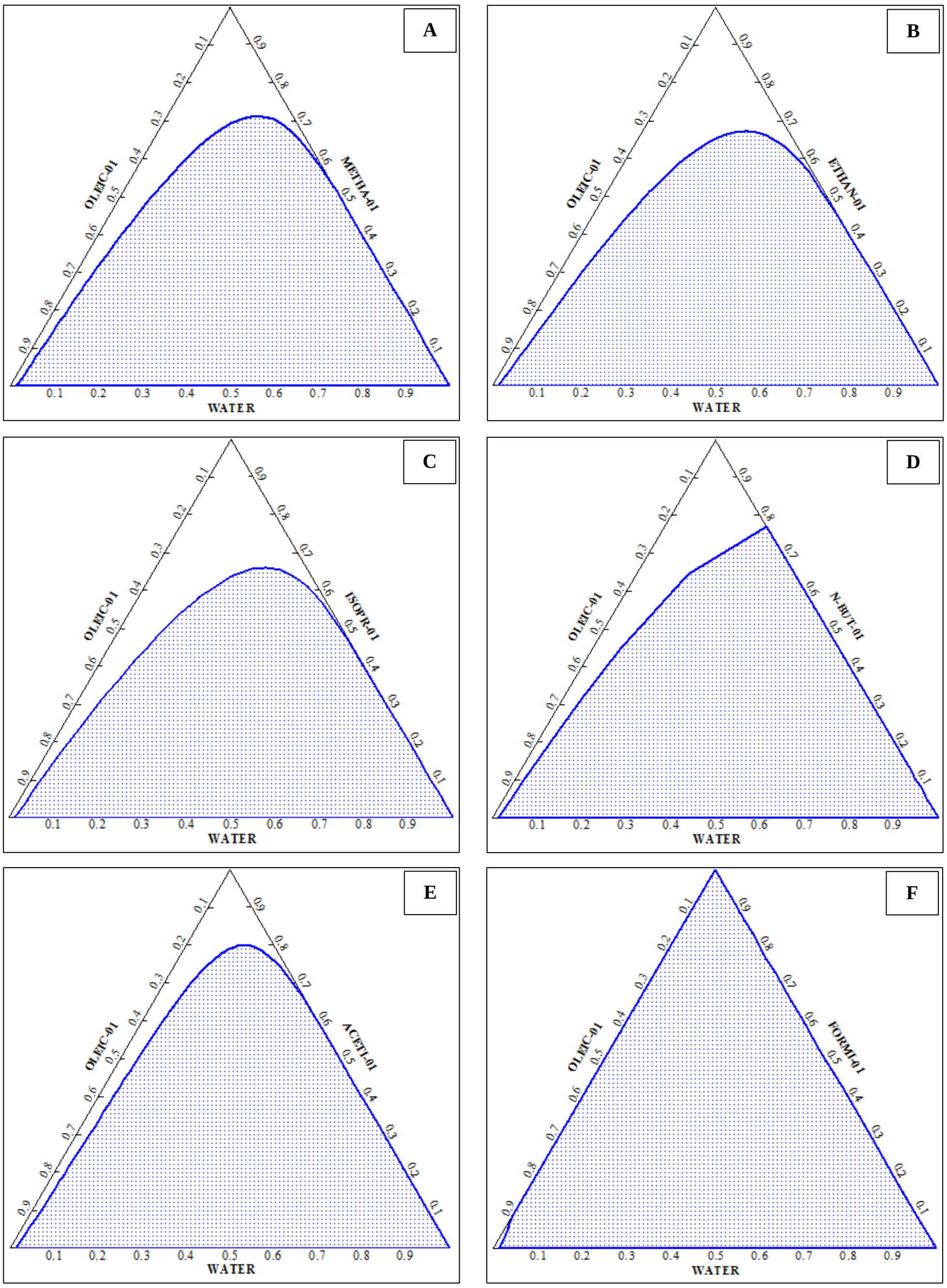

Figure 3.3 Ternary map of OL mixture at 20°C and atmospheric pressure: A = methanol, B = ethanol, C = iso-propanol, D = n-propanol, E = acetic acid, and F = formic acid

Table 3.4 Reaction rate constants of ozonolysis of alcohols at different temperatures

k ($M^{-1}\cdot s^{-1}$)	**Temperature (°C)**		
	20	**25**	**30**
Methanol	0.049	0.072	0.108
Ethanol	0.540	0.740	1.100
N-propanol	0.670	0.890	1.180
Iso-propanol	2.710	3.460	4.390
N-butanol	0.560	0.760	1.100

3.4 Minimum fluid level in the bubble column reactor

The minimum fluid level in the bubble column reactor is a crucial parameter in terms of reactor design. This parameter can be estimated by multiplying the bubble rise velocity discussed in Chapter 2 by the total time. The total time (τ_{total}) is the summation of the time that it takes the reactant to diffuse from the gas phase to the liquid interface ($\tau_{O_3,air}$) from the liquid interface to the liquid bulk ($\tau_{O_3,OL}$) and the reaction time (τ_R). The total time can be used to define the residence time for which the bubbles should exist in the bubble column reactor.

With the assumption of single-direction mass transfer along the radius, $\tau_{O_3,air}$ can be calculated using Eq. 3-4, which is a function of the diffusion coefficient of ozone in air and the bubble diameter. The worst case is also assumed if molecules of ozone are packed at the centre of the bubble surrounded by molecules of air because the diffusion time from this point is the longest diffusion due to the longest distance. The diffusion coefficient of ozone in air (D_{O_3Air}) at different temperatures can be calculated using Eq. 3-5 through Eq. 3-10. Moreover, the $\tau_{O_3,air}$ can be modelled using COMSOL Multiphysics. Details are described in Section 3.4.1.

$$\tau_{O_3,air} = \frac{r_b^2}{2D_{O_3air}} \tag{3-4}$$

$$D_{O_3Air} = \frac{0.00266T^{3/2}}{PM_{O_3Air}^{1/2}\sigma_{O_3Air}^2\Omega_D} \tag{3-5}$$

$$M_{O_3Air} = 2/\left[(1/MW_{O_3}) + (1/MW_{Air})\right] \tag{3-6}$$

$$\sigma_{O_3Air} = \frac{\sigma_{O_3} + \sigma_{Air}}{2} \tag{3-7}$$

$$\Omega_D = \frac{1.06036}{T^{*0.1561}} + \frac{0.1930}{\exp(0.47635T^*)} + \frac{1.03587}{\exp(1.52996T^*)} + \frac{1.76464}{\exp(3.89411T^*)} \tag{3-8}$$

$$T^* = \frac{k_B T}{\varepsilon_{O_3Air}} \tag{3-9}$$

$$\varepsilon_{O_3Air} = \left(\varepsilon_{O_3}\varepsilon_{Air}\right)^{0.5} \tag{3-10}$$

In these equations, r_b = radius of the bubble, T = temperature (K), P = pressure (bar), σ = characteristic length (A^o), Ω = diffusion collision integral (dimensionless), ε = characteristic Lennard-Jones energy, and k_B = Boltzmann's constant (1.381×10^{-23} J/K). Both the characteristic length and characteristic Lennard-Jones energy are presented in Table 3.5.

Table 3.5 Lennard-Jones potentials of air and ozone

Substance	$\sigma, \overset{o}{A}$	$\varepsilon / k, K$
Air	3.711[a]	78.6[a]
Ozone	3.875[b]	208.4[b]
Air -Ozone	3.793	127.98
a = (Poling *et al.* 2000), b = (Ivanov *et al.* 2007)		

For $\tau_{O_3,OL}$, single-direction mass transfer over a plane surface can be assumed because the diffusive length of ozone in OL is much smaller than the bubble radius; thus, $\tau_{O_3,OL}$ can be determined using Eq. 3-11. It should also be assumed that no chemical reaction occurs during the diffusion from the liquid interface to the liquid bulk.

$$\tau_{O_3,OL} = \frac{D_{O_3OL}}{k_l^2} = \frac{\delta_r^2}{2D_{O_3OL}} \tag{3-11}$$

In this equation, δ_r = the reacto-diffusive length of ozone in oleic acid (2 nm – 20 nm) (Moise and Rudich 2002, Morris *et al.* 2002, Smith *et al.* 2002, King *et al.* 2009), and D_{O_3OL} = the diffusion coefficient of ozone in OL, which is described in Chapter 4.

In this section, the τ_R shown in Eq. 3-12 can be minimised because the reaction rate constant of ozonolysis of unsaturated compounds is notably high, thus resulting in a rather short period for the reaction time (Beltrán 2004, King *et al.* 2009).

$$\tau_R = \frac{1}{k_1 C_{OLb}} \tag{3-12}$$

3.4.1 Diffusion time of ozone in the bubble using COMSOL Multiphysics

In addition to Eq. 3-4, COMSOL Multiphysics is used to predict the diffusion time of molecules of ozone in the bubble such that the results can be used to determine the minimum level of OL in the reactor. The model assumes the worst case in which all molecules of ozone are packed at the centre of the bubble. From this point, molecules of ozone diffuse to the liquid interface over the longest distance, resulting in the longest diffusion time.

$$\frac{\partial c}{\partial t} + \nabla \cdot \left(-D \nabla c\right) = 0 \tag{3-13}$$

The diffusion module in COMSOL Multiphysics with transient analysis and no chemical reactions was employed in this study. The mass transfer equation for this module is shown in Eq. 3-13. Only half of the bubble was modelled using 2D axial symmetry. The inner circle represents pure ozone surrounded by pure air, which makes up the outer circle, as shown in Figure 3.4A. The radius ratio between the inner and outer circle was set at 1:10 such that the concentration of ozone in the bubble at steady-state conditions would be approximately 1000 ppm. The initial concentration of pure ozone is 41.757 mol/m^3, and the diffusion coefficients of ozone in air used in this model are estimated using Eq.3-5. The boundary conditions and the simulation result are shown in Figure 3.4A and Figure 3.4B, respectively.

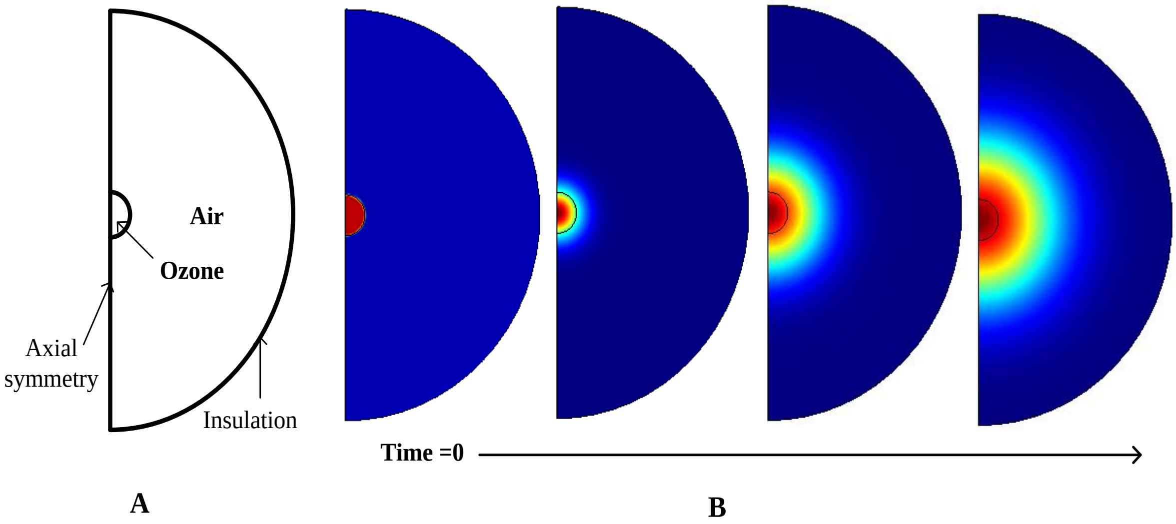

Figure 3.4 Diffusion time of ozone in the bubble: (A) bubble geometry and boundary conditions, (B) simulation results at different times

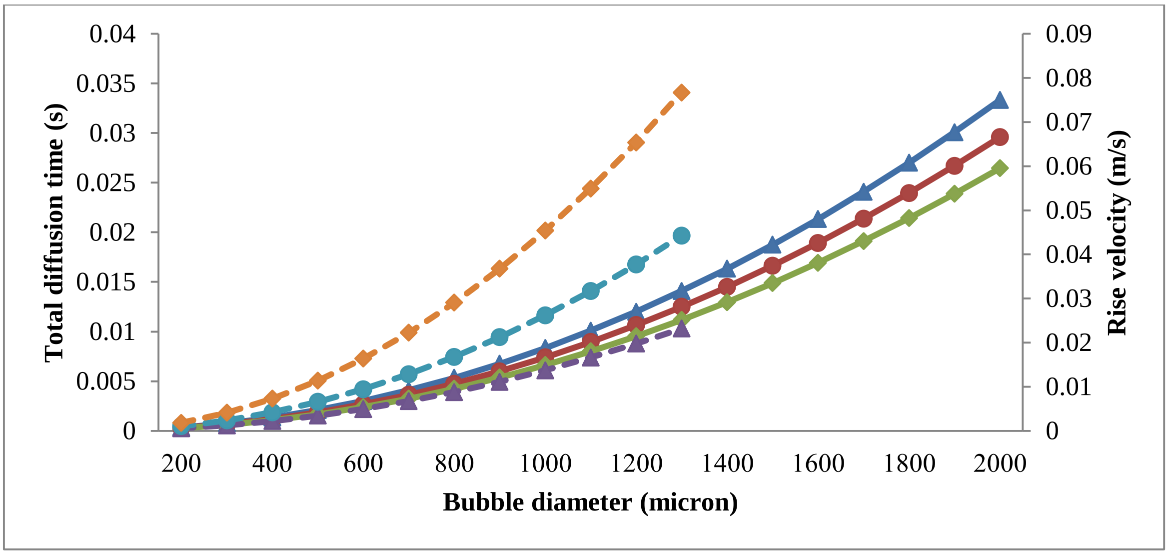

Figure 3.5 Total diffusion time of ozone from air to OL and bubble rise velocity

Diffusion time at 20°C (—▲—), 40°C (—●—), 60°C (—◆—)

Rise velocity at 20°C (--▲--), 40°C (--●--), 60°C (--◆--)

Results and discussions of the minimum fluid level

The values of $\tau_{O_3,air}$ obtained from the simulation results and from Eq. 3-4 are identical. This result confirms that both techniques are correct. Therefore, τ_{total} can be plotted as a function of bubble diameter, as shown in Figure 3.5. The result shows that τ_{total} increases with increasing bubble diameter but decreases with increasing fluid temperatures. The τ_{total} is dominated only by the $\tau_{O_3,air}$ because $\tau_{O_3,OL}$ is quite rapid due to the notably short reacto-diffusive length of ozone in OL. Therefore, bubble size is a crucial parameter for specifying the level of the liquid in the bubble reactor.

For the rise velocity of the bubbles calculated by Eq. 2-49, which is suitable for a bubble with a diameter smaller than 1.3 mm, the results illustrated in Figure 3.5 show that the rise velocity increases with increasing bubble diameter and fluid temperature; this value is much smaller than the rise velocity of the bubble in the water, as shown in Figure 2.10, because the fluid viscosity of OL is 35 times higher than the fluid viscosity of water, and the density of OL is lower than the density of water.

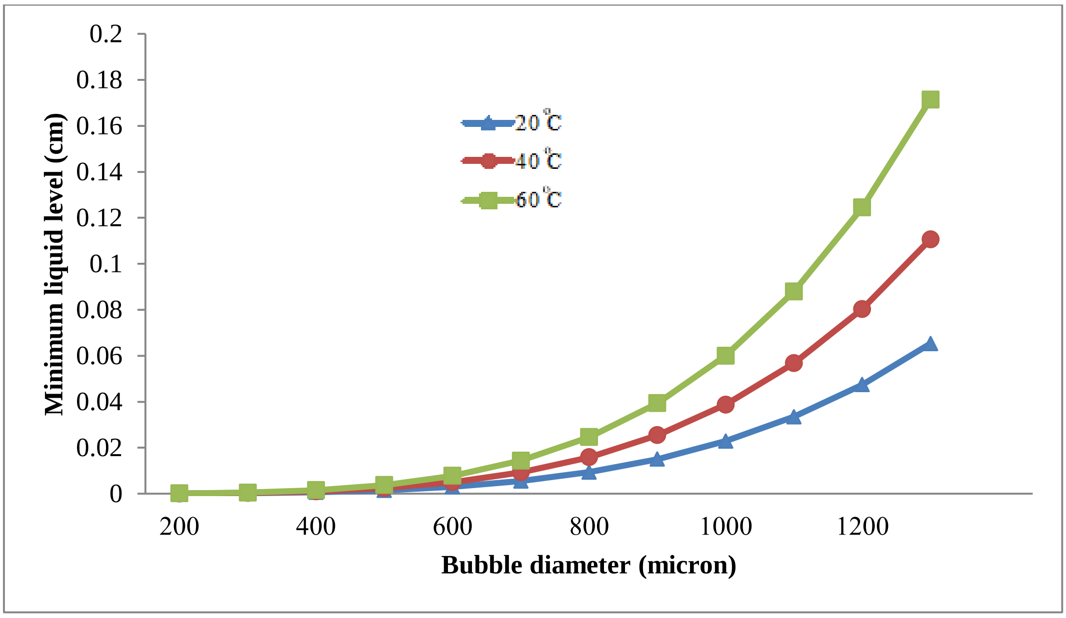

Figure 3.6 Minimum OL level in the reactor at different temperatures

The minimum level of OL in the reactor can be determined by multiplying the summation of the total time by the rise velocity, as shown in Figure 3.6. The results show that the minimum liquid level increases with increasing fluid temperature and bubble size. For example, at a bubble diameter of 1300 microns and a fluid temperature of 20°C, the minimum level of fluid is approximately 0.17 cm, which means that at this level, ozone molecules have sufficient time to diffuse from the gas phase to the liquid interface before reacting with OL at the interface. Therefore, in this research, the level of OL in the reactor must be greater than 0.17 cm if the bubble size is approximately 1300 microns and the reaction time is assumed to be rapid.

3.5 Reactor design using COMSOL Multiphysics

The COMSOL Multiphysics software is used to find a suitable location for the sampling tube and the thermometer by modelling only half of the reactor to reduce the solution memory, as shown in Figure 3.7.

The bubbly flow module and heat transfer module were selected to model the two-phase flow fluid. The geometry details and boundary conditions of both the liquid and gas phases are shown in Figure 3.8. The diameter of the bubbles and the flow rate of air were set at 1000 µm and 0.1 L/min, respectively.

The momentum transport of the bubbly flow can be written as shown in Eq. 3-14.

$$\phi_l \rho_l \frac{\partial u_l}{\partial t} + \phi_l \rho_l u_l \cdot \nabla u_l = -\nabla p + \nabla \cdot \left[\phi_l \mu_l \left(\nabla u_l + \nabla u_l^T \right) \right] + \phi_l \rho_l g \tag{3-14}$$

In this expression, ϕ_l is the volume fraction of the liquid phase (m^3/m^3), ρ_l is the liquid density (kg/m^3), u_l is the liquid phase velocity (m/s), p is the pressure (Pa), μ_l is the liquid dynamic viscosity (Pa·s), and g is the gravity vector (m/s^2). The equation for the gas phase transport can be written as shown in Eq. 3-15.

$$\frac{\partial \rho_g \phi_g}{\partial t} + \nabla \cdot \left(\phi_g \rho_g u_g \right) = -m_{gl} \tag{3-15}$$

In this case, u_g is the gas phase velocity (m/s), ρ_g is the gas density (kg/m^3), ϕ_g is the volume fraction of gas (m^3/m^3), and m_{gl} is the mass transfer rate from gas to liquid (kg/(m^3·s)). The gas density, which is calculated from the ideal gas law, can be written as shown in Eq. 3-16.

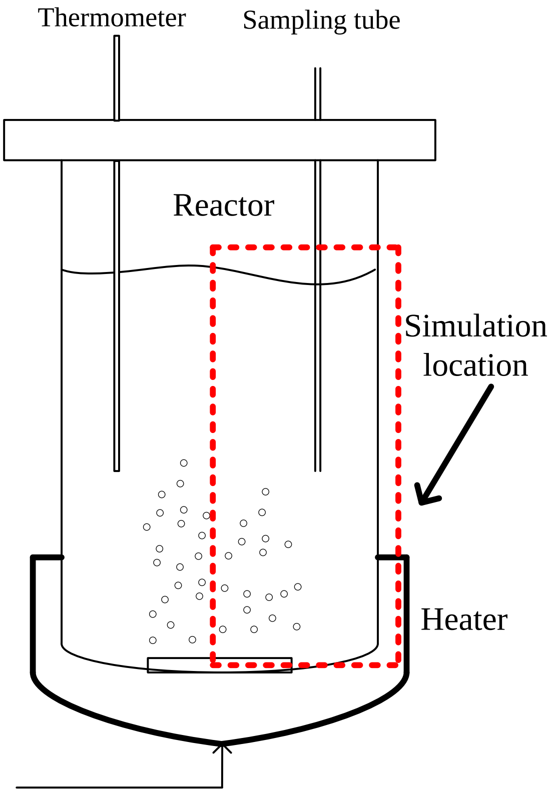

Figure 3.7 Simulation part of reactor design

$$\rho_g = \frac{\left(p + p_{ref}\right)MW}{RT} \tag{3-16}$$

In this expression, MW is the molecular weight of the gas (kg/mol), R is the ideal gas constant (8.314 J/mol·K), p_{ref} is the reference pressure (10^5 Pa), and T is the temperature. The equation for the liquid volume fraction and the gas velocity can be written as displayed in Eq. 3-17 and Eq. 3-18, respectively.

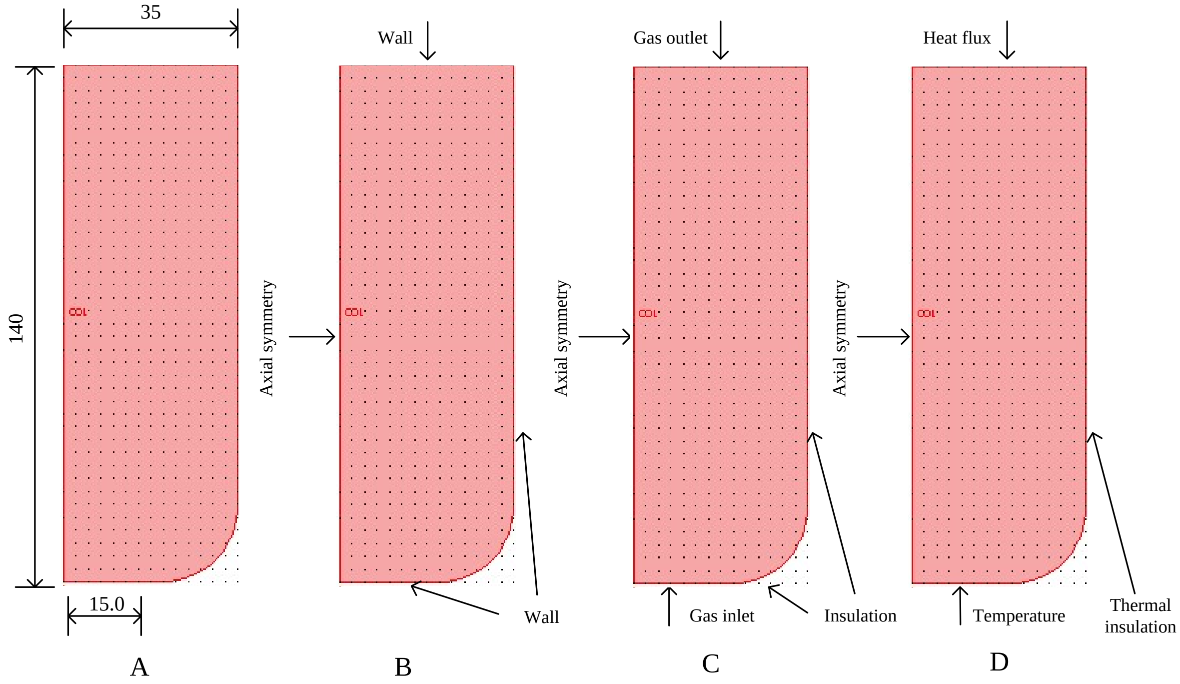

Figure 3.8 Model definition of reactor design; geometry modelling (A), boundary condition of liquid (B), boundary condition of gas (C), boundary condition of heat transfer (D)

$$\phi_l = 1 - \phi_g \tag{3-17}$$

$$u_g = u_l + u_{slip} \tag{3-18}$$

In these expressions, u_{slip} is the relative velocity between the gas and liquid (m/s). In addition, the relative velocity between the gas phase and the liquid phase can be written as illustrated in Eq. 3-19.

$$\frac{3}{4}\frac{C_d}{d_b}\rho_1 \left|u_{slip}\right| u_{slip} = -\nabla p \tag{3-19}$$

where C_d is the drag coefficient, and d_b is the bubble diameter (m). In addition to the momentum transport equation, the heat transfer equation used in this model can be written as shown in Eq. 3-20.

$$\rho_l C_{pl}\frac{\partial T}{\partial t} + \nabla\cdot\left(-k_l \nabla T\right) = Q - \rho C_{pl} u_l \cdot \nabla T \tag{3-20}$$

In this case, C_{pl} is the heat capacity at a constant pressure of the liquid (J/kg·K), k_l is the thermal conductivity of the liquid (W/m·K), and Q is the heat source (W/m^3). The simulation steps and all parameters used in this model appear in Appendix C. Moreover, COMSOL Multiphysics is employed for 3D modelling. The simulation details are listed in Appendix C.

Before running the simulation, the geometry must be divided into mesh cells, as shown in Figure 3.10A. In this simulation, triangle mesh elements (unstructured mesh) are set with three different numbers of mesh elements for mesh dependency study. The number of mesh elements and degrees of freedom calculated by COMSOL Multiphysics are listed in Table 3.6.

Table 3.6 Mesh dependency study

Mesh	Number of Mesh elements	Number of degrees of freedom
A	11313	74564
B	14532	95638
C	19281	126671

Results and discussions of the reactor design by COMSOL MULTIPHYSICS

As shown in Figure 3.9, the liquid velocity along the radius of the reactor at the liquid level of 10 cm is selected to represent the effect of mesh dependency. The result shows that the liquid velocity at the centre of the reactor (r=0) and at the radius between 1.0 – 1.5 cm is slightly different. A part from that the liquid velocity is identical. Because of identical results, the highest number of unstructured mesh elements (Mesh C) as listed in Table 3.6 is used in this study. Note that the higher numbers of mesh elements can be employed, if high performance of a computer is available.

For the reactor design, the simulation results of the liquid velocity and the arrow liquid velocity are shown in Figure 3.10B and Figure 3.10C, respectively. These figures show that the bubbles rise through the liquid phase between the centre of the reactor and the tip of the diffuser (represented in red colour). When the bubbles rise, the liquid phase also rises with the same direction and velocity, resulting in a circulating motion of the liquid phase inside the reactor. Therefore, it is not necessary to insert the internal tube in the bubble column reactor used in this study.

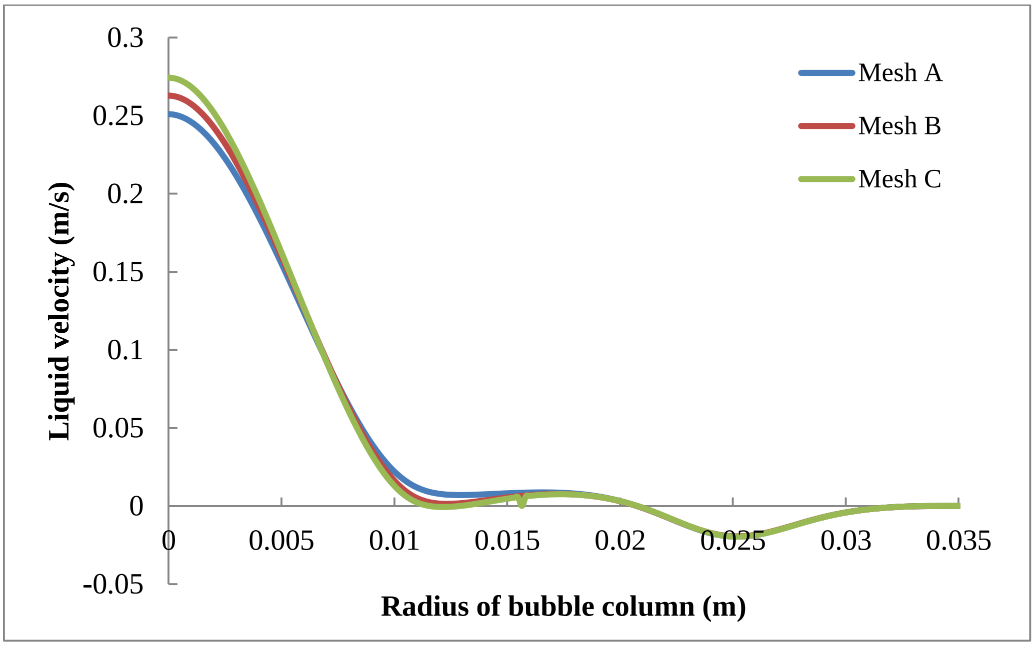

Figure 3.9 Liquid velocity of different mesh elements: Mesh A =11313, Mesh B = 14532, and Mesh C =19281

Two locations are suitable for installation of the sampling tube. The first location is the area within the diffuser length that shows a strong flow of the liquid phase (red colour), and the other is the area in which the liquid flows down along the edge of the reactor. However, certain regions are inappropriate for sampling tube installation because the liquid displays slight movement in these regions. The mentioned locations are the blue coloured zone at the top and the bottom of the reactor, and the blue coloured zone near the red colour zone along the reactor (the interface between the liquid phases rise up and down).

In addition to installing the sampling tube, a thermometer is required for detecting the reaction temperature. Therefore, the heat transfer model is added to predict the characteristics of heat transfer in the reactor to find an appropriate location for the thermometer. A heating mantle is employed in this study to heat the OL in the reactor such that the heating zone is set at the bottom of the reactor. The temperature is set at 60°C. The inlet temperature of the feed gas (at the diffuser) and the initial fluid temperature are also set to 20°C. The fluid properties, which are a function of temperature, are estimated using Aspen Plus, as listed in Appendix B.

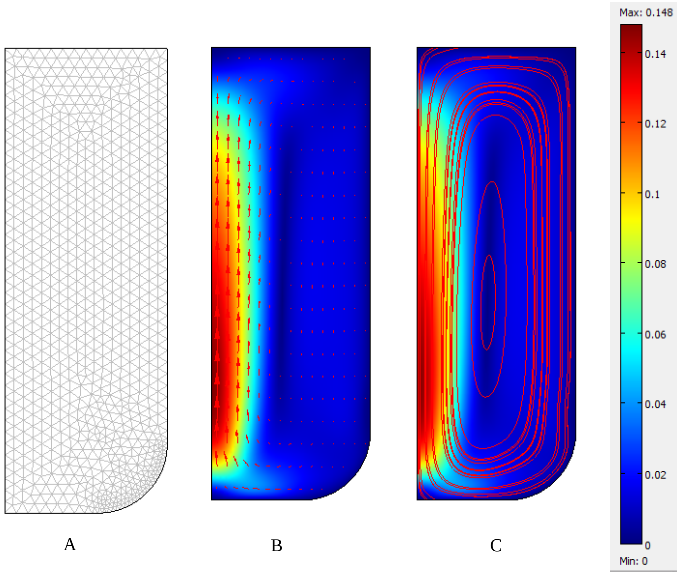

Figure 3.10 Simulation results by COMSOL Multiphysics; Mesh (A), Liquid velocity and arrow liquid velocity (B), and Liquid velocity and stream line liquid velocity (C)

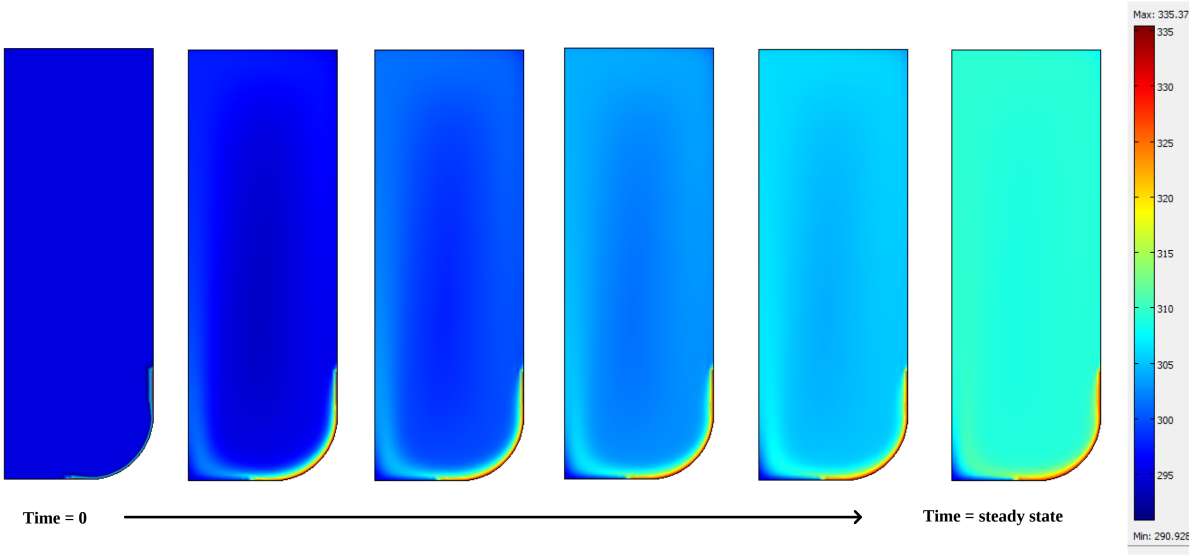

Figure 3.11 Heat transfer inside the reactor

The simulation result displayed in Figure 3.11 shows that the fluid temperature inside the reactor increases with increasing contact time. In the beginning, the fluid temperature is much lower than the set temperature of the heating zone. Next, generated heat is transferred from the heating zone to the fluid via convection heat transfer, resulting in a sharp increase of the fluid temperature. At steady state, as shown in the last slide of Figure 3.11, a good distribution of the fluid temperature in the reactor exists, except at the heating zone and the diffuser. Therefore, the thermometer might be inserted into the reactor at any location except the locations near the diffuser and the heating zone because the fluid temperature near the diffuser is quite low compared with the average fluid temperature inside the reactor, whereas the fluid temperature near the heating zone is quite high.

For 3D modelling, simulation results of the liquid velocity and stream line liquid velocity are illustrated in Figure 3.12. The results are identical to those of 2D modelling as described above. Therefore, axial symmetry (2D) is acceptable for the reactor design using COMSOL Multiphysics.

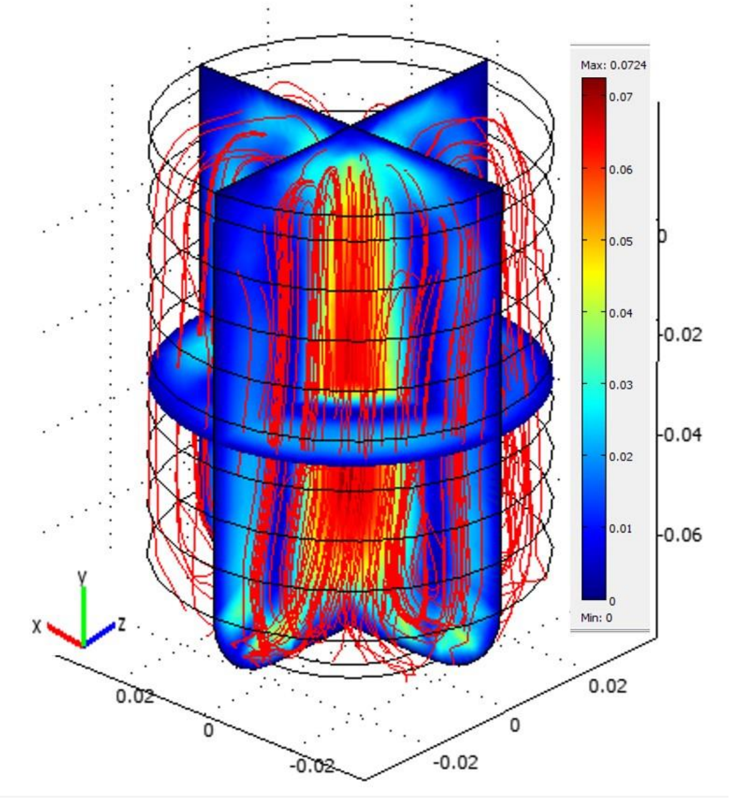

Figure 3.12 Simulation result (3D): liquid velocity and stream line liquid velocity

Note that the diameter of the vent tube should be larger than the diameter of the feed tube for the purpose of preventing pressure build-up inside the reactor because methanol (which has the lowest boiling point) might evaporate during the reaction. The bubble column reactor and other equipment used in this experiment are shown in Figure 3.13.

3.6 Summary

The heat of formation and the standard free energy of formation of all possible products from the ozonolysis of OL are determined using Aspen Plus software, and the heat of reaction, standard free energy, and entropy are calculated to find the possible reactions. Eight reactions take place during ozonolysis at standard conditions, and all are exothermic reactions. For process simulation, all molecules of ozone react with OL to form NN, OcA, and carbon dioxide and are considered to be the major products. Small amounts of AA, NA, and OA are also observed. Moreover, the product yield is slightly dependent on the reaction temperatures within the studied range. Six protic solvents (i.e., methanol, ethanol, n-propanol, iso-propanol, n-butanol, and acetic acid) are mixed with OL to increase the product yield. For the reactor design, the level of OL in the reactor is primarily a function of the bubble size. A conventional condenser must be installed on the top of the bubble column for condensation of all volatile products. The most appropriate location for installation of the thermometer and the sampling tube is at the centre of the bubble column reactor.

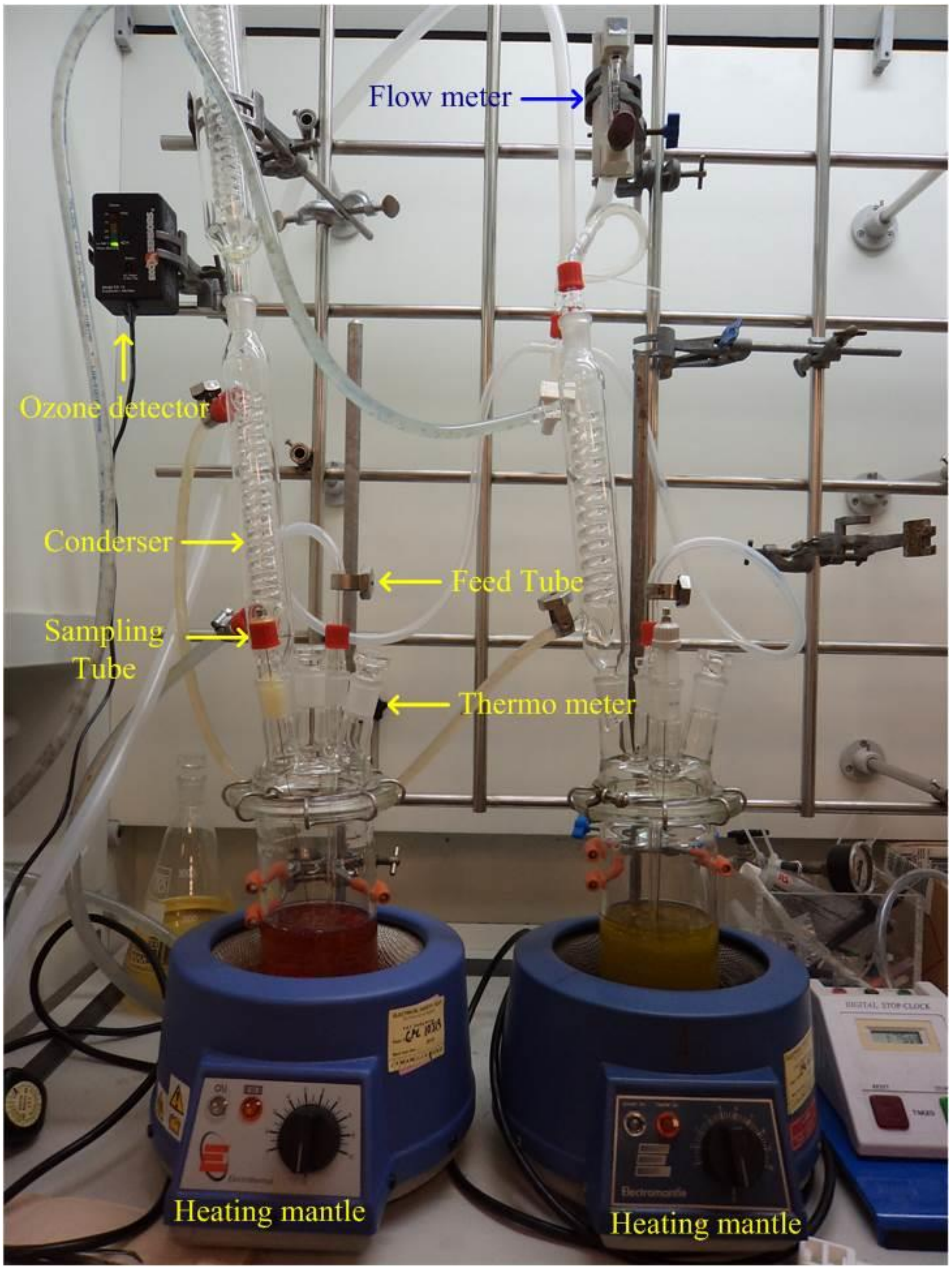

Figure 3.13 Bubble column reactor used in this study

CHAPTER 4

ESTIMATION OF THE HENRY'S LAW CONSTANT, DIFFUSION COEFFICIENT, INLET OZONE CONCENTRATION, AND BUBBLE CHARACTERISATION

As discussed in Chapter 2, several parameters must be calculated prior to determination of the reaction rate constant. Therefore, this chapter focuses on the estimation of these parameters i.e., the Henry's Law constant, diffusion coefficient, inlet ozone concentration, and bubble characterisation. Section 4.1 describes a new technique for estimation of the Henry's Law constant using Aspen Plus. Section 4.2 focuses on estimation of the fluid properties to find the diffusion coefficient using Aspen Plus. The estimated fluid properties are density, viscosity, surface tension, and molecular weight of mixtures and are provided in Appendix B. Section 4.3 describes the measurement of inlet ozone concentration using the KI method. The effect of thermal decomposition of ozone is also studied in this section using COMSOL Reaction Engineering Lab. Section 4.4 presents the experimental setup for bubble characterisation based on the reactor design from Chapter 3 for the purpose of determination of the specific interfacial area using a high-speed camera and ImageJ software. Section 4.5 provides a summary.

4.1 Henry's Law constant at different temperatures based on thermodynamic properties

The Henry's Law constant is one of the crucial parameters that must be calculated before determining the reaction rate constants. The Henry's Law constant is strongly temperature dependent but also slightly dependent on pressure, and its value also strongly depends on the nature of the solvent. For the vapour/liquid equilibrium (VLE) in the solute and solvent system, the Henry's Law constant can be evaluated using the correlation of fugacity (f_i), mole fraction of i in the vapour phase $\left(y_i\right)$, and mole fraction of i in the liquid phase (x_i), as shown in Eq. 4-1. By plotting f_i versus x_i, the limiting slope at $x_i = 0$ of this curve is calculated and gives the Henry's Law constant (Wilhelm *et al.* 1977, Smith *et al.* 2005).

$$\lim_{x_i \to 0} \frac{f_i}{x_i} = \left(\frac{df_i}{dx_i} \right)_{x_i = 0} = H_i^{px} \qquad (i = 1, 2, ...N) \qquad \text{(4-1)}$$

$$f_i = y_i \phi_i P \tag{4-2}$$

For the VLE at low pressure (P≤ 1 bar), the vapour phase can be assumed to be an ideal gas such that the fugacity coefficient (ϕ_i) is equal to 1, and thus, Eq. 4-2 can be rewritten as Eq. 4-3:

$$f_i = y_i P \tag{4-3}$$

Several superscripts are used to denote the specific forms of the Henry's Law constant: H^{cp} = Henry's Law constant via concentration (M/atm), H^{cc} = dimensionless Henry's Law constant, H^{bp} = Henry's Law constant via molality (mol/kg·Pa), H^{pc} = inverse Henry's Law constant via concentration (atm/M), and H^{px} = inverse Henry's Law constant via aqueous-phase mixing ratio (atm). The conversion factors for several Henry's Law constants as a function of H^{cp} are shown in Eq. 4-4 through Eq. 4-6 (Sander 1999):

$$H^{cc} = H^{cp} \times RT \tag{4-4}$$

$$H^{bp} = \frac{H^{cp}}{\rho_{solvent}} \tag{4-5}$$

$$H^{pc} = \frac{1}{H^{cp}} \tag{4-6}$$

$$H^{px} = \frac{\rho_{solvent}}{MW_{solvent} \times H^{cp}} \tag{4-7}$$

It is impossible to measure the mole fraction of ozone in both the vapour and liquid phases because it reacts simultaneously with OL. Therefore, in this section, Aspen Plus is used to estimate the thermodynamic properties ($f_i, y_{i,} x_i$) between OL and ozone as well as the mixture of OL with protic solvents using WILSON as the property model. Polymath V5.1 is also applied to solve the mathematics equations. The techniques are described in Appendix A. In addition, similar techniques are used to estimate the Henry's Law constant of ozone in olive oil, mixtures of olive oil with methanol, and used cooking oil mixed with methanol.

4.1.1 Results and discussion of the Henry’s Law constant estimation

After plotting the graph between the fugacity and the mole fraction of ozone in the liquid phase of OL, as shown in Figure 4.1, Polymath V5.1 software was used to determine the slope of this graph at x = 0. The Henry’s Law constant with units of pressure is subsequently converted to units of concentration and pressure using the density and molecular weight of OL, as shown in Table 4.1. The result shows that the Henry’s Law constant as estimated by Aspen Plus increases with increasing temperature. The Henry’s Law constants at 20°C, 40°C, and 60°C are 2.23 atm/M, 2.87 atm/M, and 3.56 atm/M, respectively. It is interesting to note that the values of the Henry’s Law constants at 20°C used by Hung and Ariya (2007) and Smith and co-workers (2002) for determination of the reactive uptake coefficients are 10 atm/M and 2.08 atm/M, respectively. These values were estimated based on the measured solubility constant for ozone in a variety of organic solvents instead of OL (Smith *et al.* 2002) because ozone reacts simultaneously in OL while it is dissolving, resulting in difficulties in measuring the mole fraction of ozone in both the gas and liquid phases. The Henry’s Law constants evaluated by Aspen Plus, which can be set for un-reaction mode based on molecular thermodynamics, are therefore acceptable for investigation of the kinetic parameters because its value at 20°C is in the range used by previous studies.

Similar to the estimation of the Henry’s Law constant of pure OL, Polymath V5.1 software is used to determine the slope of a graph plotted between the fugacity and mole fraction of ozone in the liquid phase of pure olive oil at x = 0. The results listed in Table 4.1 show that the Henry’s Law constants increase with increasing temperatures. The Henry’s Law constants at 20°C, 40°C, and 60°C are 114.03 atm/M, 173.01 atm/M, and 249.38 atm/M, respectively. These values are slightly lower than that of oxygen in olive oil, which is approximately 194.17 atm/M at 20°C (Battino *et al.* 1968, Chaix *et al.* 2014). Therefore, the Henry’s Law constants of ozone in olive oil evaluated by Aspen Plus are acceptable for investigation of the kinetic parameters. Moreover, if methanol is mixed at a molar ratio of 1.0:1.0 with olive oil and at 1.0:3.0 with used cooking oil, the Henry’s Law constants are approximately two times and four times lower than those of pure olive oil, respectively

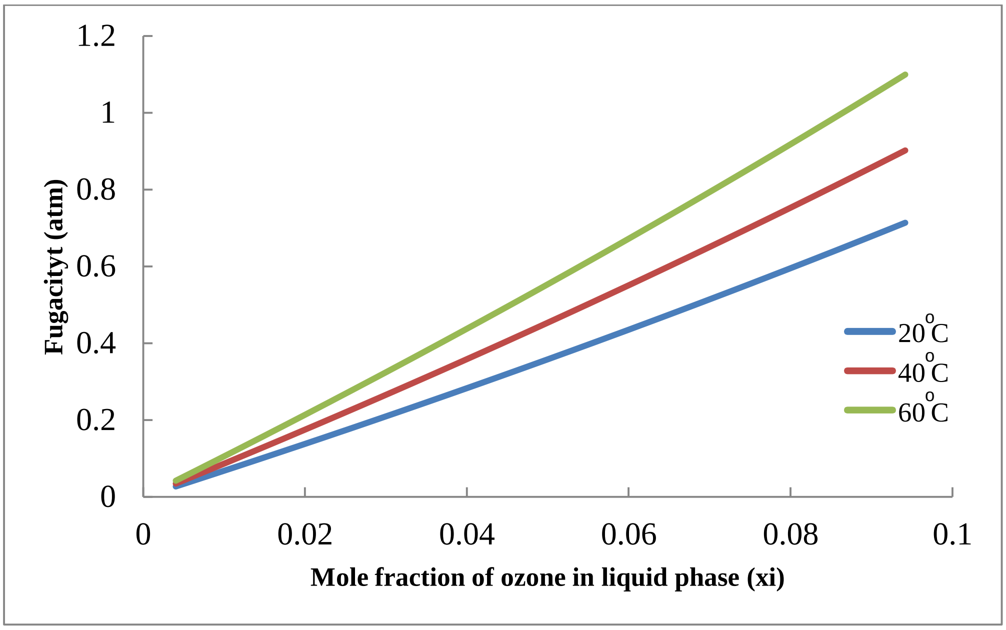

Figure 4.1 Composition dependence of fugacity for ozone in OL at different temperatures

Table 4.1 Henry's Law constant of ozone with pure OL, olive oil, used cooking oil, and its mixtures

The Henry's Law constant (atm/M)	**20°C**	**40°C**	**60°C**
Pure OL	2.23	2.87	3.56
OL : methanol (1:1)	1.65	2.10	2.26
OL : ethanol (1:1)	1.70	1.94	2.40
OL : n-propanol (1:1)	1.74	1.97	2.50
OL : iso-propanol (1:1)	1.75	1.98	2.46
OL : n-butanol (1:1)	1.79	1.99	2.47
OL : acetic acid (1:1)	1.81	2.12	2.53
Pure olive oil	114.03	173.01	249.38
Olive oil : methanol (1:1)	59.95	89.17	126.46
Used cooking oil : methanol (1:3)	32.86	48.87	69.30

4.2 Diffusion coefficient at different temperatures

In addition to the Henry's Law constants, the diffusion coefficient is a crucial parameter used in the reaction rate constant calculation. Many correlations are available to determine the diffusion coefficients in binary liquids. In this study, the correlation used for binary liquid at different temperatures is expressed in Eq. 4-8 (Poling *et al.* 2000).

$$D_{O_3OL} = 7.4\times10^{-8}\frac{(\phi_s MW)^{0.5}T}{\mu_s V_A^{0.6}} \tag{4-8}$$

where MW and μ_s are the molecular weight and the viscosity of the solvent (cP), respectively, V_A is the molar volume of ozone at its normal boiling temperature and is 35.5 cm^3/mol, and T is the temperature (K), and association factor of solvent B (ϕ_s =1). All parameters described above were estimated using Aspen Plus.

4.2.1 Results and discussion of the diffusion coefficient estimation

For a binary gas mixture of ozone and air, the diffusion coefficients calculated by Eq. 3-5 increase with increasing gas temperature. The diffusion coefficients at 20°C, 40°C, and 60°C at atmospheric pressure are 0.150 cm^2/s, 0.169 cm^2/s, and 0.189 cm^2/s, respectively. These estimated values are close to the experimental results reported by Laisk and co-workers (1989) (D_{o_3Air} = 0.133 cm^2/s at 20°C, 1 atm). Therefore, these diffusion coefficients can be used to estimate the minimum liquid level, as described in Chapter 3.

For binary liquid mixtures, the density, viscosity, and molecular weight of OL evaluated by Aspen Plus are shown in Appendix B. These values were used to determine the diffusion coefficient of ozone in OL using Eq. 4-8, which is the same as the Henry constants in that the diffusion coefficient of ozone in OL increases with increasing fluid temperature. The estimated diffusion coefficients at 20°C, 40°C, and 60°C are 1.21×10^{-6} cm^2/s, 2.52×10^{-6} cm^2/s, and 4.72×10^{-6} cm^2/s, respectively. It is interesting to note that the estimated value at 20°C falls between the diffusion coefficients used by Smith and co-workers (2002) and Moise and Rudich (2002); these values are 1×10^{-5} cm^2/s and 1×10^{-6} cm^2/s, respectively, and were estimated based on the diffusion coefficient of oxygen in a variety organic solvents instead of ozone in OL (Smith *et al.* 2002).

Therefore, using the estimated values from Aspen Plus and the Eq. 4-8, the diffusion coefficient of ozone in OL at different temperature appears to be accurate for the reaction rate constant calculation. For the self-diffusion coefficient of OL used to verify the kinetic regimes, as listed in Table 2.6, Iwahashi and co-workers (2000) reported that the values of the self-diffusion coefficients at 20°C, 40°C, and 60°C are ~5×10^{-7} cm^2/s, ~7×10^{-7} cm^2/s, ~1.5×10^{-6} cm^2/s, respectively.

In addition to pure OL, the diffusion coefficients of ozone in the mixtures (OL and protic solvents) at different molar ratios are calculated as listed in Table 4.2. The results show a similarity to pure OL in that the diffusion coefficient of ozone in the mixtures increases with increasing fluid temperature; however, it decreases as the molecular weight of the alcohols increase. Therefore, the highest diffusion coefficient of ozone is found in the mixture of OL with methanol.

Table 4.2 Diffusion coefficients of ozone in air, OL, olive oil, used cooking oil and mixtures

Diffusion coefficient (cm^2/s)	**20^{o}C**	**40^{o}C**	**60^{o}C**
D_{O_3Air}	0.150	0.169	0.189
D_{O_3OL}	1.21×10^{-6}	2.52×10^{-6}	4.72×10^{-6}
$D_{O_3OL_{mixed}}$ (1:1 of methanol)	7.09×10^{-6}	1.20×10^{-5}	1.88×10^{-5}
$D_{O_3OL_{mixed}}$ (1:1 of ethanol)	5.05×10^{-6}	9.04×10^{-6}	1.51×10^{-5}
$D_{O_3OL_{mixed}}$ (1:1 of n-propanol)	3.79×10^{-6}	7.08×10^{-6}	1.23×10^{-5}
$D_{O_3OL_{mixed}}$ (1:1 of iso-propanol)	3.64×10^{-6}	7.22×10^{-6}	1.31×10^{-5}
$D_{O_3OL_{mixed}}$ (1:1 of n-butanol)	3.36×10^{-6}	6.40×10^{-6}	1.12×10^{-5}
$D_{O_3OL_{mixed}}$ (1:1 of acetic acid)	5.12×10^{-6}	8.79×10^{-6}	1.41×10^{-5}
$D_{OL,OL}$	5.00×10^{-7}	7.00×10^{-7}	1.50×10^{-6}
$D_{O_3\,\text{olive oil}}$	8.51×10^{-7}	2.27×10^{-6}	4.73×10^{-6}
$D_{O_3\,\text{olive oil}}$ (1:1 of methanol)	7.62×10^{-6}	1.46×10^{-5}	2.24×10^{-5}
$D_{O_3\,\text{used}\,oil}$ (1:3 of methanol)	1.41×10^{-5}	2.35×10^{-5}	3.57×10^{-5}

For the diffusion coefficients of ozone in olive oil, used cooking oil, and their mixtures, the results also listed in Table 4.2 show that the diffusion coefficients in all cases are observed to increase with increasing temperatures. The highest diffusion coefficient was noted in used cooking oil mixed with methanol (1.0:3.0), whereas the lowest diffusion coefficient was found in pure olive oil because the fluid viscosity of used cooking oil mixed with methanol is approximately 31 times lower than that of pure olive oil and 2.5 times lower than olive oil mixed with methanol (1.0:1.0). However, the diffusion coefficient of ozone is slightly lower than that of oxygen as a result of a higher molar volume of ozone at its normal boiling temperature (Chaix *et al.* 2014).

4.3 Experimental setup for inlet ozone concentration measurement

As discussed previously in Chapter 2 using Eq. 2-40, the inlet ozone concentration is also a crucial parameter that must be determined prior to the reaction rate constant calculation. In this section, the inlet ozone concentration from the ozone generator was measured off-line using the KI method (otherwise known as the iodometric method). The same set-up as for the kinetic experiments was used in this measurement. The equipment, preparation techniques, and methodologies are described in the following sub-sections (Rakness *et al.* 1996).

4.3.1 Equipment

1. The glass reactor designed in the previous chapter was used instead of a standard gas washing bottle, as suggested by Rakness and co-workers (Rakness *et al.* 1996).

2. All equipment must be resistant to ozone, i.e., tubing for connections with an ozone generator, glassware, and diffuser (Gottschalk *et al.* 2009).

3. A glass diffuser with a diameter of 2.2 cm (ROBU Glasfilter-Gerate GmbH, Grade P4) made from borosilicate glass 3.3 was used in this work. Rakness and co-workers recommended that use of the diffuser should be avoided to prevent ozone loss at the diffuser (Rakness *et al.* 1996). However, in this study, the glass diffuser was used to represent the actual ozone concentration at the diffuser outlet.

4.3.2 Reagent preparation

Potassium iodide (99%), Sodium trisulfate (99%), Sulfuric acid (98%), Zinc cholide (99%), Potassium dichromate (>99.5%) were purchased from Sigma-Aldrich.

1. Unbuffered KI: 20 g of potassium iodide (KI) was dissolved into 1 litre of distilled water.

2. Sulphuric acid 2N: 56 ml of concentrated sulphuric acid was mixed with 946 mL of distilled water.

3. Sodium thiosulphate ($Na_2S_2O_3$) 1 N: 250 g sodium thiosulphate was dissolved in 1 L of distilled water.

4. Zinc chlorine starch: 4 g of soluble starch was mixed with cold distilled water and dispersed as a thin starch paste into 100 mL of water containing 20 g of zinc chlorine. The solution was boiled until the volume decreased to 100 mL. The solution was diluted with distilled water to a total volume of 1 litre and mixed with 2 g of $ZnCl_2$.

5. Sodium thiosulphate ($Na_2S_2O_3$) 0.1 N: 100 ml of 1 N sodium thiosulphate was mixed into 900 ml of distilled water.

6. Potassium dichromate ($K_2Cr_2O_7$) 0.1 N: 4.904 g of potassium dichromate was dissolved in 1 L of distilled water.

7. Distilled water: Conductivity should be less than 10 micro-ohms/cm.

4.3.3 Methodology

1. Preparation of the standardisation titrant (0.1 N sodium thiosulphate): The reagents, which consist of 150 mL of distilled water, 1 mL of concentrated sulphuric acid, 20 mL of 0.1 N of potassium dichromate, and 2 g of KI, were mixed in a 250 mL Erlenmeyer flask for 6 minutes in a dark container. Sodium thiosulphate 0.1 N was used for titration until the yellow colour had nearly disappeared. One millilitre of the starch indicator solution was added, and titration was continued until the blue colour vanished. The normality of the $Na_2S_2O_3$ titrant = 2/$Na_2S_2O_3$.

2. A 50 ml Class A burette was filled with the 0.1 N sodium thiosulphate titrant.

3. A gas washing bottle was filled with unbuffered KI (400 mL).

4. A bubble flow of ozone from the plasma ozone generator (Adjustable OZ500 Ozone Generator, Dryden Aqua) was fed through the reactor with a flow rate of 0.1-0.2 L/min. Better accuracy is obtained if the ozone volume is at least 2 litres.

5. Immediately after the bubbling process was completed, 10 ml of the 2N sulphuric acid was quickly added.

6. The liquid was transferred from the reactor to a 1-litre Erlenmeyer flask.

7. The solution was titrated with 0.1 N of sodium thiosulphate until the solution turned pale yellow in colour.

8. An amount of 5 ml of the starch solution was added to the Erlenmeyer flask, and titration was continued until the blue colour disappeared.

9. The volume of the titrant used was recorded.

Calculation of ozone concentration

$$\text{Ozone concentration (mg/L)} = \frac{24 \times V_t \times N_t}{V} \tag{4-9}$$

In this case, V is volume of bubble, V_t is volume of sodium triosulfate used (mL), and N_t is normality of sodium triosulfate (mg/me). $N_t = 0.17$

4.3.4 Thermal ozone decomposition using COMSOL Reaction Engineering Lab

As discussed in Chapter 2, ozone decomposition depends strongly on the temperature as well as the composition of the gases (air). Therefore, the decomposition rate of ozone in the bubbles at different temperatures must be studied because the subsequent experiments were performed at various temperatures.

In this section, COMSOL Reaction Engineering Lab is used to model the effects of temperatures and composition of gases on the ozone decomposition at atmospheric pressure. The equation used for solution is based on the batch reactor, as shown in Eq. 4-10, because all gases are trapped in a bubble; therefore, it can be assumed as a batch system. The reaction rate constants of the thermal decomposition are summarised in Table 4.4. The initial volume percentages of O_3, O_2, N_2, Ar, and CO_2 in the bubbles are set at 0.1, 20.85, 78.08, 0.91, and 0.033, respectively.

$$\frac{dc_i}{dt} = r_i \qquad \left(i = O, O_2, O_3, N_2, Ar, and\, CO_2\right) \tag{4-10}$$

Table 4.3 Reaction rate constants for ozone decomposition with various gases

No.	Reaction	Reaction rate constant	Reference
1	$O_3+O_3 \underset{k_{-1}}{\overset{k_1}{\longleftrightarrow}} O_3+O_2+O$	$k_1 = 4.31\times10^{14}\exp(-11{,}161/T)$ $k_{-1} = 1.2\times10^{13}\exp(+976/T)$	1, 2
2	$O_3+O \underset{k_{-2}}{\overset{k_2}{\longleftrightarrow}} 2O_2$	$k_2 = 1.14\times10^{13}\exp(-2{,}300/T)$ $k_{-2} = 1.19\times10^{13}\exp(-50{,}600/T)$	1,2
3	$O+O+O_2 \underset{k_{-3}}{\overset{k_3}{\longleftrightarrow}} O_2+O_2$	$k_3 = 1.38\times10^{18}T^{-1}\exp(-171/T)$ $k_{-3} = 2.75\times10^{19}T^{-1}\exp(-59{,}732/T)$	2
4	$O_3+O_2 \underset{k_{-4}}{\overset{k_4}{\longleftrightarrow}} O_2+O_2+O$	$k_4 = 0.44k_1$ $k_{-4} = 0.44k_{-1}$	1,2
5	$O_3+O \underset{k_{-5}}{\overset{k_5}{\longleftrightarrow}} O+O_2+O$	$k_5 = 0.44k_1$ $k_{-5} = 0.44k_{-1}$	2
6	$O_3+N_2 \underset{k_{-6}}{\overset{k_6}{\longleftrightarrow}} N_2+O_2+O$	$k_6 = 0.41k_1$ $k_{-6} = 0.41k_{-1}$	1
7	$O_3+Ar \underset{k_{-7}}{\overset{k_7}{\longleftrightarrow}} Ar+O_2+O$	$k_7 = 0.34k_1$ $k_{-7} = 0.34k_{-1}$	1
8	$O_3+CO_2 \underset{k_{-8}}{\overset{k_8}{\longleftrightarrow}} CO_2+O_2+O$	$k_8 = 1.06k_1$ $k_{-8} = 1.06k_{-1}$	1
9	$O+O+O \underset{k_{-9}}{\overset{k_9}{\longleftrightarrow}} O+O_2$	$k_9 = 3.6k_3$ $k_{-9} = 3.6k_{-3}$	2
10	$O+O+O_3 \underset{k_{-10}}{\overset{k_{10}}{\longleftrightarrow}} O_3+O_2$	$k_{10} = k_3$ $k_{-10} = k_{-3}$	2
1= (Benson and Axworthy 1957), 2 = (Heimerl and Coffee 1980). The unit of the reaction rate constant of k_1, k_2, k_{-2}, and k_{-3} are cm^3/mol·s, while k_{-1} and k_3 are cm^6/mol^2·s.			

4.3.5 Results and discussion of inlet ozone concentration measurement

Three different ozone concentrations were used in this study and are listed in Table 4.4.

Table 4.4 Ozone concentrations by the KI method

Ozone levels	**Gas flow 0.1 L/min**			**Gas flow 0.2 L/min**		
	mg/L	mol/L	ppm	mg/L	mol/L	ppm
A1	5.87	1.22×10^{-4}	2935	3.26	6.79×10^{-5}	1630
A2	6.67	1.39×10^{-4}	3335	4.18	8.71×10^{-5}	2090
A3	8.87	1.85×10^{-4}	4435	5.63	1.17×10^{-4}	2815

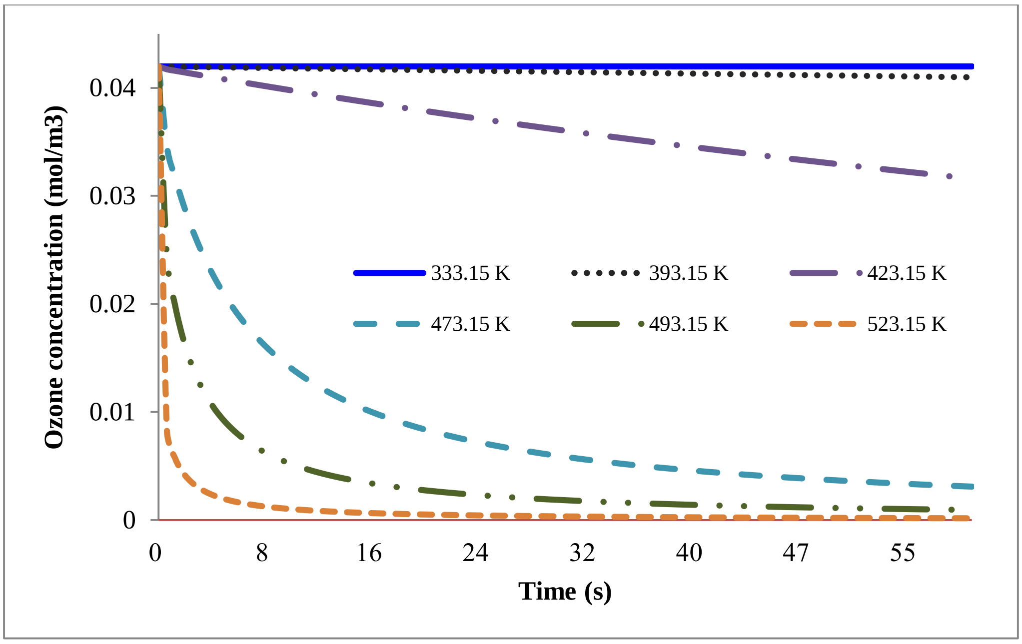

Figure 4.2 Thermal decomposition of ozone at different temperatures

For thermal decomposition of ozone, the simulation results show that the concentration of ozone at 60°C, which is the highest temperature employed in this study, appears to be constant during the studied time. Therefore, the effects of thermal decomposition of ozone at 20°C, 40°C, and 60°C are assumed to be negligible, which means that the inlet ozone concentration is constant during the reaction time. It can also be assumed that the loss of ozone is only caused by chemical reactions. In contrast, at high temperature, ozone decomposition is notably fast, as shown in Figure. 4.2. The half-lives of ozone are 2500 s and 0.5 s at temperatures of 120°C and 250°C, respectively. The rather high thermal decomposition rate was used to destroy excess ozone in the vent gas as a safety precaution (Gottschalk *et al.* 2009).

4.4 Specific interfacial area estimation

In addition to the Henry's Law constant, diffusion coefficient, and inlet ozone concentration, the specific interfacial area must be evaluated prior to calculation of the reaction rate constant. In this research, an optical method with a high-speed camera was used for bubble characterisation to determine the size distribution, gas holdup, and specific interfacial area, as described in Chapter 2.

4.4.1 Experimental setup for bubble characterisation

Measurement of the specific interfacial area poses the main difficulty in the kinetic study of the gas-liquid reactions, and this value is only obtained from experiments. In this research, a high-speed camera was used for bubble characterisation to determine the size distribution, gas holdup, and volume-surface mean bubble diameter. These parameters were subsequently used to determine the specific interfacial area. The experiment was performed in a clear glass reactor equipped with a sampling tube used as a referent scale as shown in Figure 4.3. It should be noted that for accuracy in measurement, the size of the referent scale should be the same as that of the bubbles. To generate the bubbles, two techniques were used in this study, i.e., with and without the FO. In the case of operation with the FO, dry air at 60 L/min, 20±1°C, and 15.1 psig was fed to the fluidic oscillator designed by Zimmerman and co-workers (2008) to generate a pulse-jet stream. Dry air at only 0.1 L/min was fed to the diffuser, and the remainder of the dry air (59.9 L/min) was purged. However, in the case of operation without the FO, dry air at 0.1 L/min and the same temperature and pressure as used with the FO was directly fed to the diffuser, and the purge valve was closed. The diffuser used in this measurement has a diameter of 2.2 cm (ROBU Glasfilter-Gerate GmbH, Grade P4) and is made from borosilicate glass 3.3.

The liquids (i.e., pure OL, OL mixed methanol, pure olive oil, olive oil mixed methanol, and used cooking oil mixed with methanol) were heated using a heating mantle connected to a temperature controller. The liquid temperatures were set to 20±1°C, 40±1°C, and 60±1°C. Bubble images were obtained from a high-speed camera (Photron SA-3) that is able to capture 2000 frames/second. Halogen lamps (Model no: HM-682C: 150 W Argos, UK) were used as a light source. It should be noted that the quality of the bubble images is primarily dependent on the light source such that the location of the lamps should be carefully considered; in this experiment, the appropriate location is behind the diffuser for clear images.

Taken pictures from the high speed camera were uploaded to ImageJ software. Although using this software is time consuming, it is free software to download. Before measuring the diameter of bubbles using ImageJ software, a reference scale, which is a sampling tube with diameter of 900 micron, was set. A number of bubbles (150-200bubbles) were selected in various locations and their diameters were measured.

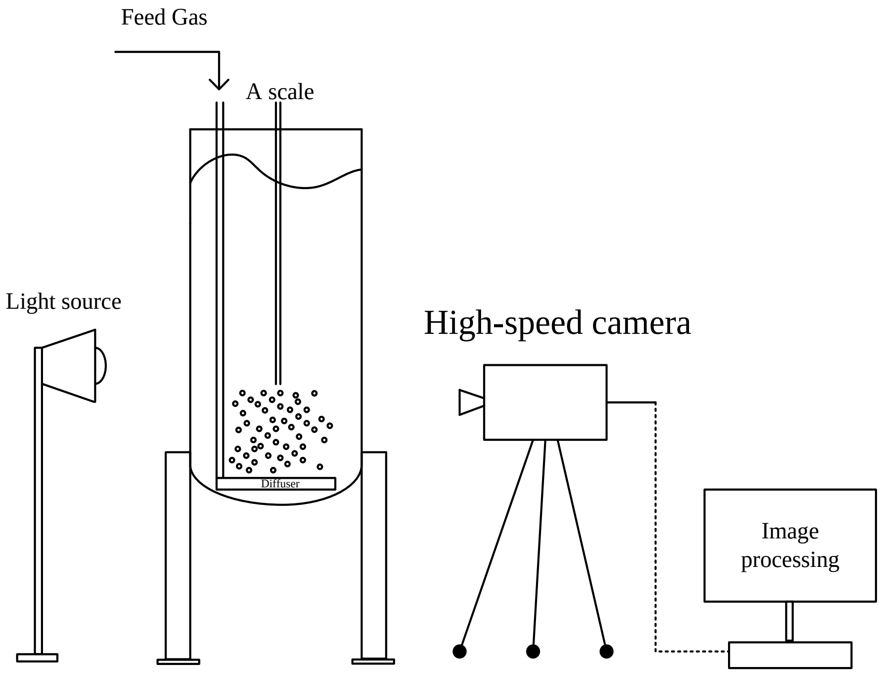

Figure 4.3 Experimental set up for bubble characterisation

The bubble size distribution, probability density function, gas holdup, and specific interfacial area were calculated. The calculation details described in Chapter 2 are presented in the following section.

4.4.2 Results and discussion of bubble characterisation

As shown in Figure 4.4, at identical air flow rate and temperature, a smaller bubble size was observed in water (as illustrated in Figure 4.4A), and a larger size was formed in OL (as shown Figure 4.4B), which has a higher fluid viscosity and lower fluid density. This result occurs because the bubble size always increases with decreasing liquid density as a result of low buoyancy force (Gerlach *et al.* 2007, Ma *et al.* 2012). However, in this case, the fluid viscosity exerts the main effect on the formation of the larger bubbles because the viscosity of OL is approximately 35 times higher than that of water. This observation is supported by Figure 4.5A, Figure 4.5C, and Figure 4.5E; the fluid density and surface tension of OL are quite similar except for the notably large difference in fluid viscosity. The fluid properties at different temperatures of 20°C, 40°C, and 60°C estimated by Aspen Plus are shown in Appendix B. For example, the viscosities of OL at 20°C, 40°C, and 60°C are 35.26 cP, 18.17 cP, and 10.32 cP, respectively. According to these figures at different operating temperatures, the bubble size decreases with decreasing fluid viscosity. Moreover, the smaller size was observed when the system was operated with the FO, as shown in Figure 4.5B, Figure 4.5D, and Figure 4.5F, which is the same trend in the system operated without the fluidic oscillator in that the bubble size decreases with increasing temperature.

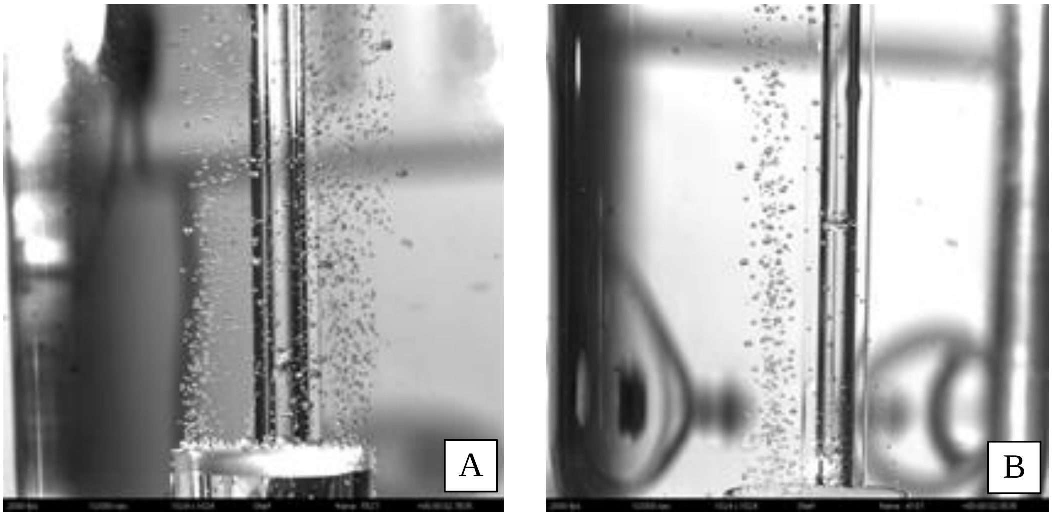

Figure 4.4 Photographs of microbubbles; A = Bubbles generated under water with FO. B = Bubbles generated under oleic acid with FO

After collecting photographs of the bubbles in the bubble column using the high-speed camera and analysis with ImageJ software, the bubble size distribution with and without the FO at an air flow of 0.1 L/min was plotted at 20°C, 40°C, and 60°C, as shown in Figure 4.6 (pure OL and OL mixed with methanol), Figure 4.7 (pure olive oil and olive oil mixed with methanol), and Figure 4.8 (used cooking oil mixed with methanol), respectively. The results show that the bubble size distribution without the FO appears as a normal size distribution, which is bell-shaped and symmetrically shaped, whereas the bubble size distribution with the FO appears as a left-skewed distribution. The narrower size distribution is also observed using the FO. This characteristic of the FO can be described using the log-normal size distribution, according to the experiment performed by Hanotu and co-workers (2012).

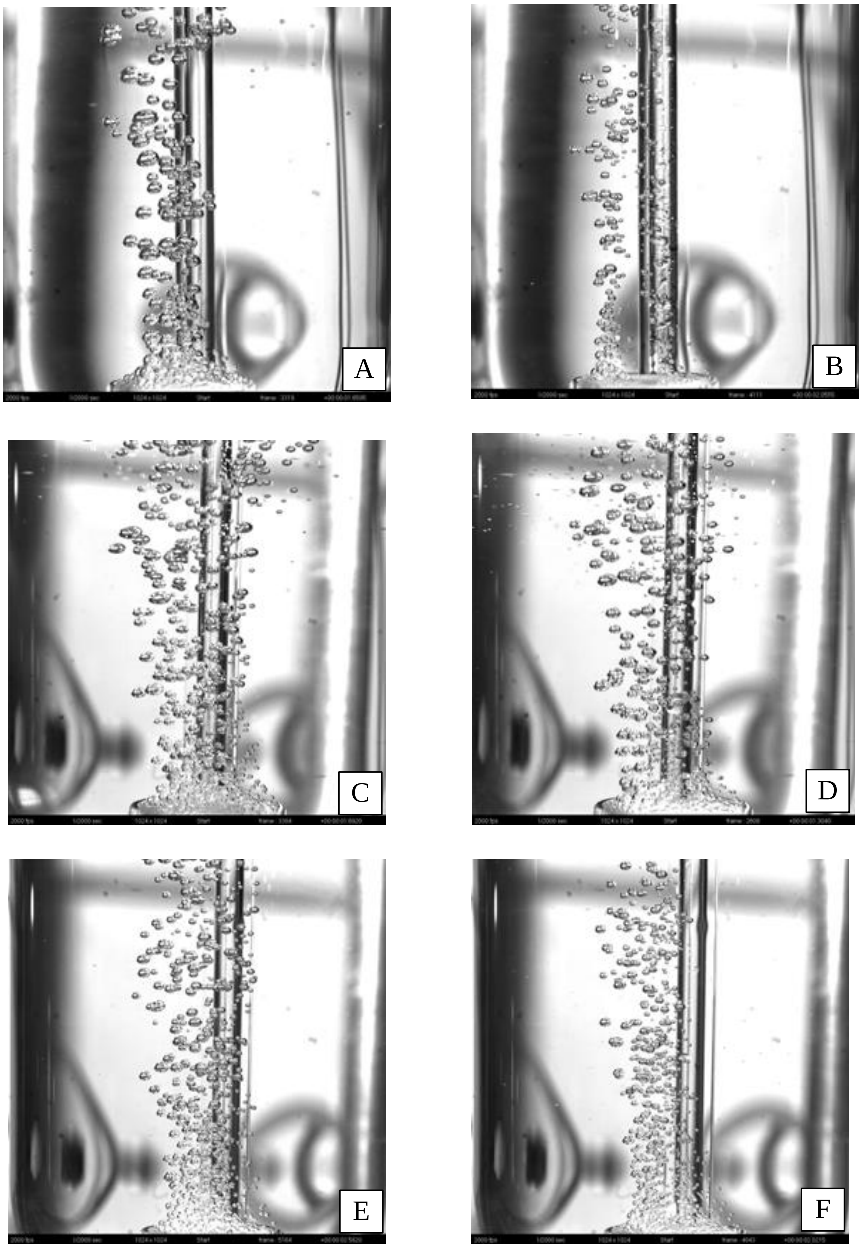

Figure 4.5 Images of the bubbles generated under OL with air flow 0.1 L/min; at 20^{o}C (A) without FO, (B) with FO, at 40^{o}C (C) without FO, (D) with FO, at 60^{o}C (E) without FO, (F) with FO

In addition to the difference in size distribution, at the same temperature, the bubble size of the system operated with the FO is smaller than that of the system operated without the FO as a result of the pulse-jet stream (Zimmerman *et al.* 2011b). Bubble size generally increases with decreasing buoyant force, which is primarily a function of liquid density. Although, in this experiment, the density of OL decreases slightly with increasing fluid temperature and results in the formation of larger bubbles, the observed bubble size decreases with increasing fluid temperature because of a sharp reduction in fluid viscosity (Gerlach *et al.* 2007, Ma *et al.* 2012). As listed in Table 6.2, the mean bubble sizes of pure OL without the FO at 20°C, 40°C, and 60°C are 1614 µm, 1388 µm, and 940 µm, respectively, whereas the mean bubble sizes with FO at 20°C, 40°C, and 60°C are 1000 µm, 760 µm, and 618 µm, respectively. The mean bubble sizes of OL mixed with methanol without the FO at 20°C, 40°C, and 60°C are 1320 µm, 1077 µm, and 818 µm, respectively, whereas the mean bubble sizes with the FO at 20°C, 40°C, and 60°C are 790 µm, 734 µm, and 491 µm, respectively.

In the system with pure olive oil, which has viscosity higher than OL, larger bubbles are formed, and the mean bubble sizes without the FO at 20°C, 40°C, and 60°C are 2596 µm, 2452 µm, and 1719 µm, respectively, whereas those with the FO at 20°C, 40°C, and 60°C are 2149 µm, 2082 µm, and 1296 µm, respectively. In the system of olive oil mixed with methanol, the mean bubble sizes without the FO at 20°C, 40°C, and 60°C are 2119 µm, 1819 µm, and 1307 µm, respectively, whereas those with the FO at 20°C, 40°C, and 60°C are 1647 µm, 1304 µm, and 1007 µm, respectively.

By varying the flow rate up to 0.3 L/min with the FO at 20°C, as shown in Figure 4.9, the bubble size increases with increasing air flow rate due to the increase of the outlet gas velocity at the diffuser (Ma *et al.* 2012). Although the system was operated with the FO, the bubble size distribution at high rates of air flow (0.20 L/min and 0.30 L/min) appears to be bell-shaped, whereas an air flow rate of 0.1 L/min still produces the left-skewed shape distribution. The average sizes of bubbles at 0.10 L/min, 0.15 L/min, 0.20 L/min, and 0.30 L/min are 999 µm, 1140 µm, 1647 µm, and 1819 µm, respectively. Thus, the optimum gas flow rate for the diffuser used in this study is 0.10 L/min because it produces a left-skewed shape distribution.

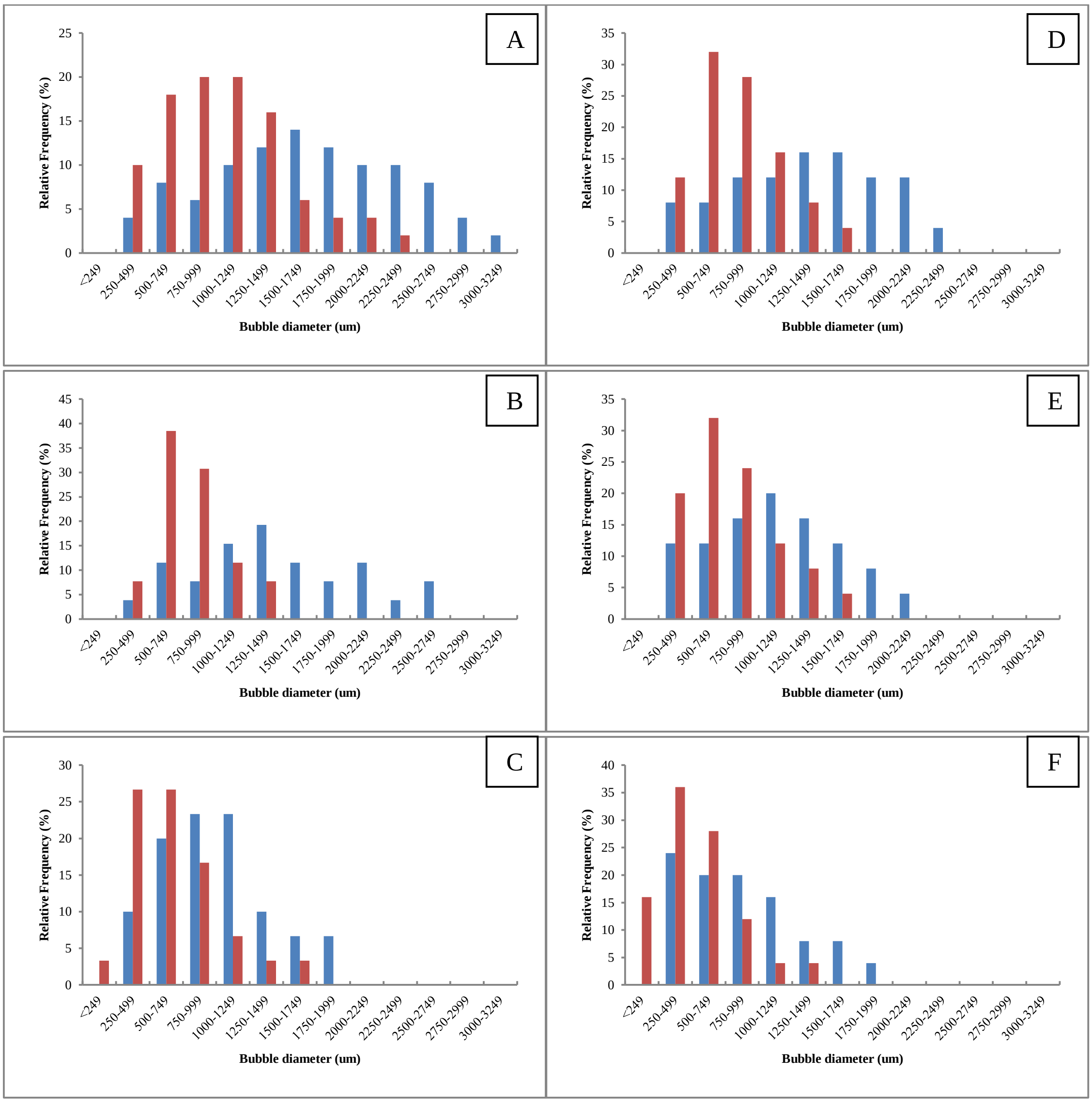

Figure 4.6 Bubble size distributions of air flow 0.1 L/min of OL and its mixture, at different fluid temperatures with FO (red) and without FO (blue): A, B and C are pure OL at 20^{o}C, 40^{o}C and 60^{o}C, respectively. D, E and F are OL mixed with methanol at 20^{o}C, 40^{o}C and 60^{o}C, respectively.

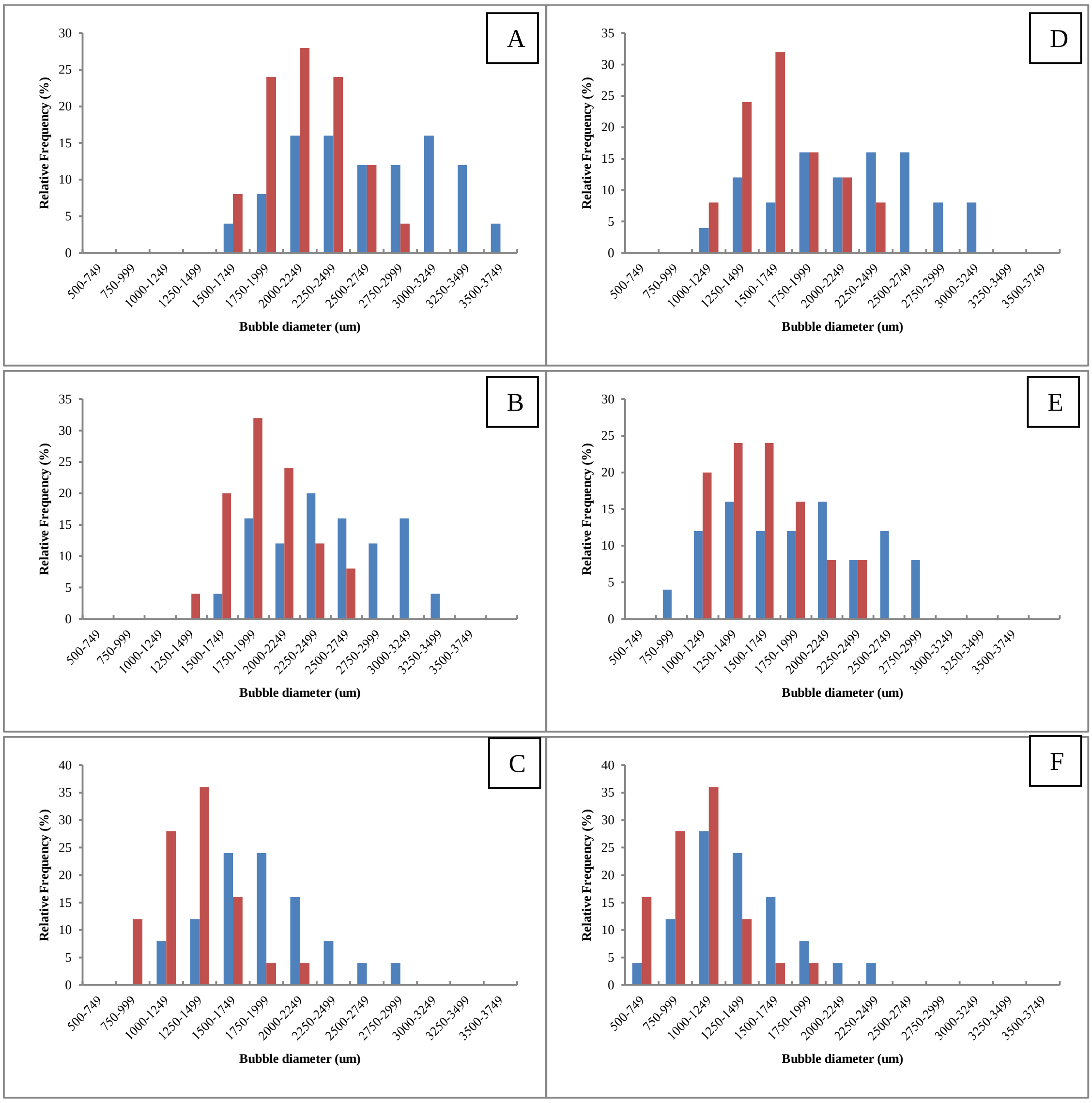

Figure 4.7 Bubble size distributions of air flow 0.1 L/min of olive oil and its mixture, at different fluid temperatures with FO (red) and without FO (blue): A, B and C are pure olive oil at 20°C, 40°C and 60°C, respectively. D, E and F are olive oil mixed with methanol at 20°C, 40°C and 60°C, respectively.

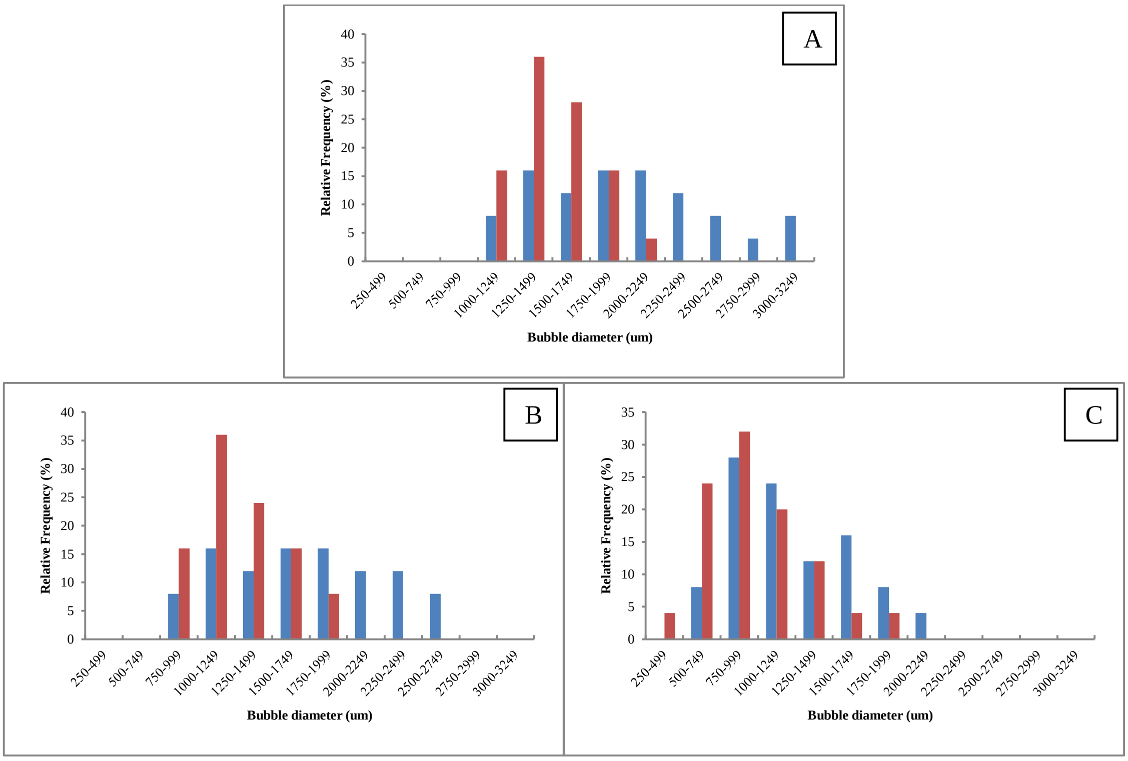

Figure 4.8 Bubble size distributions of air flow 0.1 L/min of used cooking oil and its mixture, at different fluid temperatures with FO (red) and without FO (blue): A, B and C are used cooking oil mixed with methanol at 20^{o}C, 40^{o}C and 60^{o}C, respectively.

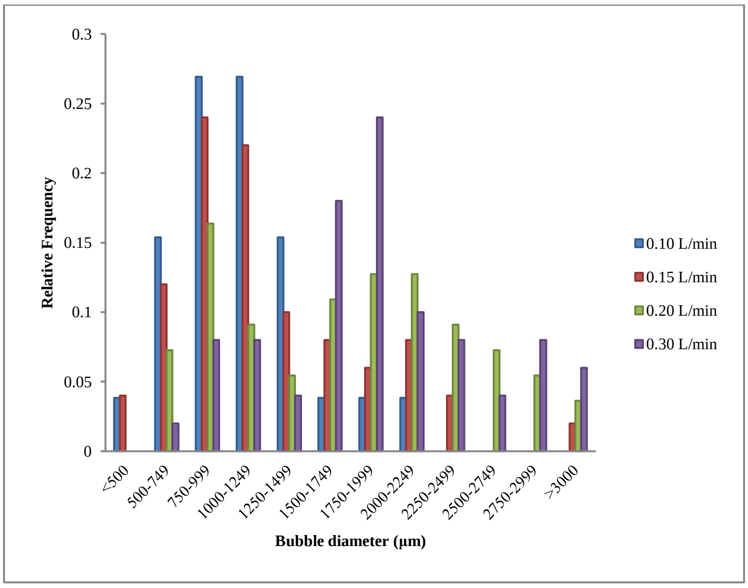

Figure 4.9 Bubble size distributions at different air flow rates, 20^{o}C, with FO

An example of the specific interfacial area calculation at 20°C and 0.1 L/min without the FO is shown in Table 4.5. The details in each column are described in Chapter 2. It should be noted that bubbles are assumed to be spherically shaped, although bubbles sizes over 2000 μm in diameter are ellipsoidally shaped based on Eq. 2-45, Eq. 2-46, and Figure 2.9.

Table 4.5 Example of bubble characterisation at 20°C, 0.1 L/min without FO

Range (μm)	x_i (μm)	No of bubble	$\Delta F_i \times 100$	$\Delta F \times 100$	$\Delta \mu_2'$, mm^2	$\Delta \mu_3'$, mm^2
<249	249	0	0	0	0	0
250-499	353.1997	6	4	4	4990	1762466.305
500-749	611.9641	12	8	12	29960	18334442.97
750-999	865.5923	12	8	20	59940	51883601.43
1000-1249	1117.587	15	10	30	124900	139586577
1250-1499	1368.85	18	12	42	224850	307785896
1500-1749	1619.722	21	14	56	367290	594907766.3
1750-1999	1870.361	15	10	66	349825	654299011.5
2000-2249	2120.849	15	10	76	449800	953957829.2
2250-2499	2371.234	15	10	86	562275	1333285516
2500-2749	2621.545	12	8	94	549800	1441325631
2750-2999	2871.803	6	4	98	329890	947378949.8
3000-3249	3122.019	3	2	100	194940	608606301.6
Σ		150	100	-	3248460	7053113990
a = $\pi \cdot N \cdot \int_0^1 x^n dF = 0.046\, cm^{-1}$						

The specific interfacial areas of bubbles in the reactor at different fluids and temperatures with and without the FO are shown in Table 4.6. For example, the specific interfacial areas of pure OL at 20°C, 40°C, and 60°C without the FO are 0.0468 cm^{-1}, 0.0513 cm^{-1}, and 0.0734, respectively, whereas those with the FO are 0.0709 cm^{-1}, 0.0753 cm^{-1}, and 0.1111, respectively. This result means that the specific interfacial areas increase by approximately 45% when the reactor is operated with the FO at an identical inlet gas flow rate. Therefore, based on Eq. 2-39, the reduction of both OL and olive oil during ozonolysis with the FO is faster than ozonolysis without the FO, resulting in more rapid formation of short-chain valuable products.

Table 4.6 Specific interfacial areas of bubbles at different temperatures of 0.1 L/min

Temperature (°C)	Mean diameter (μm)		Specific interfacial area (cm^{-1})	
	Without FO	With FO	Without FO	With FO
Pure OL				
20	1614	1000	0.0468	0.0709
40	1388	760	0.0513	0.0753
60	940	618	0.0734	0.1111
OL+ methanol				
20	1320	790	0.0504	0.0739
40	1077	734	0.0640	0.0920
60	818	491	0.0924	0.1350
Pure Olive oil				
20	2596	2149	0.0413	0.0595
40	2452	2082	0.0433	0.0642
60	1796	1296	0.0607	0.0892
Olive oil+ methanol				
20	2119	1647	0.0445	0.0652
40	1819	1304	0.0535	0.0763
60	1307	1007	0.0712	0.1028
Used Cooking oil+ methanol				
20	1936	1487	0.0460	0.0666
40	1666	1248	0.0572	0.0832
60	1166	916	0.0775	0.1128

4.5 Summary

Four essential parameters, i.e., the Henry's Law constant, diffusion coefficient, inlet ozone concentration, and specific interfacial area, were estimated and measured at different temperatures using both simulation and experimental techniques. The Henry's Law constant and the diffusion coefficient estimated by Aspen Plus are within the ranges of values reported in previous studies that used oxygen instead of ozone. Three different inlet ozone concentrations were selected for the reaction study, and thermal decomposition was negligible within the studied ranges. The specific interfacial areas at different temperatures and in fluid mixtures with and without the FO were estimated. All of these parameters are used for the reaction study in the following chapters.

CHAPTER 5

OZONOLYSIS OF OLEIC ACID

This chapter primarily considers a reaction study of the ozonolysis of OL. Section 5.1 describes the materials and methods used for the ozonolysis of OL, i.e., chemicals, experimental setup, and analytical techniques. Section 5.2 presents the experimental results and discussions of ozonolysis of pure OL and of mixed OL with alcohols as well as the reaction rate constant estimation. Section 5.3 provides a summary.

5.1 Materials and methods for ozonolysis of OL

5.1.1 Chemicals

Chemicals used in this chapter were obtained from Sigma-Aldrich: oleic acid (99%), oleic acid (technical grade), 1-nonanal (95%), nonanoic acid (99.5%), azelaic acid (98%), acetone (HPLC grade), methanol (HPLC grade), ethanol (HPLC grade), n-propanol (99.5%), iso-propanol (99.5%), butanol (99.8%), acetic acid (99.7%), methyl oleate (≥99%), methyl palmitate (≥99%), methyl nonanoate (≥99.8), methyl octanoate (99%), and sodium hydroxide (≥98%).

5.1.2 Experimental set up

To generate bubbles, two techniques were used in this study, i.e., with and without the FO. In case of FO use, dry air at 60 L/min, 20±1°C, and 15.1 psig was fed into the fluidic oscillator designed by Zimmerman and co-workers (2008) to a generate pulse-jet stream. Dry air at only 0.1 L/min was fed into a plasma ozone generator (Adjustable OZ500 Ozone Generator, Dryden Aqua), and the remainder of dry air (59.9 L/min) was purged. However, without use of the FO, dry air at 0.1 L/min with the same temperature and pressure as those with use of the FO was directly fed into the plasma ozone generator, and the purge valve was closed.

After passing through the ozone generator, mixtures of ozone and dry air were fed into a glass bubble reactor with a diameter of 7.5 mm filled with a total of 325 ml of solvents. The glass reactor was equipped with a diffuser with a diameter of 2.2 cm (ROBU Glasfilter-Gerate GmbH, Grade P4) made from borosilicate glass 3.3, a thermocouple, and a sampling tube. The heating mantle was connected to a temperature controller. Because of volatile products that are possibly formed during the reaction, especially NN, a glass condenser with a surface area greater than 200 cm^2 was used to condense all volatile products and recycle them to the reactor using water as a cooling medium. The surface area of the condenser was determined using Aspen Plus, as discussed in Chapter 3. The schematic of the experimental setup is shown in Figure 5.1. All tubing and connections were made of PTFE, glass or stainless steel for ozone resistance. It should be noted that the experiments were performed using different protic solvents and molar ratios, and the compositions of the solvents used in each batch are provided in Appendix B.

The experiments were conducted at 20±1°C, 40±1°C, and 60±1°C at atmospheric pressure and at three different ozone concentrations. Samples of 1 mL were collected every 4 hrs for 36 hrs and stored in a refrigerator (< 4°C) prior to further analysis via GC-MS.

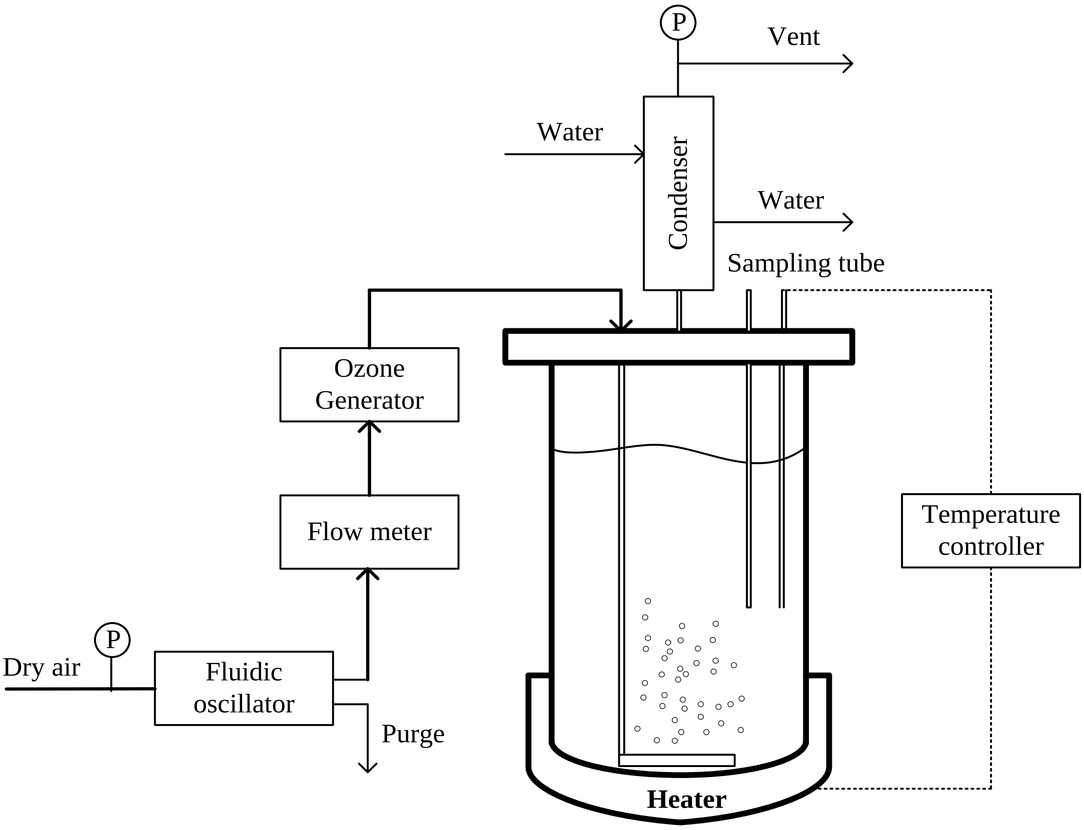

Figure 5.1 Schematic representation of an experimental unit

5.1.3 GC-MS analysis

Samples of 10 µL were dissolved in 1 mL of acetone with a volume ratio of 1:100 before qualitative and quantitative analysis. The GC-MS used in these experiments is an HP 6890 series equipped with an HP 5973 mass selective detector and a HP1 19091Z-433 column, and helium was used as a carrier gas. The injection volume was set to 0.2 µL with an auto-sampler, and the pressure was set to 54 kPa. The temperature program was isothermal at 60°C for 2 minutes, increased at 10°C/min up to 300°C, and was held at 300°C for 6 minutes.

5.2 Results and discussion

5.2.1 Ozonolysis pure OL

The chromatograms for ozonolysis of OL at 20°C for reaction times of 0, 16, and 32 hours are shown in Figure 5.2A, Figure 5.2B, and Figure 5.2C, respectively. At the beginning, two species of FFAs are observed, as shown in Figure 5.2A, i.e., palmitic acid (PA) at RT 16.0 min and OL at RT 17.8 min. These results occur because OL purchased from Sigma-Aldrich is a technical grade product with 90% OL. After blowing of ozone bubbles to react with OL, as shown in Figure 5.2B, two new species are observed, i.e., NN at RT 5.7 min and OA at RT 10.7 min, and the concentration of both species increases with increasing reaction time, as shown in Figure 5.2C, whereas the concentration of OL decreases. This observation proves that the decomposition of PO follows both pathways reviewed in Chapter 2 with 93.3±3.4% following pathway 1. Moreover, the concentration of PA remains constant, which means that PA might not react with ozone during the studied period.

It is interesting that no signs appear of CIs and their isomerisation products, i.e., OcA, AA, and NA are observed, although both NN and OA are formed. A possible explanation for this observation is that the CIs might react with other products or with themselves to form higher molecular weight products (HMWPs) that cannot be detected by GC-MS under the studied conditions. However, in this study, the formation of HMWPs can be simply proven by the increase of the fluid viscosity during the ozonolysis.

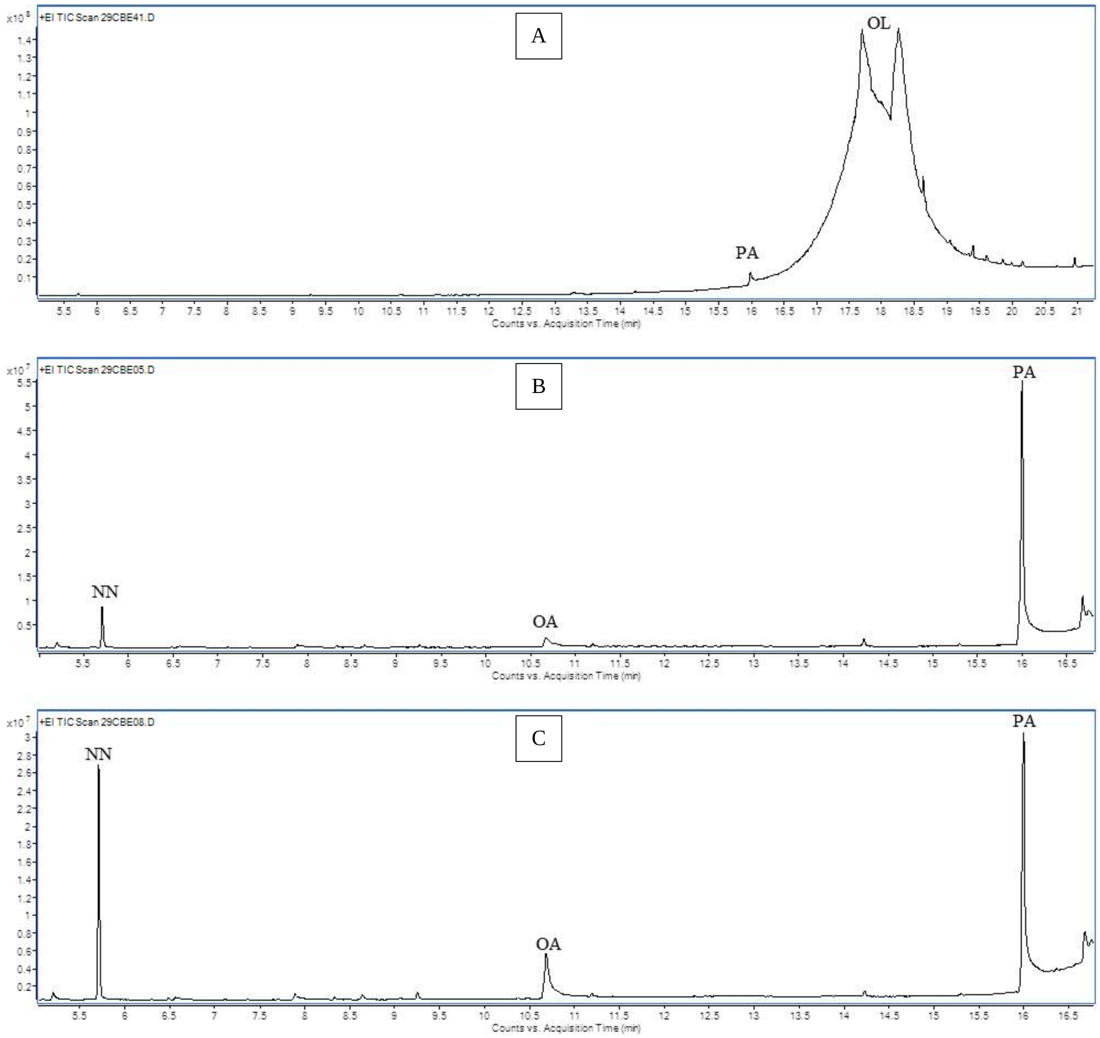

Figure 5.2 Ozonolysis of OL at 20^{o}C; 0 hr A), 16 hrs (B), and 32 hrs (C)

For the reaction at 40°C, the chromatograms at reaction times of 4, 16, and 32 hours are shown in Figure 5.3A, Figure 5.3B, and Figure 5.3C, respectively. Many unidentified products (UPs) are observed at RTs between 7.5 min and 9.5 min, and the amount of these species increases with increasing reaction time. The concentration of NN also increases with the reaction time, whereas the concentration of OA appears to remain constant. Similar to ozonolysis at 20°C, the concentration of PA remains constant.

Compared with ozonolysis at 20°C, the concentration of NN at 40°C increases by 30%, whereas the concentration of OA remains the same. This result demonstrates that the increase of NN and the formation of UPs are a result of the decomposition of HMWPs.

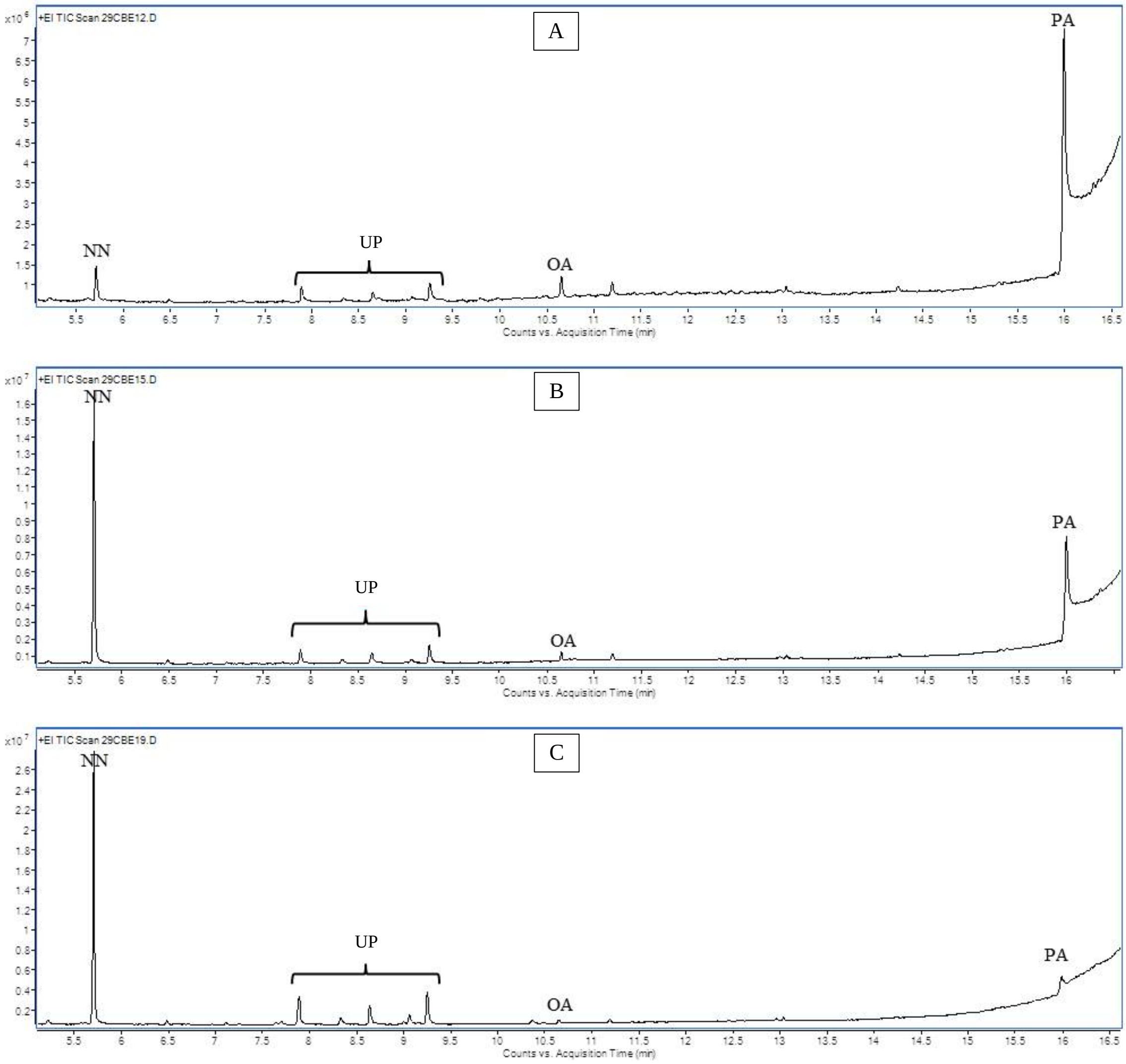

Figure 5.3 Ozonolysis of OL at 40^{o}C; 4 hr (A), 16 hrs (B), and 32 hrs (C)

The chromatograms of the reaction times of 4, 16, and 32 hours at 60°C are shown in Figure 5.4A, Figure 5.4B, and Figure 5.4C, respectively. Several UPs are found; in contrast with the reaction at 40°C, their retention times are between 3.9 min and 9.2 min, and their concentrations increase with reaction time. For the expected products, the concentrations of OA and AA (RT = 13.1) remain constant over the study period, whereas the concentration of NN increases. In addition, the amount of PA appears to remain constant, and its concentration is the same as that for ozonolysis at 20°C and 40°C. According to this result, no reactivity between PA and ozone can be assumed within the studied temperature range because the reaction rate of ozone and PA is notably low compared with that of OL.

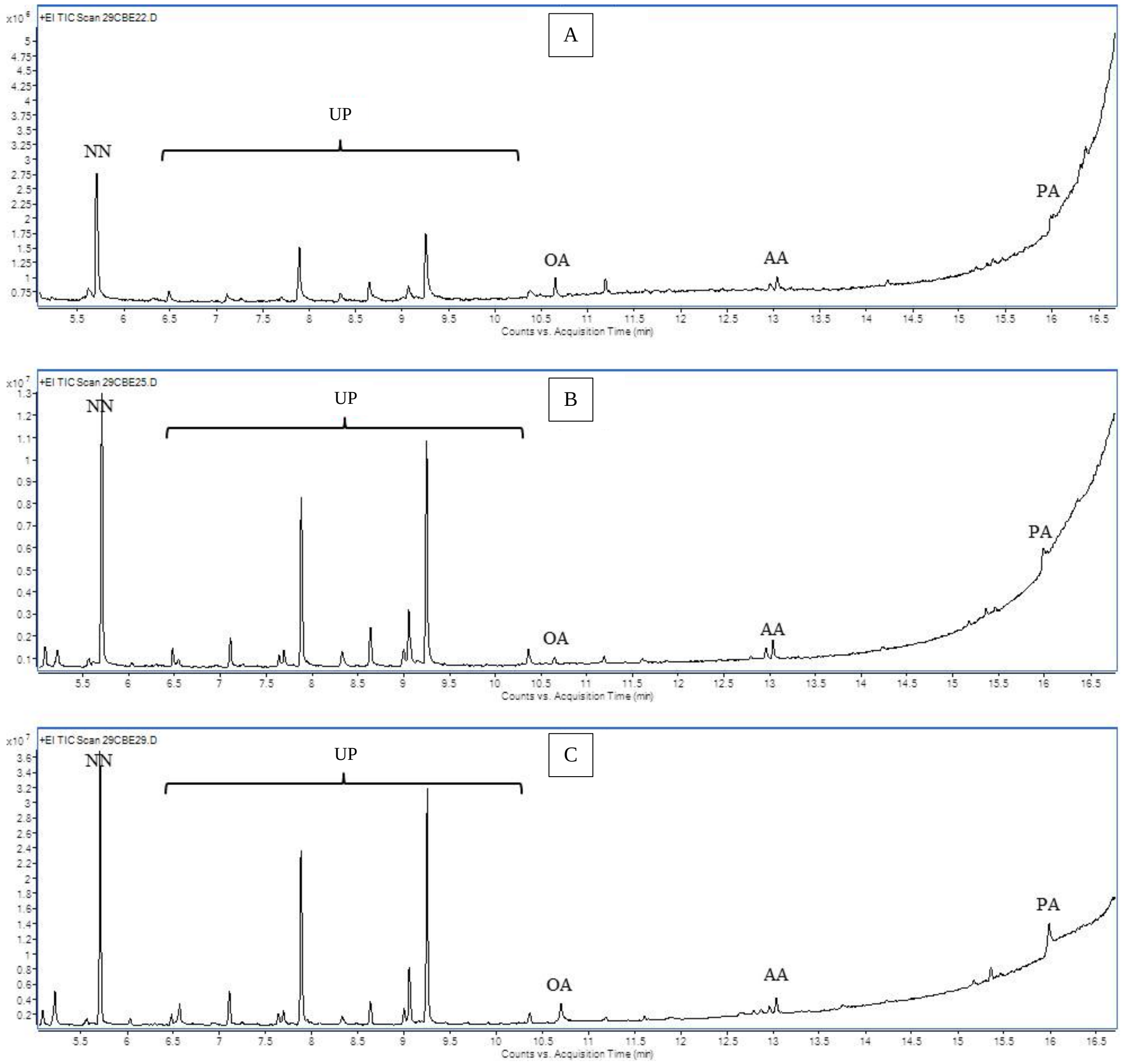

Figure 5.4 Ozonolysis of OL at 60°C; 4 hr (A), 16 hrs (B), and 32 hrs (C)

Several species are considered as unidentified products, as shown in Figure 5.3 and Figure 5.4. The word "unidentified products" means that their molecular structures and spectra are only predicted by GC-MS without calibration curve confirmation. The products found at RTs of 3.9, 4.2, 4.4, 5.1, 5.2, 6.5, 7.1, 7.9 and 9.2 min might be hexanoic acid ($C_6H_{12}O_2$), furan, 2 pentyl ($C_9H_{14}O$), octenol ($C_8H_{16}O$), 2-octenal ($C_8H_{14}O$), heptanoic acid ($C_7H_{14}O_2$), 2-nonenal ($C_9H_{16}O$), 1,9 nonanedial ($C_{10}H_{22}O_2$), cis-7-decen-1-al ($C_{10}H_{18}O$) and 10-undecenal ($C_{11}H_{20}O$), respectively. The results prove that these materials are products from the decomposition of HMWPs formed by the reactions among CI1, CI2 and other products because no peaks for CI1 and CI2 or their related products (i.e., OcA, AA, CHAP1, and

NA) are detected at low temperature, whereas a substantial amount of NN and a small amount of OA are observed.

Although many species are formed in the reactor during ozonolysis, OL is the only possible species that might react with both CI1 and CI2 because of a substantial amount of OL in the reactor compared with other materials. This observation leads to loss of OL over the stoichiometry ratio of 1:1 (Sage *et al.* 2009). Therefore, HMWPs might be formed by OL attacking the double bond reaction (Hung and Ariya 2007). These products decompose at elevated temperatures. Several possible reaction mechanisms based on the products are listed in Table 5.1. The enthalpy of formation and the free energy of formation of these products are estimated using Aspen Plus.

To verify the reactions listed in Table 5.1, Aspen Plus was applied using an equilibrium reactor. The simulation results are in good agreement with the experimental results in that most of the UPs are formed at high temperatures via thermal decomposition. The simulation results also show that a substantial amount of NN is formed during the decomposition via reactions 3, 9, and 10, which means that ozonolysis by one mole of ozone with OL can form more than one mole of NN. According to both the experimental and simulation results, one mole of fed ozone results in two moles of NN formation and two moles of OL loss. In other words, ozonolysis of one mole of OL can generate one mole of NN. This result illustrates an advantage of ozonolysis at high temperature because of the increase in productivity, especially for NN and 10-undecenal. Both of these materials are used in the food and perfume industries (Surburg *et al.* 2006).

However, continuous ozonolysis at high temperature over a long duration produces energy loss. To achieve the same result using low temperature ozonolysis, two-step processes are employed. The first step is ozonolysis at low temperature to obtain a substantial amount of NN and HMWPs. The second step creates decomposition of HMWPs at high temperatures to form the products listed in Table 5.1. Further study is necessary to find the optimum temperature and decomposition time.

As shown in Figure 5.2 through Figure 5.4, the concentration of NN increases with increasing fluid temperatures, which is in good agreement with the results provided by Moise and Rudich (2002) and Thornberry and Abbatt (2004). The concentration of NN increases by 100% with a 40°C increment. According to Eq. 2.39, the increase of NN is a function of several parameters, i.e., the specific interfacial area, Henry's Law constant, diffusion coefficient, and reaction rate constant. By substitution of the specific interfacial area, Henry's Law constant, and diffusion coefficient at different temperatures provided in Chapter 4 into Eq. 2.39 with the assumption of an identical inlet ozone concentration and reaction time, the value of ($aT\sqrt{D}/H$) increases by 31% from a reaction temperature of 20°C to 40°C and by 100% from reaction temperature of 20°C to 60°C. This observation may not confirm that the ozonolysis of OL appears to behave in an Arrhenius manner because the increase in $aT\sqrt{D}/H$ is similar to the increase of NN formation.

Table 5.1 Possible decomposition reaction of HMPWs

No.	**Reactions**	ΔH^o_{rxn} (kJ/mol) $\times10^2$	ΔG^o_{rxn} (kJ/mol) $\times10^2$
1	$C_{27}H_{50}O_6 \rightarrow C_9H_{16}O_3 + C_{11}H_{20}O + C_7H_{14}O_2$	-3.87	-6.145
2	$C_{27}H_{50}O_6 \rightarrow C_9H_{16}O_3 + C_{10}H_{18}O + C_8H_{16}O_2$	-4.03	-6.217
3	$C_{27}H_{50}O_6 \rightarrow C_9H_{18}O + C_{10}H_{18}O + C_7H_{14}O_2 + CO_2$	-4.14	-6.627
4	$C_{27}H_{50}O_6 \rightarrow C_{10}H_{16}O + C_{11}H_{20}O + C_6H_{12}O_2 + H_2 + O_2$	1.48	-1.365
5	$C_{27}H_{50}O_6 \rightarrow C_9H_{16}O + C_{11}H_{20}O + C_7H_{14}O_2 + O_2$	0.93	-1.701
6	$C_{27}H_{50}O_6 \rightarrow C_9H_{14}O + C_{11}H_{20}O + C_7H_{14}O_2 + H_2 + O_2$	0.35	-2.362
7	$C_{27}H_{50}O_6 \rightarrow C_8H_{16}O + C_{11}H_{20}O + C_7H_{14}O_2 + CO_2$	-0.14	-2.655
8	$C_{27}H_{50}O_6 \rightarrow C_8H_{14}O + C_{11}H_{20}O + C_8H_{16}O_2 + O_2$	0.71	-1.856
9	$C_{27}H_{52}O_4 \rightarrow C_9H_{18}O + C_{11}H_{20}O + C_7H_{14}O_2$	-15.11	-6.815
10	$C_{27}H_{52}O_4 \rightarrow C_9H_{18}O + C_{10}H_{18}O + C_8H_{16}O_2$	-15.27	-6.887
11	$C_{27}H_{52}O_4 \rightarrow C_9H_{16}O + C_{10}H_{22}O_2 + C_8H_{14}O$	-13.81	-5.157

5.2.2 Ozonolysis of OL and alcohols

As discussed, the formation of HMWPs results in the loss of OL. Although certain lower molecular weight products (i.e., NN, OA, OcA, and HeA) are formed to increase productivity, the reaction must be performed at high temperature for higher molecular weight product decomposition. To increase the productivity at low temperature, short-chain alcohols are mixed with OL before starting the reaction. The chromatograms of OL ozonolysis at 20°C for 32 hours with methanol, ethanol, n-propanol, iso-propanol, and n-butanol are shown in Figure 5.5A, Figure 5.5B, Figure 5.5C, Figure 5.5D, and Figure 5.5E, respectively. It is interesting to note that not only NN but also many ester species are found after the reaction, depending on the molecular structure of the alcohols. For example, mixing with methanol produces NN, octanoic acid, methyl ester (M-OcA), nonanoic acid, methyl ester (M-NA), nonanal dimethyl acetal (DM-NN), 9-oxononanoic acid, methyl ester (M-OA), azelaic acid, dimethyl ester (DM-AA), 2-Octanol, 8, 8-dimethoxy (DM-2OcA), palmitic acid, methyl ester (M-PA), and heptadecanoic acid, methyl ester (M-HA). Both NN and DM-NN are considered to be major products and can be used as flavouring and fragrance agents in the perfume and food industries (Surburg *et al.* 2006, Waddell *et al.* 2007). The possible reaction mechanisms of the observed products are described below.

In addition to methanol, ozonolysis of ethanol and OL is studied under the same conditions as with methanol, and production of NN, octanoic acid, ethyl ester (E-OcA,), nonanoic acid, ethyl ester (E-NA), nonanal diethyl acetal (DE-NN), 9-oxononanoic acid, ethyl ester (E-OA), azelaic acid, diethyl ester (DE-AA), 2-octanol, nonane, 1, 1-diethoxy (DE-NA), palmitic acid, ethyl ester (E-PA), and heptadecanoic acid, ethyl ester (E-HA) is observed. The formation of propyl ester, isopropyl ester and butyl ester (all carboxylic acids) are also observed by ozonolysis with n-propanol, iso-propanol or n-butanol, respectively.

According to the chromatograms shown in Figure 5.5, the greatest amount of NN is produced by ozonolysis of OL with methanol, and the remainder represents a slightly greater amount compared with that of pure OL ozonolysis. No sign of OA, which was observed at 20°C for 32 hours of reaction, is detected in mixing with alcohols because OA reacts with alcohols to form alkyl esters. All of the carboxylic acids found during ozonolysis of OL and FFAs (PA and HA) also react with alcohols to form alkyl esters. This result is quite surprising because these reactions usually occur when the reaction is performed in the presence of an acid catalyst (i.e., H_2SO_4, and HCl) at reaction temperatures between 40°C and 80°C, as used in the biodiesel production to reduce free fatty acid content.

Based on the results discussed above, ozonolysis of non-edible oils or used cooking oils mixed with alcohols might offer a new alternative technique for biodiesel production because non-edible oils or used cooking oils contain a substantial amount of FFAs that react with an alkaline catalyst (i.e., NaOH) to form soaps, resulting in difficult separation processes and decreased conversion rates (Canakci and Van Gerpen 2001, Balat 2011, Biermann *et al.* 2011, Hayyan *et al.* 2011).

There are many advantages to ozonolysis of used cooking oils or non-edible oils mixed with alcohols in the pre-treatment process for biodiesel production. For example, a substantial amount of NN might be formed if OL is the major species of free fatty acid. The NN can be simply separated due to its lowest boiling point. The reactions take place at atmospheric pressure and room temperature and without the use of acid catalysts, resulting in reductions in the use of energy, waste-water treatment, and acid-resistant materials in the piping system. Moreover, the alkyl esters of OcA, NA, AA, and OA can be separated for sale as valuable products and can be directly blended with long-chain alkyl esters to reduce the viscosity of biodiesel.

As also shown in Figure 5.5A through Figure 5.5E, methanol is a suitable protic solvent for mixing with OL to increase productivity because the highest concentration of NN is observed. Several advantages can be gained from using methanol. The first advantage is that methanol loss as a result of oxidation by ozone is quite low compared with other alcohols because of methanol’s lesser reactivity with ozone. The second reason is that the diffusion coefficient and the Henry’s Law constant for OL mixed with methanol are higher than those of the other mixtures, as listed in Appendix B, thus resulting in faster formation of NN. The last reason is that the viscosity of OL mixed with methanol is lower than that of the other mixtures, leading to the formation of smaller bubbles (increase in the specific interfacial area). Therefore, methanol is the selected protic solvent used in this study. However, the only disadvantage to use of methanol is its low boiling point because substantial amounts of methanol might evaporate during ozonolysis.

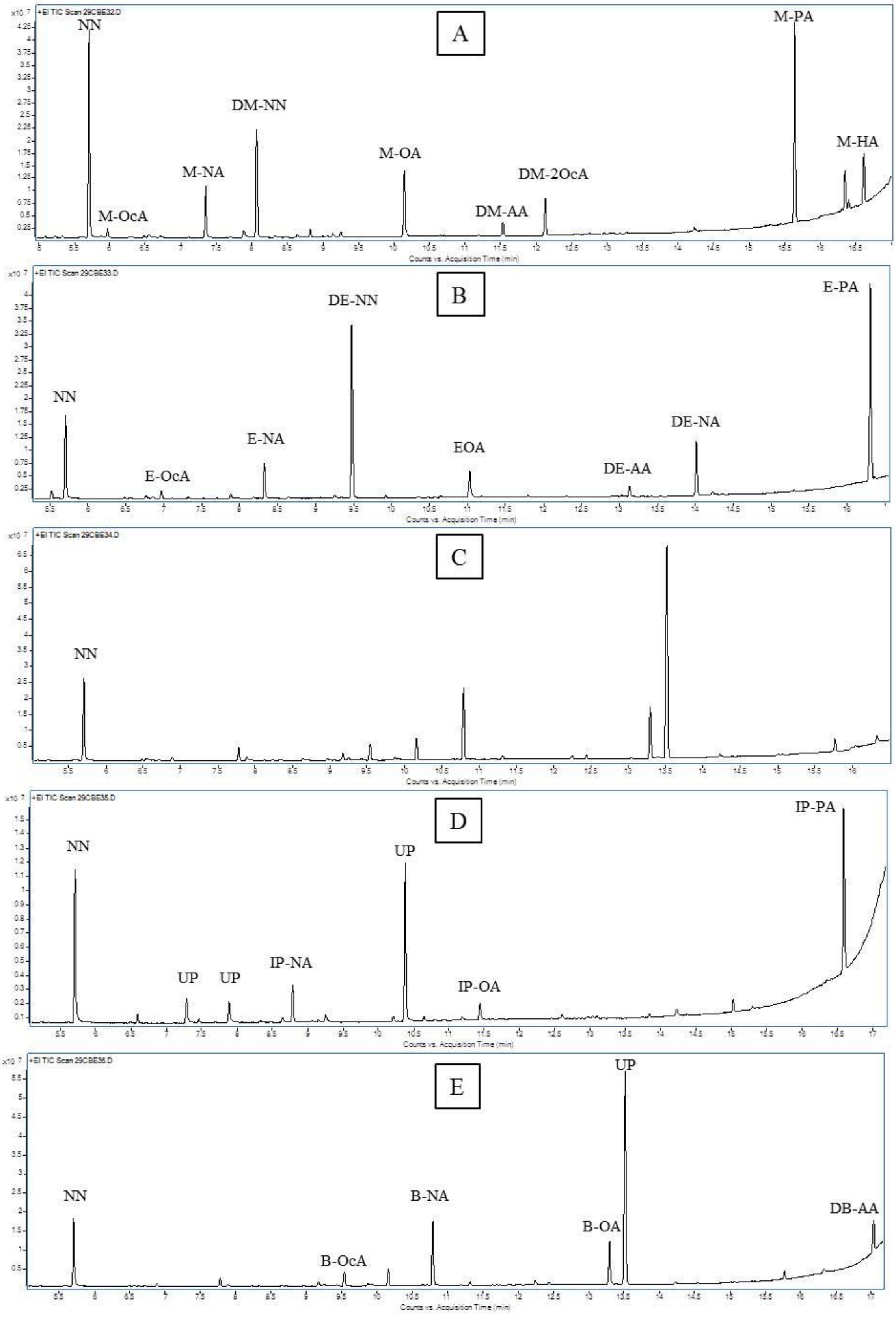

Figure 5.5 Ozonolysis of OL with alcohols (with 1:1 of molar ratio) at 20°C, 32 hrs; methanol (A), ethanol (B), n-propanol (C), iso-propanol (D), and n-butanol (E)

As discussed, methanol is the selected protic solvent used in this study. Therefore, several different molar ratios were investigated, i.e., 0.5:1.0, 0.75:1.0, 1.0:1.0, 1.5: 1.0, and 2.0:1.0, to find the optimum molar ratio between methanol and OL in terms of NN formation. As shown in Figure 5.6, the concentration of NN increases dramatically until the molar ratio is equal to 1.0:1.0 and subsequently increases slightly until the molar ratio is equal to 2.0:1.0. Theoretically, the concentration of NN should increase slightly as a result of steady increase in the Henry's Law constant, diffusion coefficient, and specific interfacial area. The reason for the sharp increase of NN at low molar ratio is that all methanol molecules might react with the CIs or other carboxylic acids to form methyl esters. Thus, in the absence of methanol, the fluid viscosity increases dramatically because of the formation of higher molecular weight products. The increase of fluid viscosity results in decreases in the specific interfacial area, Henry's Law constant and diffusion coefficient, which all affect the formation of NN.

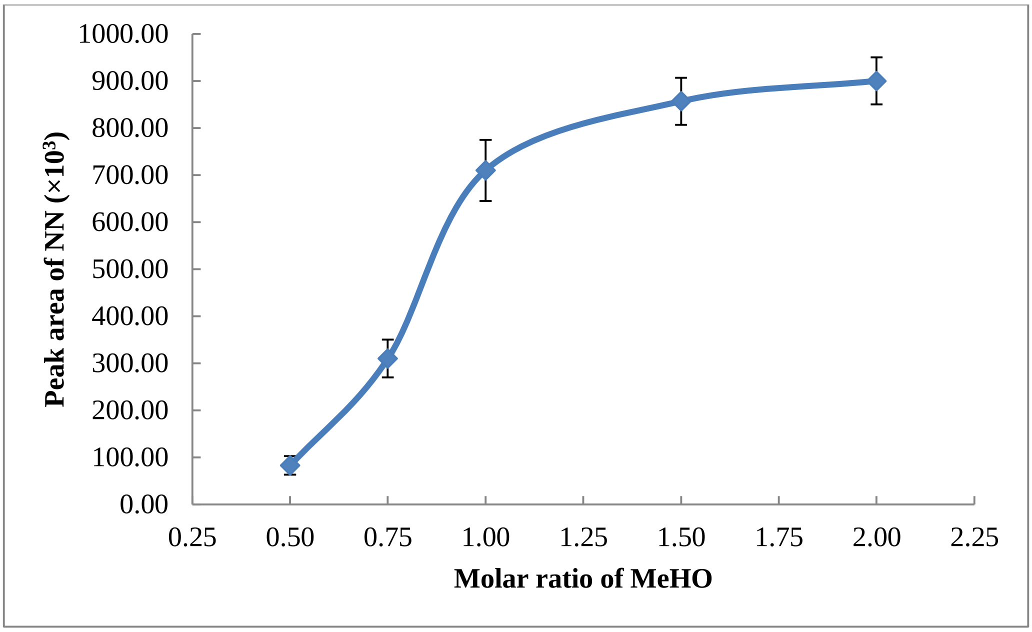

Figure 5.6 Optimum molar ratio of methanol:OL

At a molar ratio of methanol that exceeds 1:1, an amount of methanol molecules still remain in the reactor, leading to slight decreases of the specific interfacial area, Henry's Law constant and diffusion coefficient and a slight increase of NN. Therefore, the optimum molar ratio for methanol and OL in this thesis is 1.0:1.0. This molar ratio is also used to study the different reaction temperatures. It should be noted that an excess molar ratio might be required for commercial production because a small amount of ozone is fed through the reactor in this study, which results in an amount of remaining methanol in the reactor.

In considering the effect of methanol on the formation of NN, the formation of NN increases by 45% when methanol (1:1) is added. However, based on Eq. 2-49, the increase of NN might be due to the increase of the specific interfacial area, the Henry’s law constant, and the diffusion coefficient. This result proves that no reactivity between CIs and NN occurs because all of the CIs react with methanol to form DM-AA and M-NA.

As discussed, ozonolysis of OL mixed with methanol at a molar ratio of 1.0:1.0 is the optimum point, and thus, this ratio was used for study at 40°C and 60°C. As illustrated in Figure 5.7, the concentration of OL decreases with increasing reaction time, but oleic acid methyl ester (M-OL) increases at all reaction temperatures. Although the experiment was conducted for 32 hours, a small amount of M-OL is detected at a reaction temperature of 20°C, as shown in Figure 5.7A, because the reaction rates the esterification reaction and oxidation reaction are possibly the same at low temperature, resulting in the simultaneous formation of M-OL and any short-chain products.

At a reaction temperature of 40°C, a larger amount of M-OL is observed compared with that at a reaction temperature of 20°C, as shown in Figure 5.7B and Figure 5.7C. In addition, a small amount of OL is observed after 8 hours of ozonolysis at 60°C, whereas a large amount of M-OL is observed, which means that most of the OL is converted to M-OL before conversion to NN and short-chain products.

However, it is interesting to note that M-OL still increases with increasing reaction time, as shown in Figure 5.7D through Figure 5.7G. Normally, this amount should theoretically decrease because M-OL must be oxidised by ozone at the double bond position to form the products by following the reaction pathway shown in Chapter 2 (Mochida *et al.* 2006, Pfrang *et al.* 2014). According to these results, certain unknown higher molecular weight products might be formed that cannot be detected by the GC-MS under the conditions described in Section 5.3; these unknown products are formed during ozonolysis and might decompose to form M-OL. Moreover, addition of methanol can convert most of the saturated free fatty acids to methyl esters because no peaks of saturated free fatty acids, i.e., OA, PA, and HA, are observed in Figure 5.7.

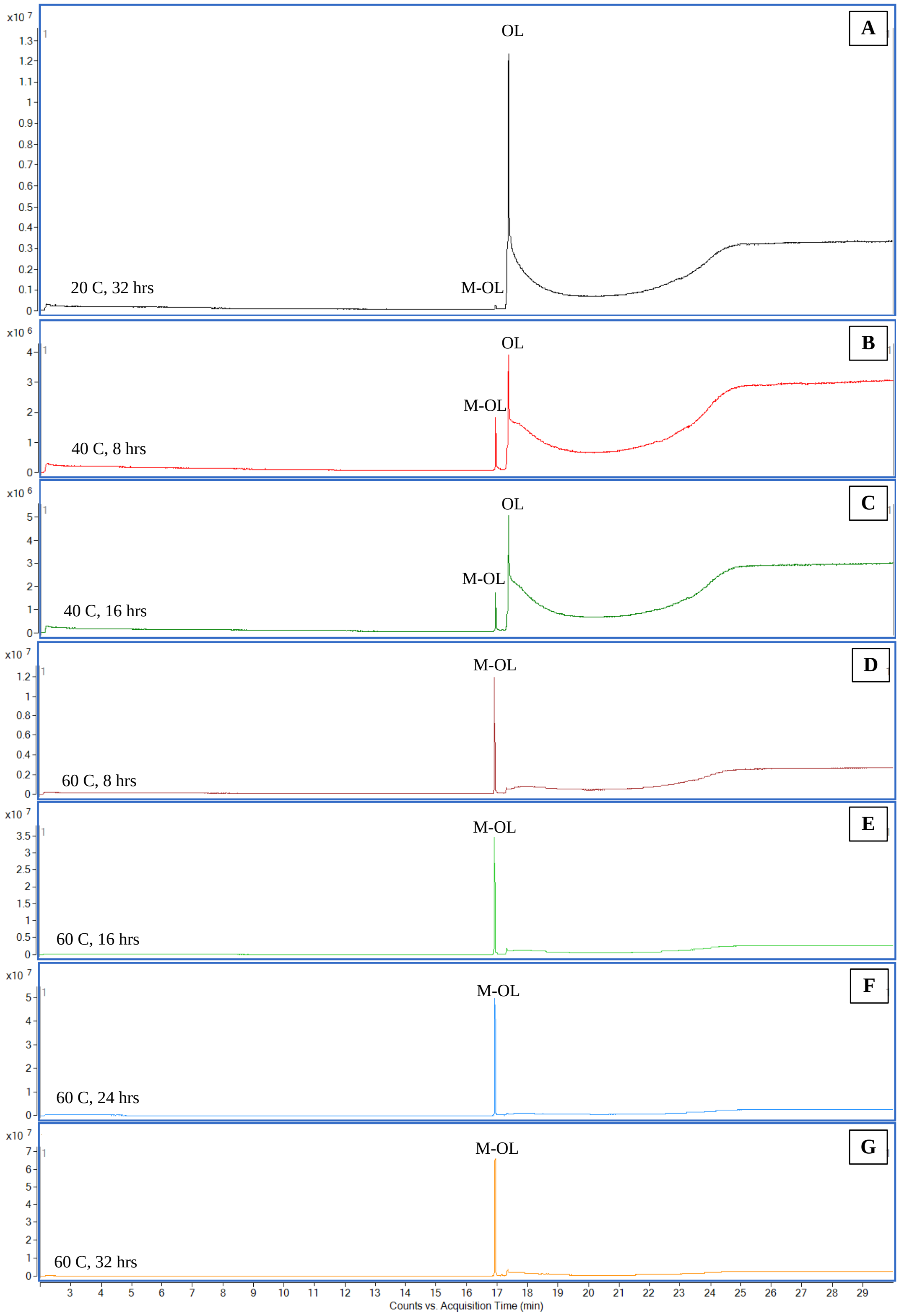

Figure 5.7 Ozonolysis of OL with methanol (1:1) at different reaction times and temperatures

Reaction mechanism of OL and alcohol ozonolysis

As proposed by Criegee (1975), methoxyhydroperoxide (MHP) is formed after ozonolysis of the mixture between alkenes and methanol. Therefore, this species might be formed during ozonolysis of OL mixed with methanol and subsequently decompose into methyl esters and water. This assumption can be used to describe only the formation of M-NA. For the formation of DM-AA, the reaction mechanism is similar to the formation of M-NA at the first stage in that the CI1 reacts with methanol to form MHP and subsequently decomposes to azelaic acid methyl ester (M-AA). The second stage involves the esterification of M-AA to form DM-AA and water. However, the reaction mechanism of this stage is unclear. Moreover, all species ending with a carboxylic acid group (i.e., palmitic acid and hexanoic acid) convert to methyl esters. It should be noted that the formation of esters depends on the solvents. For example, if ethanol is used as the solvent, ethyl ester is formed.

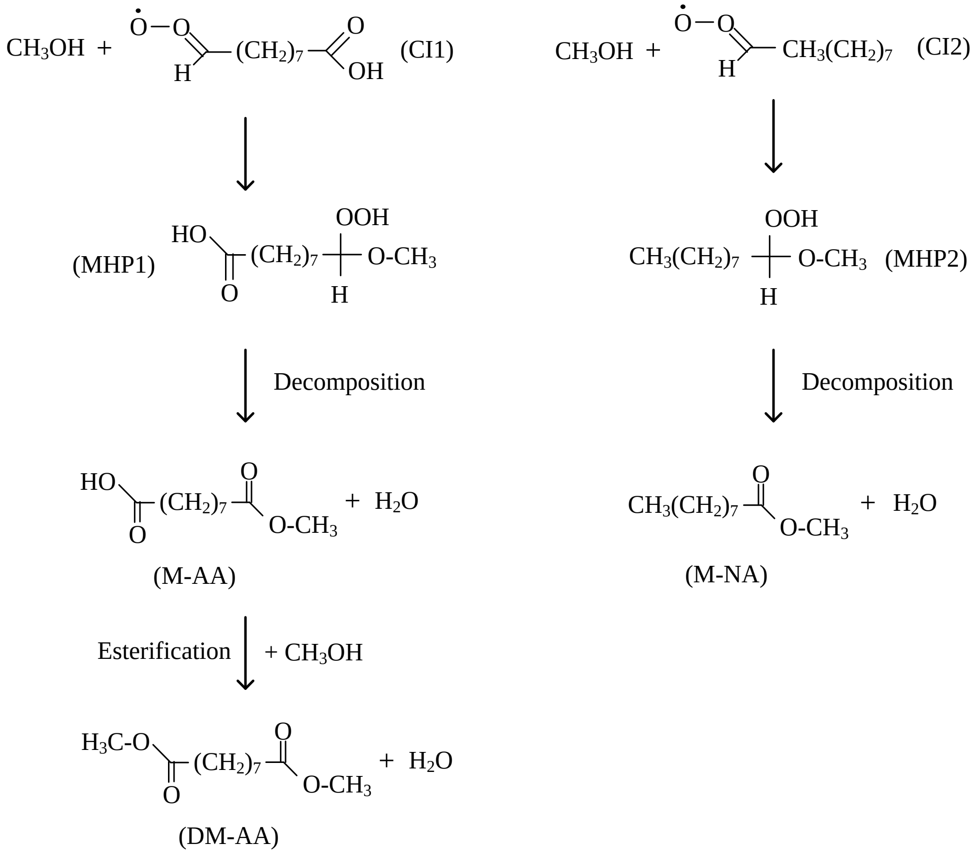

Figure 5.8 Possible reactions of ester formation

In addition to the formation of methyl esters, a substantial amount of DM-NN was observed. The reaction mechanism is still unclear, and hence, further study is required.

5.2.3 Ozonolysis of OL and methanol using FO

This section presents the results of the ozonolysis of OL and methanol with and without the FO at 20°C. The concentration of NN is used to represent the effect of the FO instead of the concentration of OL. As shown in Figure 5.9, the concentration of NN in operation with the FO is higher than that without the FO. The concentration of NN increases by 27%, 31%, 29%, and 28% at reaction times of 4, 8, 12, and 16 hours, respectively. Using the same conditions (fluid composition, temperature, and gas flowrate), the specific interfacial area increases by 45% if the experiment is performed with the FO, as discussed in Chapter 5. Although the increase of NN is slightly lower than the increase of the specific interfacial area, it can be confirmed that the formation of NN is a function of the specific interfacial area, which means that the reaction rate of ozonolysis of OL is a function of the specific interfacial area according to Eq. 2-39.

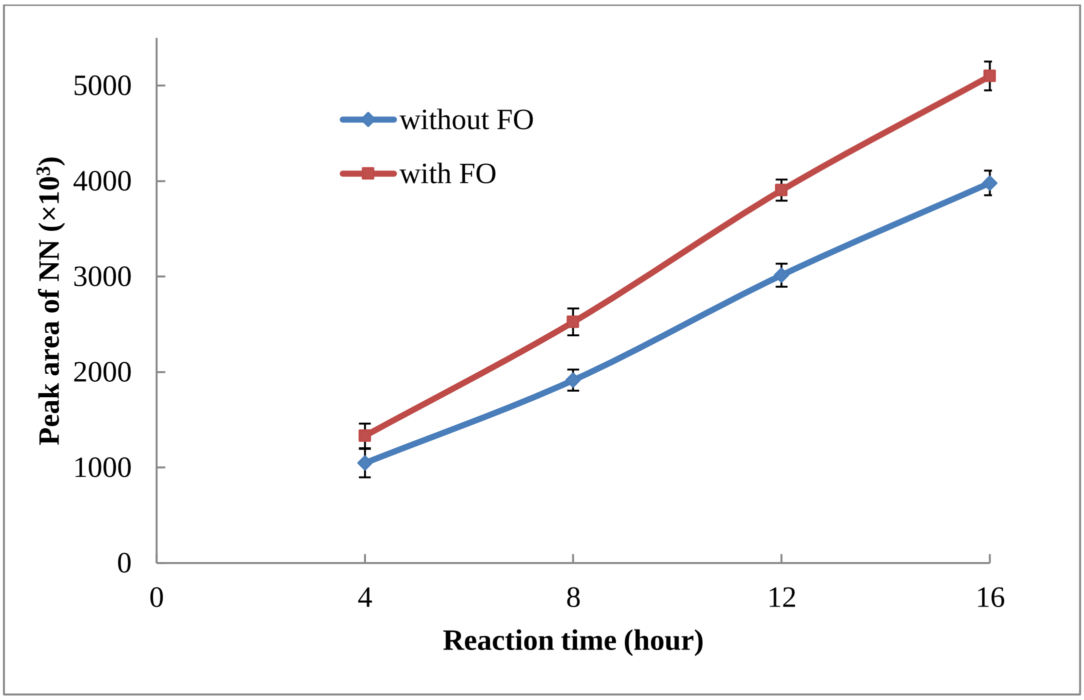

Figure 5.9 Ozonolysis of OL and methanol with and without FO

Therefore, the result proves that use of the FO is an effective technique for commercial ozonolysis. However, the use of the FO is not suggested for laboratory scale processes (< 60 L/min) using expensive gases because a substantial amount of these gases must be purged.

5.2.4 Reaction rate constant calculation of ozonolysis of pure OL

In this section, the reaction rate constant of ozonolysis of OL is calculated using Eq. 2-39 and can also be used to estimate the reaction rate constant of ozonolysis of mixed OL with alcohols, although the loss of OL is due to the esterification reaction. It should be noted that the reaction rate constants of both ozonolysis of pure OL and mixed OL with alcohol are the same.

To determine the reaction rate constant, the square root of the reduction of OL must be plotted. Polymath software is then used to estimate the slope of the graph. However, in this study, the used ozone concentration is quite low, resulting in difficulty for measurement of the reduction of OL. Therefore, the square root of the reduction of OL is plotted using the correlation between OL loss and NN formation with several provided assumptions:

1. No NN losses occur from the secondary reactions or evaporation.

2. All of the ozone reacts with OL.

3. There are no effects from impurities (PA and HA).

4. The Henry's Law constant, diffusion coefficient, inlet ozone concentration, and specific interfacial area are all constant.

As shown in Figure 5.10, linear reductions of square roots of OL at 20°C are observed at different inlet ozone concentrations because the inlet ozone concentration used in this study is quite low compared with OL. Moreover, the concentration of NN increases proportionally with the increase in ozone concentration. Referring to Eq. 2-12, this observation can prove that ozonolysis is a pseudo-first-order reaction. Moreover, by plotting the square root of the reduction of OL, straight lines are observed. The slopes of the A1, A2, and A3 lines are -3.16×10^{-8}, -4.17×10^{-8}, and -5.34×10^{-8}, respectively. The reaction rate constant can be calculated using Eq. 2-39 and all parameters provided in Chapter 4, and its value is 9.19×10^{5} $M^{-1}s^{-1}$. Further study is necessary for the reaction rate constants at 40°C and 60°C because of the complexity of the formation of UPs.

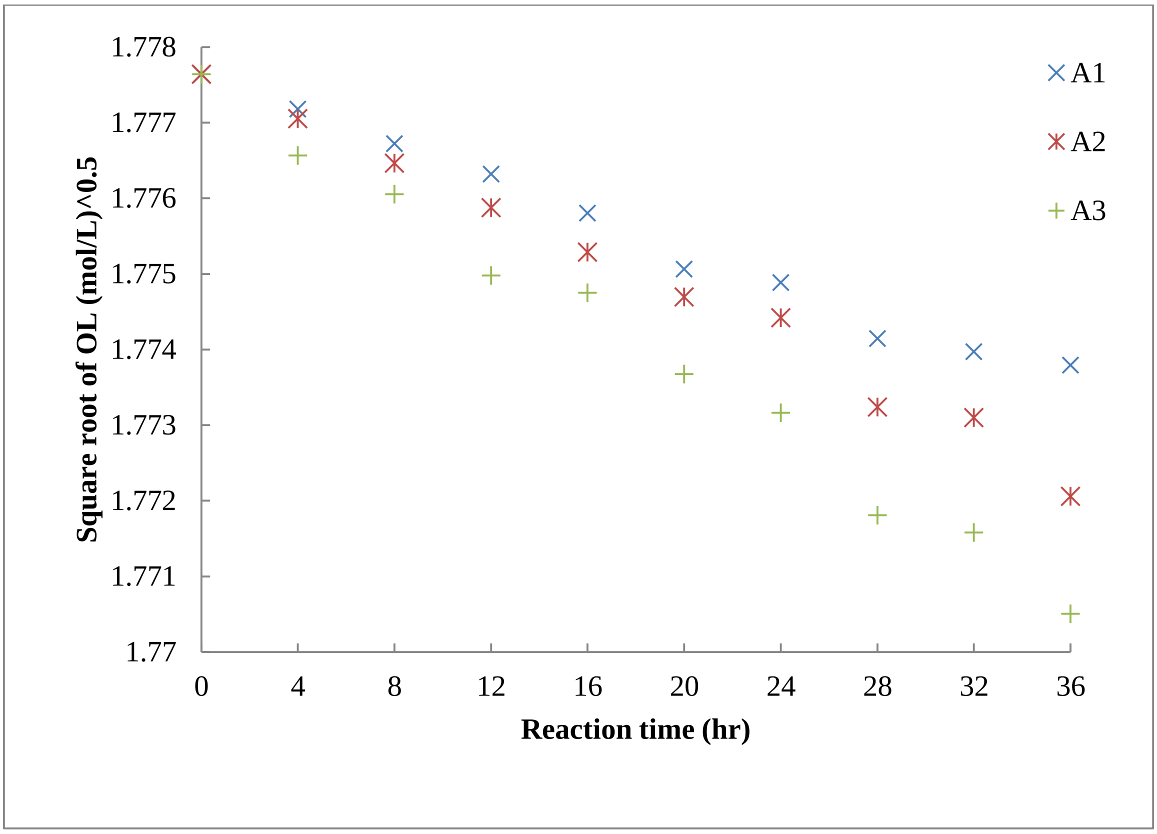

Figure 5.10 Reduction of square roots of OL at different ozone concentrations

As described previously, a fast pseudo-first-order regime is assumed prior to calculation of the reaction rate constant. Therefore, the calculated value must be used to recheck the assumption of the kinetic regime using the equation in Table 2.6. The calculation result proves that the ozonolysis of OL belongs in the fast pseudo-first-order regime because the Hatta number (3.09) is between 3 and $E_i/2$ (892), which also proves the assumption of the reactor design in that the reaction time (Equation 3-12) is notably fast. Thus, the bubble size is the only parameter that dominates the column height.

5.3 Summary

Ozonolysis of OL was evaluated at different operating temperatures with and without protic solvents (alcohols). In the case of ozonolysis of OL without alcohols, two products (i.e., NN and OA) are observed at 20°C with 93.5±3.4% following pathway 1. Additional products (the unidentified species) are also found at both 40°C and 60°C. The unidentified species are generated from decomposition of higher molecular weight species that are formed by the secondary reaction between the Criegee intermediates and oleic acid. The reaction rate constant of OL ozonolysis at 20°C is 9.19×10^5 $M^{-1}s^{-1}$ and indicates a fast pseudo-first-order reaction.

In the case of ozonolysis of OL with alcohols, a greater 1-nonanol content is observed compared with that of the system without alcohols. The increase of 1-nonanol is not influenced by the alcohols or by the increases in the Henry’s Law constant, diffusion coefficient, and specific interfacial area. Carboxylic acids and Criegee intermediates formed during ozonolysis are converted to alkyl esters depending on the molecular structure of the alcohols. To increase the productivity of 1-nonanol, methanol is a suitable protic solvent because of its physical properties. The optimum molar ratio between methanol and OL is 1:1. At low temperatures, the reaction rates of OL ozonolysis and OL esterification are identical, whereas at high temperatures, the reaction rate of OL esterification is much higher. In addition, the formation of NN increases by 30% if the fluidic oscillator is used, thus implying that the reaction rate of OL ozonolysis is a function of the specific interfacial area.

CHAPTER 6

OZONOLYSIS OF OLIVE OIL

This chapter focuses on the ozonolysis of pure olive oil and olive oil mixed with methanol for the production of short-chain products, i.e., NN and NA. Ozonised oil (by-product) is also used as the reactant for bio-kerosene production via conventional transesterification. Section 6.1 consists of several sub-sections. Methods for the reaction study and process simulation of olive oil ozonolysis via Aspen Plus are provided in Section 6.1.1. Methods for process simulation of ozonised oil transesterification using Aspen Plus are available in Section 6.1.2. Materials and methods for experimental study of pure olive oil and mixed olive oil with methanol ozonolysis are provided in Section 6.1.3. Materials and methods for the experimental study of ozonised oil transesterification are listed in Section 6.1.4. Section 6.2, in addition to the results and discussion, also contains several sub-sections. The results and discussions from Section 6.1.1, Section 6.1.2, Section 6.1.3, and Section 6.1.4, are presented in Section 6.2.1, Section 6.2.2, Section 6.2.3, and Section 6.2.4, respectively. The results and discussion of olive and methanol ozonolysis with the FO are contained in Section 6.2.5. The determination of reaction rate constant is illustrated in Section 6.2.6. The possible reaction mechanisms of both pure olive oil and mixed olive oil in methanol ozonolysis are proposed in Section 6.3.1 and Section 6.3.2, respectively. Section 6.4 provides a summary.

6.1 Materials and methods for ozonolysis of olive oil

6.1.1 Reaction study and process simulation of ozonolysis of olive oil via Aspen Plus

Similar to OL ozonolysis, olive oil and most of the possible products from ozonolysis are not found in the Aspen Plus database, and hence, their molecular structures (shown in Figure 6.1), i.e., ozonised oils, aldehydes, and carboxylic acids, must be drawn and added into the software. The enthalpy of formation and the free energy of formation of these chemicals are subsequently estimated. Furthermore, the enthalpy of reaction, free energy of reaction and entropy are calculated using the equation shown in Chapter 3. It should be noted that the reaction mechanisms of ozonolysis of olive oil shown in Figure 6.1 are based on the reaction mechanism of OL ozonolysis reviewed in Chapter 2.

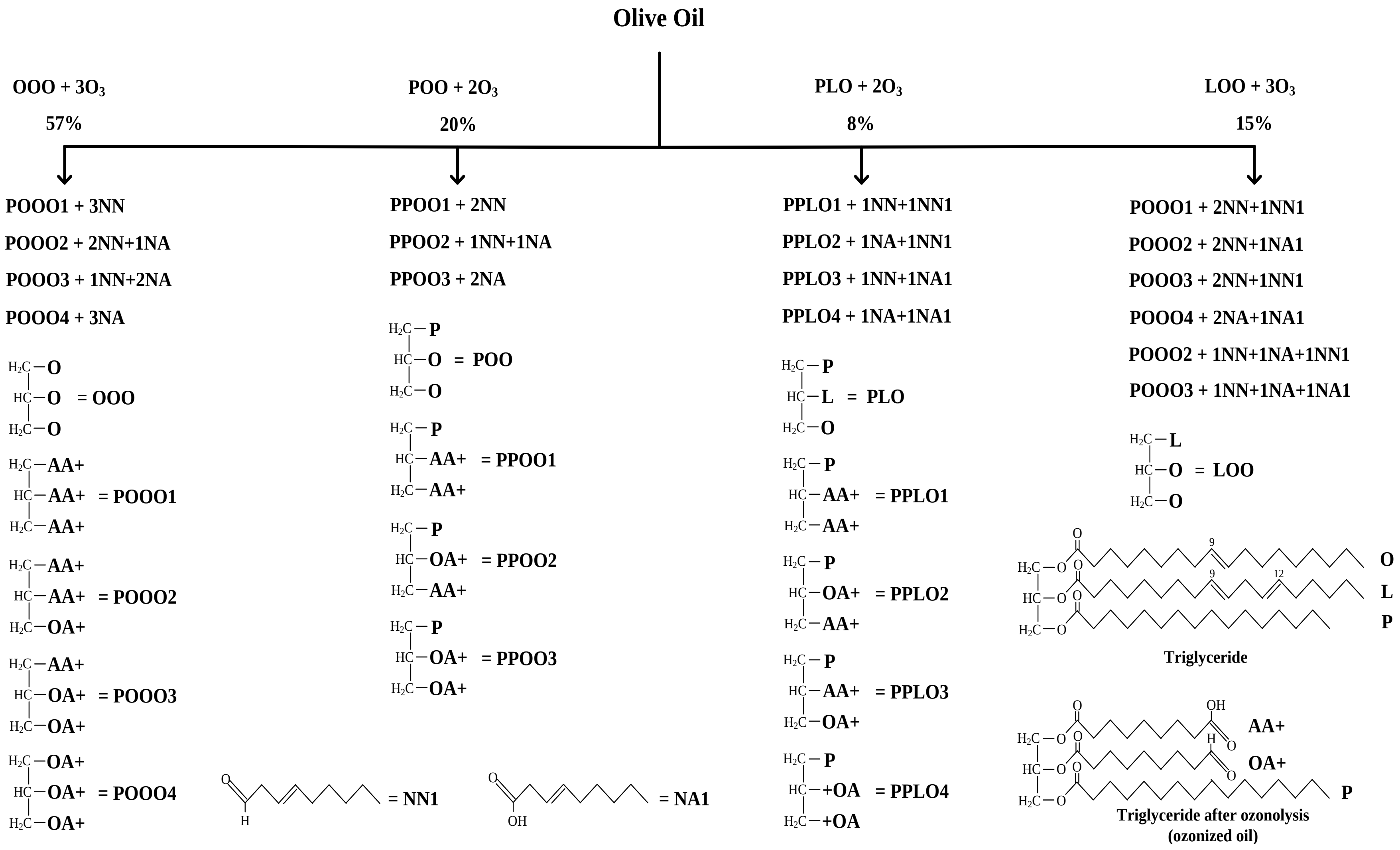

Figure 6.1 Possible reaction mechanisms of ozonolysis of olive oil

In the case of the process simulation shown in Figure 6.2, Aspen Plus is also used to estimate the product yields of olive oil ozonolysis at atmospheric pressure and various operating temperatures, i.e., 20°C, 40°C, and 60°C, with WIISON as the property method. The process flow diagram, operating conditions, and inlet ozone concentration used in this section are the same as those used in the OL ozonolysis described in Chapter 3. The compositions of triglycerides in the feed stream are based on the information for olive oil listed in Table 2.2. Although many triglycerides are found in olive oil, four major triglycerides, i.e., LOO, PLO, OOO, and POO, are selected for the process simulation; however, the fractions of LOO, PLO, OOO, and POO in olive oil used in the simulation are slightly adapted to values of 0.15, 0.08, 0.57, and 0.20, respectively. The molar flow rate of the feed stream of olive oil was set to 1 mol/min at 20°C and atmospheric pressure. All possible reactions as listed in Figure 6.1 were added into the reactor (R1). In this simulation, all CI2 molecules formed during ozonolysis are assumed to be completely converted to NA.

6.1.2 Process simulation of transesterification of ozonised oil via Aspen Plus

In this section, Aspen Plus is used to determine product compositions after transesterification of the ozonised oil. As shown in Figure 6.2, all liquid products and air from the previous section are fed to the phase separator (SEP1) to separate the liquid phase products and gas phase products. Hence, the liquid phase products from SEP1, i.e., ozonised oil, NN, and NA, are mixed with methanol (20°C, atmospheric pressure) at a molar ratio of 1:3 and subsequently fed to the reactor (R2). The possible reactions and possible products listed in Table 6.1 are added into the reactor. These reactions and products are based on the conventional transesterification mechanisms of biodiesel production (Sarin 2012). The substances referred to as M-AA, M-OA, and M-PA are mono-methyl azelate, 9-oxononanoic acid methyl ester, and methyl palmitate, respectively. The temperature and pressure of R2 are controlled at 60°C and atmospheric pressure, respectively. The products from R2 (mixtures of aldehydes, free fatty acids, methyl esters, and glycerol) are separated in the separator (SEP2). Next, the fluid properties of methyl esters (ESTER stream), i.e., density, distillation temperature, boiling point, and viscosity, are estimated using Aspen Plus. These fluid properties are compared with the standard for petroleum kerosene (ASTM D3699).

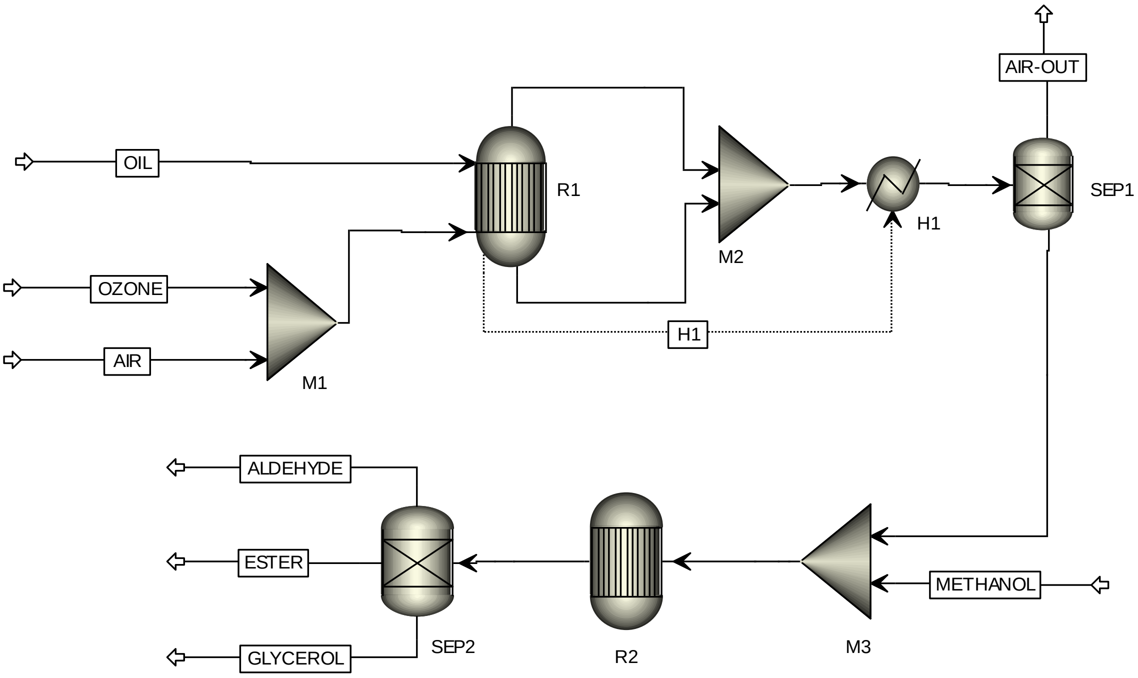

Figure 6.2 Process simulation of ozonolysis of olive oil followed by transesterification of ozonized oil with methanol

Table 6.1 Possible transesterification reactions of ozonized oil with methanol

No.	Reactions
1	POOO1 + 3MeOH→3M-AA + Glycerol
2	POOO2 + 3MeOH→2M-AA + 1M-OA + Glycerol
3	POOO3 + 3MeOH→1M-AA + 2M-OA + Glycerol
4	POOO4 + 3MeOH→3M-OA + Glycerol
5	PPOO1 + 3MeOH→2M-AA + 1M-PA + Glycerol
6	PPOO2 + 3MeOH→1M-AA + 1M-OA + 1M-PA + Glycerol
7	PPOO3 + 3MeOH→2M-OA + 1M-PA + Glycerol
8	PPLO1 + 3MeOH→2M-AA + 1M-PA + Glycerol
9	PPLO2 + 3MeOH→1M-AA + 1M-OA + 1M-PA + Glycerol
10	PPLO3 + 3MeOH→1M-AA + 1M-OA + 1M-PA + Glycerol
11	PPLO4 + 3MeOH→2M-OA + 1M-PA + Glycerol

6.1.3 Ozonolysis of pure olive oil and mixed olive oil with methanol

The same chemicals described in Chapter 5 were used in this chapter, except for the extra virgin olive oil, which was obtained from Napolina Ltd. The experimental setup, operating conditions, sampling time, sample storage conditions, and all analytical techniques for ozonolysis of pure olive oil and mixed olive oil with a protic solvent are similar to those used for OL ozonolysis.

For olive oil ozonolysis with a protic solvent, methanol is a protic solvent suitable for increasing productivity, as discussed in the previous chapter. Therefore, in this section, only methanol was mixed with olive oil for ozonolysis. The minimum molar ratio between olive oil and methanol should be 1:3 with the assumption that all of the triglycerides in olive oil are oleic acid molecules (OOO).

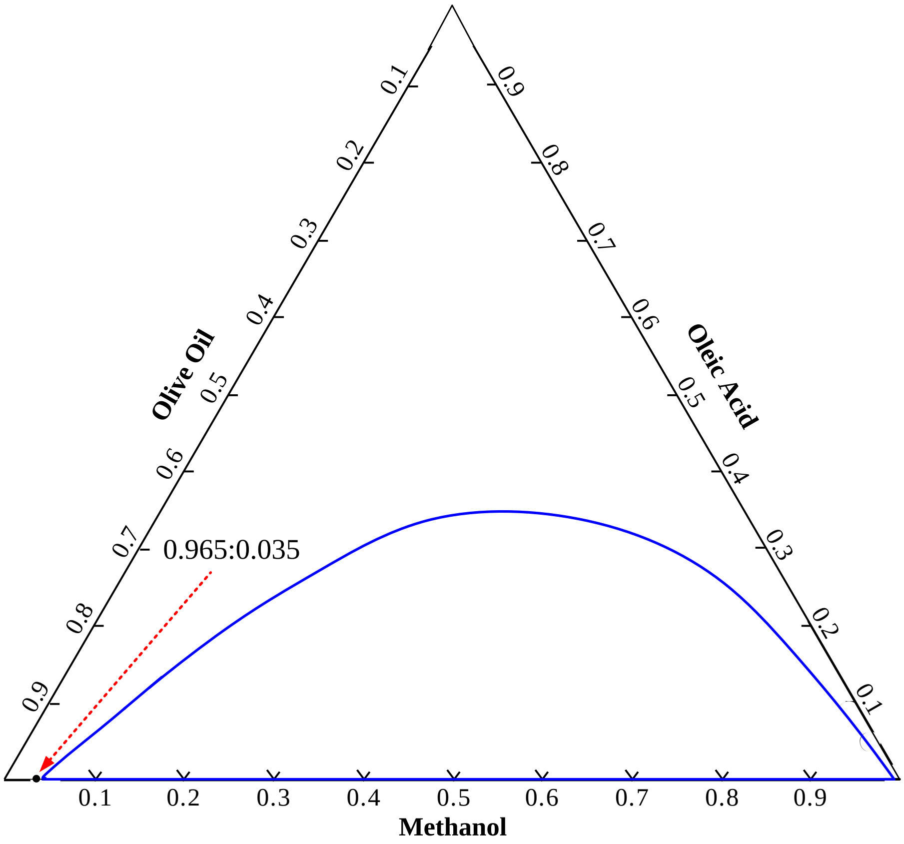

Figure 6.3 Three phase diagram of olive oil, oleic acid, and methanol

As shown in Figure 6.3, which was created in Aspen Plus, the maximum molar ratio between olive oil and methanol used to form homogeneous phases is 1:1. Therefore, only a molar ratio of 0.965:0.035 (volume fraction), or 314.0 mL of olive oil and 11.0 mL of methanol, was used in this study. In addition, the formation of NN and short-chain methyl esters and the reduction of methanol during ozonolysis result in an increase of methanol solubility, and therefore, extra methanol can be added during the reaction. It should be noted that the homogeneous phase must be considered after adding methanol.

6.1.4 Ozonised oil transesterification with methanol

Two types of ozonised oils are used in this study depending on the ozonolysis processes. The first type is ozonised oils from pure olive oil ozonolysis (OOP) at various temperatures, and the second is ozonised oils from olive oil and methanol ozonolysis (OOM) at different temperatures.

After ozonolysis, both OOP and OOM were used for transesterification with methanol to observe the product composition and the reaction mechanism during ozonolysis. Sodium hydroxide (NaOH) was also used as an alkaline catalyst. The molar ratio between ozonised oil to methanol and the percentage of catalyst are 1:8 and 1% by weight, respectively. To obtain the highest conversion, the reaction temperature was controlled at 60°C for 1 hour (Balat 2011).

The mixed solution is composed of 300 ml of ozonised oil, 100 ml of methanol, and 2.8 g of NaOH. The reaction was carried out in a 500 ml conical flask over a stirrer hotplate (LabPlant, Huddersfield, England). The temperature was controlled using a temperature controller. The rotational speed of the magnetic stirrer was set to 600 rpm.

After physical separation of the free fatty acid methyl esters (FFMAs) and glycerine using a conical funnel, deionised water was used to wash the crude oil to meet the European Standard for biodiesel fuel (EN 14214). The optimum volume ratio of crude oil to water is 1:1, and the washing time is 30 minutes with a 200 rpm magnetic stirrer. Gravity settling for 30 minutes in the conical funnel was the process used for separation of the final products (Berrios and Skelton 2008). The samples were held in a refrigerator at less than 4°C for GC-MS analysis. It should be noted that certain products dissolve in water during the washing process, and therefore, the detected concentrations of these products might be lower than the concentrations prior to the washing process (Pfrang *et al.* 2014).

6.2 Results and Discussions

6.2.1 Reaction study and process simulation of ozonolysis of olive oil

The molecular weight, enthalpy of formation, standard free energy of formation at 25°C and atmospheric pressure in the liquid phase of all possible reactants and products are listed in Table 6.2.

Table 6.2 Enthalpy and standard free energy of formation at 25^{o}C and 1 atm

No.	Name	Formula	MW	ΔH_f^o (kJ/mol)×10^2 (liquid)	ΔG_f^o (kJ/mol)×10^2 (liquid)
1	OOO	$C_{57}H_{104}O_6$	885.45	-18.42	-2.66
2	POO	$C_{57}H_{102}O_6$	859.41	-19.22	-3.63
3	PLO	$C_{57}H_{100}O_6$	857.39	-17.99	-2.83
4	LOO	$C_{57}H_{102}O_6$	883.43	-17.28	-1.86
5	POOO1	$C_{30}H_{50}O_{12}$	602.72	-27.42	-18.22
6	POOO2	$C_{30}H_{50}O_{11}$	586.72	-24.88	-15.80
7	POOO3	$C_{30}H_{50}O_{10}$	570.72	-22.27	-13.36
8	POOO4	$C_{30}H_{50}O_9$	554.72	-19.59	-10.91
9	PPOO1	$C_{37}H_{66}O_{10}$	670.93	-24.75	-13.94
10	PPOO2	$C_{37}H_{66}O_9$	654.93	-22.17	-11.53
11	PPOO3	$C_{37}H_{66}O_8$	638.93	-19.60	-9.11
12	PPLO1	$C_{37}H_{66}O_{10}$	670.93	-24.75	-13.94
13	PPLO2	$C_{37}H_{66}O_9$	654.93	-22.17	-11.53
14	PPLO3	$C_{37}H_{66}O_9$	654.93	-22.17	-11.53
15	PPLO4	$C_{37}H_{66}O_8$	638.93	-19.60	-9.11
16	NN1	$C_9H_{16}O$	140.23	-2.41	-0.11
17	NA1	$C_9H_{16}O_2$	156.22	-5.23	-2.67
18	HN	$C_6H_{12}O$	100.16	-2.92	-1.12
19	HA	$C_6H_{12}O_2$	116.16	-5.74	-3.62
20	MaA	$C_3H_4O_4$	104.06	-8.66	-7.12
21	OpA	$C_3H_4O_3$	88.06	-5.68	-4.36
22	PA	$C_3H_4O_2$	72.06	-3.19	-2.33

Table 6.3 Enthalpy of reaction and standard free energy of reaction of olive oil ozonolysis at 25^{o}C and 1 atm

No.	Reactions	ΔH^{o}_{rxn} (kJ/mol) $\times 10^{2}$	ΔS^{o} (J/mol·K) $\times 10^{2}$	ΔG^{o}_{rxn} (kJ/mol) $\times 10^{2}$
1	OOO+3O_3 → POOO1+3NN	-24.12	4.63	-25.50
2	OOO+3O_3 → POOO2+2NN+1NA	-24.52	-2.65	-23.73
3	OOO+3O_3 → POOO3+1NN+2NA	-24.85	-3.39	-23.84
4	OOO+3O_3 → POOO4+3NA	-25.11	-3.92	-23.94
5	POO+2O_3 → PPOO1+2NN	-15.61	0.20	-15.67
6	POO+2O_3 → PPOO2+1NN+1NA	-15.97	-0.54	-15.81
7	POO+2O_3 → PPOO3+2NA	-16.34	-1.34	-15.94
8	PLO+2O_3 → PPLO1+1NN+1NN1	-15.57	0.20	-15.63
9	PLO+2O_3 → PPLO2+1NA+1NN1	-15.93	-0.54	-15.77
10	PLO+2O_3 → PPLO3+1NN+1NA1	-15.81	-0.10	-15.78
11	PLO+2O_3 → PPLO4+1NA+1NA1	-16.18	-0.91	-15.91
12	LOO+3O_3 → POOO1+2NN+1NN1	-23.97	-1.38	-23.56
13	LOO+3O_3 → POOO2+2NN+1NA1	-24.27	-1.91	-23.70
14	LOO+3O_3 → POOO3+2NA+1NN1	-24.72	-3.09	-23.80
15	LOO+3O_3 → POOO4+2NA+1NA1	-24.86	-3.19	-23.91
16	LOO+3O_3 → POOO2+1NN+1NA+1NN1	-24.39	-2.35	-23.69
17	LOO+3O_3 → POOO3+1NN+1NA+1NA1	-24.60	-2.65	-23.81
18	NN1+O_3 → OpA+HN	-7.55	-1.51	-7.10
19	NN1+O_3 → MDA+HA	-8.60	-3.45	-7.57
20	NA1+O_3 → OpA+HA	-7.55	-1.71	-7.04
21	NA1+O_3 → MaA+HN	-7.71	-1.38	-7.30

All possible reactions shown in Figure 6.1 were used to estimate the enthalpy of reaction and free energy of reaction. It should be noted that this list might contain additional reactions if all triglycerides listed in Table 2.2 are considered. The results listed in Table 6.3 show that all reactions are the spontaneous reactions at standard conditions because the standard free energy of these reactions is negative, and all are exothermic reactions. Moreover, reactions 1, 5 and 8 are spontaneous at all temperatures due to the negative sign of both ΔH and -TΔS. Therefore, the possible products might be NN, NA, NN1 (2-nonenal), NA1 (E-non-2-enoic acid), and short chains of triglycerides that are considered by-products during ozonolysis. In addition, based on the Criegee mechanism, NN1 was oxidised to form OpA (3-oxopropanoic acid), HN (hexanol), MDA (malondialdehyde) or HA (hexanoic acid), and NA1 was oxidised to form OpA, HA, HN or MaA (malonic acid).

Table 6.4 Liquid product yields at different reaction temperatures using the REqui

Volume fraction	**Temperature (^oC)**		
	20	**40**	**60**
NN	0.015	0.016	0.022
NA	0.147	0.144	0.135
NN1	-	-	-
NA1	-	-	-
HN	0.002	0.004	0.006
HA	0.009	0.007	0.005
OpA	481ppm	433ppm	385ppm
MDA	52ppm	138ppm	264ppm
MaA	0.005	0.005	0.005
POOO1	38ppm	325ppm	0.003
POOO2	0.002	0.007	0.024
POOO3	0.040	0.072	0.122
POOO4	0.393	0.358	0.294
PPOO1	135ppm	619ppm	0.003
PPOO2	0.008	0.017	0.035
PPOO3	0.267	0.257	0.235
PPLO1	53ppm	235ppm	0.001
PPLO2	0.003	0.007	0.012
PPLO3	0.003	0.007	0.012
PPLO4	0.104	0.098	0.085

In case of the process simulation, all reactions listed in Table 6.3 were added into Aspen Plus because the free energy of formation of all reactions has negative signs. The simulation results listed in Table 6.4 show that NA is the major short-chain product with 14.7% found in the solution, and NN is the minor short-chain product with 1.5% observed. The by-product of this reaction is short-chain triglycerides (80% found). If the operating temperatures are varied, the amount of NN increases slightly, and the amount of NA decreases. Moreover, the outlet temperature of the product stream is 92°C, which increases by 72°C. The higher outlet temperature compared with that of ozonolysis of OL is due to higher exothermic reactions. A cooling system should be considered for commercial production using this technique. However, at the laboratory scale, the effect of the exothermic reaction is negligible because in an uninsulated reactor, the heat accumulation can be minimised by heat loss to the surrounding.

6.2.2 Process simulation of ozonised oil transesterification

The simulation results using ozonised oil at different reaction temperatures of ozonolysis are listed in Table 6.5. The table shows that all short-chain triglycerides react with methanol to form methyl esters, i.e., M-AA, M-OA, and M-PA. The highest composition of short-chain methyl esters belongs to M-OA with 36.7%, and the lowest composition is M-AA with 1.2%. These compositions depend on the temperature of ozonolysis. The composition of M-OA decreases with increasing temperature, whereas the composition of M-AA increases. For the long-chain methyl esters, only M-PA is formed with 8.2%. It should be noted that if different types of oils are used, the long-chain methyl esters produced might be different. For example, if the oil contains myristic acid or stearic acid, the long-chain methyl ester will be myristic acid, methyl ester or stearic acid.

In contrast, if ozonised oil mixed with methanol is used during ozonolysis for transesterification, the product composition listed in Table 6.5 might be different because all carboxylic acids formed during ozonolysis will be converted to methyl ester, which is primarily composed of M-NA, as discussed in Chapter 5. Therefore, three main groups of chemicals that might be formed using ozonised olive oil mixed with methanol during ozonolysis for transesterification are aldehydes (NN and HN), methyl esters (M-NA, M-AA, M-OA, M-PA, etc.), and glycerol.

Table 6.5 Expected products and product yields estimated by Aspen Plus

Volume fraction	**Ozonized oil**		
	20	**40**	**60**
NN	0.037	0.041	0.057
NA	0.372	0.367	0.342
OpA	0.001	0.001	0.001
MaA	0.013	0.013	0.013
HA	0.022	0.017	0.012
HN	0.006	0.010	0.014
MDA	132ppm	351ppm	670ppm
M-AA	0.012	0.024	0.037
M-OA	0.367	0.357	0.047
M-PA	0.082	0.082	0.082
Glycerol	0.069	0.069	0.069

Table 6.6 Detailed requirement for kerosene

Property	**Standard of petroleum kerosene (ASTM D3699)**	**Estimated by Aspen Plus**
Density at 15 ^oC (kg/m^3)	775 - 840	928
Distillation temperature (^{o}C)		
10% volume recovery, max	205	211
90% volume recovery	-	283
Final boiling point, max (^{o}C)	300	315
Kinematic viscosity at 40 ^{o}C (mm^2/s)		1.58
Min	1.0	
max	1.9	

After separation of the mixtures, the methyl esters (which primarily consist of C9 molecules at approximately 72% by volume) might be used as bio-kerosene for jet engines. However, the fluid properties must be tested to meet the standard for jet fuel, but this study does not focus on bio-kerosene production. Therefore, the properties reported in this thesis are taken only from Aspen Plus and compared with the ASTM D3699 standard (www.astm.org).

As listed in Table 6.6, the physical properties of bio-kerosene estimated by Aspen Plus, i.e., density, distillation temperature, and final boiling point, are slightly higher than the standard properties of petroleum kerosene, except for the kinematic viscosity, which is within the standard range. Although most of the physical properties do not meet the standard for petroleum kerosene, it is possible that this bio-kerosene can be blended with petroleum kerosene to meet the specifications for petroleum kerosene. However, further study of the mixing percentages between bio-kerosene and petroleum kerosene is necessary.

6.2.3 Ozonolysis of pure olive oil and mixed olive oil with methanol

The experimental results show that only NN is observed during ozonolysis of pure olive oil at any reaction temperature, and its concentration increases with increasing reaction time. Although short-chain triglycerides are undetectable by GC-MS, certain of them are present in the mixtures because NN can be formed after the double bond of olive oil is cleaved, resulting in the simultaneous formation of short-chain triglycerides. As shown in Figure 6.4, at reaction temperatures of 20°C, 40°C, and 60°C and a reaction time of 32 hrs, the highest concentration of NN is found at an operating temperature of 60°C. This situation occurs for the same reason as ozonolysis of OL in terms of NN formation in which the reduction of fluid viscosity at higher temperature results in an increase of the specific interfacial area (smaller bubble formation) and the diffusion coefficient. The Henry's Law constant also increases with increasing reaction temperature. The possible reaction mechanisms of pure olive oil ozonolysis are described in the following sections.

For ozonolysis of mixed olive oil with methanol, the experimental results at 20°C for 0, 8, 16, 24, and 32 hours are shown in Figure 6.5. Overall, two main products are observed, i.e., NN and M-NA. Similar to OL ozonolysis, all of the carboxylic acid/carbonyl oxides formed in the system are converted to methyl ester. The amounts of these products increase with increasing reaction time and fluid temperature, as shown in Figure 6.6. The formation of M-NA can be explained by the Criegee intermediate formed during ozonolysis reacting with methanol to form methoxyhydroperoxide (MHP). Such a product subsequently decomposes to M-NA and water. The short-chain triglycerides that are transformed into the Criegee intermediate might also react with methanol and decompose to short-chain triglycerides, which are eventually transformed into an end product. The possible reaction mechanisms of these results are described in the following sections. Moreover, the amount of squalene remains constant during ozonolysis; it might be assumed that the reaction rate between ozone and squalene is quite low compared with that at the double bonds, resulting in a constant composition.

In addition, because of the formation of M-NA, this result proves that the decomposition of PO follows both pathways, with 88±2.6% following pathway 1.

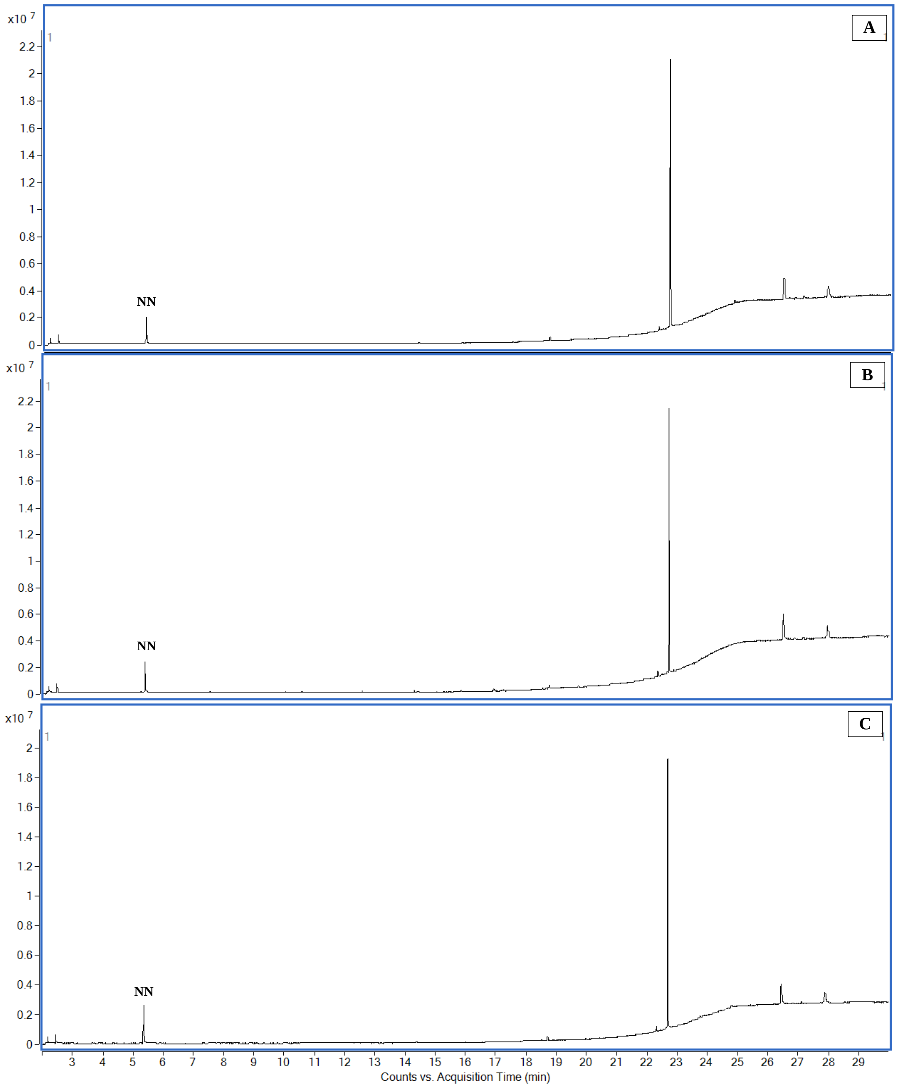

Figure 6.4 Chromatogram of ozonolysis of olive oil at 32 hrs; A = 20°C, B = 40°C, and C = 60°C

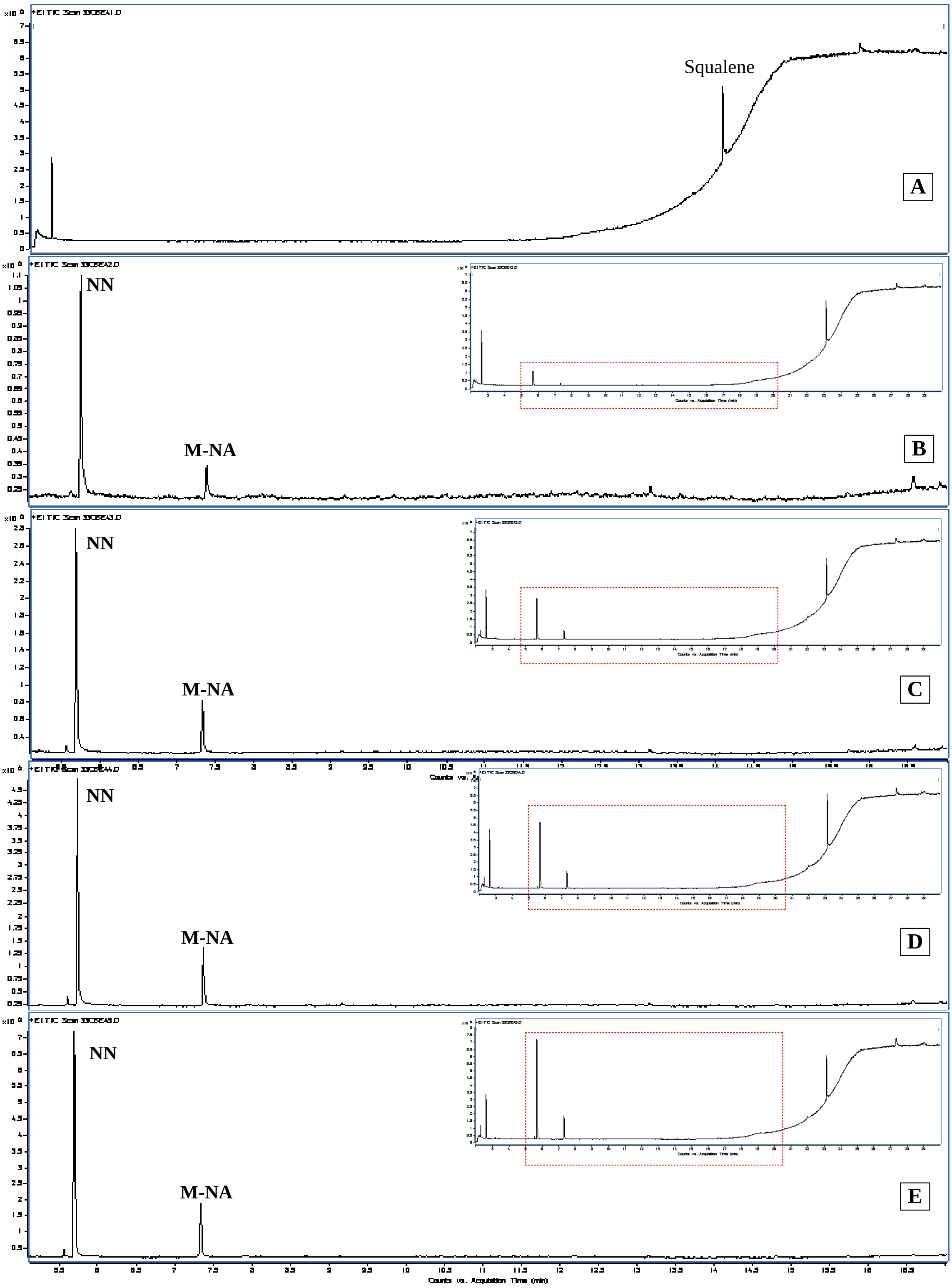

Figure 6.5 Chromatogram of ozonolysis of olive oil and methanol at 20°C: A = 0 hr, B = 8 hrs, C = 16 hrs, D = 24 hrs, and D = 32 hrs

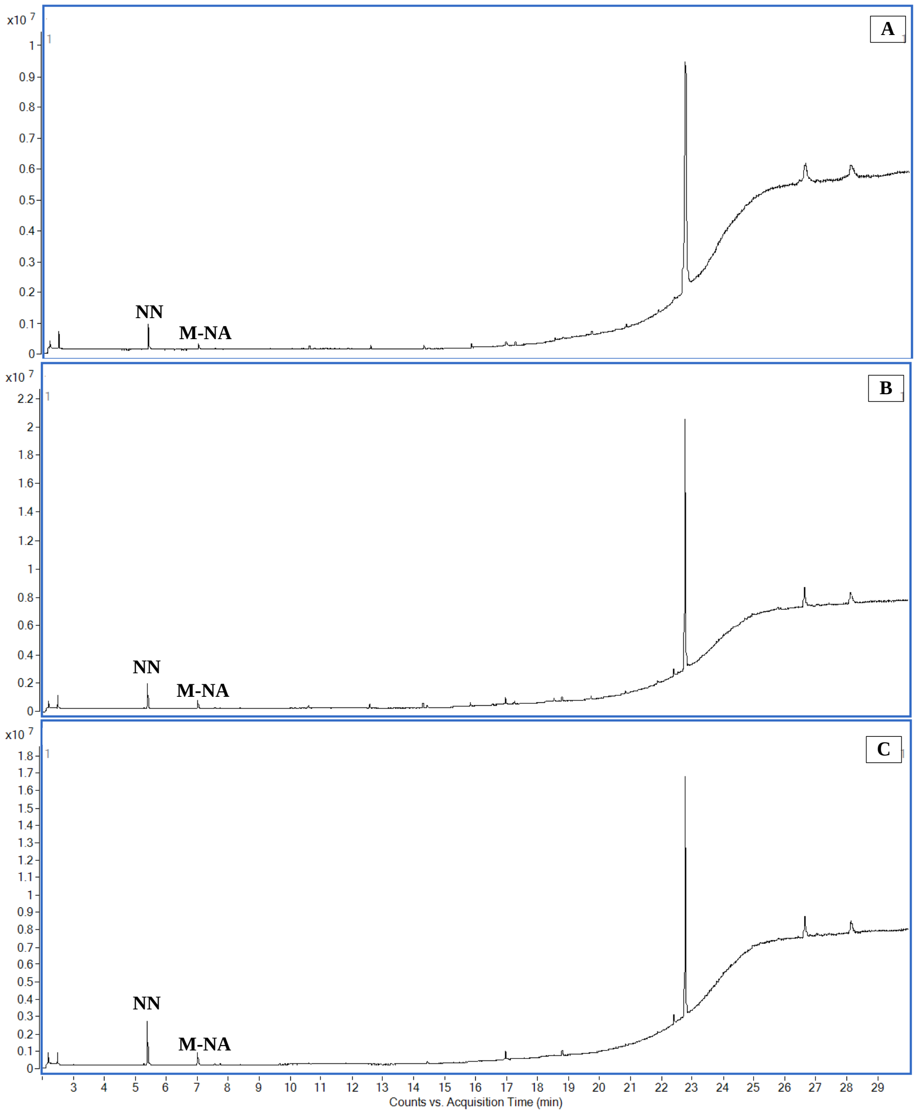

Figure 6.6 Chromatogram of ozonolysis of olive oil and methanol at 32 hrs: A = 20°C, B = 40°C, and C = 60°C

6.2.4 Ozonised oil transesterification with methanol

If OOP is used for transesterification, as shown in Figure 6.7, long-chain methyl esters, i.e., palmitic acid methyl ester, stearic acid methyl ester, and myristic acid methyl ester, and also several short-chain methyl esters are found after transesterification, i.e., octanoic acid methyl ester (M-OcA), M-NA, 9-oxononanoic acid methyl ester (M-OA), and dimethyl azelaic acid (DM-AA). The major short-chain methyl esters are M-OcA and M-OA, and the minor short-chain versions are M-NA and DM-AA. The concentration of M-NA and DM-AA slightly increases with increasing ozonolysis temperature, whereas that of M-OA decreases and that of M-OcA appears to remain constant over the studied temperatures.

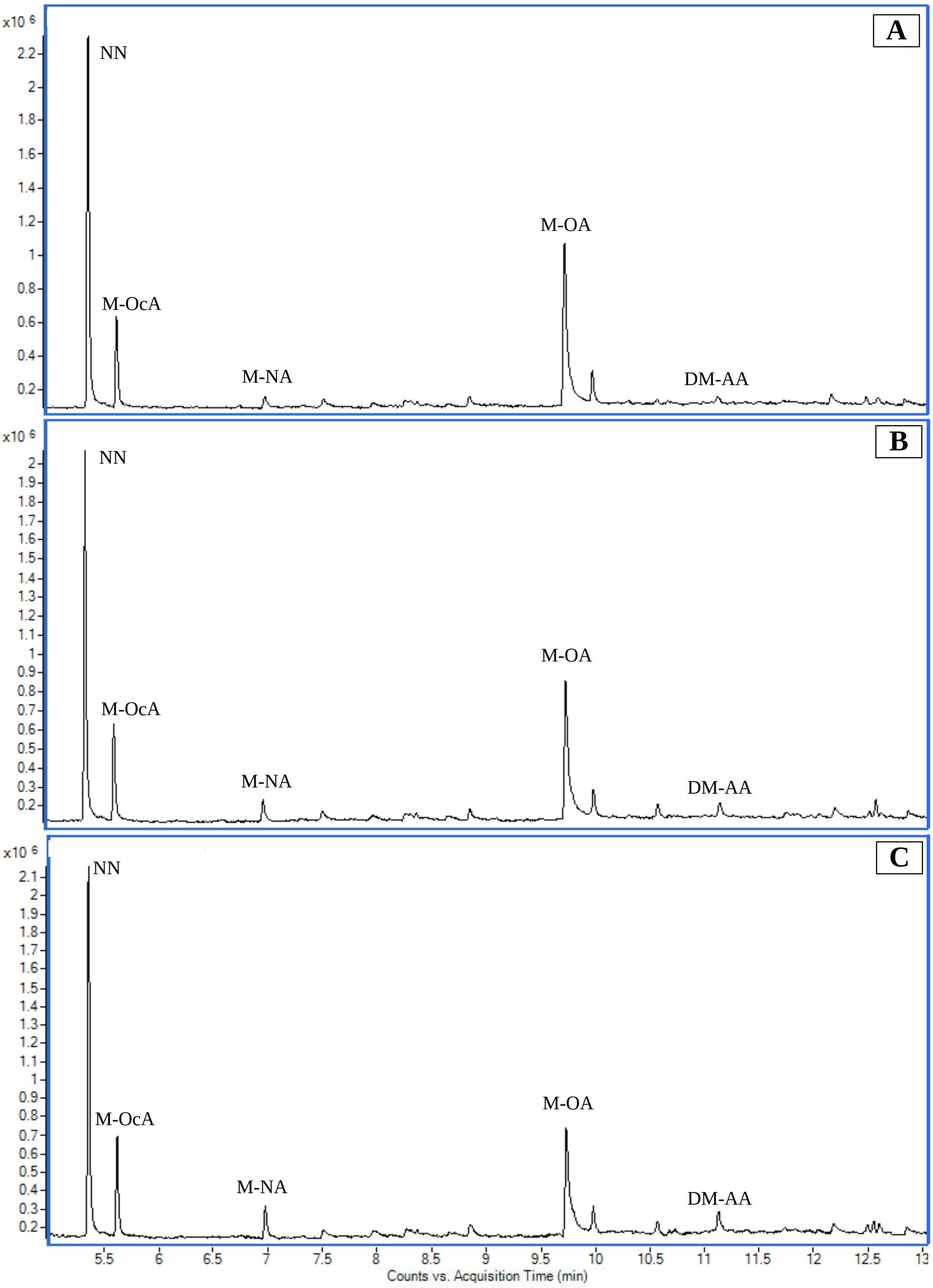

Figure 6.7 Chromatogram of transesterification of ozonised oil at 32 hrs: A = ozonised oil at 20°C, B = ozonised oil at 40°C, and C = ozonised oil at 60°C.

If OOM is used for transesterification, as shown in Figure 6.8, the result shows a significant increase in M-NA and DM-AA concentrations, and the concentrations of M-OcA and M-OA remain unchanged. The substantial amount of M-NA detected is a consequence of the previous process (ozonolysis with methanol). However, the concentration of M-NA is slightly lower than its concentration before transesterification, which results from the loss of this species during the washing process. The appearance of a substantial amount of DM-AA might be due to esterification during ozonolysis of the olive oil product (Criegee intermediate) followed by transesterification. The reaction mechanism details of both ozonolysis techniques are described in the next section.

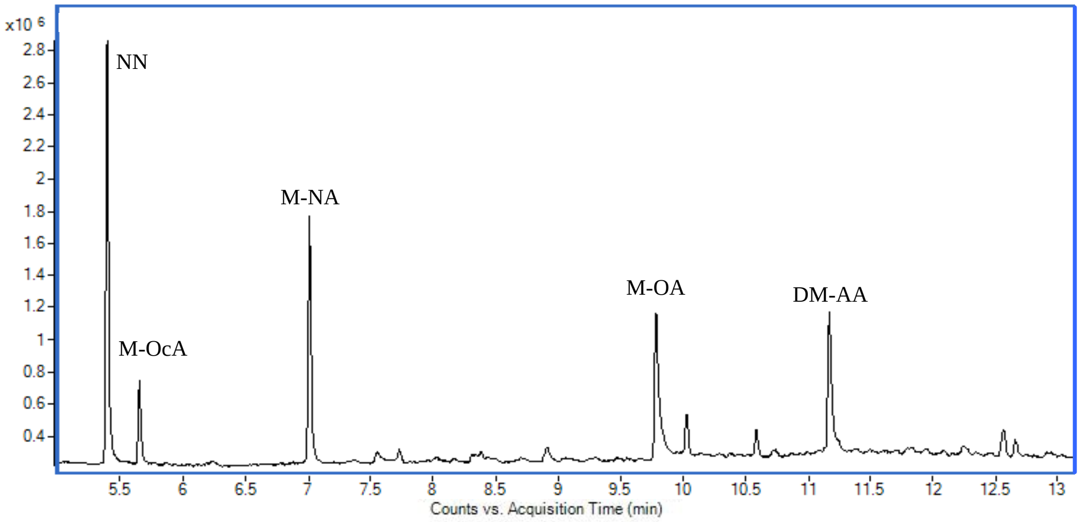

Figure 6.8 Chromatogram of transesterification of ozonised oil with methanol at 32 hrs of ozonised oil at 40^{o}C.

Moreover, the concentration of M-NA found after transesterification is higher than that during ozonolysis at low temperatures, although its concentration should be lower because of losses during the washing process. Thus, the extra amount of M-NA might be formed via the decomposition of methoxyhydroperoxide, which might confirm that the decomposition rate of methoxyhydroperoxide from methyl ester and water increases with increasing reaction temperature because the transesterification is performed at 60°C.

After quantitative analysis of the concentration of M-OcA, the result proves that a yield of 6.6±0.23% of short-chain triglycerides ending with OCI1 converts to OOcA and carbon dioxide, which means that the remaining short-chain triglycerides ending with OCI1 convert to OAA in the case of pure olive oil ozonolysis and convert to OMAA in the case of olive oil and methanol ozonolysis. Based on mole balance, this results shows that ozonolysis of one mole of olive oil (OOO) in methanol followed by transesterification can produce (3)0.88 moles of NN, (3)0.82 moles of DM-AA, (3)0.06 moles of M-OcA, (3)0.12 moles of M-NA, and (3)0.12 moles of M-OA.

The compositions of short-chain methyl esters found during ozonolysis and transesterification are different from the previous values estimated by Aspen Plus. Therefore, the fluid properties listed in Table 6.6 must be recalculated using the compositions described above (only short-chain methyl esters). The result shows that the density at 15°C is 985 kg/m^3. The distillation temperature of 10% volume recovery is 213°C. The final boiling point is 302°C, and kinematic viscosity at 40°C is 2.57 mm^2/s. Although the fluid properties of the mixtures are higher than the standard for petroleum kerosene, these methyl esters might be blended with petroleum kerosene to meet the standard.

6.2.5 Ozonolysis of olive oil and methanol with the FO

This section presents the results obtained from of ozonolysis of olive oil mixed with methanol relative to performance in the system with and without the FO at 20°C. Similar to OL ozonolysis, the concentration of NN is used to represent the effect of the FO instead of the reduction of olive oil.

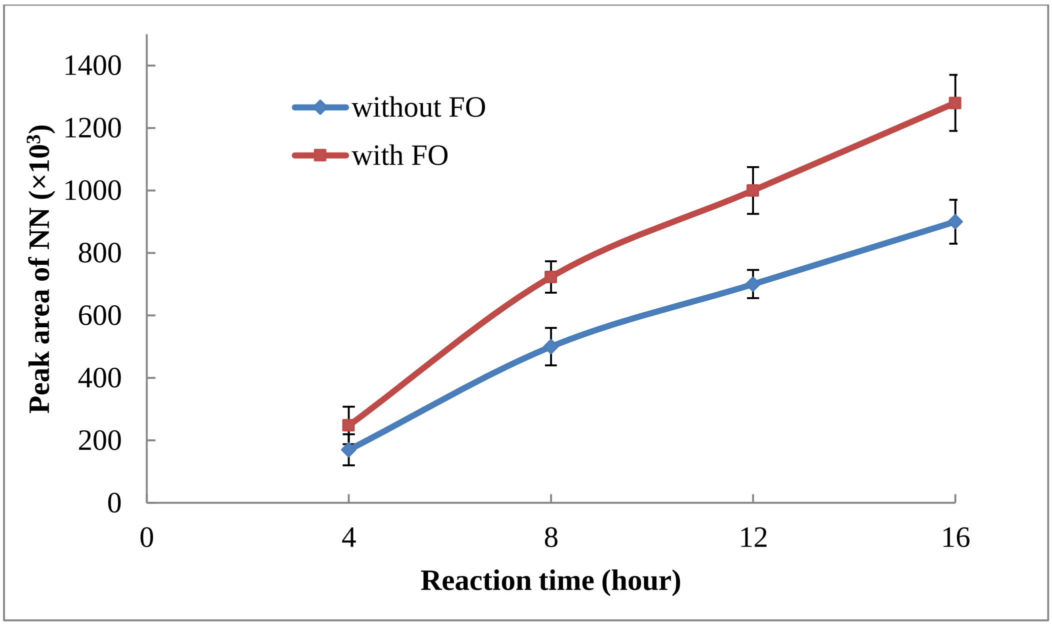

Figure 6.9 Ozonolysis of olive oil and methanol with and without FO

As shown in Figure 6.9, the concentration of NN increases by 43.8±2.5% when the system is used with the FO. The increase of NN is in good agreement with the increase of the specific interfacial area discussed in Chapter 5. This result can confirm that the formation of NN is a function of the specific interfacial area. Therefore, the reaction rate of ozonolysis of olive oil is a function of the specific interfacial area, according to Eq. 2-39.

6.2.6 Reaction rate constant of pure olive oil ozonolysis

Similar to OL ozonolysis, the inlet ozone concentration used in this study is notably low, leading to difficulty in measurements of the reduction of olive oil. Therefore, the reduction of olive oil is plotted using the relationship between the loss of olive oil and NN formation with several assumptions provided.

1. No NN loss occurs from the secondary reactions or evaporation.

2. All molecules of ozone react with olive oil.

3. All molecules of olive oil consist of OOO, $z = 3$.

4. The Henry's Law constant, diffusion coefficient, inlet ozone concentration, and specific interfacial area are constant.

It is interesting to note that the concentration of NN observed during olive oil ozonolysis is quite similar to that of OL ozonolysis. Therefore, the slope of the reduction of olive oil must be identical to that of OL ozonolysis and can be used to determine the reaction rate constant of olive oil ozonolysis. Using the slope of OL ozonolysis calculated in Chapter 5 and the parameters provided in Chapter 4 (the Henry's Law constant, diffusion coefficient, specific interfacial area, and inlet ozone concentration), the calculated reaction rate constant of olive oil at 20°C is 4.88×10^{8} $M^{-1}s^{-1}$.

6.3 Possible reaction mechanisms

The reaction mechanism shown in Figures 6.10 and 6.11 can be used to describe many questions from the experimental results discussed, including:

1. Why is only NN observed with ozonolysis of pure olive oil?

2. Why are both M-OcA and M-OA the major products, whereas M-NA and DM-AA are the minor products after transesterification of ozonised oil (pure olive oil)?

3. Why are both NN and M-NA observed from ozonolysis of olive oil mixed with methanol?

4. Why are greater amounts of both M-NA and DM-AA observed after transesterification of ozonised oil (olive oil mixed with methanol)?

6.3.1 Pure olive oil ozonolysis and transesterification

Based on the reaction mechanism of pure OL ozonolysis (Hung *et al.* 2005), two decomposition pathways of primary ozonide (a product formed after ozone reacts at the double bond of olive oil) are suggested, including pathway 1 and pathway 2. As shown in Figure 6.9, if the decomposition follows pathway 1, NN and ozonised oil ending with a CI1 molecule (OCI1) will be formed. However, if the decomposition follows pathway 2, CI2 and ozonised oil ending with an aldehyde molecule (OOA) will be formed.

Considering the result shown in Figure 6.5, the decomposition of primary ozonide follows both decomposition pathways because NN, which is a product from pathway 1, is observed during ozonolysis, whereas M-OA formed by transesterification of OOA from pathway 2 is observed after transesterification. Thus, four products are present after the decomposition of primary ozonide, i.e., NN, OCI1, CI2, and OOA.

After decomposition of primary ozonide, OCI1 might decompose to ozonised oil ending with an octanoic acid molecule (OOcA) and carbon dioxide because a substantial amount of M-OcA is detected after transesterification. The OCI1 might also rearrange to form ozonised oil, resulting in carboxylic acid molecules (OAA) and might subsequently react with CI2 to form ozonised oil, resulting in AAHP1NA molecules (OAAHP1NA). Moreover, OCI1 might react with CI2 to form ozonised oil ending with a DP3 molecule (ODP3). In addition to reacting with ozonised oil and creating CI1 or a related product, CI2 molecules might react with each other to form DP2 and subsequently decompose to two molecules of NN and one molecule of oxygen, as discussed in Chapter 2. As a result of its high reactivity, no CI2 or its related product (NA) is detected after ozonolysis. Therefore, many liquid-phase products are generated after ozonolysis of pure olive oil, including NN, OOcA, OAA, OAAHP1NA, ODP3, and DP2, and two gas phase products, i.e., carbon dioxide and oxygen. However, certain of these species are undetectable by GC-MS under the conditions used in this work.

In addition to pure olive oil ozonolysis, the ozonised oil is used for transesterification with methanol. Substantial amounts of both M-OcA and M-OA are observed, whereas trace amounts of both M-NA and DM-AA are detected. Four possible reaction mechanisms are believed be responsible for the formation of the products described above, i.e., OOcA, OAA, OAAHP1NA, and ODP3. In the first reaction mechanism, if OOcA reacts with three molecules of methanol, three major products will be formed, i.e., M-OcA, M-OA, M-PA (or long-chain saturated methyl esters) and glycerol. It should be noted that the lack of glycerol observed in the chromatograms results from phase separation between methyl esters and glycerol prior to the washing process. The second reaction mechanism is the transesterification of OAA resulting in the formation of M-AA, M-OA, M-PA, and glycerol. In the presence of methanol, M-AA might convert to form DM-AA and water via an esterification reaction. The third reaction mechanism is transesterification of ODP3, leading to the formation of M-DP3, M-OA, M-PA, and glycerol. Based on the decomposition theory of DP3 in OL ozonolysis (Hearn and Smith 2004), M-DP3 might decompose to NN, M-OA and oxygen. The fourth reaction mechanism is transesterification of OAAHP1NA, which accounts for the formation of M-AAHP1NA, M-OA, M-PA, and glycerol. During transesterification, M-AAHP1NA might react with methanol to form M-AA, M-NA, and water. Hence, M-AA might react with methanol to form DM-AA and water via an esterification reaction.

Considering the amount of observed products, the probabilities of the last three reaction mechanisms are low compared with that of the first reaction mechanism because trace amounts of both M-NA and DM-AA are found after transesterification. However, the probabilities of these reactions might be higher in case of the low reaction rate of M-DP3 decomposition, the low reaction rate of M-AAHP1NA esterification and the inability of the GC-MS to detect M-DP3 and M-AAHP1NA.

6.3.2 Olive oil and methanol ozonolysis and transesterification

The reaction mechanism of olive oil and methanol ozonolysis is quite simple compared with that of pure olive oil ozonolysis, as shown in Figure 6.10. Similar to the case of pure olive oil ozonolysis, the decomposition pathways of primary ozonide can follow both pathway 1 and pathway 2. The products NN and OCI1 will be formed if the decomposition follows pathway 1. In contrast, CI2 and OOA will be generated if the decomposition follows pathway 2. Therefore, the same four products will be formed, i.e., NN, OCI1, CI2, and OOA.

As discussed earlier, in the presence of methanol or any alcohols, the Criegee intermediates prefer to react with methanol to form methoxyhydroperoxide. As a result of this reaction, CI2 might react with methanol to form methoxyhydroperoxide and subsequently decompose to M-NA and water during ozonolysis of olive oil mixed with methanol. The OCI1 also reacts with methanol to form ozonised oil ending with methoxyhydroperoxide and subsequently decomposes to ozonised oil ending with ester (OMAA) and water. Moreover, certain of the OCI1 might also convert to form OOcA and carbon dioxide. Therefore, four products of NN, M-NA, OOcA, and OMAA are observed after ozonolysis.

Similar to the transesterification of pure olive oil, ozonised oil is used as a reactant for transesterification with methanol. Based on the result during ozonolysis, two possible reaction mechanisms are suggested. The first reaction is the transesterification reaction of OOcA, which results in the formation of M-OcA, M-OA, M-PA, and glycerol. The other reaction is the transesterification reaction of OMAA, leading to the formation of DM-AA, M-OA, M-PA, and glycerol. Therefore, substantial amounts of NN, M-NA, M-OcA, DM-AA, and M-OA are observed after transesterification.

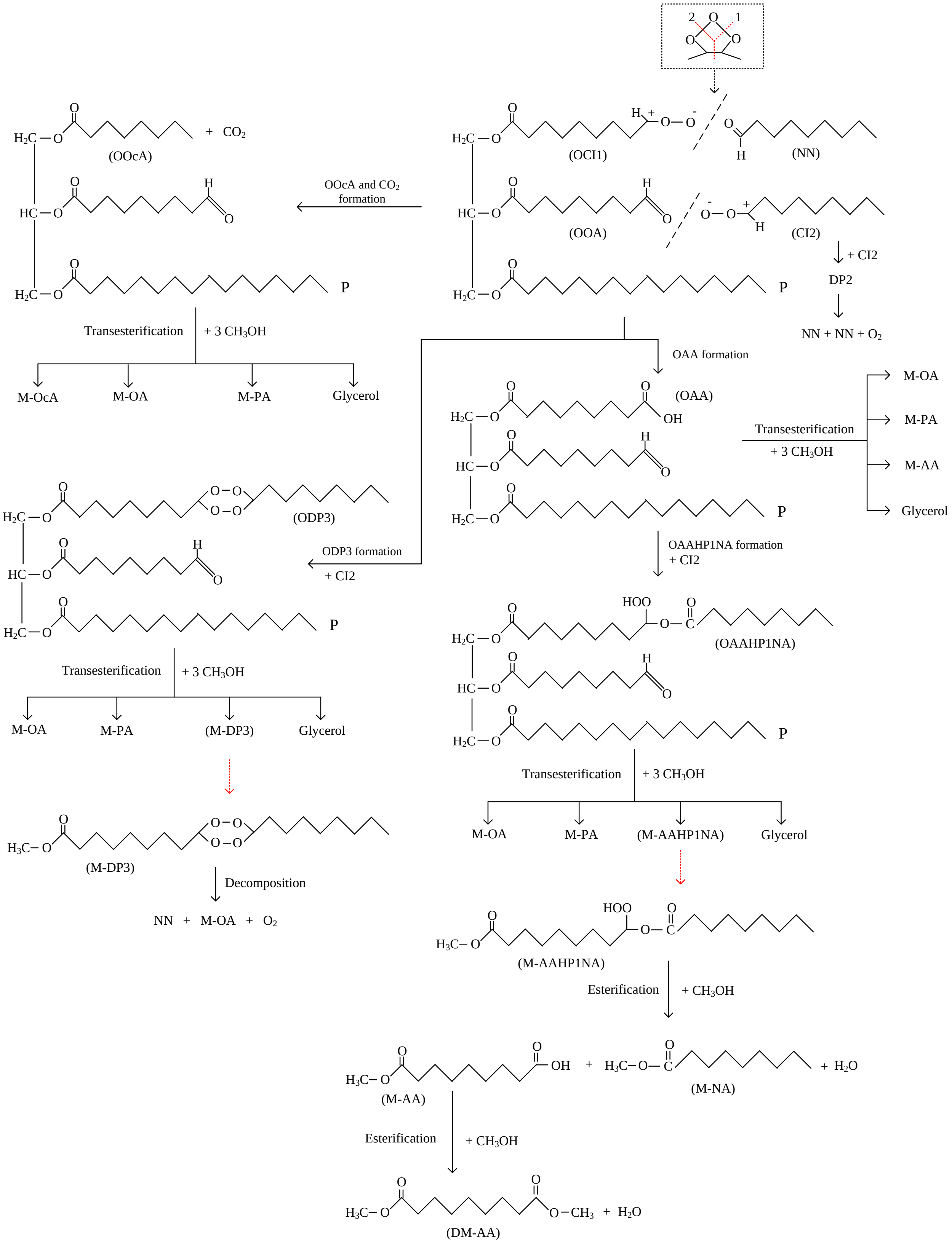

Figure 6.10 Reaction mechanisms of ozonolysis of pure olive oil followed by transesterification

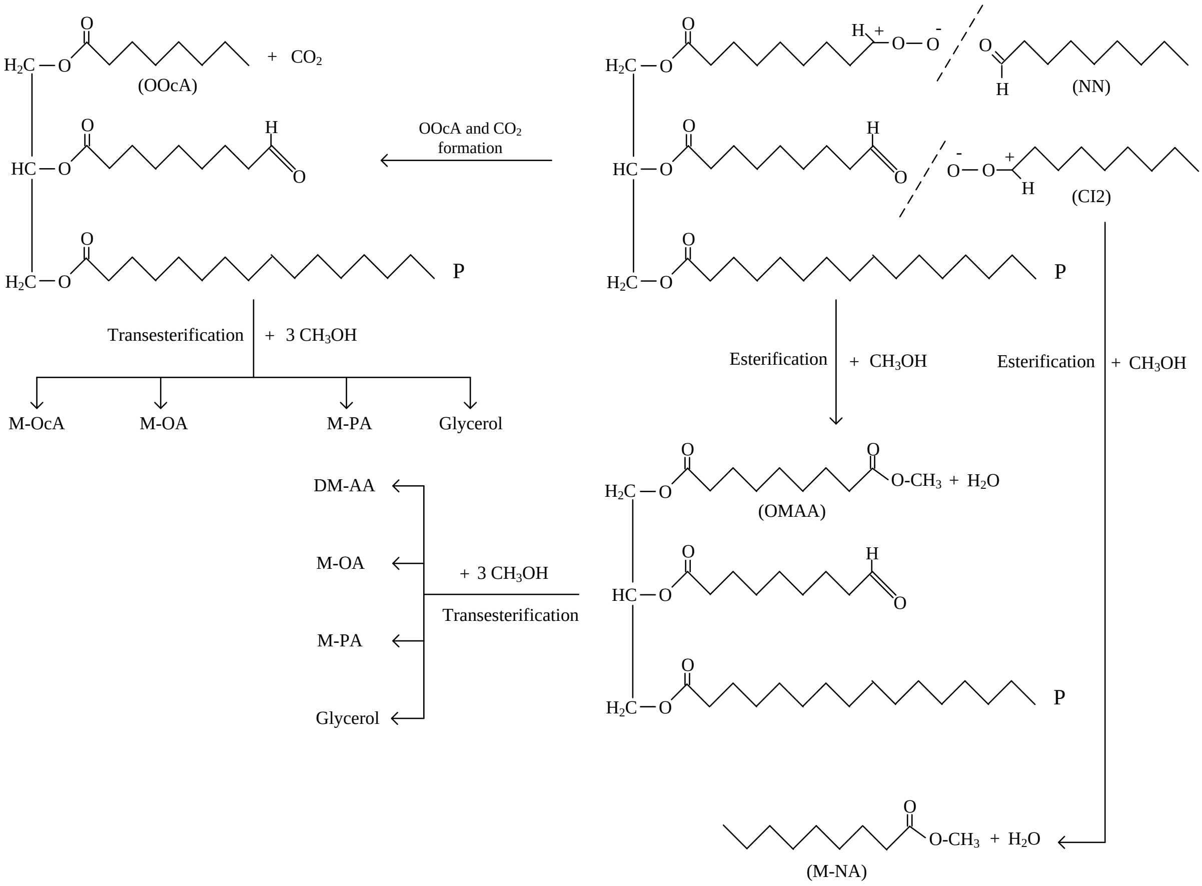

Figure 6.11 Reaction mechanisms of ozonolysis of olive oil and methanol followed by transesterification

According to a comparison between ozonolysis of pure olive oil and mixed olive oil in terms of product concentrations, it is clear that ozonolysis and transesterification of olive oil mixed with methanol is a suitable technique for NN and short-chain methyl ester production. Ozonolysis can be processed at room temperature. A number of reasons are responsible for this achievement, including the increase of the Henry's Law constant, diffusion coefficient, and interfacial surface area (smaller bubble formation) and the decrease of product loss by reducing the effect of the Criegee intermediate.

It should be noted that this approach for bio-kerosene production could be applied to any vegetable oils that contain a large amount of unsaturated molecules, i.e., soybean, corn, peanut, and cottonseed, and also might be applied for bio-gasoline production if oils that contain sufficient linoleic acid molecules are used.

6.4 Summary

Ozonolysis of olive oil was evaluated at different operating temperatures with and without methanol. In the case of pure olive oil ozonolysis, only NN is observed as the short-chain product. Short-chain triglycerides ending with CI1 are the by-product, although they cannot be detected by GC-MS. The reaction rate constant of olive oil ozonolysis at 20°C is estimated as 4.88×10^{8} $M^{-1}s^{-1}$. For ozonolysis of mixed olive oil with methanol, two short-chain products are observed. The major product is NN with 88.0±2.6% yield, and the minor product is M-NA. Moreover, a yield of 6.6±0.23% of short-chain triglycerides ending with CI1 for both OOP and OOM decomposes to short-chain triglycerides ending with octanoic acid.

In case of transesterification of short-chain triglycerides, M-OA is the major short-chain product from use of OOP, whereas DM-AA is the major product from use of OOM. The liquid volume fractions of M-NA, M-OA, DM-AA, and M-OcA found using OOM are 0.093, 0.08, 0.776, and 0.052, respectively.

Based on mole balance, ozonolysis of one mole of olive oil (OOO) mixed with methanol followed by transesterification can produce 2.64 moles of NN, 2.46 moles of DM-AA, 0.18 moles of M-OcA, 0.36 moles of M-NA, and 0.36 moles of M-OA. In addition, the formation of NN increases by 43.8±2.5% if the FO is used, implying that the reaction rate of olive oil ozonolysis is a function of the specific interfacial area.

CHAPTER 7

OZONOLYSIS OF USED COOKING OIL

This chapter focuses on the formation of NN or other short-chain products and also on the reduction of free fatty acid content in used cooking oil, which can be used directly as the reactant for biodiesel production. The hypothesis of this chapter is based on the experimental results from both Chapter 5 and Chapter 6. Therefore, an introduction to biodiesel production from used cooking oil is provided in Section 7.1. The materials and methods for ozonolysis of used cooking oil are also presented in Section 7.2, which contains several sub-sections. Section 7.2.1 lists the chemicals used in this study. Section 7.2.2 describes the preparation technique for used cooking oil and the suitable amounts of methanol used. Section 7.2.3 and Section 7.2.4 summarises the ozonolysis techniques and sample analysis, i.e., ASTM D974 and GC-MS, respectively. Section 7.3 contains the experimental results and discussions from ASTM D974 and GC-MS that are provided in Section 7.3.1 and Section 7.3.2, respectively. Section 7.4 presents a summary.

7.1 Introduction of used cooking oil

Currently, energy is a basic demand in economic development, i.e., agriculture, transportation, and industry. The world’s energy consumption has been increasing, resulting in a notable large energy demand from fossil fuels. Use of fossil fuels creates many problems, i.e., increasing fossil fuel prices and air pollution from combustion engines. Moreover, the main problem of fossil fuel is that the supply will run out in the next few decades. To overcome these problems, renewable energy sources is needed, including wind power, hydropower, solar energy, biomass, and biofuel (Sarin 2012).

Biodiesel is an alternative renewable energy source that can be produced from vegetable oils and animal fats via transesterification reactions. For vegetable oils, both edible oils and non-edible oils can be used as the reactants, but use of the first material is quite expensive and might cause a shortage of food supply, whereas use of the second causes many serious problems because of high FFA content. For transesterification reaction via an alkaline catalyst, the presence of high FFAs content results in soap formation that can slow down the reaction conversion and creates difficulty in the separation processes. Moreover, used cooking oils from restaurants and households represent an alternative feedstock for biodiesel production to avoid the food versus fuel issue and environmental pollution. However, used cooking oils also have a high level of FFA content, which can cause the same serious problems as use of non-edible oils.

A two-step transesterification must be used for biodiesel production with non-edible oils or used cooking oil as the reactants. The first step reduces the FFAs content in non-edible oils or used cooking oil via an esterification reaction with alcohols over acid catalysts, i.e., H_2SO_4. Methanol is also used in high excess over FFAs, and the reaction temperature ranges from 40°C to 80°C. The reaction might take several minutes to several hours to complete (Canakci and Van Gerpen 2001, Biermann *et al.* 2011, Hayyan *et al.* 2011). The suitable percentage of FFAs in non-edible oils or used cooking oils for the transesterification reaction should be less than 3% (Aransiola *et al.* 2014). The second process is conventional transesterification with use of an alkaline catalyst (Meher *et al.* 2006). All of these methods suffer from the drawbacks of biodiesel production using non-edible oils or used cooking oils. Moreover, another disadvantage is the need for acid-resistant materials in the reactor and piping system.

Based on the experimental results from Chapter 5 and Chapter 6, ozonolysis of either non-edible oils or used cooking oil in the presence of alcohols is an alternative technique that can be applied to reduce the FFAs content in oils, and this technique can replace the esterification process for biodiesel production. Ozonolysis of oils that contain high FFAs offers many advantages. For example, in terms of economics, this technique could reduce the operating cost because it can run at room temperature, atmospheric pressure, and without the use of a mechanical stirrer. This technique can also reduce the excess amount of methanol required because FFAs can be converted to methyl esters at a molar ratio of 1:1. The materials for the reactor and the piping system are lower cost than those used in the esterification process because no acid catalyst is contained in the solution. Moreover, a large amount of NN will be formed because OL is the major species of free fatty acids in used cooking oils, and NN is simply separated due to its low boiling point. Alkyl esters of octanoic acid, nonanoic acid, azelaic acid, 9-oxononanoic acid can be directly fed into the transesterification process for biodiesel production or can be separated to sell as valuable products because the boiling point of these products is lower than that of long-chain alkyl esters. In terms of the environment, e.g., less waste-water is produced because this process can be conducted without addition of acid catalysts.

Therefore, in this chapter, used cooking oil with different percentages of FFAs is used for ozonolysis instead of fresh vegetable oils because its price is 2.5 to 3.5 times lower than that of fresh vegetable oils of (Canakci and Van Gerpen 2001, Balat 2011, Biermann *et al.* 2011, Hayyan *et al.* 2011). Methanol is also used as the solvent for the reasons described in previous chapters. The main objective of the work described in this chapter is to produce NN or any short-chain methyl ester and also to reduce FFAs content such that ozonised oil from this reaction can directly be used in transesterification.

7.2 Materials and methods for ozonolysis of used cooking oil

7.2.1 Chemicals

Myristic acid (≥98%), Stearic acid (95%), Palmitic acid (≥98%), Toluene (HPLC grade, 99.9%), Alpha-Naphtholbenzein (indicator grade), Potassium hydroxide (reagent grade, >90%), and Barium hydroxide (technical grade, 95%) were obtained from Sigma-Aldrich. Other chemicals used in this study were described in the previous chapter.

7.2.2 Used cooking oil preparation

Because used cooking oil contains a great amount of FFAs, and their composition must be the same in every experiment, the used cooking oil treated in this study was prepared by mixing pure olive oil with different percentages of FFAs (10%, 15%, and 20%) and different compositions of FFAs. The compositions of FFAs (15.7%) in used cooking oil measured by Russbueldt and Hoelderich (2009) are myristic acid (0.1%), palmitic acid (2.5%), palmitoleic acid (0.1%), stearic acid (1.2%), oleic acid (7.7%), linoleic acid (3.7%), and linolenic acid (0.4%). Therefore, four major FFAs, i.e., oleic acid, palmitic acid, stearic acid, and myristic acid, were selected to blend with olive oil for used cooking oil preparation; however, the compositions of oleic acid, palmitic acid, stearic acid, and myristic acid used in this study are slightly adapted to 75.8%, 16.5%, 7.6%, and 0.1%, respectively, and their details are listed in Table 7.1.

After the preparation process, used cooking oil was mixed with methanol for ozonolysis. It should be noted that the solution must exist as a single phase (homogeneous phase) after blending with methanol, and the minimum molar ratio of olive oil to methanol should be 1:3. To avoid two phases (heterogeneous phase), the ternary map of olive oil, OL and methanol was plotted using Aspen Plus with UNIFAC-LL as the property method. As plotted in Figure 7.1, this simulation result is quite similar to the experiment performed by Batista and co-workers (1999), and Hirata and co-workers (2013), who used canola oil instead. Two possible regions for the homogeneous phase were observed by fixing the percentages of FFAs in olive oil at 10%, 15%, and 20% and varying the molar ratio of olive oil to methanol. The first region is located on the left-hand side, where the molar ratio of FFAs to methanol is low, whereas the second region is located on the right-hand side, where the molar ratio of FFAs to methanol is quite high. A low molar ratio between olive oil and methanol was selected in this study because the high molar ratio might not be possible in terms of economy.

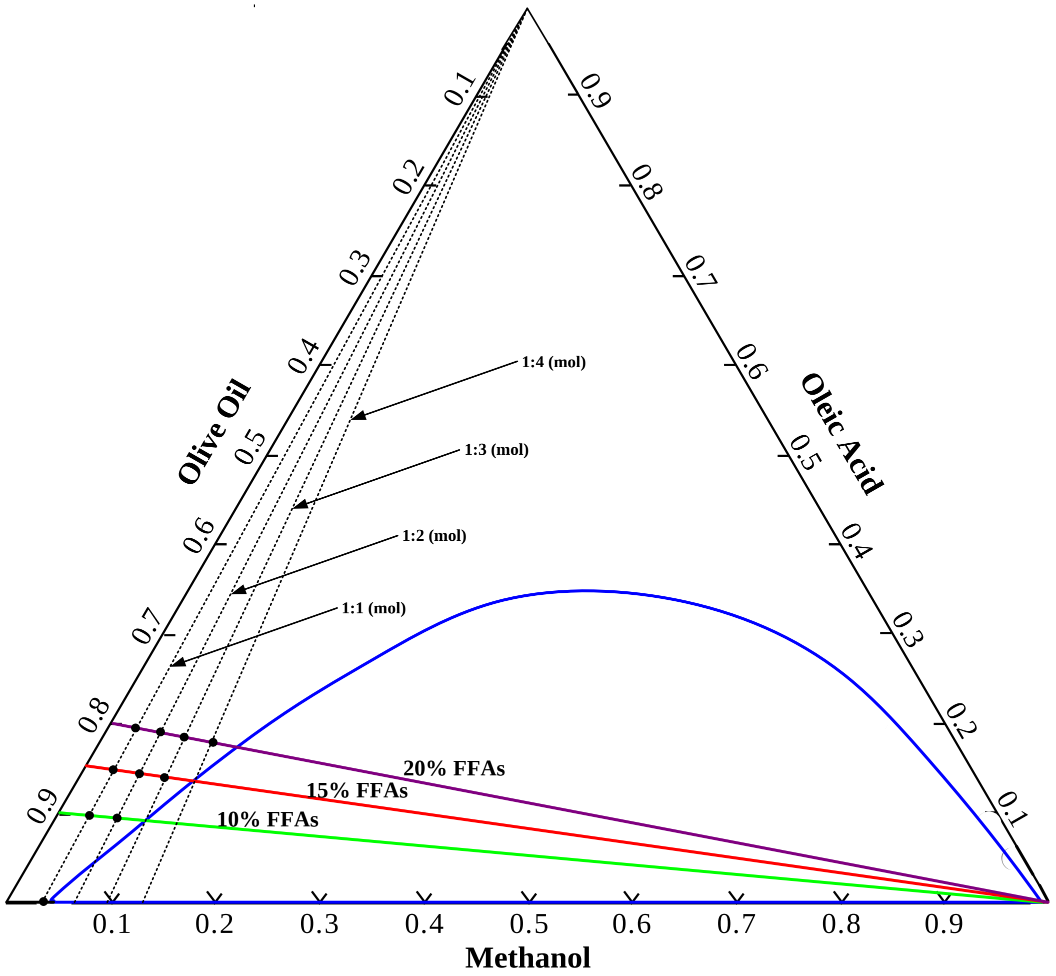

Figure 7.1 Ternary map of the mixture of oil, oleic acid, and methanol

To obtain the composition of each component, three linear lines were drawn from the positions of 0.90:0.10, 0.85:0.15, and 0.80:0.20 of oil and FFAs to the position of pure methanol. The ratio of olive oil to FFAs remains constant by following these coloured lines. For molar ratios of olive oil to methanol at 1:1, 1:2, 1:3, and 1:4, four dashed lines were also drawn at the positions of 0.965:0.035, 0.932:0.068, 0.902:0.098, and 0.874:0.126 of olive oil and methanol to the position of pure OL. The ratio of olive oil to methanol also remains constant by following these dashed lines, as also shown in Figure 7.1. The maximum molar ratio of 10% and 15% FFAs to methanol for the homogeneous phase on the left-hand side is 1:3, whereas the maximum molar ratio of 20% FFAs to methanol is 1:4. Therefore, a molar ratio between olive oil and methanol of 1:3 was used in this study because a homogeneous phase at different percentages of FFAs can be formed using this ratio.

In addition to the graphical technique, Aspen Plus was employed to determine the accurate value of each component used in this study, as listed in Table 7.1. It should be noted that the molar ratio of FFAs to methanol is approximately 1:4, although the molar ratio between olive oil and methanol is equal to 1:3. With excess of methanol, all FFAs can be converted to the desired products (methyl esters).

Table 7.1 Chemical compositions of synthesised used cooking oil

Chemicals (wt.%)	**FFAs (wt.%)**		
	10	**15**	**20**
Olive oil	0.821	0.779	0.736
Oleic acid (OL)	0.068	0.103	0.139
Palmitic acid (PA)	0.015	0.023	0.031
Stearic acid (SA)	0.007	0.010	0.014
Myristic acid (MA)	576 ppm	875 ppm	0.001
Methanol	0.089	0.085	0.080

7.2.3 Ozonolysis of used cooking oil

In this section, 325 mL of synthesised used cooking oils and methanol at different percentages of FFAs (as listed in Table 7.1) were used for ozonolysis at different reaction temperatures. The experimental setup, inlet ozone concentrations, and all operating conditions are the same as those used in the ozonolysis of OL described in Chapter 5.

7.2.4 Sample analysis via ASTM D974 and GC-MS

7.2.4.1 Standard test method for acid number by colour indicator titration

In this study, the standard test method (ASTM D974) was used to determine the acid number of used cooking oil mixed with methanol after ozonolysis. This test method is commonly used to determine both acid and base numbers in petroleum products and lubricants that are soluble in the mixture of toluene, isopropyl alcohol, and water. This method can also be used for either new oils (light oils) or used oils (dark-coloured oil). All details can be found at the ASTM website (www.astm.org).

Reagent preparation

1. Titration solvent: This solvent was prepared by mixing toluene, water, and anhydrous isopropyl alcohol at a volume ratio of 100:1:99.

2. Alpha-naphtholbenzein indicator: This indicator was prepared by mixing alpha-naphtholbenzein in a titration solvent to reach a concentration of 10±0.01 g/L.

3. Potassium hydroxide solution (standard alcoholic, 0.1 M): This solution was prepared by mixing 6 g of solid KOH in approximately 1 L of anhydrous isopropyl alcohol. The mixture was boiled for 10 to 15 minutes. A magnetic stirrer was used during boiling to prevent the solid from forming a cake on the bottom. Next, barium hydroxide (2 g) was added and boiled for 5 to 10 minutes. The solution was filtered using fine sintered glass and stored in a chemically resistant dispensing bottle.

Methodology

1. Used cooking oil (0.2-2.0 g) was mixed with 100 mL of titration solvent and 0.5 mL of indicator solution and swirled simultaneously until entirely dissolved by the solvent. The solution should be a yellow-orange colour as a result of acid content.

2. The solution was immediately titrated with a KOH solution until the end point at which the orange colour changes to a green or green-brown.

3. To perform a blank titration, 100 mL of the titration solvent and 0.5 mL of the indicator solution were mixed and titrated by KOH solution. It should be noted that the volume of KOH solution should be less than 0.1 mL.

Acid number calculation

The acid number is calculated using Eq. 7-1.

$$Acid\ number, mg\ of\ KOH/g = \left[(A-B)M \times 56.1\right]/W \tag{7-1}$$

In this equation, A is the KOH volume required for titration of the sample (mL), B is the KOH volume required for titration of the blank (mL), M is the molarity of the KOH solution, and W is the sample used.

7.2.4.2 GC-MS analysis

The sample preparation, column, and operating conditions for GC-MS are the same as those described in Chapter 5.

7.3 Results and discussion of ozonolysis of used cooking oil

7.3.1 ASTM D974

Ozonolysis of used cooking oil with 20% FFAs at 20°C, 40°C, and 60°C is shown in Figure 7.2. Overall, the acid numbers decrease by 25% after 36 hours of ozonolysis. The decrease in the acid numbers relates directly to the reaction temperatures. The lowest value of acid number is observed in high temperature ozonolysis, whereas these numbers are slightly higher for low temperature ozonolysis. The value of acid number decreases dramatically during the first 12 hours and eventually plateaus. It is interesting that a similar feature of the decreased acid numbers is observed at both 15% and 10% FFAs, as shown in Figure 7.3 and Figure 7.4, respectively.

Because of the low FFAs content in olive oil used in this study (Peri 2014), it can be assumed that all FFAs in the mixtures before ozonolysis are a combination of OL, PA, SA, and MA. As listed in Table 7.1, the percentage of saturated FFAs and unsaturated FFAs in the mixtures are 24.8% (PA, SA, and MA) and 75.2 % (OL), respectively.

Based on the experimental results from both Chapter 5 and Chapter 6, the loss of olive oil in the mixtures during ozonolysis must be higher than that of OL for two reasons: (i) a much higher (~500 times) reaction rate constant of olive oil ozonolysis than that of OL ozonolysis and (ii) a substantial amount of olive oil present in the mixtures. It might be assumed that most of the ozone reacts with olive oil to form NN and M-NA. If the reaction follows this assumption, the reduction of FFAs is only due to esterification of both saturated and unsaturated FFAs. For the worse case, however, if OL reacts with most of the ozone, its concentration will be reduced by 10% (0.01467 mole, 4.63 mL or 4.14 g) over 36 hours of ozonolysis, which means that the acid number must be reduced by direct ozonolysis from 43.63 mg of KOH/g to 40.20 mg of KOH/g or a 7.5% reduction. Therefore, this result can confirm that FFAs are converted to methyl esters via esterification.

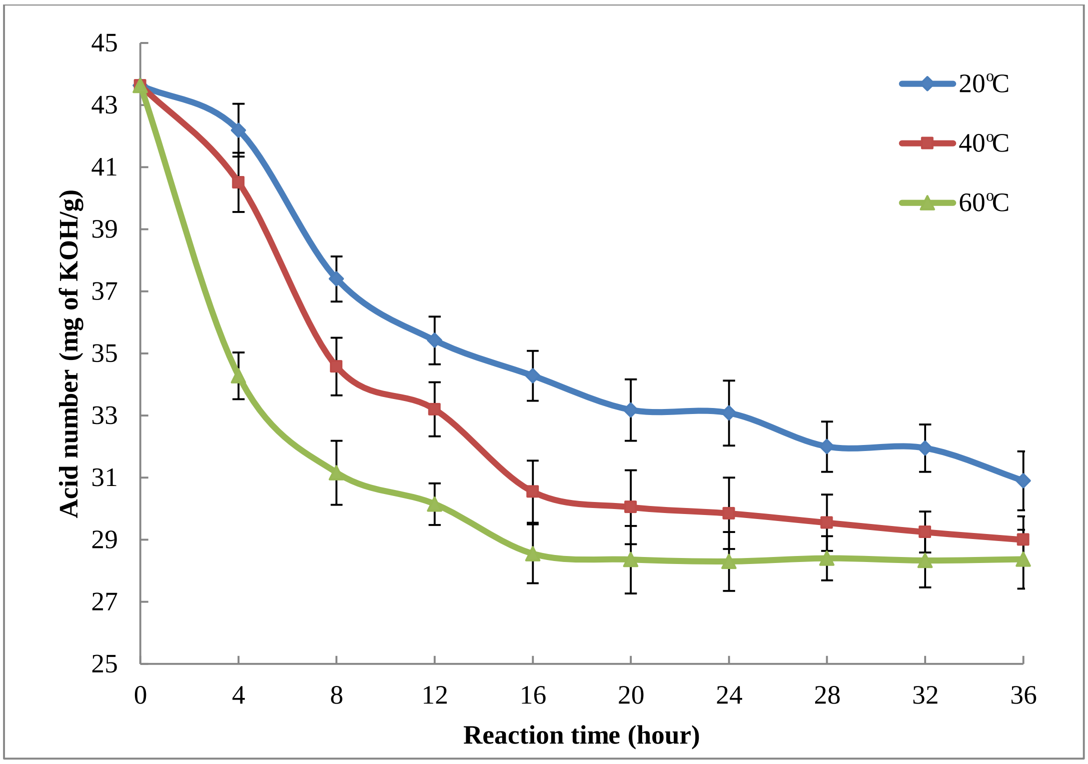

Figure 7.2 Ozonolysis of used cooking oil at 20% FFAs

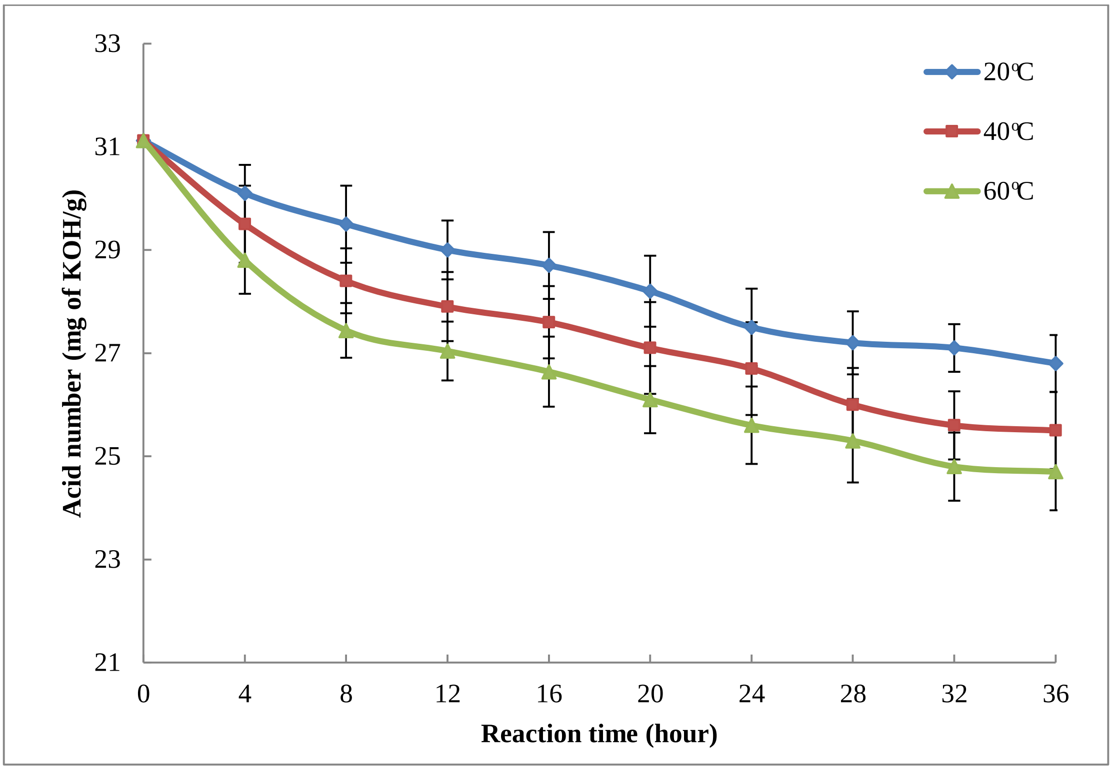

Figure 7.3 Ozonolysis of used cooking oil at 15% FFAs

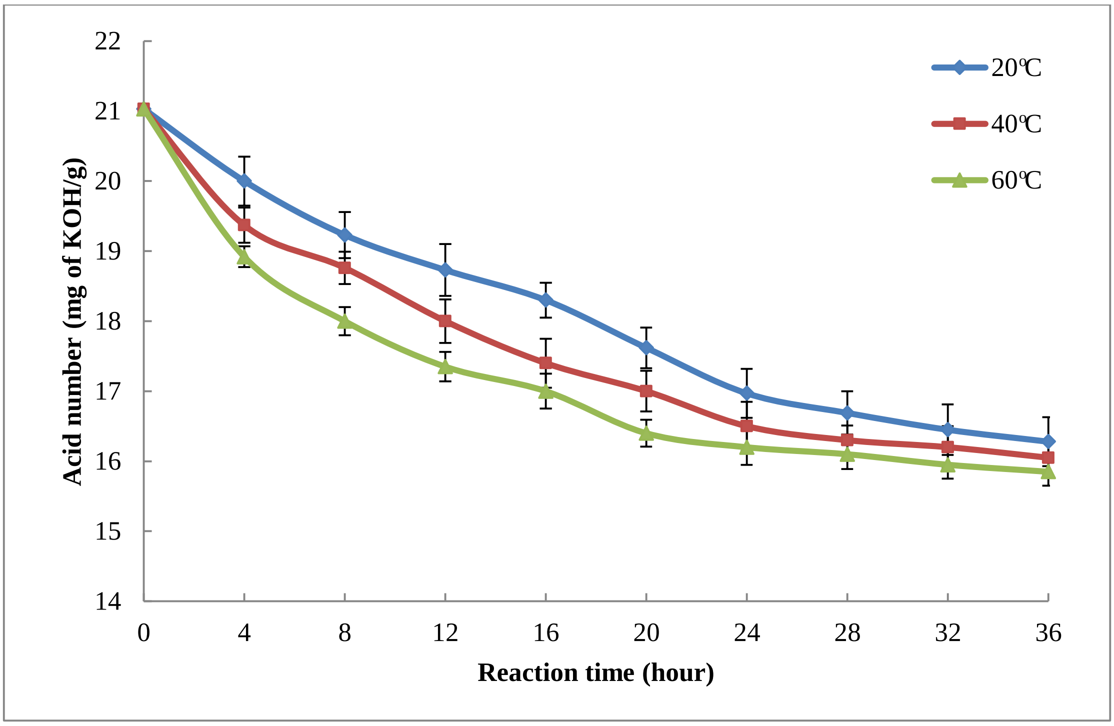

Figure 7.4 Ozonolysis of used cooking oil at 10% FFAs

7.3.2 GC-MS

Figure 7.5 shows the chromatogram of 20% FFAs ozonolysis of at 20°C, 40°C, and 60°C for 32 hours. At 20°C, NN is observed as the major short-chain product, as shown in Figure 7.5A, whereas M-OL and M-PA are considered to be the major long-chain products. Although M-PA and M-OL are detected, an amount of PA and OL still remains in the system, which is similar to OL ozonolysis in that certain of the carboxylic acids convert to methyl ester in the presence of methanol. In case of ozonolysis at 40°C, as shown in Figure 7.5B, the amount of OL and PA decreases slightly, resulting in a slight increase of NN, M-PA, and M-OL. The increase of NN and decrease of OL are due to the increase of the Henry's Law constant, diffusion coefficient, and specific interfacial area at higher temperatures, as discussed in Chapter 5 and Chapter 6, respectively. For ozonolysis at 60°C, as shown in Figure 7.5C, a greater amount of NN, M-PA, and M-OL is observed compared with that of 20°C and 40°C ozonolysis, whereas no peak of PA was detected after 16 hours of ozonolysis. Moreover, although both SA and MA were added into the mixtures, no peaks of these compounds or their relative products, i.e., M-SA and M-MA, were observed because the concentration of the samples injected into the GC-MS is quite low. However, it might be assumed that the reactivities of both SA and MA are similar to that of PA.

In addition to the observation from the chromatograms, the mole balances of PA and M-PA were examined. Although no peak for PA was observed after 16 hours of 60°C ozonolysis, the peak of M-PA still increases up to 20 hours, which means that PA is not simultaneously converted to M-PA; nevertheless, it is converted to unknown species. Such species subsequently decompose to M-PA. However, this result proves that PA is completely converted to M-PA within 20 hours of ozonolysis at 60°C.

Similar to high temperature ozonolysis, most PA is converted to unknown species in low temperature ozonolysis. A difference is that a small amount of unknown species decompose to M-PA. In the case of 20°C and 40°C ozonolysis, for example, the loss of PA is approximately 100% over 32 hours, whereas the formations of M-PA are 16.38% and 35.28%, respectively, which means that the formation of M-PA from unknown species is a function of temperature. In other words, the decomposition rate appears to behave in an Arrhenius manner.

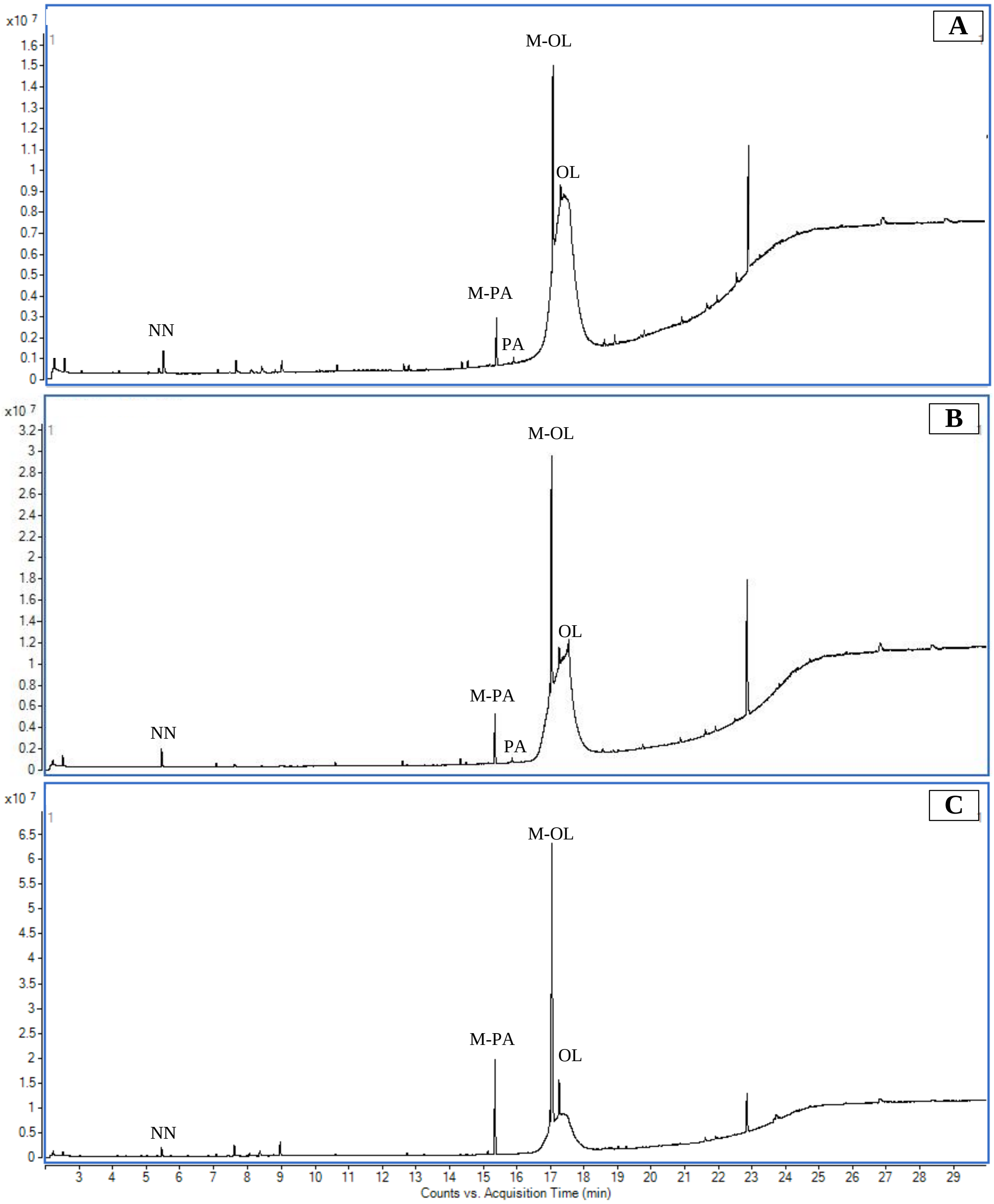

Figure 7.5 Chromatogram of ozonolysis of used cooking oil at 20% FFAs for 32 hrs:

A = 20°C, B = 40°C, and C = 60°C

Considering the mole balances of OL and M-OL, the results show that OL is converted to M-OL by 19.46% and 43.79% at 20°C and at 40°C, respectively. The highest conversion of OL to form M-OL is found at 60°C by 91.16%, which means that only OL at 8.84% remains in the system after 32 hours because all of the saturated fatty acids transform to methyl esters, as described previously. Based on the results provided by GC-MS, the percentage of FFAs must be less than 1.33%. This result proves that ozonolysis of used cooking oil is a suitable technique for reduction of free fatty acid content prior to use in biodiesel production.

It is surprising that the results provided by GC-MS are not in good agreement with those provided by ASTM D974. One assumption is that the ASTM D974 technique might have interfered with certain products from ozonolysis of OL and olive oil, as described in Chapter 5 and Chapter 6, respectively. This hypothesis is supported by the change in acid number with reaction time, which decreases sharply at the beginning of ozonolysis and subsequently plateaus. The reason for this observation is that the reaction rate of esterification is higher than that of ozonolysis, resulting in a substantial loss of FFAs. After most of the FFAs are converted to methyl esters, the remaining OL and olive oil still react with ozone to form NN and other products. The loss of OL and the formation of such products are the same, leading to the constant acid numbers. Another supporting piece of evidence is that identical features of the reduction in acid numbers are observed at all different percentages of FFAs. However, further study of the ozonolysis products that affect the determination of acid number is necessary.

7.4 Summary

Ozonolysis of used cooking oils at 10%, 15%, and 20% FFAs were performed at various temperatures. Two techniques were employed to characterise the FFAs content, i.e., ASTM D974 and GC-MS. Using the ASTM D974 technique, the acid numbers decrease dramatically by approximately 25% and subsequently plateau. Similar features of the reduction in acid numbers are observed at all different percentages of FFAs. The lowest values of acid numbers are found in 60°C ozonolysis. Using GC-MS, all of the saturated FFAs, i.e., PA, SA, and MA, convert to methyl esters within 20 hours of 60°C ozonolysis, whereas a small amount remain at lower temperatures. Moreover, after 32 hours of 20% FFAs ozonolysis at 60°C, the conversion of OL is found to be 91.16%, indicating that the FFAs content in used cooking oil is less than 1.33%. This observation confirms that ozonolysis of used cooking oil is an alternative technique for reduction of free fatty acid content for biodiesel production.

CHAPTER 8

GENERAL CONCLUSIONS AND SUGGESTIONS FOR FUTURE WORK

8.1 General conclusions

In this thesis, ozonolysis of oleic acid, olive oil, and used cooking oil was performed via bubbling technique at 20°C, 40°C, and 60°C to upgrade these biofuels for formation of valuable chemicals. The bubble column reactor used in this study was designed using Aspen Plus, COMSOL Multiphysics, and COMSOL Reaction Engineering Lab, and the condenser was designed with Aspen Plus only. Two techniques were used to generate bubbles, i.e., with and without a fluidic oscillator. Protic solvents, i.e., methanol, ethanol, iso-propanol, n-propanol, and n-butanol, were added to oleic acid for the purpose of increasing productivity, whereas methanol was added only to olive oil. Four crucial parameters used for the reaction rate constant calculation were evaluated, i.e., Henry's Law constant, diffusion coefficient, inlet ozone concentration, and specific interfacial area. The Henry's Law constant and the diffusion coefficient of ozone in the solvents were determined using Aspen Plus. The specific interfacial area and the inlet ozone concentration were determined using an optical technique (high-speed camera) and the KI method, respectively. The decomposition of ozone at different temperatures was studied using COMSOL Reaction Engineering Lab. The fluid properties of the solvents, i.e., molecular weight, density, and surface tension, were also estimated using Aspen Plus. Moreover, transesterification of ozonised olive oil was performed to produce bio-kerosene or other valuable products. All samples collected in this study were analysed by GC-MS.

In addition to ozonolysis of oleic acid and olive oil, ozonolysis of used cooking oil mixed with methanol was performed to reduce the free fatty acid content for biodiesel production. Both GC-MS and ASTM D974 were used to analyse the reduction of free fatty acid content.

8.1.1 Ozonolysis of OL

***Pure ozonolysis*:** Two expected short-chain products, i.e., 1-nonanal and 9-oxononanoic acid, are observed during ozonolysis. The amount of these products increases with reaction time and temperature. Following pathway 1, 1-nonanal is the major short-chain product with 93.5±3.4% yield. No sign of Criegee intermediates and their relative products, i.e., azelaic acid and nonanoic acid, are detected at all studied temperatures. Additional short-chain products are found in 40°C and 60°C ozonolysis. These products are formed by the decomposition of higher molecular species, which are formed in the secondary reaction between Criegee intermediates and oleic acid. Moreover, ozonolysis of oleic acid was found to be a fast pseudo-first-order reaction, and the reaction rate constant at 20°C is 9.19 $\times 10^5$ $M^{-1}s^{-1}$.

***Mixed with protic solvents ozonolysis*:** The 1-nonanal is observed as the short-chain product, and its yield increases with addition of alcohols. The increase of this aldehyde is a result of the increase of the Henry's Law constant, diffusion coefficient, and specific interfacial area. The Criegee intermediates and all carboxylic acids observed during pure oleic acid ozonolysis are converted to alkyl esters via esterification depending on the molecular structure of the alcohols. The reaction rate of esterification is a function of temperature that behaves in an Arrhenius manner. The reaction rate of ozonolysis of OL is as same as that of esterification at low temperature but is much lower at high temperatures. Compared with many alcohols, methanol is the best protic solvent for increasing the productivity of 1-nonanal. The optimum molar ratio of methanol to oleic acid is 1:1. Moreover, the amount of 1-nonanal increases by 30% if the system is connected with the fluidic oscillator.

8.1.2 Ozonolysis of olive oil

***Pure ozonolysis and transesterification*:** A short-chain product observed during ozonolysis is 1-nonanal, and its concentration increases with time and temperature. A short-chain triglyceride ending with Criegee intermediate 1 is the by-product, although it is undetected by GC-MS. The reaction rate constant of olive oil ozonolysis at 20°C is estimated to be 4.88 $\times 10^8$ $M^{-1}s^{-1}$.

In case of transesterification of short-chain triglycerides, 9-oxononanoic methyl ester is the major short-chain ester, and nonanoic acid methyl ester, octanoic acid methyl ester and azelaic acid dimethyl ester are considered to be the minor short-chain esters.

***Olive oil and methanol ozonolysis and transesterification*:** Two short-chain products, i.e., 1-nonanal and nonanoic methyl ester, are observed. The major product is 1-nonanal with 88.0±2.6% yield, and the minor product is nonanoic methyl ester. Two short-chain triglycerides ending with Criegee intermediate 1 and Criegee intermediate 2 are considered the by-products. Moreover, a yield of 6.6±0.23% for short-chain triglycerides ending with Criegee intermediate 1 decomposes to short-chain triglycerides ending with octanoic acid.

In the case of transesterification of short-chain triglycerides, azelaic acid dimethyl ester is the major product. The liquid volume fractions of short-chain methyl esters, i.e., nonanoic acid methyl ester, 9-oxononanoic methyl ester, azelaic acid dimethyl ester, and octanoic acid methyl ester, are 0.093, 0.08, 0.776, and 0.052, respectively. Based on this result, ozonolysis one mole of olive oil (OOO) in methanol followed by transesterification can produce 2.64 moles of 1-nonanal, 2.46 moles of azelaic acid dimethyl ester, 0.18 moles of octanoic acid methyl ester, 0.36 moles of nonanoic acid methyl ester, and 0.36 moles of 9-oxononanoic methyl ester. Moreover, the productivity of 1-nonanal increases by 43.8±2.5% if the fluidic oscillator is used to generate bubbles.

8.1.3 Ozonolysis of used cooking oil

The acid numbers in used cooking oil as determined by ASTM D974 decrease by 25% during 36 hours of ozonolysis. The lowest value is found for 60°C ozonolysis, and higher values are found at lower temperature ozonolysis. Moreover, it is obvious that for all free fatty acid contents, the acid numbers decrease dramatically at the beginning of ozonolysis and subsequently plateau.

In case of analysis by GC-MS, all saturated free fatty acids are converted to methyl esters within 20 hours of 60°C ozonolysis, whereas a small amount of these materials remains at lower temperature ozonolysis. The conversion of oleic acid to form oleic acid methyl ester is 91.16% at 60°C ozonolysis, resulting in the reduction of free fatty acid content in used cooking oil to less than 1.33% after 32 hours of ozonolysis.

8.2 Suggestions for future work

Based on the experimental results from Chapter 5 to Chapter 7, many interesting points of ozonolysis are available for further study.

8.2.1 Ozonolysis of OL

1. Because the inlet ozone concentration used in this study is low, higher concentrations up to that of commercial production (20% by volume) could be used to observe the effect of exothermic reaction and product formation.

2. The reaction mechanism used to form higher molecular weight products, the decomposition mechanism that forms lower molecular weight products, and the optimum decomposition temperature should all be studied.

3. In case of addition of alcohols, the reaction mechanism of esterification and the optimum temperature should be investigated.

8.2.2 Ozonolysis of olive oil

1. Ozonolysis of different plant oils, which contain many double bonds, should be studied for bio-kerosene or bio-gasoline production.

2. Because the fluid properties of bio-kerosene estimated in this study do not meet the standards for petroleum kerosene, the optimum mixing percentages should be investigated.

8.2.3 Ozonolysis of used cooking oil

1. Because the used cooking oil employed in this study was prepared by adding free fatty acids into fresh cooking oil, ozonolysis of used cooking oil from restaurants and households could be studied.

2. The effect of products formed during ozonolysis on the determination of acid numbers by ASTM D974 could be examined.

References

Akbas, M. Y. and Ozdemir, M. (2008) 'Application of gaseous ozone to control populations of Escherichia coli, Bacillus cereus and Bacillus cereus spores in dried figs', *Food Microbiology*, 25(2), 386-391.

Akita, K. and Yoshida, F. (1974) 'Bubble size, interfacial area, and liquid phase mass-transfer coefficient in bubble columns', *Industrial & Engineering Chemistry Process Design and Development*, 13(1), 84-91.

Amaya-Bower, L. and Lee, T. (2011) 'Numerical simulation of single bubble rising in vertical and inclined square channel using lattice Boltzmann method', *Chemical Engineering Science*, 66(5), 935-952.

Aransiola, E. F., Ojumu, T. V., Oyekola, O. O., Madzimbamuto, T. F. and Ikhu-Omoregbe, D. I. O. (2014) 'A review of current technology for biodiesel production: State of the art', *Biomass & Bioenergy*, 61, 276-297.

Azarpazhooh, A. and Limeback, H. (2008) 'The application of ozone in dentistry: A systematic review of literature', *Journal of Dentistry*, 36(2), 104-116.

Bailey, P. S. (1978) *Ozonation in organic chemistry*, New York: Academic Press.

Balat, M. (2011) 'Potential alternatives to edible oils for biodiesel production - A review of current work', *Energy Conversion and Management*, 52(2), 1479-1492.

Batista, E., Monnerat, S., Kato, K., Stragevitch, L. and Meirelles, A. J. A. (1999) 'Liquid-liquid equilibrium for systems of canola oil, oleic acid, and short-chain alcohols', *Journal of Chemical and Engineering Data*, 44(6), 1360-1364.

Battino, R., Evans, F. D. and Danforth, W. F. (1968) 'Solubilities of 7 gases in olive oil with reference to theories of transport through cell membrane', *Journal of the American Oil Chemists Society*, 45(12), 830.

Becker, K. H. (2005) *Non-equilibrium air plasmas at atmospheric pressure*, Bristol: Institute of Physics Publishing.

Beltrán, F. J. (2004) *Ozone reaction kinetics for water and wastewater systems*, Boca Raton, Fla.: Lewis Publishers.

Benson, S. W. and Axworthy, A. E. (1957) 'Mechanism of the gas phase, thermal decomposition of ozone', *Journal of Chemical Physics*, 26(6), 1718-1726.

Berrios, M. and Skelton, R. L. (2008) 'Comparison of purification methods for biodiesel', *Chemical Engineering Journal*, 144(3), 459-465.

Biermann, U., Bornscheuer, U., Meier, M. A. R., Metzger, J. O. and Schaefer, H. J. (2011) 'Oils and Fats as Renewable Raw Materials in Chemistry', *Angewandte Chemie-International Edition*, 50(17), 3854-3871.

Bouaifi, M., Hebrard, G., Bastoul, D. and Roustan, M. (2001) 'A comparative study of gas hold-up, bubble size, interfacial area and mass transfer coefficients in stirred gas-liquid reactors and bubble columns', *Chemical Engineering and Processing*, 40(2), 97-111.

Brackbill, J. U., Kothe, D. B. and Zemach, C. (1992) 'A continuum method for modelling surface-tension', *Journal of Computational Physics*, 100(2), 335-354.

Brown, T. L. (2006) *Chemistry : the central science*, AP* - 10th ed., Upper Saddle River, N.J.: Pearson-Prentice Hall.

Canakci, M. and Van Gerpen, J. (2001) 'Biodiesel production from oils and fats with high free fatty acids', *Transactions of the Asae*, 44(6), 1429-1436.

Chaix, E., Guillaume, C. and Guillard, V. (2014) 'Oxygen and Carbon Dioxide Solubility and Diffusivity in Solid Food Matrices: A Review of Past and Current Knowledge', *Comprehensive Reviews in Food Science and Food Safety*, 13(3), 261-286.

Clift, R., Grace, J. R. and Weber, M. E. (1978) *Bubbles, drops, and particles*, New York ; London: Academic Press.

Conrads, H. and Schmidt, M. (2000) 'Plasma generation and plasma sources', *Plasma Sources Science & Technology*, 9(4).

Criegee, R. (1975) 'Mechanism of ozonolysis', *Angewandte Chemie-International Edition in English*, 14(11), 745-752.

Degaleesan, S., Dudukovic, M. and Pan, Y. (2001) 'Experimental study of gas-induced liquid-flow structures in bubble columns', *Aiche Journal*, 47(9), 1913-1931.

Diaz, M. F., Hernandez, R., Martinez, G., Vidal, G., Gomez, M., Fernandez, H. and Garces, R. (2006) 'Comparative study of ozonized olive oil and ozonized sunflower oil', *Journal of the Brazilian Chemical Society*, 17(2), 403-407.

Dimitrios, B. (2006) *Olive Oil : Chemistry and Technology*, Second ed., AOCS.

Eliasson, B. and Kogelschatz, U. (1991) 'Nonequilibrium volume plasma chemical-processing', *Ieee Transactions on Plasma Science*, 19(6).

Fang, J. S. E., Kawamura, K., Ishimura, Y. and Matsumoto, K. (2002) 'Carbon isotopic composition of fatty acids in the marine aerosols from the Western North Pacific: Implication for the source and atmospheric transport', *Environmental Science & Technology*, 36(12), 2598-2604.

Finlayson-Pitts, B. J. and Pitts, J. N. (2000) *Chemistry of the upper and lower atmosphere : theory, experiments and applications*, San Diego, Calif. ; London: Academic Press.

Fogler, H. S. (2006) *Elements of chemical reaction engineering*, 4th ed., Upper Saddle River, N.J.: Prentice Hall PTR.

Galtier, O., Dupuy, N., Le Dreau, Y., Ollivier, D., Pinatec, C., Kister, J. and Artaud, J. (2007) 'Geographic origins and compositions of virgin olive oils determinated by chemometric analysis of NIR spectra', *Analytica Chimica Acta*, 595(1-2), 136-144.

Garcia-Salas, S., Alfaro, M. E. R. P., Porter, R. M. and Thalasso, F. (2008) 'Measurement of local specific interfacial area in bubble columns via a non-isokinetic withdrawal method coupled to electro-optical detector', *Chemical Engineering Science*, 63(4), 1029-1038.

Gerlach, D., Alleborn, N., Buwa, V. and Durst, E. (2007) 'Numerical simulation of periodic bubble formation at a submerged orifice with constant gas flow rate', *Chemical Engineering Science*, 62(7), 2109-2125.

Gnyloskurenko, S. V., Byakova, A. V., Raychenko, O. I. and Nakamura, T. (2003) 'Influence of wetting conditions on bubble formation at orifice in an inviscid liquid. Transformation of bubble shape and size', *Colloids and Surfaces a-Physicochemical and Engineering Aspects*, 218(1-3), 73-87.

Gonzalez-Labrada, E., Schmidt, R. and DeWolf, C. E. (2007) 'Kinetic analysis of the ozone processing of an unsaturated organic monolayer as a model of an aerosol surface', *Physical Chemistry Chemical Physics*, 9(43), 5814-5821.

Gottschalk, C., Libra, J. A. and Saupe, A. (2009) *Ozonation of Water and Waste Water [electronic resource] : A Practical Guide to Understanding Ozone and its Applications*, 2nd ed., Chichester: John Wiley & Sons.

Haapala, A., Honkanen, M., Liimatainen, H., Stoor, T. and Niinimaki, J. (2010) 'Hydrodynamic drag and rise velocity of microbubbles in papermaking process waters', *Chemical Engineering Journal*, 162(3), 956-964.

Hanotu, J., Bandulasena, H. C. H. and Zimmerman, W. B. (2012) 'Microflotation performance for algal separation', *Biotechnology and Bioengineering*, 109(7), 1663-1673.

Hayyan, A., Alam, M. Z., Mirghani, M. E. S., Kabbashi, N. A., Hakimi, N. I. N. M., Siran, Y. M. and Tahiruddin, S. (2011) 'Reduction of high content of free fatty acid in sludge palm oil via acid catalyst for biodiesel production', *Fuel Processing Technology*, 92(5), 920-924.

Hearn, J. D., Lovett, A. J. and Smith, G. D. (2005) 'Ozonolysis of oleic acid particles: evidence for a surface reaction and secondary reactions involving Criegee intermediates', *Physical Chemistry Chemical Physics*, 7(3), 501-511.

Hearn, J. D. and Smith, G. D. (2004) 'Kinetics and product studies for ozonolysis reactions of organic particles using aerosol CIMS', *Journal of Physical Chemistry A*, 108(45), 10019-10029.

Heimerl, J. M. and Coffee, T. P. (1980) 'The detailed modelling of premixed, laminar steady state flames. 1. ozone', *Combustion and Flame*, 39(3), 301-315.

Hirata, G. F., Abreu, C. R. A., Bessa, L. C. B. A., Ferreira, M. C., Batista, E. A. C. and Meirelles, A. J. A. (2013) 'Liquid-liquid equilibrium of fatty systems: A new approach for adjusting UNIFAC interaction parameters', *Fluid Phase Equilibria*, 360, 379-391.

Hung, H.-M. and Ariya, P. (2007) 'Oxidation of oleic acid and oleic acid/sodium chloride(aq) mixture droplets with ozone: Changes of hygroscopicity and role of secondary reactions', *Journal of Physical Chemistry A*, 111(4), 620-632.

Hung, H.-M. and Tang, C.-W. (2010) 'Effects of Temperature and Physical State on Heterogeneous Oxidation of Oleic Acid Droplets with Ozone', *Journal of Physical Chemistry A*, 114(50), 13104-13112.

Hung, H. M., Katrib, Y. and Martin, S. T. (2005) 'Products and mechanisms of the reaction of oleic acid with ozone and nitrate radical', *Journal of Physical Chemistry A*, 109(20), 4517-4530.

Hyndman, C. L., Larachi, F. and Guy, C. (1997) 'Understanding gas-phase hydrodynamics in bubble columns: A convective model based on kinetic theory', *Chemical Engineering Science*, 52(1), 63-77.

Incropera, F. P. (2011) *Fundamentals of heat and mass transfer / Frank P. Incropera ... [et al.]*, 7th ed., Hoboken, N.J.: Wiley.

Ivanov, A. V., Trakhtenberg, S., Bertram, A. K., Gershenzon, Y. M. and Molina, M. J. (2007) 'OH, HO2, and ozone gaseous diffusion coefficients', *Journal of Physical Chemistry A*, 111(9), 1632-1637.

Iwahashi, M., Kasahara, Y., Matsuzawa, H., Yagi, K., Nomura, K., Terauchi, H., Ozaki, Y. and Suzuki, M. (2000) 'Self-diffusion, dynamical molecular conformation, and liquid structures of n-saturated and unsaturated fatty acids', *Journal of Physical Chemistry B*, 104(26), 6186-6194.

Janssen, M., Wilting, J., Muller, C. and Vogt, D. (2010) 'Continuous Rhodium-Catalyzed Hydroformylation of 1-Octene with Polyhedral Oligomeric Silsesquioxanes (POSS) Enlarged Triphenylphosphine', *Angewandte Chemie-International Edition*, 49(42), 7738-7741.

Kantarci, N., Borak, F. and Ulgen, K. O. (2005) 'Bubble column reactors', *Process Biochemistry*, 40(7).

Katrib, Y., Biskos, G., Buseck, P. R., Davidovits, P., Jayne, J. T., Mochida, M., Wise, M. E., Worsnop, D. R. and Martin, S. T. (2005) 'Ozonolysis of mixed oleic-acid/stearic-acid particles: Reaction kinetics and chemical morphology', *Journal of Physical Chemistry A*, 109(48), 10910-10919.

Katrib, Y., Martin, S. T., Hung, H. M., Rudich, Y., Zhang, H. Z., Slowik, J. G., Davidovits, P., Jayne, J. T. and Worsnop, D. R. (2004) 'Products and mechanisms of ozone reactions with oleic acid for aerosol particles having core-shell morphologies', *Journal of Physical Chemistry A*, 108(32), 6686-6695.

Khadre, M. A., Yousef, A. E. and Kim, J. G. (2001) 'Microbiological aspects of ozone applications in food: A review', *Journal of Food Science*, 66(9), 1242-1252.

King, M. D., Rennie, A. R., Thompson, K. C., Fisher, F. N., Dong, C. C., Thomas, R. K., Pfrang, C. and Hughes, A. V. (2009) 'Oxidation of oleic acid at the air-water interface and its potential effects on cloud critical supersaturations', *Physical Chemistry Chemical Physics*, 11(35), 7699-7707.

Knopf, D. A., Anthony, L. M. and Bertram, A. K. (2005) 'Reactive uptake of O-3 by multicomponent and multiphase mixtures containing oleic acid', *Journal of Physical Chemistry A*, 109(25), 5579-5589.

Koeken, A. C. J., van den Broeke, L. J. P., Deelman, B.-J. and Keurentjes, J. T. F. (2011) 'Full kinetic description of 1-octene hydroformylation in a supercritical medium', *Journal of Molecular Catalysis a-Chemical*, 346(1-2), 1-11.

Krishna, R., Urseanu, M. I., van Baten, J. M. and Ellenberger, J. (1999) 'Wall effects on the rise of single gas bubbles in liquids', *International Communications in Heat and Mass Transfer*, 26(6), 781-790.

Kulkarni, A. A. and Joshi, J. B. (2005) 'Bubble formation and bubble rise velocity in gas-liquid systems: A review', *Industrial & Engineering Chemistry Research*, 44(16), 5873-5931.

Laisk, A., Kull, O. and Moldau, H. (1989) 'Ozone concentration in leaf intercellular air spaces is close to zero', *Plant Physiology*, 90(3), 1163-1167.

Last, D. J., Najera, J. J., Wamsley, R., Hilton, G., McGillen, M., Percival, C. J. and Horn, A. B. (2009) 'Ozonolysis of organic compounds and mixtures in solution. Part I: Oleic, maleic, nonanoic and benzoic acids', *Physical Chemistry Chemical Physics*, 11(9), 1427-1440.

Lee, J. W. L., Carrascon, V., Gallimore, P. J., Fuller, S. J., Bjoerkegren, A., Spring, D. R., Pope, F. D. and Kalberer, M. (2012) 'The effect of humidity on the ozonolysis of unsaturated compounds in aerosol particles', *Physical Chemistry Chemical Physics*, 14(22), 8023-8031.

Leifer, I., Patro, R. K. and Bowyer, P. (2000) 'A study on the temperature variation of rise velocity for large clean bubbles', *Journal of Atmospheric and Oceanic Technology*, 17(10), 1392-1402.

Levich, V. G. (1962) *Physicochemical hydrodynamics*, Englewood Cliffs, N.J.: Prentice-Hall.

Limpert, E., Stahel, W. A. and Abbt, M. (2001) 'Log-normal distributions across the sciences: Keys and clues', *Bioscience*, 51(5), 341-352.

Linstromberg, W. W. (1970) *Organic Chemistry*, Second Edition ed., Lexington, Massachusetts: D.C. Heath and Company.

Lozano-Parada, J. H. and Zimmerman, W. B. (2010) 'The role of kinetics in the design of plasma microreactors', *Chemical Engineering Science*, 65(17), 4925-4930.

Luo, X., Zhang, J., Tsuchiya, K. and Fan, L. S. (1997) 'On the rise velocity of bubbles in liquid-solid suspensions at elevated pressure and temperature', *Chemical Engineering Science*, 52(21-22), 3693-3699.

Luo, X. K., Yang, G. Q., Lee, D. J. and Fan, L. S. (1998) 'Single bubble formation in high pressure liquid-solid suspensions', *Powder Technology*, 100(2-3), 103-112.

Ma, D., Liu, M., Zu, Y. and Tang, C. (2012) 'Two-dimensional volume of fluid simulation studies on single bubble formation and dynamics in bubble columns', *Chemical Engineering Science*, 72, 61-77.

Masschelein, W. J. (1998) 'Measurement of high ozone concentrations in gases by KI titration and monitoring by UV-absorption (Also, on the design of iodometric washing flasks) (Reprinted from Proceedings of 13th Ozone World Congress, Kyoto, 1997)', *Ozone-Science & Engineering*, 20(6), 489-493.

Meher, L. C., Sagar, D. V. and Naik, S. N. (2006) 'Technical aspects of biodiesel production by transesterification - a review', *Renewable & Sustainable Energy Reviews*, 10(3), 248-268.

Metzger, J. O. (2009) 'Fats and oils as renewable feedstock for chemistry', *European Journal of Lipid Science and Technology*, 111(9), 865-876.

Mochida, M., Katrib, Y., Jayne, J. T., Worsnop, D. R. and Martin, S. T. (2006) 'The relative importance of competing pathways for the formation of high-molecular-weight peroxides in the ozonolysis of organic aerosol particles', *Atmospheric Chemistry and Physics*, 6, 4851-4866.

Mochida, M., Kitamori, Y., Kawamura, K., Nojiri, Y. and Suzuki, K. (2002) 'Fatty acids in the marine atmosphere: Factors governing their concentrations and evaluation of organic films on sea-salt particles', *Journal of Geophysical Research-Atmospheres*, 107(D17).

Moise, T. and Rudich, Y. (2002) 'Reactive uptake of ozone by aerosol-associated unsaturated fatty acids: Kinetics, mechanism, and products', *Journal of Physical Chemistry A*, 106(27), 6469-6476.

Morris, J. W., Davidovits, P., Jayne, J. T., Jimenez, J. L., Shi, Q., Kolb, C. E., Worsnop, D. R., Barney, W. S. and Cass, G. (2002) 'Kinetics of submicron oleic acid aerosols with ozone: A novel aerosol mass spectrometric technique', *Geophysical Research Letters*, 29(15).

NIST (2011) *Material Measurement Laboratory, The U.S. Secretary of Commerce*: http://webbook.nist.gov.

Noor, I. M., Hasan, M. and Ramachandran, K. B. (2003) 'Effect of operating variables on the hydrolysis rate of palm oil by lipase', *Process Biochemistry*, 39(1), 13-20.

Omonov, T. S., Kharraz, E. and Curtis, J. M. (2011) 'Ozonolysis of Canola Oil: A Study of Product Yields and Ozonolysis Kinetics in Different Solvent Systems', *Journal of the American Oil Chemists Society*, 88(5), 689-705.

Parkinson, L., Sedev, R., Fornasiero, D. and Ralston, J. (2008) 'The terminal rise velocity of 10-100 mu m diameter bubbles in water', *Journal of Colloid and Interface Science*, 322(1), 168-172.

Peri, C. (2014) *The Extra-Virgin Olive Oil Handbook*, First ed., John Wiley & Sons.

Pfrang, C., Sebastiani, F., Lucas, C. O. M., King, M. D., Hoare, I. D., Chang, D. and Campbell, R. A. (2014) 'Ozonolysis of methyl oleate monolayers at the air-water interface: oxidation kinetics, reaction products and atmospheric implications', *Physical Chemistry Chemical Physics*, 16(26), 13220-13228.

Pietsch, G. J. and Gibalov, V. I. (1998) 'Dielectric barrier discharges and ozone synthesis', *Pure and Applied Chemistry*, 70(6), 1169-1174.

Plaue, J. W. and Czerwinski, K. R. (2003) 'The influence of ozone on ligand-assisted extraction of Pu-239 and Am-241 from Rocky Flats soil', *Radiochimica Acta*, 91(6), 309-313.

Poling, B. E., Prausnitz, J. M. and O'Connell, J. P. (2000) *The properties of gases and liquids*, 5th ed., New York: McGraw-Hill.

Ponter, A. B. and Surati, A. I. (1997) 'Bubble emissions from submerged orifices - A critical review', *Chemical Engineering & Technology*, 20(2), 85-89.

Pryor, W. A., Squadrito, G. L. and Friedman, M. (1995) 'The cascade mechanism to explain ozone toxicity- the role of lipid ozonation products', *Free Radical Biology and Medicine*, 19(6), 935-941.

Rakness, K., Gordon, G., Langlais, B., Masschelein, W., Matsumoto, N., Richard, Y., Robson, C. M. and Somiya, I. (1996) 'Guideline for measurement of ozone concentration in the process gas from an ozone generator', *Ozone-Science & Engineering*, 18(3).

Rakovsky, G. E. Z. K. (2009) *Ozonation of Organic and Polymer Compounds*, Shawbury, Shrewsbury, Shropshire, SY4 4NR, UK: *i*Smithers.

Rebrovic, L. (1992) 'The peroxidic species generated by ozonolysis of oleic acid or methyl oleate in a carboxylic acid medium', *Journal of the American Oil Chemists Society*, 69(2), 159-165.

Robinson, A. L., Subramanian, R., Donahue, N. M., Bernardo-Bricker, A. and Rogge, W. F. (2006) 'Source apportionment of molecular markers and organic aerosol. 3. Food cooking emissions', *Environmental Science & Technology*, 40(24), 7820-7827.

Rosen, E. P., Garland, E. R. and Baer, T. (2008) 'Ozonolysis of Oleic Acid Adsorbed to Polar and Nonpolar Aerosol Particles', *Journal of Physical Chemistry A*, 112(41), 10315-10324.

Russbueldt, B. M. E. and Hoelderich, W. F. (2009) 'New sulfonic acid ion-exchange resins for the preesterification of different oils and fats with high content of free fatty acids', *Applied Catalysis a-General*, 362(1-2), 47-57.

Sadowska, J., Johansson, B., Johannessen, E., Friman, R., Bronlarz-Press, L. and Rosenholm, J. B. (2008) 'Characterization of ozonated vegetable oils by spectroscopic and chromatographic methods', *Chemistry and Physics of Lipids*, 151(2), 85-91.

Sage, A. M., Weitkamp, E. A., Robinson, A. L. and Donahue, N. M. (2009) 'Reactivity of oleic acid in organic particles: changes in oxidant uptake and reaction stoichiometry with particle oxidation', *Physical Chemistry Chemical Physics*, 11(36), 7951-7962.

Sam, A., Gomez, C. O. and Finch, J. A. (1996) 'Axial velocity profiles of single bubbles in water/frother solutions', *International Journal of Mineral Processing*, 47(3-4), 177-196.

Sander, R. (1999) 'Modeling atmospheric chemistry: Interactions between gas-phase species and liquid cloud/aerosol particles', *Surveys in Geophysics*, 20(1), 1-31.

Sarin, A. (2012) *Biodiesel : production and properties*, Cambridge: Royal Society of Chemistry.

Satyarthi, J. K., Srinivas, D. and Ratnasamy, P. (2011) 'Hydrolysis of vegetable oils and fats to fatty acids over solid acid catalysts', *Applied Catalysis a-General*, 391(1-2), 427-435.

Schauer, J. J., Kleeman, M. J., Cass, G. R. and Simoneit, B. R. T. (1999) 'Measurement of emissions from air pollution sources. 1. C-1 through C-29 organic compounds from meat charbroiling', *Environmental Science & Technology*, 33(10), 1566-1577.

Sehested, K., Corfitzen, H., Holcman, J., Fischer, C. H. and Hart, E. J. (1991) 'The primary reaction in the decomposition of ozone in acidic aqueous solutions', *Environmental Science & Technology*, 25(9), 1589-1595.

Smith, G. D., Woods, E., DeForest, C. L., Baer, T. and Miller, R. E. (2002) 'Reactive uptake of ozone by oleic acid aerosol particles: Application of single-particle mass spectrometry to heterogeneous reaction kinetics', *Journal of Physical Chemistry A*, 106(35), 8085-8095.

Smith, J. M., Van Ness, H. C. and Abbott, M. M. (2005) *Introduction to chemical engineering thermodynamics*, 7th ed., Boston: McGraw-Hill.

Soriano, N. U., Migo, V. P. and Matsumura, M. (2003) 'Ozonation of sunflower oil: Spectroscopic monitoring of the degree of unsaturation', *Journal of the American Oil Chemists Society*, 80(10), 997-1001.

Soriano, N. U., Migo, V. P. and Matsumura, M. (2006) 'Ozonized vegetable oil as pour point depressant for neat biodiesel', *Fuel*, 85(1), 25-31.

Sung, Y. M. and Sakoda, T. (2005) 'Optimum conditions for ozone formation in a micro dielectric barrier discharge', *Surface & Coatings Technology*, 197(2-3), 148-153.

Surburg, H., Panten, J. and Bauer, K. C. f. a. f. m. (2006) *Common fragrance and flavor materials : preparation, properties and uses*, 5th completely revised and enlarged ed. / Horst Surburg and Johannes Panten. ed., Weinheim: Wiley-VCH ; [Chichester : John Wiley, distributor].

Tesar, V., Hung, C. H. and Zimmerman, W. B. (2006) 'No-moving-part hybrid-synthetic jet actuator', *Sensors and Actuators a-Physical*, 125(2), 159-169.

Thornberry, T. and Abbatt, J. P. D. (2004) 'Heterogeneous reaction of ozone with liquid unsaturated fatty acids: detailed kinetics and gas-phase product studies', *Physical Chemistry Chemical Physics*, 6(1), 84-93.

Tiwari, B. K., Brennan, C. S., Curran, T., Gallagher, E., Cullen, P. J. and Donnell, C. P. (2010) 'Application of ozone in grain processing', *Journal of Cereal Science*, 51(3), 248-255.

Vesna, O., Sax, M., Kalberer, M., Gaschen, A. and Ammann, M. (2009) 'Product study of oleic acid ozonolysis as function of humidity', *Atmospheric Environment*, 43(24), 3662-3669.

Vesna, O., Sjogren, S., Weingartner, E., Samburova, V., Kalberer, M., Gaeggeler, H. W. and Ammann, M. (2008) 'Changes of fatty acid aerosol hygroscopicity induced by ozonolysis under humid conditions', *Atmospheric Chemistry and Physics*, 8(16), 4683-4690.

Waddell, W. J., Cohen, S. P., Feron, J. V. and Goodman, I. J. (2007) *Flavoring substances 23*, Chicago: Institute of Food Technologists.

Wilhelm, E., Battino, R. and Wilcock, R. J. (1977) 'Low pressure solubility of gases in liquid water', *Chemical Reviews*, 77(2), 219-262.

Worsnop, D. R., Morris, J. W., Shi, Q., Davidovits, P. and Kolb, C. E. (2002) 'A chemical kinetic model for reactive transformations of aerosol particles', *Geophysical Research Letters*, 29(20).

Yang, G. Q., Du, B. and Fan, L. S. (2007) 'Bubble formation and dynamics in gas-liquid-solid fluidization- A review', *Chemical Engineering Science*, 62(1-2), 2-27.

Zahardis, J. and Petrucci, G. A. (2007) 'The oleic acid-ozone heterogeneous reaction system: products, kinetics, secondary chemistry, and atmospheric implications of a model system - a review', *Atmospheric Chemistry and Physics*, 7, 1237-1274.

Ziemann, P. J. (2005) 'Aerosol products, mechanisms, and kinetics of heterogeneous reactions of ozone with oleic acid in pure and mixed particles', *Faraday Discussions*, 130, 469-490.

Zimmerman, W., Tesař, V., Butler, S. and Bandulasena, H. (2008) *Microbubble generation*.

Zimmerman, W. B., Hewakandamby, B. N., Tesar, V., Bandulasena, H. C. H. and Omotowa, O. A. (2009) 'On the design and simulation of an airlift loop bioreactor with microbubble generation by fluidic oscillation', *Food and Bioproducts Processing*, 87(C3), 215-227.

Zimmerman, W. B. and Rees, J. M. (2009) 'Optimal modelling and experimentation for the improved sustainability of microfluidic chemical technology design', *Chemical Engineering Research & Design*, 87(6A), 798-808.

Zimmerman, W. B., Tesar, V. and Bandulasena, H. C. H. (2011a) 'Towards energy efficient nanobubble generation with fluidic oscillation', *Current Opinion in Colloid & Interface Science*, 16(4), 350-356.

Zimmerman, W. B., Zandi, M., Tesar, V., Gilmour, D. J. and Ying, K. (2011b) 'Design of an airlift loop bioreactor and pilot scales studies with fluidic oscillator induced microbubbles for growth of a microalgae Dunaliella salina', *Applied Energy*, 88(10), 3357-3369.

Appendix A: Henry’s Law constant estimation with Aspen Plus

In this section, Aspen Plus was used to estimate the Henry’s Law constant. Based on the thermodynamics properties for the binary fluid system, Aspen Plus can generate the P-XY diagram between ozone and OL to determine the fugacity. All equations used to determine the fugacity are described in Chapter 4. However, for the multi-fluid system (ozone, OL, olive oil, used cooking oil and protic solvents), Aspen Plus cannot generate the P-XY diagram, but this difficulty can be overcome using the Flash model. In this model at the equilibrium conditions, the compositions of ozone in both the gas and liquid phases are estimated at different temperatures and pressures. These compositions can also be used to determine the fugacity, and Polymath is employed to solve the mathematics equations. The simulation steps for estimating the Henry’s Law constant via Aspen Plus and Polymath are described below.

A1.1 Binary fluid system

1. From the **Aspen Plus** list, select **Aspen Plus User Interface**.

2. Select **Material Stream and Mixer unit**, connect them together, and click **Next**.

3. At the **Components** tab, add ozone and OL as the chemicals, and click **Next**.

4. At the **Physical Properties** tap, select **Wilson,** and click **Next**.

5. At the **Streams** tab, add temperature, pressure, and mole flow of ozone and OL, and finally, click **Next**.

6. At the **Blocks** tab, set no pressure drop at the Mixer unit, and click **Next**.

7. From the **Tool** tab > **Analysis** > **Property** > **Binary** > **Analysis type**, and select **Pxy.**

8. Select **Component 1** as OL and **Component 2** as ozone; set **Temperature** at 20°C, 40°C, and 60°C, in turn; and Click **GO** to obtain the simulation result.

9. After plotting the fugacity versus the mole fraction of ozone in the liquid phase, Polymath software is used to create the polynomial equation of this relationship. This

equation is used to estimate the slope of this equation at x=0, which is the Henry' Law constant in units of pressure (atm).

A1.2 Multi-fluid system

The conditions from the binary fluid system can be used continuously for multi-fluid system, but the separation unit (Flash) and the protic solvents must be added to obtain the mole fraction of ozone in both gas and liquid phase. The details are described below.

1. Select **Flash 2** from the **Separators**, and connect with the material stream as shown in Figure B1.

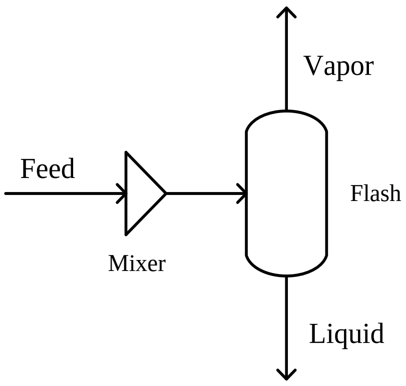

Figure A1 Process model for Henry's Law constant estimation

2. Select the **Components** tab, add methanol, ethanol, n-propanol, iso-propanol, and n-butanol as the chemicals, and click **Next**.

3. From the **Streams** tab, add the mole flow of the protic solvents, and click **Next**.

4. From the **Flash 2** at the **Specification** tap, set temperature and pressure.

5. To obtain the mole fraction of ozone in both the gas and liquid phases at different pressures, select **Model analysis tool** > **Sensitivity.** At the **Define** tab, set X for the mole fraction of ozone in the liquid phase and Y for the mole fraction of ozone in the gas phase. At the **Vary** tab, select **Block-Var** > **Flash** > **PRES**, vary the pressure from 0.001 atm to 167 atm, and click **Next** to obtain the simulation result. The Henry's Law constant can be estimated by following the details discussed in the previous section.

A1.3 Example of Henry's Law constant of ozone in water

Using the techniques described above with ozone and water, the fugacity versus the mole fraction of ozone in water and the polynomial equations generated by Polymath software at temperatures of 20°C, 40°C, and 60°C are plotted as shown in Figure A2. The Polymath software is also used to solve the polynomial equations via the derivative at x=0. The results show that the Henry's Law constants of ozone in water at temperatures of 20°C, 40°C, and 60°C are 3856.47 atm, 6100.04, and 9657.91 atm, respectively.

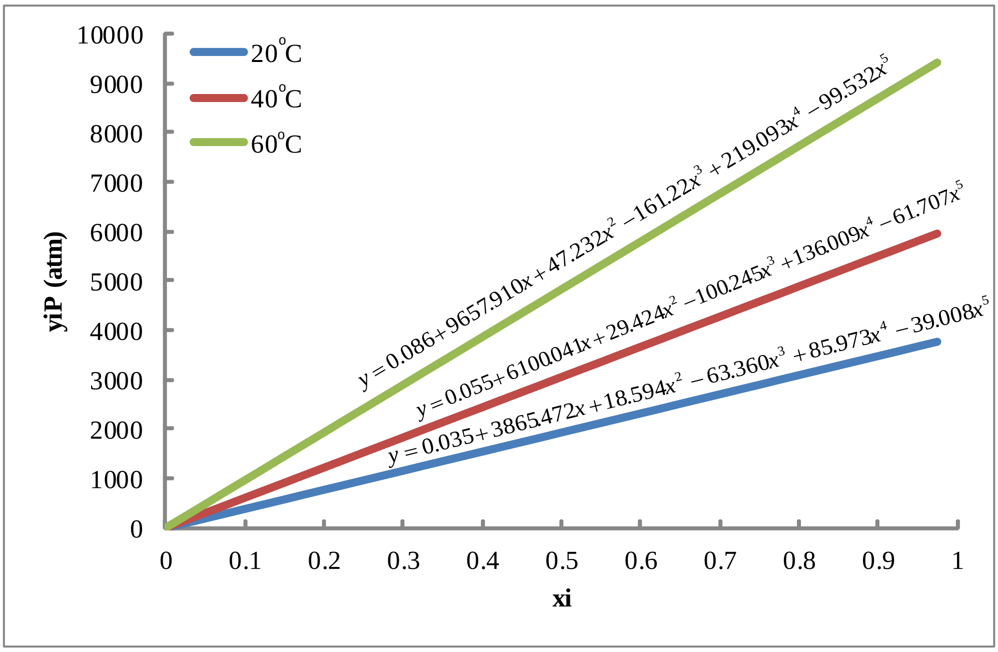

Figure A2 Composition dependence of the fugacity for ozone in water at different temperatures

In addition to the simulation results, the Henry's Law constants of ozone in water obtained from the measured value at temperatures of 20°C, 40°C, and 60°C are 3808.26 atm, 5887.92 atm, and 8639.26 atm, respectively (NIST 2011). Compared with the simulation results, the Henry's Law constants obtained from the experiments are slightly different. The percentage errors of the Henry's Law constants at temperatures of 20°C, 40°C, and 60°C are 4.2%, 6.5%, and 14.7%, respectively. Therefore, the simulation technique used in this study is acceptable for estimation of the Henry's Law constant between ozone and other solvents.

Appendix B: Fluid properties at atmospheric pressure

Table B1 Fluid properties of pure OL and mixtures

Temperature (°C)	**Density** (g/cm^3)	**Viscosity** (cP)	**Surface tension (**N/m)	**Diffusion coefficient** (cm^2/s)	**Henry constant** (atm)
Pure OL, MW = 282.47					
20	0.887	35.264	0.033	1.21×10^{-6}	6.997
40	0.874	18.170	0.031	2.52×10^{-6}	8.872
60	0.861	10.320	0.030	4.72×10^{-6}	10.842
Methanol:OL, 1.0:0.5, (0.941:0.059 based on volume fraction). MW = 198.99					
20	0.881	8.945	0.029	4.02×10^{-6}	8.083
40	0.868	5.283	0.028	7.27×10^{-6}	9.862
60	0.855	3.373	0.026	1.21×10^{-5}	10.949
Methanol:OL, 1.0:0.75 (0.914:0.086 based on volume fraction). MW = 175.14					
20	0.878	6.044	0.028	5.58×10^{-6}	8.265
40	0.865	3.712	0.027	9.70×10^{-6}	10.775
60	0.852	2.451	0.025	1.56×10^{-5}	11.481
Methanol:OL, 1.0:1.0 (0.888:0.112 based on volume fraction). MW = 157.25					
20	0.876	4.505	0.027	7.09×10^{-6}	9.178
40	0.863	2.849	0.026	1.20×10^{-5}	11.684
60	0.850	1.928	0.025	1.88×10^{-5}	12.553
Methanol:OL, 1.0:1.5 (0.841:0.159 based on volume fraction). MW = 132.21					
20	0.871	2.985	0.026	9.81×10^{-6}	10.912
40	0.858	1.966	0.025	1.59×10^{-5}	13.499
60	0.845	1.378	0.024	2.42×10^{-5}	15.341
Methanol:OL, 1.0:2.0 (0.799:0.201 based on volume fraction). MW = 115.517					
20	0.867	2.269	0.026	1.21×10^{-5}	12.075
40	0.854	1.536	0.024	1.90×10^{-5}	15.049
60	0.841	1.102	0.023	2.82×10^{-5}	18.552

Table B1 Fluid properties of pure OL and mixtures (con't)

Temperature (^{o}C)	**Density** (g/cm^3)	**Viscosity** (cP)	**Surface tension (**N/m)	**Diffusion coefficient** (cm^2/s)	**Henry constant** (atm)
Ethanol:OL, 1.0:1.0, (0.846:0.154 based on volume fraction). MW = 164.270					
20	0.871	6.467	0.028	5.05×10^{-6}	8.987
40	0.859	3.856	0.026	9.04×10^{-6}	10.284
60	0.847	2.454	0.024	1.51×10^{-5}	12.689
n-propanol:OL, 1.0:1.0, (0.811:0.189 based on volume fraction). MW = 171.280					
20	0.872	8.801	0.028	3.79×10^{-6}	8.840
40	0.859	5.030	0.026	7.08×10^{-6}	9.972
60	0.848	3.089	0.025	1.23×10^{-5}	12.711
Iso-propanol:OL, 1.0:1.0, (0.807:0.193 based on volume fraction). MW = 171.28					
20	0.867	9.163	0.027	3.64×10^{-6}	8.833
40	0.855	4.936	0.025	7.22×10^{-6}	9.994
60	0.843	2.885	0.024	1.31×10^{-5}	12.445
n-butanol:OL 1.0:1.0, (0.778:0.222 based on volume fraction). MW = 178.29					
20	0.869	10.123	0.029	3.36×10^{-6}	8.706
40	0.856	5.681	0.027	6.40×10^{-6}	9.690
60	0.843	3.440	0.026	1.12×10^{-5}	11.981
Acetic acid:OL, 1.0:1.0, (0.847:0.153 based on volume fraction). MW = 171.26					
20	0.905	6.511	0.030	5.12×10^{-6}	9.605
40	0.893	4.052	0.028	8.79×10^{-6}	11.261
60	0.881	2.692	0.027	1.41×10^{-5}	13.833

Table B2 Fluid properties of pure olive oil and used cooking oil with methanol

Temperature (°C)	**Density** (g/cm^3)	**Viscosity** (cP)	**Surface tension** (N/m)	**Diffusion coefficient** (cm^2/s)	**Henry constant** (atm)
Pure Olive oil, MW = 885.45					
20	0.912	89.12	0.035	8.51×10^{-7}	118.72
40	0.899	35.67	0.033	2.27×10^{-6}	175.63
60	0.885	18.20	0.032	4.73×10^{-6}	249.08
Olive oil: methanol, 1.0:1.0, (0.965:0.035 based on volume fraction). MW = 458.74					
20	0.904	7.162	0.029	7.62×10^{-6}	118.13
40	0.891	3.992	0.027	1.46×10^{-5}	175.71
60	0.879	2.561	0.026	2.42×10^{-5}	249.20
Used cooking oil : methanol 1:3 at 10% FFAs, MW = 248.22					
20	0.895	2.549	0.026	1.57×10^{-5}	118.14
40	0.883	1.647	0.025	2.60×10^{-5}	175.72
60	0.870	1.164	0.023	3.20×10^{-5}	249.20
Used cooking oil : methanol 1:3 at 15% FFAs, MW = 248.63					
20	0.893	2.848	0.026	1.41×10^{-5}	118.14
40	0.882	1.825	0.025	2.35×10^{-5}	175.72
60	0.868	1.278	0.023	3.57×10^{-5}	249.20
Used cooking oil : methanol 1:3 at 20% FFAs, MW = 250.62					
20	0.892	3.237	0.027	1.25×10^{-5}	118.14
40	0.880	2.053	0.025	2.10×10^{-5}	175.72
60	0.869	1.423	0.024	3.22×10^{-5}	249.20

Appendix C: Simulation steps for the reactor design by COMSOL Multiphysics

The simulation steps of 2D and 3D for modelling the bubbly flow application mode and heat transfer mode are followed;

C1.1 Reactor design: Axial symmetry 2D

Model Navigator

1. From the **Space dimension** list, select **Axial symmetry (2D).**

2. Select **Chemical Engineering Module > Momentum Transport > Multiphase Flow > Bubbly Flow**, then click **OK**.

Geometry Modelling

1. From the **Draw** menu, draw the model geometry as shown in Figure 3.8, then Click **OK**.

Subdomain Setting

1. From the **Physics** menu, select **Subdomain Settings**.

2. Putting the parameter as shown in Table C1 in **Subdomain Settings**, then click **OK**.

Table C1 Subdomain settings parameters for momentum transfer

Description	**Value/Expression**	**Unit**
Liquid density	1079.86 - 0.66T	kg/m^3
Dynamic viscosity of liquid	$14.22 – 0.158T + 6.651\times10^{-4}T^2 – 1.246\times10^{-6}T^3 + 8.776\times10^{-10}T^4$	Pa·s
Temperature	T	K
Molecular weight of gas	28×10^{-3}	kg/kmol
Gravity	-9.81	m/s^2
Bubble diameter	1000×10^{-6}	m

Point Setting

1. From the **Physics** menu, select **Point Settings**.

2. Select point at the top of the reactor, then select the **Point constraint** check box, then click **OK**.

Boundary Conditions

1. From the **Physics** menu, select **Boundary Settings**.

2. At the centre of the reactor, from the **Boundary type** list, select **Symmetry boundary**, and from the **Boundary condition** list, select **Axial symmetry**.

3. At the rest of the reactor, from the **Boundary type** list, select **Wall**, and from the **Boundary condition** list, select **No slip**.

4. Click the **Gas Phase** tab.

5. At the centre of the reactor, select the boundary condition **Axial symmetry**.

6. At the bottom of the reactor, select the boundary condition **Gas flux**. In the **N_P** edit field, type 0.002839.

7. At the top of the reactor, select the boundary condition to **Gas outlet**, then click **OK**.

Mesh Generation

1. From the **Mesh** menu, select **Free Mesh Parameters**.

2. On the **Subdomain** page, set the **Maximum element size** to 0.001.

3. On the **Boundary** page at the bottom of the reactor, set the **Maximum element size** to 0.001.

4. Click **Remesh**, then click **OK**.

Computing the Solution

1. Click the **Solver Parameters** button on the main toolbar.

2. In the **Times** edit field, type range (0, 300), then click **OK**.

3. Click the **Solve** button on the Main toolbar to start the calculation.

Adding Heat Transfer Module

1. From the Multiphysics menu, select Model navigator, then select Chemical Engineering Module > Energy Transport > Convection and Conduction > click **OK**, then click **Add**.

Subdomain Setting

1. From the **Physics** menu, select **Subdomain Settings**.

2. Putting the parameter as shown in Table C2 in **Subdomain Settings**, then click **OK**.

Table C2 Subdomain settings parameters for heat transfer

Description	Value/Expression	Unit
Liquid density	1079.86 - 0.66T	kg/m^3
Heat capacity at constant pressure	4.39T + 488.84	J/(kg·K)
Thermal conductivity	$0.208 – 1.928\times10^{-4}T$	
Initial temperature	293.15	K
Velocity field	ul and vl	m/s

Boundary Conditions

1. From the **Physics** menu, select **Boundary Settings**.

2. At the centre of the reactor, from the **Boundary type** list, select **Symmetry boundary**, and from the **Boundary condition** list, select **Axial symmetry**.

3. At the top of the reactor, select **Heat flux** from the **Boundary condition** list, and type -15× (T-293.15).

4. At the reactor wall, select **Thermal insulation** from the **Boundary condition** list.

5. At the bottom of the reactor, type 293.15 at the gas outlet area, and 333.15 at the rest, and click **OK**.

Computing the Solution

1. Click the **Solver Parameters** button on the main toolbar.

2. In the **Times** edit field, type range (0, 300), and click **OK**.

3. Click the **Solve** button on the Main toolbar to start the calculation.

C1.2 Reactor design: 3D

Axial symmetry (2D) as described in previous section can simply be converted to 3D using Revolve mode. The details are described below;

1. From the **Draw** menu of **Axial symmetry (2D)**, click the **Revolve** bottom.

2. From **Multiphysics** menu, select **Model Navigator**.

3. Select **Chemical Engineering Module > Momentum Transport > Multiphase Flow > Bubbly Flow**, then click **Add**.

4. Subdomain Setting, Point Setting, Boundary Conditions, Mesh Generation, and Computing the Solution are the same as **Axial symmetry (2D)**.